

Universität Potsdam

Mathematisch-Naturwissenschaftliche Fakultät
Institut für Physik & Astronomie
Ultraschnelle Dynamik in kondensierter Materie



Ultrafast Lattice Dynamics in Photoexcited Nanostructures

Femtosecond X-ray Diffraction with Optimized Evaluation Schemes

Publikationsbasierte Dissertation

zur Erlangung des akademischen Grades

doctor rerum naturalium

(Dr. rer. nat.)

in der Wissenschaftsdisziplin: Experimentalphysik

eingereicht an der
Mathematisch-Naturwissenschaftlichen Fakultät
der Universität Potsdam

von

Daniel Schick

geboren am 30.04.1985 in Rostock

Gutachter: Prof. Dr. Matias Bargheer
Dr. Klaus Sokolowski-Tinten
Prof. Dr. Aaron Lindenberg

Eingereicht am: 13. August 2013
Disputation am: 30. Oktober 2013

Published online at the
Institutional Repository of the University of Potsdam:
URL <http://opus.kobv.de/ubp/volltexte/2013/6882/>
URN <urn:nbn:de:kobv:517-opus-68827>
<http://nbn-resolving.de/urn:nbn:de:kobv:517-opus-68827>

to CARMEN

Abstract

Within the course of this thesis, I have investigated the complex interplay between electron and lattice dynamics in nanostructures of perovskite oxides. Femtosecond hard X-ray pulses were utilized to probe the evolution of atomic rearrangement directly, which is driven by ultrafast optical excitation of electrons. The physics of complex materials with a large number of degrees of freedom can be interpreted once the exact fingerprint of ultrafast lattice dynamics in time-resolved X-ray diffraction experiments for a simple model system is well known.

The motion of atoms in a crystal can be probed directly and in real-time by femtosecond pulses of hard X-ray radiation in a pump-probe scheme. In order to provide such ultrashort X-ray pulses, I have built up a laser-driven plasma X-ray source. The setup was extended by a stable goniometer, a two-dimensional X-ray detector and a cryogen-free cryostat. The data acquisition routines of the diffractometer for these ultrafast X-ray diffraction experiments were further improved in terms of signal-to-noise ratio and angular resolution. The implementation of a high-speed reciprocal space mapping technique allowed for a two-dimensional structural analysis with femtosecond temporal resolution.

I have studied the ultrafast lattice dynamics, namely the excitation and propagation of coherent phonons, in photoexcited thin films and superlattice structures of the metallic perovskite SrRuO_3 . Due to the quasi-instantaneous coupling of the lattice to the optically excited electrons in this material a spatially and temporally well-defined thermal stress profile is generated in SrRuO_3 . This enables understanding the effect of the resulting coherent lattice dynamics in time-resolved X-ray diffraction data in great detail, e.g. the appearance of a transient Bragg peak splitting in both thin films and superlattice structures of SrRuO_3 . In addition, a comprehensive simulation toolbox to calculate the ultrafast lattice dynamics and the resulting X-ray diffraction response in photoexcited one-dimensional crystalline structures was developed in this thesis work.

With the powerful experimental and theoretical framework at hand, I have studied the excitation and propagation of coherent phonons in more complex material systems. In particular, I have revealed strongly localized charge carriers after above-bandgap femtosecond photoexcitation of the prototypical multiferroic BiFeO_3 , which are the origin of a quasi-instantaneous and spatially inhomogeneous stress that drives coherent phonons in a thin film of the multiferroic. In a structurally imperfect thin film of the ferroelectric $\text{Pb}(\text{Zr}_{0.2}\text{Ti}_{0.8})\text{O}_3$, the ultrafast reciprocal space mapping technique was applied to follow a purely strain-induced change of mosaicity on a picosecond time scale. These results point to a strong coupling of in- and out-of-plane atomic motion exclusively mediated by structural defects.

Kurzdarstellung

Im Rahmen dieser Arbeit habe ich mich mit den komplexen Wechselwirkungen zwischen Elektronen- und Gitterdynamik in oxidischen Perowskit-Nanostrukturen beschäftigt. Dazu wurden verschiedene Proben mit intensiven, ultrakurzen Laserpulsen angeregt. Um die zeitliche Entwicklung der induzierten atomaren Umordnung zu untersuchen, wurden Femtosekunden-Pulse harter Röntgenstrahlung genutzt. Zunächst wurde die ultraschnelle Gitterdynamik in einfachen Modellsystemen mit zeitaufgelösten Röntgendiffraktionsexperimenten untersucht, um im Anschluss ähnliche Experimente an komplexeren Materialien mit mehreren Freiheitsgraden interpretieren zu können.

Die Bewegung der Atome in einem Kristall kann über Anrege-Abtast-Verfahren direkt mit gepulster, harter Röntgenstrahlung gemessen werden. Die Dauer der Röntgenpulse muss dafür einige hundert Femtosekunden kurz sein. Um diese ultrakurzen Röntgenpulse zu erzeugen, habe ich eine lasergetriebene Plasma-Röntgenquelle aufgebaut. Der Aufbau wurde um ein stabiles Goniometer, einen zweidimensionalen Röntgendetektor und einen kryogenfreien Kryostat erweitert und in Bezug auf das Signal-zu-Rausch-Verhältnis und die Winkelaufösung optimiert. Durch die Entwicklung einer schnellen Methode zur Vermessung des reziproken Raums konnte erstmals an solch einer Quelle eine zweidimensionale Strukturanalyse mit Femtosekunden-Zeitaufösung realisiert werden.

Die Anregung und Ausbreitung von kohärenten Phononen habe ich in optisch angeregten Dünnschicht- und Übergitterstrukturen untersucht. Eine entscheidende Rolle spielen dabei metallische SrRuO_3 Schichten. Durch die quasi-instantane Kopplung des Gitters an die optisch angeregten Elektronen in SrRuO_3 wird ein räumlich und zeitlich wohldefiniertes Druckprofil erzeugt. Dadurch kann der Einfluss der resultierenden kohärenten Gitterdynamik auf die zeitaufgelösten Röntgendiffraktionsdaten im Detail verstanden werden. Beobachtet wurde z.B. das Auftreten einer transienten Aufspaltung eines Bragg-Reflexes bei Dünnschicht- und Übergitterstrukturen aus SrRuO_3 . Außerdem wurde eine umfangreiche Simulationsumgebung entwickelt, mit deren Hilfe die ultraschnelle Dynamik und die dazugehörigen Röntgendiffraktionssignale in optisch angeregten eindimensionalen Kristallstrukturen berechnet werden können.

Der von mir entwickelte experimentelle Aufbau sowie das Simulationspaket zur Datenanalyse und -interpretation wurden anschließend für die Untersuchung kohärenter Phononen in komplexeren Materialsystemen eingesetzt. Im Speziellen konnte ich in multiferroischem BiFeO_3 eine stark lokalisierte Ladungsträgerverteilung nach einer optischen Femtosekunden-Anregung nachweisen. Sie ist die Ursache für einen quasi-instantanen und räumlich inhomogenen Druck, der die kohärenten Phononen in einem dünnen Film dieses Multiferroikums erzeugt. Außerdem habe ich die ultraschnelle Vermessung des reziproken Raums angewendet, um eine verzerrungsinduzierte Veränderung der Mosaizität in einem strukturell unvollkommenen Film aus ferroelektrischem $\text{Pb}(\text{Zr}_{0.2}\text{Ti}_{0.8})\text{O}_3$ zu verfolgen. Die Ergebnisse deuten auf eine ausschließlich durch strukturelle Defekte vermittelte Kopplung der atomaren Bewegungen parallel und senkrecht zur Flächennormalen des Filmes hin.

Contents

1. Introduction	1
2. List of Papers	5
3. Discussion	11
3.1. Setup of the laser-driven plasma X-ray source	11
3.2. Fundamentals of excitation and propagation of coherent phonons	14
3.3. Highlights	17
3.3.1. Ultrafast lattice dynamics in multiferroic BiFeO ₃	17
3.3.2. Ultrafast strain-induced changes of mosaicity in a ferroelectric thin film of Pb(Zr _{0.2} Ti _{0.8})O ₃	19
3.4. Context to other work in the group	20
4. Summary	21
5. Papers	25
I. Time-Resolved X-Ray Scattering	27
II. Normalization schemes for ultrafast x-ray diffraction using a table-top laser-driven plasma source.	39
III. Ultrafast reciprocal-space mapping with a convergent beam	49
IV. Ultrafast x-ray diffraction studies of photoexcited coherent phonons in SrRuO ₃ thin films	59
V. Comparing the oscillation phase in optical pump-probe spectra to ultrafast x-ray diffraction in the metal-dielectric SrRuO ₃ /SrTiO ₃ superlattice	71
VI. udkm1Dsim - A Simulation Toolkit for 1D Ultrafast Dynamics in Condensed Matter	79
VII. Localized excited charge carriers generate ultrafast inhomogeneous strain in the multiferroic BiFeO ₃	93
VIII. Following Strain-Induced Mosaicity Changes of Ferroelectric Thin Films by Ultrafast Reciprocal Space Mapping	101
Abbreviations	109
Bibliography	111
Danksagung	119
Selbständigkeitserklärung	121

A. Appendix	123
A.1. Additional papers	123
A.2. X-ray spectra from different tape materials	203
A.3. Low-temperature ultrafast X-ray diffraction data	205

1. Introduction

Functional materials allow for various applications in science and technology due to their intrinsic properties such as ferroelectricity, ferromagnetism, or superconductivity. In the last century, the discovery and tailoring of novel functional materials led to a tremendous progress in many fields such as information storage and communication, data processing, as well as energy harvesting and storage [1, 2]. Past and present, the increase in speed, the reduction in size, and the increase in efficiency have been the driving motivation to understand and control functionality in all kinds of matter.

Besides of the technological aspect, understanding functionality has always been of fundamental interest for scientists. In general, macroscopic functionality is linked to microscopic properties of matter such as its atomic structure. This insight has driven an enormous effort in improving structural analysis in various scientific fields such as biology, chemistry and physics. Today, X-ray, electron, and neutron scattering techniques allow for determining structural details with sub-atomic resolution even in three dimensions [3–5].

However, the detailed knowledge of structure can only be the initial step to understand functionality completely. Function manifests in non-equilibrium states of matter. Therefore, it is necessary to resolve transient states in order to disentangle the complex interplay between structure and functionality. The fundamental processes involved can be classified as electron dynamics, which occur on a few femtosecond time scale and below, as well as nuclear rearrangement on an atomic length scale, namely translational, rotational, or vibrational motion, which has a lower limit of approx. 10 fs to 100 fs [6, 7].

In order to resolve such ultrafast processes, sophisticated experimental methods are required. In particular, the advances in the development of femtosecond laser systems have pushed the temporal resolution in optical spectroscopy down to the time scales of fundamental electronic excitations. For time-resolved experiments the so-called pump-probe technique is typically employed. In this experimental scheme the investigated sample is prepared in a coherent state by an initial pump pulse. The subsequent dynamics of the excited system are detected with a delayed probe pulse as a function of the temporal delay between the two pulses. The highest temporal resolution achievable is determined by the duration and jitter of the two pulses [8].

Although femtosecond optical spectroscopy has proved to be a versatile tool to probe electron dynamics, it is a rather indirect method to follow the related nuclear motion. Novel sources of femtosecond electron and X-ray pulses provide new opportunities to access these missing pieces of information directly [7, 9–12]. They enable a more complete understanding of the coupling between electronic (charge, spin, orbital) and lattice degrees of freedom [13–17]. The final aim is to reach beyond a pure observation to selective control of functionality in complex materials.

On the one hand, suitable accelerator-based X-ray sources such as slicing facilities at

3rd generation synchrotrons and free electron lasers (FELs) have been recently developed [18–22]. On the other hand, laser-driven plasma X-ray sources (PXSs) have proved to be a practical alternative for ultrafast X-ray diffraction (UXRD) experiments with no beam-time limitation, relatively low costs for build-up and maintenance as well as an intrinsic synchronization between the optical pump and X-ray probe pulses [23–28]. In a PXS, electrons are accelerated by the electric field of an incident laser pulse with an intensity of more than $10^{16} \text{ W cm}^{-2}$. They penetrate a metal target and generate characteristic line emission (K-shell ionization and recombination) together with a broad bremsstrahlung background similar to conventional X-ray tubes. The released X-ray pulses typically have a duration of a few hundred femtoseconds which is generally determined by the interaction period of the electrons with the metallic target [29, 30]. In recent years, PXS-based UXRD experiments have been applied successfully, e.g. to follow the ultrafast lattice dynamics due to coherent phonon excitation and photoinduced phase transition [31–34].

In this cumulative thesis I present UXRD experiments utilizing a PXS in order to follow the photoinduced lattice dynamics in nanostructures on a femtosecond time scale. This thesis is based on eight selected publications which yield a coherent picture of this central task of my graduate work. Eight additional publications, to which I made contributions during my PhD studies, e.g., by performing measurements, conducting simulations, discussing physics, and commenting on or writing the manuscript, shall not be part of this thesis to increase the readability and to focus on one main topic. All of the 16 manuscripts are listed in Chapter 2 providing a complete citation as well as my personal contributions to each individual work. The manuscripts are referred to by their roman numerals, e.g. Paper I, throughout this thesis.

The central achievements of my doctoral work are grouped into three parts in this thesis:

1. The first three papers deal with the technical realization of the PXS and describe most of the experimental details of the setup (Paper I, II). Besides of various examples for application of the PXS, I discuss improvement strategies of the data acquisition (Paper II, III). Furthermore, the integration of a multidimensional structural analysis, which is known as reciprocal space mapping (RSM) [35–37], into the UXRD setup at the PXS is described (Paper III).
2. The next set of papers addresses the process of light-matter interaction within the model system of metallic SrRuO₃ (SRO). Especially the nature (speed and magnitude) of the electron-lattice coupling is of great importance to understand the subsequent coherent phonon dynamics that can be probed directly with UXRD techniques (Paper IV, V). The presented experimental results can be modeled successfully within a framework of numerical simulations which I have ported into a user-friendly toolbox for quick and easy comparison of experiment and theory (Paper VI).
3. The last two papers report on lattice dynamics in more complex material systems. The detailed understanding of the evolution of coherent phonons in the SRO model system allows to interpret ultrafast processes in materials with more degrees of freedom. As two highlights, I present UXRD measurements which reveal the excitation mechanism of coherent phonons in the prototype multiferroic

BiFeO₃ (BFO) (Paper VII), and secondly, experiments which focus on the coupling of in- and out-of-plane lattice dynamics in a structurally imperfect layer of ferroelectric Pb(Zr_{0.2}Ti_{0.8})O₃ (PZT) on a picosecond time scale (Paper VIII).

In the discussion in Chapter 3 the interconnection of these three parts is clarified and supplementary information is given. Furthermore, the additional eight publications, to which I contributed but which are not part of the main scope of this thesis, are briefly described.

2. List of Papers

In total I am author/co-author of 16 published and unpublished manuscripts which have been prepared during my doctoral studies in the work group ULTRAFAST DYNAMICS IN CONDENSED MATTER of Prof. Dr. Matias Bargheer at the University of Potsdam. In this thesis, however, I will focus on eight selected manuscripts, which are specified first. The following list contains the complete citation as well as my personal contribution to each individual manuscript. The papers are ordered with regards to their contents rather than their publication date.

The first three papers discuss the technical details of the plasma X-ray source (PXS) and present various examples for its application. The improvement of the data acquisition techniques for the demanding ultrafast X-ray diffraction (UXRD) experiments is one of the major topics. Furthermore, the implementation of a high-speed reciprocal space mapping (RSM) setup at the PXS is described in order to carry out multidimensional structure analysis with femtosecond temporal resolution.

- I. **Time-Resolved X-Ray Scattering** 27
D. Schick, C. von Korff Schmising, A. Bojahr, M. Kiel, P. Gaal, and M. Bargheer, *Ultrafast Phenomena in Semiconductors and Nanostructure Materials XV* 7937, (2011)
-

For this contribution I carried out the X-ray and all-optical experiments at the PXS, analyzed the data, and wrote the manuscript.

- II. **Normalization schemes for ultrafast x-ray diffraction using a tabletop laser-driven plasma source.** 39
D. Schick, A. Bojahr, M. Herzog, C. von Korff Schmising, R. Shayduk, W. Leitenberger, P. Gaal, and M. Bargheer, *Rev. Sci. Instrum.* 83, 2 (2012)
-

I implemented the different normalization schemes at the PXS and conducted the UXRD experiments. Furthermore, I analyzed the data and wrote the manuscript.

- III. **Ultrafast reciprocal-space mapping with a convergent beam** 49
D. Schick, R. Shayduk, A. Bojahr, M. Herzog, C. von Korff Schmising, P. Gaal, and M. Bargheer, *J. Appl. Cryst.* 46, 5 (2013)
-

I implemented the time-resolved reciprocal space mapping setup at the PXS and collected the presented experimental data. I analyzed the data, was responsible for most of the interpretation of the data, and wrote the manuscript.

The next set of papers addresses the fundamentals of the excitation and propagation of coherent phonons in the metal SrRuO₃ (SRO). The presented UXRD experiments further allow for deriving a detailed theoretical framework which is presented here.

- IV. **Ultrafast x-ray diffraction studies of photoexcited coherent phonons in SrRuO₃ thin films** 59
D. Schick, P. Gaal, A. Bojahr, W. Leitenberger, R. Shayduk, A. Hertwig, I. Vrejoiu, M. Herzog, and M. Bargheer, *arxiv* 1301.3324, (2013)
-

For this publication I conducted the experiments, participated in the interpretations, and commented on the manuscript.

- V. **Comparing the oscillation phase in optical pump-probe spectra to ultrafast x-ray diffraction in the metal-dielectric SrRuO₃/SrTiO₃ superlattice** 71
A. Bojahr, **D. Schick**, L. Maerten, M. Herzog, I. Vrejoiu, C. von Korff Schmising, C. J. Milne, S. L. Johnson, and M. Bargheer, *Phys. Rev. B* 85, 22 (2012)
-

I conducted the UXRD and all-optical experiments at the PXS and analyzed these data. Furthermore, I participated actively in the interpretation of the data and commented on the manuscript.

- VI. **udkm1Dsim - A Simulation Toolkit for 1D Ultrafast Dynamics in Condensed Matter** 79
D. Schick, A. Bojahr, M. Herzog, R. Shayduk, C. von Korff Schmising, and M. Bargheer, *Comput. Phys. Commun.* in press, (2013)
-

I have adapted the mathematical routines for the theoretical models which were already available in different programming languages from within our work group and combined them as a single object-orientated MATLAB toolbox with additional functionalities. I further wrote the complete manuscript and ran the included simulations.

The last two manuscripts discuss the deviations of the coherent phonon excitation and propagation from the ideal model system in two materials with a larger number of internal degrees of freedom.

In Paper VII, the excitation mechanism of coherent acoustic phonons in the prototypical multiferroic BiFeO₃ (BFO) after above-bandgap femtosecond optical excitation is discussed.

- VII. **Localized excited charge carriers generate ultrafast inhomogeneous strain in the multiferroic BiFeO₃** 93
D. Schick, M. Herzog, H. Wen, P. Chen, C. Adamo, P. Gaal, D. G. Schlom, P. G. Evans, Y. Li, and M. Bargheer, *Phys. Rev. Lett.* under review, (2013)
-

I conducted the UXRd experiments at the PXS, analyzed the data, and ran the simulations. I developed most of the presented interpretations and wrote the manuscript.

The propagation of coherent phonons in a ferroelectric thin film of Pb(Zr_{0.2}Ti_{0.8})O₃ (PZT) with a high density of structural imperfections is evaluated in Paper VIII.

- VIII. **Following Strain-Induced Mosaicity Changes of Ferroelectric Thin Films by Ultrafast Reciprocal Space Mapping** 101
D. Schick, A. Bojahr, M. Herzog, P. Gaal, I. Vrejoiu, and M. Bargheer, *Phys. Rev. Lett.* 110, 9 (2013)
-

I carried out the UXRd experiments and analyzed the data. Moreover I developed most of the presented interpretations, conducted the simulations, and wrote the manuscript.

The following manuscripts present further results which have been achieved during my graduate work. Since these papers are not part of the main scope of this thesis they are not discussed in detail. Below, the manuscripts are listed in chronological order and are also reprinted in the Appendix A.1 to give the reader quick access to their contents.

- IX. **Tailoring interference and nonlinear manipulation of femtosecond x-rays** 125
M. Herzog, **D. Schick**, W. Leitenberger, R. Shayduk, R. M. van der Veen, C. J. Milne, S. L. Johnson, I. Vrejoiu, and M. Bargheer, *New J. Phys.* 14, 1 (2012)
-

I participated in the experiments at the FEMTO slicing beamline at the Swiss Light Source (SLS).

2. List of Papers

- X. **Analysis of ultrafast X-ray diffraction data in a linear-chain model of the lattice dynamics** 137

M. Herzog, **D. Schick**, P. Gaal, R. Shayduk, C. von Korff Schmising, and M. Bargheer, *Appl. Phys. A* 106, 3 (2011)

I conducted the PXS-based experiments, analyzed this data and commented on the manuscript.

- XI. **Calibrated real-time detection of nonlinearly propagating strain waves** 151

A. Bojahr, M. Herzog, **D. Schick**, I. Vrejoiu, and M. Bargheer, *Phys. Rev. B* 86, 14 (2012)

I participated in the UXRD experiments at the PXS and commented on the manuscript.

- XII. **Time-domain sampling of x-ray pulses using an ultrafast sample response** 159

P. Gaal, **D. Schick**, M. Herzog, A. Bojahr, R. Shayduk, J. Goldshteyn, H. A. Navirian, W. Leitenberger, I. Vrejoiu, D. Khakhulin, M. Wulff, and M. Bargheer, *Appl. Phys. Lett.* 101, 24 (2012)

For this publication I conducted the UXRD experiments at the PXS, participated in the discussion, and commented actively on the manuscript.

- XIII. **Ultrafast Switching of hard x-rays** 165

P. Gaal, **D. Schick**, M. Herzog, A. Bojahr, R. Shayduk, J. Goldshteyn, H. A. Navirian, W. Leitenberger, I. Vrejoiu, D. Khakhulin, M. Wulff, and M. Bargheer, *J. Synchrotron Rad.* accepted, (2013)

For this publication I conducted the UXRD experiments at the PXS, participated in the discussion, and commented actively on the manuscript.

- XIV. **Direct time-domain sampling of subterahertz coherent acoustic phonon spectra in SrTiO₃ using ultrafast x-ray diffraction** 173

R. Shayduk, M. Herzog, A. Bojahr, **D. Schick**, P. Gaal, W. Leitenberger, H. A. Navirian, M. Sander, J. Goldshteyn, I. Vrejoiu, and M. Bargheer, *Phys. Rev. B* 87, 18 (2013)

I participated in the simulations and commented on the manuscript.

XV. **Brillouin scattering of visible and hard X-ray photons from optically synthesized phonon wavepackets** 183
A. Bojahr, M. Herzog, S. Mitzscherling, L. Maerten, **D. Schick**, J. Goldshteyn, W. Leitenberger, R. Shayduk, P. Gaal, and M. Bargheer, *Opt. Express* 21, 18 (2013)

For this publication I commented on the manuscript.

XVI. **Thermoelastic study of nanolayered structures using time-resolved x-ray diffraction at high repetition rate** 195
H. A. Navirian, **D. Schick**, P. Gaal, W. Leitenberger, R. Shayduk, and M. Bargheer, *Appl. Phys. Lett.* under review, (2013)

I analyzed part of the experimental data and conducted the simulations. I participated in the interpretation of the data and wrote major parts of the manuscript.

3. Discussion

In this chapter, I will discuss the individual results and the interconnection of the eight selected manuscripts which represent the central parts of my PhD work. After the discussion of the experimental setup in Section 3.1, I will focus on the fundamentals of excitation and propagation of coherent phonons due to ultrafast light-matter interaction for a simple model system in Section 3.2. In Section 3.3, I further apply the experimental and theoretical insights to study coherent phonons in more complex materials with a larger number of internal degrees of freedom. These results are highly relevant to the current discussion of equivalent systems in the community. In particular, I will discuss the excitation of phonons due to a complex electron-lattice coupling in the prototypical multiferroic BiFeO_3 (BFO) which reveals an ultrafast localized charge transfer within the unit cells of the material. Moreover, I will discuss the propagation of coherent phonons in a ferroelectric thin film of $\text{Pb}(\text{Zr}_{0.2}\text{Ti}_{0.8})\text{O}_3$ (PZT) where the in- and out-of-plane atomic motion are directly coupled by structural inhomogeneities. Finally, in Section 3.4 I will briefly describe how these achievements are related to other work in the group of ULTRAFAST DYNAMICS IN CONDENSED MATTER at the University of Potsdam.

3.1. Setup of the laser-driven plasma X-ray source

The main requirement to achieve most of the experimental results presented in this thesis is the plasma X-ray source (PXS) setup. Similar table-top setups were recently realized and applied to measure the ultrafast lattice dynamics of photoexcited solids [31–34]. The new PXS machine at the University of Potsdam was developed within the close collaboration with the INSTITUTE FOR SCIENTIFIC INSTRUMENTS GMBH (IfG) and is a development based on the setup presented in Ref. 28. A detailed description of the complete setup in Potsdam is given in Paper I and Paper II. Within the collaboration the IfG was responsible for the construction and testing of the central PXS components, namely the vacuum chamber, the electro-mechanical devices (i.e. stages and spools), the computer control of the machine, and radiation safety.

Another key component of the experimental setup is the 1 kHz laser system consisting of a mode-locked Ti:sapphire oscillator (Mantis, COHERENT, INC.) and a two-stage Ti:sapphire amplifier (Legend Duo, COHERENT, INC.) providing ultrashort laser pulses with a duration of 40 fs at a central wavelength of 800 nm containing an energy of up to 8 mJ per pulse. With the use of a 90° off-axis parabolic mirror a focus size of the optical laser light of less than 10 μm is achievable which allows for peak intensities of up to $10^{18} \text{ W cm}^{-2}$ in the focus. These extremely high intensities are focused onto a metallic target in the PXS and eventually generate a plasma. The released electrons are subsequently accelerated back into the metal by the electric field of the laser and emit X-rays

similar to conventional X-ray tubes but with a temporal profile related to the driving laser [29, 30]. Since less than 70 % of the laser power is utilized to pump the plasma generation the remaining optical power can be used to excite the samples in a pump-probe scheme. In order to provide optimal conditions to operate the PXS, I characterized the laser setup, including spectral, temporal, and contrast parameters, by various linear and non-linear optical measurements.

After building and characterizing the PXS and the laser system, both of these major components of the ultrafast X-ray diffraction (UXRD) setup were married in order to generate femtosecond hard X-rays in the laboratory. I characterized and enhanced the X-ray emission of the PXS by optimizing several optical and mechanical parameters of the setup, such as the laser light polarization, optical pulse length, optical focus distance to the copper tape, tape thickness, tape velocity and tension. In addition, I tested the applicability of different tape materials such as aluminum or brass in respect to their X-ray emission energy, maximum achievable X-ray flux, and mechanical stability. These results are shown in Appendix A.2 and provide a reference for future use of the setup.

In order to allow for advanced UXRD experiments a complete diffractometer setup was realized employing the PXS as an ultrashort X-ray source. The main components of this diffractometer are a Montel multilayer X-ray optics (INCOATEC GMBH) which collects the emitted X-rays from the PXS [38] and focuses them in the center of rotation of a two-circle goniometer (HUBER DIFFRAKTIONSTECHNIK GMBH & CO. KG). We have decided for a hybrid-pixel CMOS area detector (Pilatus 100k, DECTRIS, LTD.) for accumulating diffracted X-rays because of its high quantum efficiency of 98 % at 8 keV in single-photon counting mode, its zero electronic noise, its high dynamic range, and its fast read-out rate [39]. In addition, I implemented a pump-probe scheme including a mechanical delay stage in order to carry out time-resolved experiments as described in Paper I and II. A rather time-consuming but very important part of my work was the software implementation of the above listed hardware devices into the PC-based calibration, adjustment, and measurement routines, which I have developed using the LabView (NATIONAL INSTRUMENTS CORPORATION) programming language.

Finally, all of these intermediate steps allowed for preliminary static X-ray scattering experiments such as wide-angle X-ray scattering (WAXS), Debye-Scherrer diffraction, and X-ray reflectivity (XRR) as well as for time-resolved X-ray diffraction (XRD) measurements repeating the experiment given in Ref. 40. Paper I is the first publication containing these static as well as transient experimental results. These data do not only prove the versatile applicability of the PXS as source for different X-ray scattering geometries [41–43], they also establish the PXS at the University of Potsdam as a reliable source for UXRD experiments with sub-ps temporal resolution as well as sufficient X-ray flux and stability.

The experimental part of my PhD focused on UXRD measurements of epitaxial thin films and multilayer structures in WAXS geometry. At the beginning, I mainly measured transient Bragg peak intensities at a fixed scattering vector \vec{q} in reciprocal space, e.g. to follow the zone-folded longitudinal acoustical phonon (ZFLAP) mode in a photoexcited superlattice (SL) structure [34]. It turned out that large intensity fluctuations of the PXS are the dominant source of noise in the setup. In Paper II, I discuss several direct and

indirect normalization methods for the PXS intensity fluctuations such as rapid looping [44], substrate normalization [34], and direct normalization techniques utilizing an ionization chamber in the primary beam or an X-ray beam splitter [43]. In the manuscript, I introduce a normalization technique which employs the single reflection of the Montel X-ray optics. I was able to show that this quasi-monochromatic single reflection of the X-ray optics allows for a direct PXS intensity normalization which increases the signal-to-noise ratio (SNR) of time-resolved experiments significantly. In combination with a fast looping algorithm of the relevant scanning parameter UXR experiments can be performed much faster. This is of utmost importance due to the inevitable mechanical instabilities of the setup which prohibit very long integration times over days or weeks without readjustments of the experiment. The direct normalization technique further allows for a calibration of the normalization signal in order to record absolute intensities of the diffracted X-rays.

More detailed information on the structural dynamics in photoexcited nanostructures can be obtained by carrying out time-resolved rocking scans with the PXS diffractometer. In Paper III, I show that the relatively low resolution of the diffractometer in reciprocal space is dominated by the energy bandwidth and convergence of the incoming X-rays from the PXS. Due to the low brilliance of the PXS it is not reasonable to introduce additional monochromators or slits into the incoming X-ray beam for time-resolved experiments. Therefore, I derived a correction routine for rocking scans of laterally perfect samples utilizing the X-ray area detector in order to increase the resolution of the diffractometer without discriminating incoming or diffracted photons. When applying this correction method the resolution function of the diffractometer is determined solely by the energy bandwidth of the incoming X-rays and allows for high-resolution rocking scans with optimal counting statistics. As a novel application that goes beyond the previously demonstrated transfer of static X-ray technologies to the ultrafast time domain, I describe the implementation of a high-speed reciprocal space mapping (RSM) setup at the PXS utilizing the X-ray area detector as an angle-resolving detector [45–51]. This ultrafast reciprocal space mapping (URSM) technique with femtosecond temporal resolution allows for measuring the in- and out-of-plane lattice dynamics simultaneously and was already applied successfully in order to follow a purely strain-induced change of mosaicity in a ferroelectric thin film after photoexcitation of a neighboring metallic transducer layer, c.f. Section 3.3.2 and Paper VIII.

In order to study correlated solids over a wide external temperature range I have further implemented a closed-cycle helium cryostat (Model 4hW204A, ADVANCED RESEARCH SYSTEMS, INC.) at the PXS diffractometer. Although the closed helium cycle is desirable from an economic point of view, the cryostat expander causes heavy vibrations directly at the sample position. Therefore, the cryostat setup includes an additional vibration-damping extension (DMX-20 Interface) to carry out the very sensitive UXR pump-probe experiments from sample temperatures of 450 K down to 30 K. The vibration-damping extension and the sample holder are mounted directly to the goniometer sample manipulator, which allows for x, y, z translation and rotation of the sample by $\omega = \pm 10^\circ$. In addition, the complete cryostat including turbo vacuum pump is movable all over the experimental hutch in order to follow the goniometer position or to easily remove the cryostat from the experiment. For UXR experiments with optical pump pulses the

vacuum chamber of the cryostat must fulfill special requirements. On the one hand, X-ray photons must enter the chamber at a defined position and eventually exit the chamber under various Bragg angles through appropriate X-ray transparent windows, e.g. Kapton foil. On the other hand, the pump laser beam must enter the chamber through a special optical window and any reflected pump light from the sample must be blocked before it damages the sensitive Kapton foil. Last but not least, the vacuum chamber must hold pressures of 10^{-7} mbar which are necessary for low temperatures down to 30 K. Since at present there are no published results utilizing the cryostat at the PXS, I present low-temperature data of an SL sample in Appendix A.3, including a preliminary discussion of the data.

3.2. Fundamentals of excitation and propagation of coherent phonons

Ultrashort laser pulses allow for direct coherent excitation of internal degrees of freedom in condensed matter. One of the most elementary and low-energetic excitations are phonons. Phonons are coherently excited, i.e. the lattice oscillation has a fixed phase relation to the initial trigger, if the excitation of the phonons is faster than their vibrational period. The excitation mechanisms of coherent phonons are manifold, depending on the material and optical excitation wavelength. However, the different excitation mechanisms can be distinguished by the temporal and spatial profile of the lattice motion as well as from a displacive or impulsive excitation character. Hence, one can determine the excitation mechanism of coherent phonons directly by studying the excited atomic motion with UXRD techniques. The fundamental understanding of the evolution of coherent phonons is necessary to interpret more complex ultrafast dynamics in correlated solids with a strong coupling of the lattice to electronic degrees of freedom.

Perovskite oxide materials are of high technological relevance due to their wide spectrum of solid phases such as insulating dielectrics, metals, ferro- and antiferroelectrics, ferro- and antiferromagnets, multiferroics, superconductors, and thermoelectrics [52, 53]. The perovskite structure ABO_3 (A and B are cations) enables a large chemical and structural compatibility within various elements of the periodic table that can occupy the A- and B-sites. This allows for growing epitaxial thin films and nanoscale heterostructures with structural control down to the atomic level. Today, one can tailor the properties of functional oxides by various growth parameters such as crystallographic orientation, strain- and defect-states, chemical composition, interface density and boundary conditions, as well as confinements due to a reduced dimensionality. Additionally, the high structural perfectness of the epitaxial perovskite samples provide optimal conditions for UXRD experiments. Thus, perovskites are an ideal model system to study correlated electron-lattice phenomena with ultrafast methods and they are also the material class of choice of this work.

The metallic perovskite $SrRuO_3$ (SRO) is of particular physical interest, e.g., due to its $4d$ itinerant ferromagnetism below the Curie temperature of $T_C = 150$ K [54, 55] and its non-Fermi-liquid behavior [56]. However, the possibility to grow high-quality epitaxial

films [57], its high damage threshold [Paper IX], and its rapid electron-phonon coupling [58] render SRO as an ideal transducer layer for the generation of coherent phonons. We choose SRO as a model system to study the photoexcitation and propagation of coherent acoustic phonons with means of UXRd experiments at the PXS.

The dominant phonon excitation process in metals is electron-phonon coupling [59]. Within a two-temperature model (TTM) [60] the laser excitation instantaneously heats up the free electrons in the conduction band into a non-Fermi-Dirac distribution via inter- or intraband transitions. The non-thermalized electrons may travel ballistically through the metal until they thermalize due to electron-electron scattering. The phononic system is heated subsequently due to electron-phonon scattering until both subsystems equilibrate. Longitudinal acoustic phonons are generated either by electronic and/or phononic thermal pressure depending on the temperatures and Grüneisen parameters [61] of the individual subsystems. Finally, incoherent acoustic phonons are excited which remove the deposited energy from the system in a diffusion process (heat transport).

In Paper IV, we investigate two SRO layers of different thicknesses grown epitaxially onto a SrTiO₃ (STO) substrate. The UXRd data reveal a transient Bragg peak splitting or shifting for the thicker or thinner film, respectively. Although the observed UXRd patterns seem to be rather different, we can link the discrepancies solely to the layer thickness and the related spatial excitation profile. In order to simulate the experimental data, we assume an instantaneous thermal stress due to the rapid electron-phonon coupling in the SRO layer after photoexcitation of the free electrons. We further assume a spatial profile of the thermal stress which corresponds to the exponentially decaying optical excitation. We calculate the subsequent lattice dynamics by a linear-chain model (LCM) of masses and springs and derive the resulting UXRd pattern from dynamical X-ray theory. The excellent agreement between the experimental UXRd data and the simulation confirms that the photoexcited electrons in SRO must couple rapidly to the lattice and significant ballistic and/or diffusive electron transport is negligible, since this would additionally smear out the spatial excitation profile. Interestingly, the impulsive optical heating of the metal layer leads initially to a rapid expansion of only part of the film. Moreover, for a strongly inhomogeneous spatial stress profile the weaker excited regions exhibit even a compressive strain. As a consequence, for the SRO layer with a thickness of more than double the optical penetration depth of the pump light, a transient Bragg peak splitting in the according UXRd data is observable. From the comparison of the UXRd data for the two different samples we can further deduce universal features of the coherent phonon evolution in similar thin film samples.

These findings are also applicable to more complex structures, such as SLs of e.g. metallic SRO and dielectric STO. The according lattice dynamics and UXRd patterns can be modeled similarly to what is described above and show an excellent agreement with the experimental data, c.f. Paper IX. In Paper X we also observe a transient Bragg peak splitting for an SL structure which again points to the presence of the same coherent phonons in both thin films and SL structures of SRO. In an SL, all excitations and interactions are described in a mini-Brillouin zone, which is substantially smaller than the Brillouin zone of the constituting crystal unit cells. Hence, the acoustic dispersion is folded into the mini-Brillouin zone, establishing so-called zone-folded longitudinal acous-

tical phonons (ZFLAPs). Optical excitation yields ZFLAPs close to the center of the mini-Brillouin zone ($k = 0$, $\omega \neq 0$) in addition to the acoustic modes driving the transient Bragg peak splitting discussed above. The excited ZFLAPs are observable as intensity oscillations of an SL Bragg peak in UXRD experiments and exhibit very short oscillation periods of only few picoseconds and less, depending on the thickness of the individual sublayers in the SL [34]. Even for a few nanometer thickness per sublayer the Bragg peak intensity can be rather high for a sufficiently large number of double layer repetitions. This allows for deducing the onset of the atomic motion in the SL with much higher accuracy compared to thin film samples. However, determining the exact time delay between X-ray probe and optical pump pulse is elusive because the actual arrival time of the optical pump pulse cannot be determined without hard X-ray-optical cross correlation techniques. To solve this problem, we used a combined optical and X-ray pump-probe experiment at the PXS in order to record the lattice motion and optical response of an SRO/STO SL in the same setup, c.f. Paper V. With the help of the combined X-ray and all-optical pump-probe experiment we were able to determine the electron-phonon coupling time in SRO to approx. 100 fs. This is again in excellent agreement with the former assumption of the build-up of a quasi-instantaneous thermal stress in SRO after photoexcitation. Individual X-ray and all-optical experiments at higher fluences evidence a relative shift of the onset of the lattice motion to earlier times, which would be consistent with an instantaneous “displacive excitation of coherent phonons” (DECP) mechanism in SRO for this high-excitation regime. In total, the presence of both, the peak shift/splitting and the rapid intensity oscillations, render similar SL structures to be ideal cross correlators for UXRD experiments with hard X-ray radiation [62, 63].

The theoretical framework described above consists of a set of analytical and numerical simulations which model the excitation and propagation of coherent [Paper IV, IX, X] as well as of incoherent phonons [64, Paper XVI], and calculate the final experimental observable: the transient X-ray diffraction response. Our simulations have been tested and refined against a collection of high-quality UXRD data from different short pulse X-ray sources, namely the PXS, the FEMTO slicing beamline at the Swiss Light Source (SLS), the ID09B beamline at the ESRF, and the XPP/KMC3 beamline at BESSY II. However, the execution of these simulation was rather tedious and limited in speed, since the individual parts of the scripts were written by different authors in different programming languages with incompatible interfaces and without optimization regarding the computational speed. In my PhD work, I developed a toolbox, named `UDKM1DSIM`, using the `MATLAB` (The MathWorks Inc.) programming language in order to simulate the structural dynamics and the according X-ray diffraction response in one-dimensional (1D) sample structures after ultrafast photoexcitation. The `UDKM1DSIM` toolbox was applied to calculate most of the simulation presented in my thesis. The major theory and part of the documentation of the `UDKM1DSIM` toolbox are presented in Paper VI. Within the toolbox the user is supported by a rich database of element-specific parameters in order to create arbitrary 1D layered sample structures down to the atomic level. The optical excitation is realized within an N -temperature model (NTM) which allows for a finite duration of the excitation pulse. The lattice dynamics (coherent and incoherent) are calculated in an LCM of masses and springs which allows to include phonon damping and

interatomic anharmonicities. These simulations of anharmonic linear chains form a substantial part of the papers collected in Section 3.4. The X-ray diffraction response of the photoexcited sample is derived from dynamical X-ray theory and is optimized in speed by utilizing MATLAB's parallel computing capabilities. Furthermore, the UDKM1DSIM toolbox is highly modular and allows for introducing user-defined results at any step in the simulation procedure. Last but not least, the complete toolbox is open source and published under the BSD license. It can be downloaded from the following website: <http://www.udkm.physik.uni-potsdam.de/udkm1dsim>.

3.3. Highlights

In this section I will discuss the excitation mechanism of coherent phonons in the multiferroic BiFeO₃ (BFO), c.f. Paper VII, and the propagation of coherent phonons in structurally imperfect ferroelectric Pb(Zr_{0.2}Ti_{0.8})O₃ (PZT), c.f. Paper VIII. It is important to see that before the interpretation of finer details of lattice dynamics, which are modified by the subtle interaction in complex materials, we had to safely and fully understand the dynamics of simpler structures as described in Section 3.2, where e.g. the excitation is instantaneous and the propagation of acoustic phonons is not coupled to other degrees of freedom.

3.3.1. Ultrafast lattice dynamics in multiferroic BiFeO₃

The recent advances in UXR methods allowed for revealing the complex interplay between electronic and lattice degrees of freedom for ferroelectric [14, 16, 65], magnetic [58], as well as for charge- and orbital-order related phenomena [15, 17, 66] in selected prototypical material systems. We investigated the excitation of coherent acoustic phonons in a multiferroic thin film after above-bandgap excitation with femtosecond laser pulses in order to conclude on the inherent electron dynamics.

Multiferroics are one of the most promising material classes for applications due to their intrinsic coupling of ferroelectricity and magnetism [67–69]. The only known stable multiferroic at room temperature is the perovskite BFO [70, 71]. Due to its relatively small band gap of approx. 2.7 eV, BFO is a promising candidate for applications in spintronics and memory devices [71] with a perspective for ultrafast optical switching, as it has been recently realized for purely ferroelectric [14] and purely magnetic [72] materials.

Ultrafast carrier dynamics after above-bandgap femtosecond optical excitation are believed to cause the photovoltaic effect [73–75] as well as the excitation of coherent phonons in BFO [76, 77]. In a recent synchrotron-based UXR study with a temporal resolution of 100 ps a linear dependence between the transient lattice strains and the number of excited charge carriers in BFO over several nanoseconds was revealed [65]. The authors concluded that depolarization field screening (DFS) including macroscopic transport of the carriers to the interfaces and a successive inverse piezoelectric effect could be the dominant process of coherent phonon excitation in the thin BFO film.

In Paper VII we present PXS-based UXR data of the very same sample that was investigated in Ref. 65 under similar excitation conditions. Due to the higher temporal

resolution of the PXS compared to the synchrotron experiments, we were able to follow the excitation of the coherent phonons. From the comparison of the experiments with our simulations, c.f. Paper VI, we identified a sound-velocity limited evolution of the structural response within 10 ps indicating a quasi-instantaneous stress driving the coherent phonons. This finding was only possible due to the exact knowledge of the temporal overlap of the optical pump and X-ray probe pulses, as described in the previous section.

We further observed a significant Bragg peak broadening of the BFO film, which indicates an inhomogeneous spatial strain profile in the layer. The peak broadening is observable from picosecond to several nanosecond delays which was reconfirmed by new synchrotron-based UXRD data recorded at the Advanced Photon Source (APS). We can rule out a dominant thermal contribution for the long-lasting inhomogeneous spatial strain profile, since heat would equilibrate too fast in the thin BFO film.

From the PXS-based data we can firmly conclude, that DFS cannot be the dominant mechanism of the coherent phonons excitation in the thin BFO film because:

- DFS would require a finite time for the excited charge carriers to travel to the interfaces which is in contradiction to the quasi-instantaneous stress that is required to drive the observed coherent lattice dynamics
- DFS should result in a rather homogeneous spatial strain profile due to the capacitor-like geometry which is in contradiction to the significant Bragg peak broadening
- at high excitation fluences the depolarization field would be fully screened and the resulting strain amplitude saturates – this was not observed for the BFO film even for fluences close to the damage threshold of the film

Therefore, we propose a model of localized charge carrier displacement within the BFO unit cells after above-bandgap excitation resulting in a lattice distortion possibly due to the inverse piezoelectric effect. According charge-transfer excitonic states have been recently reported in BFO by theory and experiment and are able to drive the instantaneous stress most likely together with contributions resulting from the population of anti-bonding orbitals [73, 78]. Due to the fast trapping of the excited charge carriers in the film, the stress is maintained according to the optical excitation profile over several nanoseconds until the carriers decay radiatively [73].

We believe, that this study provides an important benchmark for testing theoretical models of the photovoltaic response of ferroelectric oxide materials [16, 79] which can also predict the contribution of the deformation potential from anti-bonding orbitals. The subtle distinction between these processes could in principle be given by more nontrivial UXRD experiments where an additional (e.g. electronic) control over the polarization is implemented.

3.3.2. Ultrafast strain-induced changes of mosaicity in a ferroelectric thin film of $\text{Pb}(\text{Zr}_{0.2}\text{Ti}_{0.8})\text{O}_3$

Although the progress in preparing epitaxial films of functional oxides permits controlling most growth parameters down to the atomic level [52, 53, 80], the origin of several types of dislocations especially in domain-forming materials is still elusive [81]. The influence of structural defects and nanoscale inhomogeneities on the properties of functional materials has been studied in detail by experiment and theory [82, 83]. In UXR D experiments only the influence of nanodomains in respect to the formation of transient phases has been considered [66]. The role of static structural defects, however, remained unexplored on such an ultrafast time scale.

In Paper VIII we investigate the coherent phonon propagation in a thin film of ferroelectric PZT after photoexcitation of an underlying SRO transducer layer. The sample geometry is rather typical for capacitors of thin PZT films and very similar to structures which are used in real applications. Due to a lattice mismatch, the epitaxial PZT film encounters misfit dislocations at the SRO interface and threading dislocations expanding through the entire layer due to stress relaxation [81]. We employed the ultrafast reciprocal space mapping (URSM) technique implemented at the PXS, as described in Paper III, to obtain information on the reversible in- and out-of-plane lattice dynamics simultaneously with sub-ps temporal resolution. The pump light is exclusively absorbed in the metallic SRO and triggers coherent phonon wavepackets at the SRO interface. While the SRO layer starts to expand, a compression wave is sent to the PZT layer. The compression wave in PZT is later reflected at the sample-air interface and eventually changes its sign. The subsequent expansion wave in PZT travels back into the SRO layer and finally into the STO substrate.

With the help of our theoretical models, c.f. Paper VI, we simulated the photoinduced 1D lattice dynamics and the according symmetrical UXR D signals. In order to fit the transient out-of-plane shift and width of the PZT and SRO Bragg peaks to these models, we introduced a variable phonon damping of PZT as an adjustable parameter which mimics the excitation of in-plane lattice dynamics. We achieved the best fit of the out-of-plane data for a 50 times larger phonon damping in PZT for the expansion than for the compression wave. At the same time, we observed a significant broadening of the reciprocal lattice point (RLP) of the PZT layer in the q_x dimension, which we interpret as a change of its mosaicity. Essentially, this means that for the expansion wave traveling through the PZT layer mechanical energy from the out-of-plane lattice dynamics is coupled into the in-plane atomic motion very efficiently. We did not observe the converse effect for the compression wave in PZT, which might be sterically forbidden, nor in rather perfect thin film samples without the existence of dislocations or defects.

These URSM experiments indicate that in mismatched epitaxial films of oxide materials in-plane phenomena emerge on a hundred picosecond time scale and are solely induced by the presence of domains and dislocations. A better understanding of such time-domain effects in novel functional oxide materials will be important for studying the influence of structural defects on the ultrafast response of collective phenomena, such as piezoelectricity.

3.4. Context to other work in the group

The results discussed above are closely related to other work in the group of ULTRAFast DYNAMICS IN CONDENSED MATTER at the University of Potsdam. Besides of UXRd experiments at the XPP/KMC3 beamline at BESSY II, which provide temporal resolution from 100 ps down to 10 ps in low- α mode [84], also all-optical spectroscopy is used to study coherent phonons [85]. On the one hand, all-optical experiments are less demanding from an experimental point of view. On the other hand, the extracted information cannot reveal the atomic motion directly, such as the absolute strain amplitudes or the true phase of the lattice motion of a ZFLAP mode in an SL, which might depend on the optical probe wavelength and pump fluence [86].

We have carried out UXRd experiments to qualitatively measure the amplitude, period, and phase of the triggered lattice oscillations in photoexcited nanostructures. This yields a calibration of the underlying lattice dynamics for the all-optical experiments even at strongly non-linear strain amplitudes, c.f. Paper V and XI. We were further able to synthesize and follow the propagation of quasi-monochromatic phonon wavepackets [87, Paper XIV]. In Paper XV, we describe the analogy between Brillouin scattering of optical and X-ray light from such optically synthesized acoustic phonon wavepackets.

We were also able to theoretically propose and experimentally test novel physical applications. One of the most promising application of coherent phonon dynamics is the manipulation of the temporal profile of X-ray pulses in order to provide additional sources for UXRd experiments [88]. We have realized three different concepts of switching of hard X-rays: by the intensity modulation of an SL Bragg peak due to the excitation of a ZFLAP mode [62], by the shift of an SL Bragg peak due to propagating strain waves in the multilayer structure [63], and by the shift of a Bragg peak of a thin film due to propagating strain waves in the layer [Paper XIII]. The last concept is also applicable to sample X-ray pulses of synchrotron storage rings, as described in Paper XII, and as an X-ray-optical cross correlator, similar to what was described in Paper V.

Due to the overlap of accessible time scales of UXRd experiments at the PXS (200 fs–8 ns) and the XPP/KMC3 beamline at BESSY II (10 ps–5 μ s), coherent and incoherent lattice dynamics can be studied also in combined experiments. Here, the synchrotron-based experiments are especially suited to follow the generally slower thermal dynamics due to the lower temporal resolution and the extremely high sensitivity for changes of the lattice constants on the order of $\Delta c/c = 10^{-6}$ [89].

In Paper XVI we applied synchrotron-based UXRd experiments at high-repetition rate to study the thermoelastic response of the very same sample that was investigated before in Paper VIII. The complex transient thermoelastic response, which is closely related to the negative thermal expansion coefficient along the ferroelectric polarization vector in PZT, provides a suitable reference for testing thermoelastic models on ultrafast time and nanometer length scales, c.f. Paper VI. The investigation of heat diffusion in even smaller sample structures, such as SLs [64], further allows to study the applicability of Fourier theory of thermal transport on the nanoscale, which might differ dramatically from bulk samples [90–93] and material properties might alter from bulk values due to size effects or a growth dependent interface resistance [94].

4. Summary

In conclusion, I built up a complete plasma X-ray source (PXS) setup, including laser system, diffractometer, as well as pump-probe and cryostat setup in order to carry out ultrafast X-ray diffraction (UXRD) experiments of photoexcited nanostructures. In addition to the optimization and testing of the experimental equipment, I implemented various PC-based calibration, adjustment, and measurement routines for the PXS setup. The direct normalization technique which utilizes a single reflection of the Montel multilayer optics allows for a significant increase of the signal-to-noise ratio (SNR) and hence, a decrease of the total integration time. I have further improved the angular resolution of the diffractometer while preserving optimal counting statistics due to the implementation of the convergence correction routine for rocking scans of laterally perfect crystalline samples. The implementation of the high-speed reciprocal space mapping (RSM) at the PXS enables two-dimensional analysis of structural dynamics with femtosecond temporal resolution for the first time.

The advanced experimental routines at the PXS allowed for fundamental insights into the excitation and propagation of coherent phonons in thin films and superlattice (SL) structures consisting of the model system SrRuO₃ (SRO). Moreover, the electron-phonon coupling time in this metallic perovskite could be deduced to be less than 100 fs which causes extremely sharp strain fronts in photoexcited SRO samples. These findings further allowed for linking the transient Bragg peak splitting in thin films and SL structures of SRO exclusively to the evolution of coherent phonons. The collection of high-quality UXRD data from different short-pulse X-ray sources lead to the development of a set of numerical simulations which I have adapted and refined in order to combine them in an unifying framework. The `UDKM1DSIM` toolbox simulates the ultrafast lattice dynamics in one-dimensional (1D) sample structures after photoexcitation and is published under an open-source license.

I have applied the comprehensive theory of coherent phonon excitation and propagation in the SRO model system to study more complex materials with additional degrees of freedom. I have investigated the ultrafast lattice dynamics in multiferroic BiFeO₃ (BFO) after above-bandgap optical excitation and identified strongly localized excited charge carriers as the origin of the quasi-instantaneous and spatially inhomogeneous strain in BFO. Furthermore, I have applied the novel ultrafast reciprocal space mapping (URSM) technique to follow a purely strain-induced change of mosaicity in a structurally imperfect film of ferroelectric Pb(Zr_{0.2}Ti_{0.8})O₃ (PZT) on a picosecond timescale, which indicates a strong coupling between in- and out-of-plane lattice dynamics even on ultrafast time scales.

The experimental setup and theoretical routines, which I have realized during my graduate work, were further applied to related work in the group of ULTRAFAST DYNAMICS

IN CONDENSED MATTER at the University of Potsdam. We have employed UXRD experiments at the PXS to calibrate the lattice motion in photoexcited nanostructures to obtain a better understanding of all-optical reflectivity data of coherent phonon propagation. We were further able to apply our knowledge in order to theoretically design and experimentally test several concepts for shortening and sampling of hard X-ray pulses from synchrotron radiation facilities. We also studied thermal transport in nanostructures after heating with femtosecond laser pulses.

Future prospects Recently, free electron laser (FEL) sources of soft and hard X-ray radiation became available, providing unprecedented brightness, coherence and ultrashort pulse durations [22]. Already the preliminary experiments at these machines have pushed the community close to the frontiers of spatial, energy, and temporal resolution. Although PXS machines are weaker in brightness by several orders of magnitude and provide no transverse coherence, they offer all-day access for UXRD experiments with femtosecond temporal resolution.

The implementation of different X-ray scattering geometries utilizing the PXS as an ultrafast source for hard X-rays, such as X-ray reflectivity (XRR), Debye-Scherrer diffraction [41, 42], diffraction in Laue geometry [43], or even small-angle X-ray scattering (SAXS), promises novel insights in material classes such as soft matter, composites, amorphous solids, or solids which are only available as powders. With the use of other target materials than copper in the PXS, one can overcome or select certain X-ray absorption edges in X-ray scattering experiments in the particular materials of interest. Aluminum targets proved to serve as a reliable source for a broad bremsstrahlung spectrum, which can be utilized for time-resolved X-ray spectroscopy at the PXS [95].

The systematic study of the dynamics in photoexcited functional materials under varying external stimuli was already initiated by the implementation of the low-temperature cryostat setup at the PXS. In addition to temperature changes, external fields and stress might be applied to the sample in order to alter its energetic landscape and to gain a deeper insight into the complex coupling of its internal degrees of freedom.

Although the measurement of nanoscale heat transport was not within the main focus of this thesis, preliminary data of photoexcited SRO films prove that PXS-based experiments are able to provide new insights into this technologically highly relevant field (data not shown). Especially the interconnection between the different heat-carrying (quasi-)particles (electrons, phonons, magnons) at ultrafast time scales might offer new routes for efficient device cooling [96]. Also the influence of thermal interfaces in nanostructures [64, 94] is of technological relevance, e.g. for future thermoelectrics [97].

The presented UXRD study of the multiferroic BFO motivates the request for complementary spectroscopic experiments, since the actual electronic origin of the observed atomic motion is not resolvable with the applied hard X-ray methods directly. The use of complementary soft X-ray techniques, such as time-resolved X-ray diffraction and spectroscopy, as well as resonant inelastic X-ray scattering, allow for probing electronic dynamics in a selective manner, thus providing the missing pieces of information [17, 98].

The novel URSM technique can be applied to gain a deeper insight into the coupled in- and out-of-plane lattice dynamics with femtosecond temporal resolution. A more detailed

study of asymmetrical and higher order Bragg reflections is required to reveal a more complete picture of defect-mediated lattice dynamics in samples similar to the structurally imperfect thin film of PZT investigated in this thesis. In addition, the theoretical models for ultrafast lattice dynamics have to be extended into three dimensions and to include structural defects and domains. However, the implementation of a similar URSM setup at a time-resolved beamline at a 3rd generation synchrotron will allow for fast and reliable two- or even three-dimensional [49] structural analysis with ideal resolution in reciprocal space to follow, e.g. ferroelastic domain formation on the relevant time scales from 100 ps to microseconds.

5. Papers

Paper I

Time-Resolved X-Ray Scattering

D. Schick, C. von Korff Schmising, A. Bojahr, M. Kiel, P. Gaal, and M. Bargheer

Ultrafast Phenomena in Semiconductors and Nanostructure Materials XV 7937, (2011)

Invited Paper

Time-Resolved X-Ray Scattering

Daniel Schick^a, Clemens von Korff Schmising^b, André Bojahr^a, Mareike Kiel^a, Peter Gaal^a,
Matias Bargheer^a

^aInstitut für Physik und Astronomie, Universität Potsdam, Karl-Liebknecht-Str. 24-25,
14476 Potsdam/Golm, Germany

^bAtomic Physics Division, Department of Physics, Lund University, P.O. Box 118,
SE-221 00 Lund, Sweden

ABSTRACT

Ultrafast x-ray diffraction (UXRD) has become more and more prevalent in various scientific disciplines that are interested in directly observing atomic motion in real time. The timescale, amplitude and phase of collective atomic motion can be determined with high accuracy, even when the induced amplitude is smaller than thermal fluctuations. The structural rearrangements induced by an ultrafast stimulus (charge carriers excitation or heat deposition by a laser pulse) can be recorded in real time. Here we report on a new laser-driven plasma-x-ray source (PXS) and discuss different applications which will be addressed in UXRD experiments.

Keywords: ultrafast x-ray diffraction

1. INTRODUCTION

Probing atomic motions in condensed matter on the fs-timescale enables the investigation of various physical effects which are directly linked to the atomic structure. Ultrafast x-ray diffraction (UXRD) is capable of monitoring such dynamics with a sub-picometer spatial and sub-picosecond temporal resolution.¹⁻³ An optical pump pulse excites atomic motion in the sample and a delayed hard x-ray probe pulse measures the lattice changes for different times, t_i , creating a series of snapshots of the atomic positions. The development of novel accelerator based and table-top sources for hard x-ray fs-pulses goes along with a large impact on physics, chemistry, biology and material science. However, each application has specific requirements regarding the x-ray pulse energy, bandwidth, pulse duration, beam profile and focusing conditions. For a long time the first limitation for experiments with time-resolution in the sub-picosecond range has been the low number of x-ray photons. The pulse width of high brilliance synchrotrons is normally limited to 50–150 ps, where the exact number is determined by the electron bunch width and the aperture limiting the spatial profile of the x-ray beam. Besides low- α -mode^{4,5} which reduces the pulse duration by an order of magnitude, the femto-slicing technique enables the generation of 100 fs pulses in undulators, however, with a flux of approx. 10^4 – 10^5 photons/s on the sample.⁶⁻⁸ The recently launched free electron laser LCLS in Stanford and the upcoming XFEL in Hamburg provide orders of magnitude higher brilliance together with sub-picosecond resolution.⁹

In parallel, laboratory-based laser plasma sources have reached sufficient reliable performance to be an alternative to the above mentioned machines.¹⁰ Sources working at kilohertz repetition rate offer high stability and large flux up to 3×10^6 photons/s on the sample using x-ray optics.^{11,12} Besides their relatively low cost for building and maintenance, laser plasma sources provide an intrinsic synchronization between pump and probe pulse. Most UXRD experiments with the above described machines have been performed on bulk crystalline solids, epitaxial thin films and multilayers.

In this contribution we briefly describe the working principle and characteristics of the laser plasma setup recently installed at the University of Potsdam. We discuss the choice of x-ray optics and detectors used. In order to show the broad applicability, the femtosecond x-ray pulses are used to generate a Debye-Scherrer diffraction pattern from quartz powder and an x-ray reflectivity curve of a colloid/polyelectrolyte multilayer. We reproduce

Further author information: (Send correspondence to Matias Bargheer)
E-mail: bargheer@uni-potsdam.de

Ultrafast Phenomena in Semiconductors and Nanostructure Materials XV,
edited by Kong-Thon Tsen, Jin-Joo Song, Markus Betz, Abdulkhem Y. Elezbi, Proc. of SPIE
Vol. 7937, 793715 2011 SPIE CCC code: 0277-786X/11/\$18 doi: 10.1117/12.877147

Proc. of SPIE Vol. 7937 793715-1

Downloaded from SPIE Digital Library on 22 Feb 2011 to 141.89.115.109. Terms of Use: <http://spiedigitallibrary.org/terms>

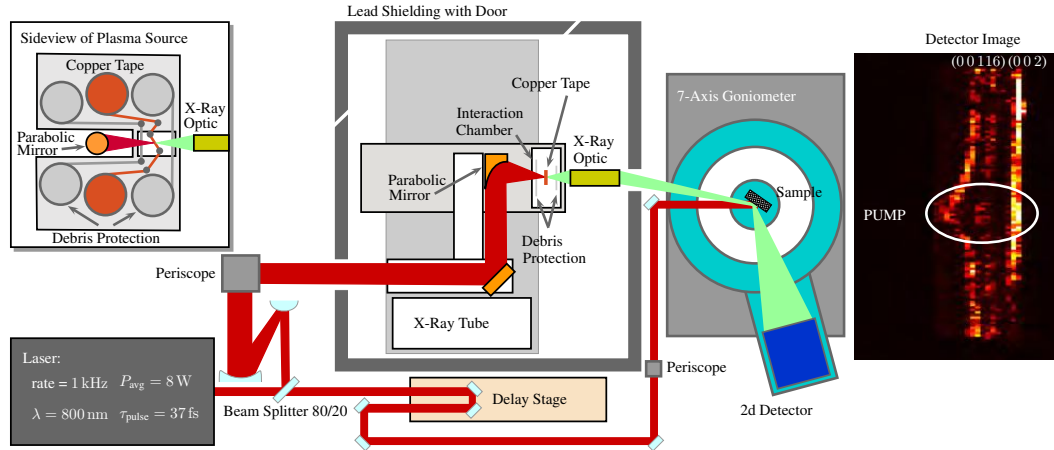


Figure 1. Topview of the setup of the plasma x-ray source. A detector image of a pumped superlattice sample taken 30 ps after the excitation is shown on the right. An obvious shift of the (00116) superlattice Bragg peak is visible in the pumped region, whereas the substrate (002) peak is unchanged.

UXRD experiments on oxide superlattices which prove that indeed the x-ray pulse duration of the source is in the range of few 100 fs. We emphasize the unique possibility to measure the zero timedelay in UXRD experiments by comparison with all-optical pump-probe experiments. This is only possible in laser-driven x-ray sources, as the laser driving the plasma can be used as an optical probe, which is difficult in the femto-slicing setup or the free electron laser.

2. LASER BASED ULTRAFAST X-RAY DIFFRACTION (UXRD)

When focusing short laser pulses (< 100 fs) with very high peak intensities of more than 10^{16} W cm $^{-2}$ onto a metal target a thin layer of plasma is generated due to the ionization of the surface atoms. Under the right conditions a single cycle of the laser's electric field can accelerate these electrons away and right back into the metal target. This effect is referred to as the Brunel effect¹³ and can be even more efficient than resonant absorption. The accelerated electrons travel into the metal and induce K-shell holes if their kinetic energy is high enough. Due to the recombination of these holes with higher core-level electrons characteristic x-ray radiation is emitted. Comparable to continuous x-ray sources a broad continuum of Bremsstrahlung accompanies these characteristic lines. The duration of the generated x-ray burst is mainly given by the temporal pulse width of the laser and the time during which the generated hot electrons have sufficient energies to ionize the K-shell in the metal target. This interaction time can be limited by using very thin foils with a thickness between 10–20 μ m as a target material. Even thinner foils reduce the efficiency of x-ray generation and are very difficult to handle mechanically.

2.1 Design of PXS

All necessary mechanical and optical requirements were fulfilled in different table-top designs in the recent years. Here we describe a further development of a femtosecond hard x-ray plasma source with a kilohertz repetition rate similar to the one reported in ref. 14. A schematic of the overall setup is shown in Fig. 1.

The laser system consists of a mode-locked oscillator and a two-stage amplifier (COHERENT Legend Duo) with a regenerative amplifier and an additional single-pass booster. The system provides up to 8 W average power at a repetition rate of 1 kHz and a center wavelength around 800 nm with a pulse length down to 37 fs. For such high pulse intensities the beam must be expanded to a beam diameter of ≈ 20 mm before propagating

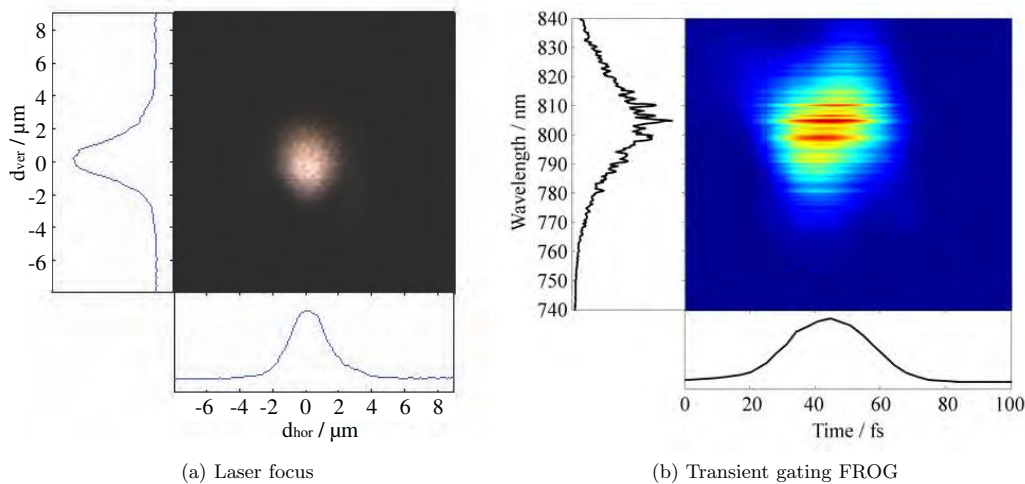


Figure 2. The spatial profile of the laser beam was characterized by an optical telescope and a CCD camera. The spot size shown in (a) is $2.8\ \mu\text{m}$. The transient gating FROG measurement depicted in (b) shows a pulse width of 37 fs and a bandwidth of approx. 30 nm.

the pulse through a beam splitter in order to prevent non-linear effects. Consequently we also avoid the usage of any dispersive optical elements to eliminate non-linear chirping of the laser pulses.

The laser beam is split up into a main part (80%) for the x-ray generation and a second part for pumping the sample. For most samples already 50% ($\approx 0.8\ \text{W}$) of the second beam provide sufficient pump fluence. This allows us to drive other all-optical experiments such as 4-wave-mixing or terahertz generation simultaneously to the UXRD experiments.

The main beam is passed into the lead housing containing the interaction chamber with the copper target. Notice, that one has to use a laser polarization providing an electric field component perpendicular to the copper foil surface in order to efficiently generate x-rays by the Brunel effect. A 90° off-axis parabolic gold mirror is used to focus the laser onto the copper foil which is placed inside a vacuum chamber to avoid non-linear effects of the focused laser beam in air. The focus of the laser pulse has been measured by an optical telescope and a CCD camera, see Fig. 2(a). It shows a homogeneous beam profile with a diameter of $2.8\ \mu\text{m}$. The pulse duration is measured using a transient gating FROG. Fig. 2(b) shows the FROG trace, i.e. the wavelengths as a function of time in the pulse, proving a pulse duration of 37 fs. From the given parameters we calculate a peak intensity of $5 \times 10^{17}\ \text{W cm}^{-2}$.

Each laser pulse hitting the foil ablates copper in a diameter of $\approx 20\ \mu\text{m}$, requiring a tape velocity of $\approx 30\ \text{mm s}^{-1}$. In addition two moving plastic foils protect the entrance and exit windows of the interaction chamber from the copper debris. The source allows for a continuous operation of over 10 h by writing multiple tracks on one 20 mm wide copper tape. Since the entrance protection band is limited in length it also has to be reused several times during such a long period. Accordingly, the x-ray flux decreases for each reuse due to laser absorption and reflection of the plastic band. In order to save resources for non-time-resolved x-ray experiments or general adjustment tasks also a standard microfocus x-ray source can automatically replace the vacuum chamber with the point source at the original laser-copper interaction region.

The ablation region of the copper ($20\ \mu\text{m}$) gives an upper limit of the x-ray source size, while the laser focus is a lower limit. For similar parameters an x-ray source size of $10\ \mu\text{m}$ has been previously measured.¹² The flux of the source depends mainly on the laser intensity on the copper tape. Therefore it is very important to have a stable focus point and copper tape. Other parameters are the target thickness (x-ray absorption) and angle

between the tape and the laser polarization. We could achieve a maximum count-rate of 8×10^{10} photons/(s 4π) of copper K_α radiation.

Besides the flux also the stability is an important factor for such sources. Because of the moving target a high shot-to-shot fluctuation is present. Also long term fluctuations appear due to the coating of the protection bands. Therefore a direct measure of the x-ray flux is required for a proper intensity normalization of the measured signals. This is often achieved by pumping only a fraction of the sample.

2.2 X-Ray Optics and Diffraction Schemes

The usage of x-ray optics can improve static and time-resolved x-ray experiments. In general, a compromise between high photon flux and resulting high signal rates, monochromatic beam as well as temporal and angular resolution must be found. All of these factors are directly influenced by the type of x-ray optic and detecting device included in the setup.

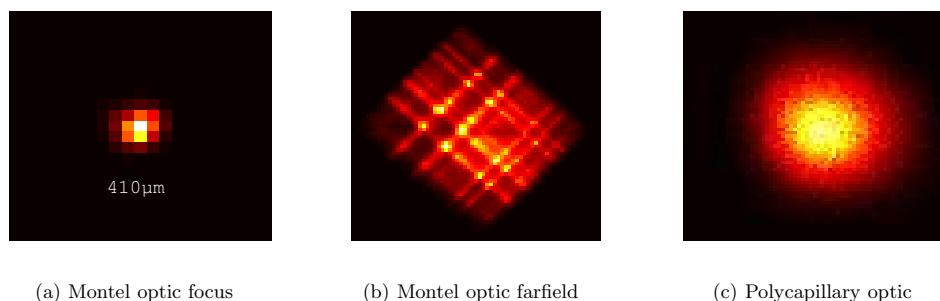


Figure 3. The focus (a) and farfield (b) images of the Montel multilayer optic were recorded with the Pilatus detector. The focus size of approx. $410 \mu\text{m}$ is accompanied by an inhomogeneous far field profile because of the structural imperfections of the optic. The nearly parallel beam of the polycapillary half lens (c) has a very homogeneous and Gaussian-like profile.

X-ray optics with long focal distances or even a parallel beam make the experimental setup more flexible, as large goniometer setups can be used and an x-ray beam with small divergence/convergence improves the angular resolution of most experiments. A drawback is the larger focal diameter which requires higher power of the optical pump pulse exciting the sample. On the other hand the pixel size of the detector determines a minimum size of the x-ray focus needed to address a single pixel.

Depending on the particular experiment we make use of the following optics: For a monochromatic beam we use a Montel multilayer optic (INCOATEC) which collects x-rays from a solid angle of 5×10^{-3} and focuses them in a magnified image (1:7) into a focal spot which is depicted in Fig. 3(a) with a diameter of less than $410 \mu\text{m}$. Here the resolution is limited by the pixel size and point spread function of the PILATUS detector. Additional air-scattering may further smear out the focus profile. However, the resolution of the optic and the detector are well matched. Polycapillary optics from Institute of Scientific Instruments (IfG) collect a larger solid angle of 3×10^{-2} . They transmit a large spectral range of hard x-rays and lead to the highest available integral x-ray flux. The half-lens produces a nearly parallel beam with 2 mm diameter (cf. Fig. 3(c)) with a divergence of 0.1° . Another slightly focusing lens (not shown here) produces a small spot with diameter of 0.7 mm at a distance of 800 mm from the source. The convergence of this optic is 0.25° .

Depending on the divergence of the x-ray beam on the sample it is possible to measure a correspondingly large q -range (much larger than a Bragg peak width) of the sample's rocking curve simultaneously using a 2D detector. Thereby one can follow intensity changes and shifts of Bragg peaks at the same time.

We use a 7-axis goniometer for manipulating the sample and the two dimensional detectors. If a large number of relatively small pixels is required we use a Princeton Instruments PI-SCX 4300/2 digital CCD camera system with a thermoelectrically cooled camera head. This front-illuminated CCD chip with 2084×2084 pixels with a pixel size of $24 \times 24 \mu\text{m}^2$ ($50 \times 50 \text{mm}^2$ image area) detects optical photons which are transmitted through

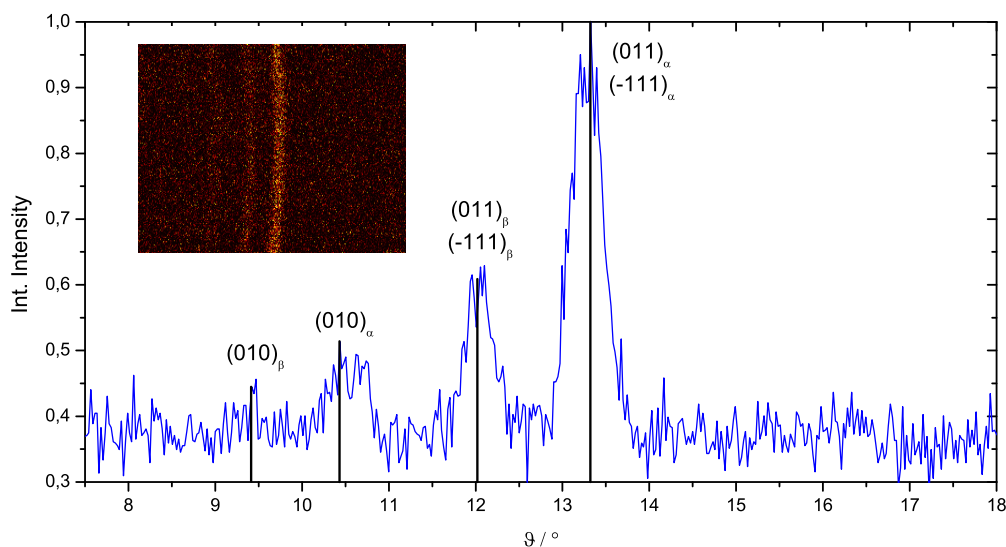


Figure 4. The integrated Debye-Scherrer reflectivity of SiO_2 powder was measured with the polycapillary half lens and the Pilatus detector. The rings of three main reflections are already visible in the detector image shown as inset. Because of the broad spectral transmission of the polycapillary lens these reflections occur as Cu K_α and K_β doublets.

a 75 mm fiber optic (1:1 taper ratio) after they are generated in a GdOS phosphor screen optimized for 8 keV photons. If a large pixel size of $172 \times 172 \mu\text{m}^2$ is acceptable and a very low dark count rate is essential we use a DECTRIS Pilatus 100K CMOS detector. This detector can be read out at a full frame rate of more than 100 Hz and allows for *rapid scanning* of the time delay in UXRD experiments which is described below.

Using a polycapillary half lens we have measured the Debye-Scherrer diffraction rings from quartz (SiO_2) powder in transmission geometry which are plotted in Fig. 4. Such images can be recorded in few minutes. A successful ultrafast x-ray diffraction experiment from an ammonium sulphate powder has been recently achieved with a similar setup.¹⁵ It is essential for the broad applicability of the technique to be able to do Debye-Scherrer diffraction, since many materials are rather available as powders than as macroscopic single crystals. Especially nanoparticles may show unknown but interesting properties on the relevant timescale. In the above measurement the width of the diffraction rings are given by the x-ray beam width emitted by the polycapillary. It may be reduced by focusing the x-rays onto the detector or by slits on the expense of integration time.

A new direction in ultrafast x-ray experiments is to look at x-ray reflectivity (XRR) of thin layers and multilayers. As a test we have used a sample with 4 layers of 10 nm gold nano-particles separated by polyelectrolyte layers with 10 nm thickness. Fig. 5 reproduces a synchrotron based XRR curve (red line) of this sample showing many orders of Kiessig fringes due to the very low roughness of this ultrathin film and seven orders of multilayer Bragg-peaks according to the clear stratification of the sample.¹⁶ The XRR curve recorded using the plasma source (black line) contains the same central features such as the Bragg peak positions and modulation according to the Kiessig fringes, although the latter have less visibility. At the angle of total reflection the peak intensity is close to unity. The inset shows the signal on the Pilatus detector for a given angle $\vartheta = 0.25^\circ$, demonstrating that for each angle setting of the goniometer a range of angles 2ϑ is observed on the detector according to the angular divergence of the incoming x-rays from the optic. Such images are recorded over 10 seconds and the XRR curve consists of 50 such measurements. In order to sum up the data for an XRR curve, we have to adjust

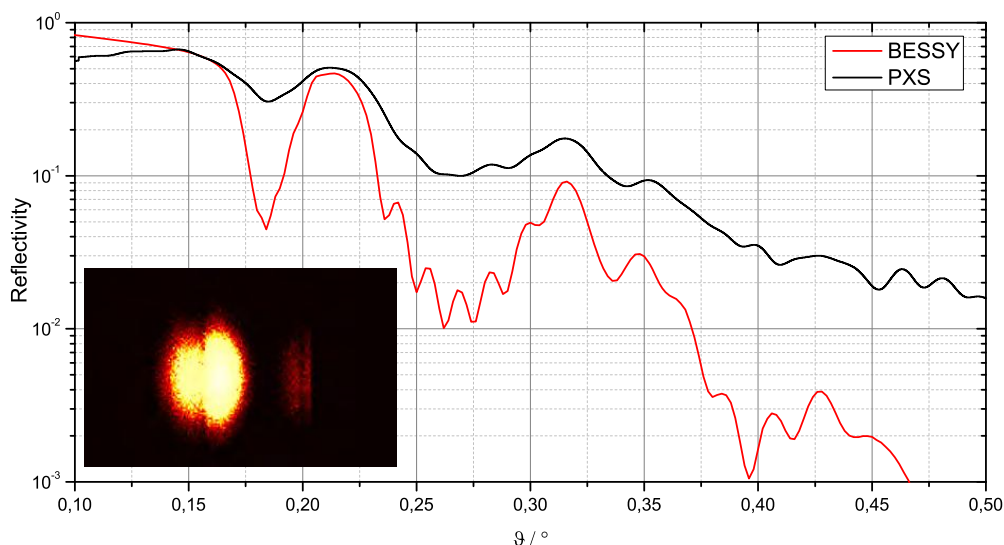


Figure 5. The XRR measurements of gold nano-particle polyelectrolyte multilayers recorded with a synchrotron (red line) and the PXS (black line) contain the same main features. The detector image (inset) visualizes the direct beam on the left (high intensity) and the total reflection as well as the first order Bragg reflection from the sample on the right side.

the data according to the Bragg reflection movement of 2ϑ on the detector if the detector position is kept fixed. However the 2ϑ range on the detector has to be calibrated. The inset also clarifies that working close to the direct beam requires detectors with a high dynamic range, little pixel cross-talk and low dark noise.

3. UXRD EXPERIMENTS ON THIN SOLID FILMS AND SUPERLATTICES

Generally time resolved x-ray diffraction yields intensity changes indicating atomic motion within the unit cell or shifting of diffraction peaks indicating changes of the unit cell shape (size). Similar to all-optical experiments the experiment statistics can be improved by difference techniques such as *chopping* the pump pulse or by *rapid scanning* of the delay stage. The former requires a count rate well beyond single photons in order to be efficient. The latter always leads to the advantage that the full pump-probe transient, i.e. diffracted intensity measured for all times, can be measured in few seconds. Repeating the delay scans many times improves the signal to noise ratio and automatically yields error bars on the data (cf. Fig. 7) which contain all noise contributions. In particular fluctuations of the source on the timescale of several seconds or minutes can be efficiently averaged out. A fast read out of the detector is mandatory for the rapid scanning scheme.

3.1 Time Zero

In any pump-probe experiment the time zero is highly relevant for the interpretation. It refers to the probe time-delay t which corresponds to the maximum (center) of the excitation pulse. If the accuracy of the time zero is not very important one can use a calibrated sample with a known and easily measured UXRD signal. The laser-based plasma x-ray source (PXS) allows for a direct measurement in many samples if it is used without an x-ray optic. The flux on the sample then depends on solid angle of x-rays collected by the sample and the sample must be positioned close to the source. However, the useful sample size is often limited, as it has to be pumped by a sufficiently high pump-fluence to make the signals observable.

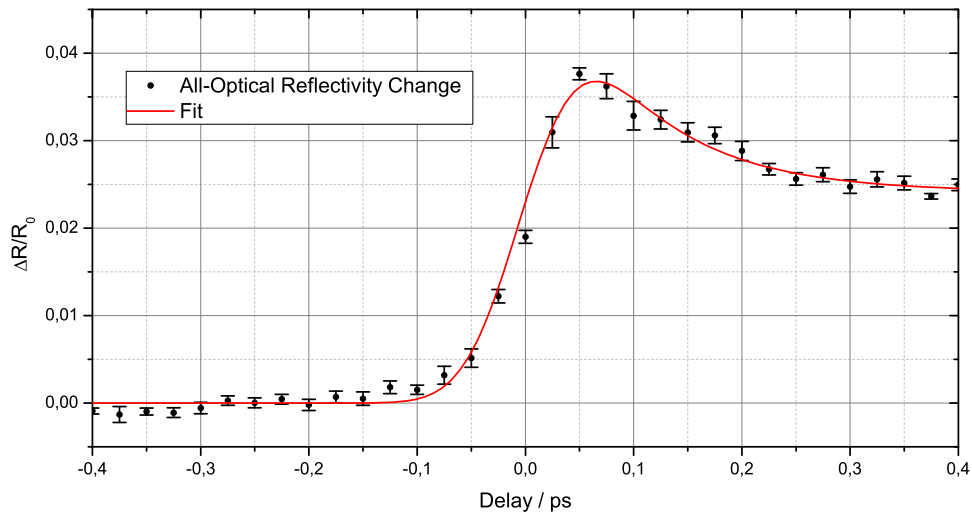


Figure 6. The transient reflectivity change of SrRuO₃ was measured at $\lambda = 800$ nm using the PXS setup. The fit (red line) extracts the width of the pump and probe pulse cross correlation of 96 fs used to measure the fast electronic response of the sample.

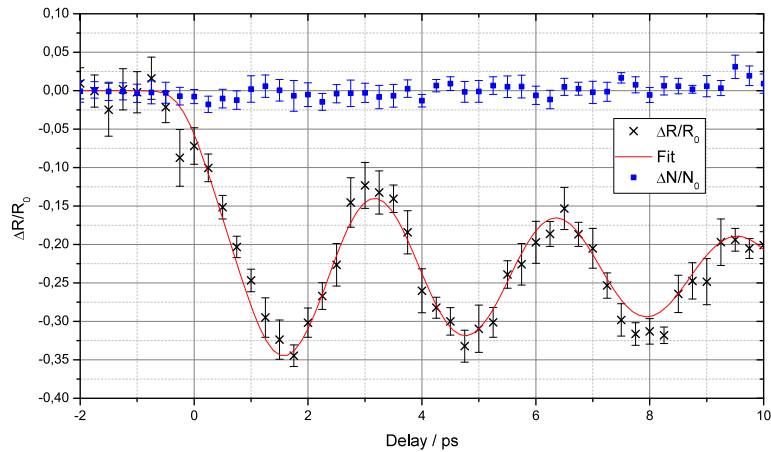
On the other hand this geometry uniquely allows for a direct comparison of UXRD signals with all-optical pump-probe measurements. The only change to the setup before the sample is to remove the copper band and the x-ray window of the vacuum chamber. Since in both materials the x-ray pulse travels with the velocity of light, the time at which the optical laser pulse which normally generates the x-rays hits the sample is identical to the time when the x-ray pulse impinges on the sample. One only has to take into account the additional group velocity delay of the optical probe laser pulse in air.

Fig. 6 shows an all-optical pump probe measurement, where the probe pulse reflected from a sample containing the metal SrRuO₃ is detected by a Si diode as a function of time-delay t . Accordingly the transient shows an instantaneous change of the optical reflectivity characteristic of the changing dielectric function for a hot electron distribution. One obtains a width (FWHM) of the correlations of the pump and probe pulse of 96 fs from the fit (red line). This agrees well with the autocorrelation function of the optical pulses used.

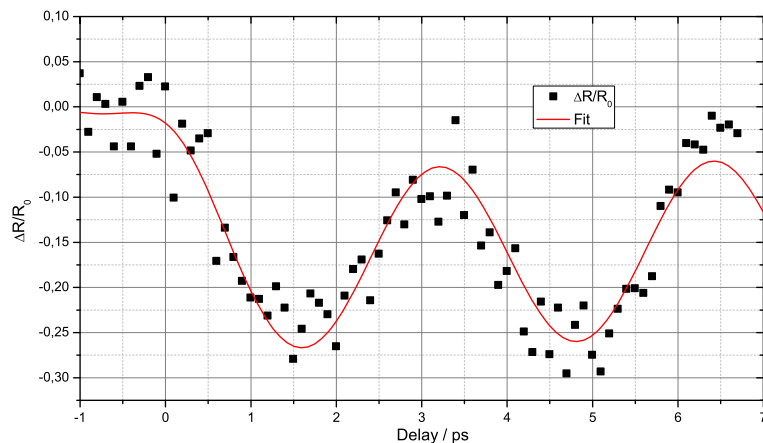
3.2 UXRD from Oxide Superlattice

In order to test and further characterize the performance of our source, we measured a well known SrRuO₃ (SRO)/SrTiO₃ (STO) superlattice (SL) in wide angle diffraction geometry.¹⁷ The source's ability to be used in x-ray reflectivity measurements of gold nanoparticle/polymer-layer systems as well as in Debye-Scherrer experiments of poly-crystalline powder samples has been shown above, however, no transient signals will be presented here.

The SLs sample consists of 10 double layers made of 7.9 nm SRO and 14.9 nm STO epitaxially grown on an SRO buffer layer and a STO substrate. The SL period $d_{SL} = d_{SRO} + d_{STO}$ leads to SL-Bragg peaks at multiple integers of $g_{SL} = 2\pi/d_{SL}$. The 800 nm pump pulse is only absorbed in the metallic SRO layers and leads to a periodic stress profile in the SL. As a result, longitudinal phonon modes are excited which lead to a coherent oscillation of the layer thicknesses of the SL. Therefore a periodic intensity change of the (00 116) Bragg peak close to the unchanged (002) substrate peak is observed.¹⁷



(a) Normalized oscillations of Bragg reflection



(b) Rapidly scanned oscillations of Bragg reflection

Figure 7. The transient Bragg reflectivity changes of a STO/SRO SL were measured in two different sampling modes. (a) The transient reflection $\Delta R/R_0$ (black crosses) is normalized by an unpumped region of the diffraction pattern; compare to the detector image in Figure 1. The transient was measured for ten times with an integration time of 10 s for each frame. The observed oscillation of the Bragg peak intensity agrees well with the predicted cosine-like fit (red line). The normalized difference of two unpumped regions $\Delta N/N_0$ (blue squares) confirms the low noise of the data. (b) The rapidly scanned data of the same sample was taken within three loops and an integrations time of only 4 s per frame. Because of the fast scanning mode the data does not need to be normalized.

Since this SL sample has a very fast response (< 500 fs) after the optical excitation and a rather short oscillation period (3.2 ps) a good temporal resolution for the UXR is required. Therefore either no x-ray optic or the Montel optic is suitable. Because of the large signal changes for this particular SL a sufficient signal-to-noise ratio can be already achieved without optic. But the usage of the Montel optic further reduces the integration time as well as the time smearing for large x-ray footprints on the sample. The fast and *no-background* Pilatus

detector is best suited when one is looking at intensity changes. Therefore we choose this combination of optic and detector for this kind of diffraction experiment. The measured SL oscillations are shown in figure 7(a). The reflectivity of the (002) substrate peak is not influenced by pump beam on short time scales and it can be simultaneously measured together with the (00116) SL reflection within the divergence of the x-ray optic. Thus it can be used for normalization of the measured intensity. However, the stability of the PXS x-ray flux allows for skipping any normalization procedure and measure intensity modulations with a sufficient resolution and signal-to-noise ratio in only a few minutes, see Fig. 7(b).

4. CONCLUSIONS

In the last years laser based plasma x-ray source proved to be a true alternative for accelerator based sub-ps x-ray sources. The PXS at the University of Potsdam captivates with its high flux of more than 8×10^{10} photons/(s 4π) of copper K_α radiation, its high stability, and run time of up to 10 h. The generated x-ray pulse of a few 100 fs are intrinsically synchronized with the pump pulse and can be focused with different x-ray optics leading to a flux of up to 3×10^6 photons/s on the sample. The variable setup allows for several different x-ray geometries e.g. wide angle diffraction, Debye-Scherrer diffraction or reflectivity measurements. Further, the possibility of all-optical experiments with the PXS enables the determination of the time zero between optical pump and x-ray probe pulse for various samples. Beside the implementation of several experimental setups, including different x-ray optics and detectors, we investigated a well known STO/SRO SL sample and measured fast intensity oscillations of a SL Bragg peak with a high signal to noise ratio as well as in a rapid scanning mode without normalization. Future experiments will be focused on the realization of time-resolved measurements of all above described x-ray setups in order to spread the utilization of UXRD to a broader range of materials.

5. ACKNOWLEDGMENT

We gratefully acknowledge the financial support by the BMBF via grant No. 03WKP03A and the Deutsche Forschungsgemeinschaft via grant No. BA2281/3-1. We thank Dr. Ionela Vrejoiu for fruitful discussions and for providing the SRO/STO SL sample experimentally investigated.

REFERENCES

- [1] Rousse, A., Rischel, C., and Gauthier, J.-C., "Femtosecond x-ray crystallography," *Rev. Mod. Phys.* **73**, 17–31 (Jan 2001).
- [2] Bargheer, M., Zhavoronkov, N., Woerner, M., and Elsaesser, T., "Recent progress in ultrafast x-ray diffraction," *ChemPhysChem* **7**(4), 783–792 (2006).
- [3] von Korff Schmising, C., Bargheer, M., Woerner, M., and Elsaesser, T., "Real-time studies of reversible lattice dynamics by femtosecond x-ray diffraction," *Z. Kristallogr.* **223**, 283–291 (May 2008).
- [4] Abo-Bakr, M., Feikes, J., Holldack, K., Wüstefeld, G., and Hübers, H.-W., "Steady-state far-infrared coherent synchrotron radiation detected at BESSY II," *Phys. Rev. Lett.* **88**, 253801 (2002).
- [5] Radu, I., Stamm, C., Pontius, N., Kachel, T., Ramm, P., Thiele, J.-U., Dürr, H. A., and Back, C. H., "Laser-induced generation and quenching of magnetization on FeRh studied with time-resolved x-ray magnetic circular dichroism," *Phys. Rev. B* **81**, 104415 (Mar 2010).
- [6] Schoenlein, R., Chattopadhyay, S., Chong, H., Glover, T., Heimann, P., Shank, C., Zholents, A., and Zolotarev, M., "Generation of femtosecond pulses of synchrotron radiation," *Science* **287**(5461), 2237 (2000).
- [7] Kahn, S., Holldack, K., Kachel, T., Mitzner, R., and Quast, T., "Femtosecond undulator radiation from sliced electron bunches," *Physical Review Letters* **97**(17), 074801 (2006).
- [8] Beaud, P., Johnson, S., Streun, A., Abela, R., Abramssohn, D., Grolimund, D., Krasniqi, F., Schmidt, T., Schlott, V., and Ingold, G., "Spatiotemporal stability of a femtosecond hard-x-ray undulator source studied by control of coherent optical phonons," *Physical Review Letters* **99**(17), 174801 (2007).
- [9] McNeil, B., "Free electron lasers: First light from hard x-ray laser," *Nature Photonics* **3**, 375 (2009).
- [10] Blome, C., Sokolowski-Tinten, K., Dietrich, C., Tarasevitch, A., and von der Linde, D., "Set-up for ultrafast time-resolved x-ray diffraction using a femtosecond laser-plasma keV x-ray source," *J. Phys. IV* **11**, 491 (2001).

- [11] Bargheer, M., Zhavoronkov, N., Bruch, R., Legall, H., Stiel, H., Woerner, M., and Elsaesser, T., "Comparison of focusing optics for femtosecond x-ray diffraction," *Applied Physics B: Lasers and Optics* **80**, 715–719 (May 2005).
- [12] Zhavoronkov, N., Gritsai, Y., Bargheer, M., Woerner, M., Elsaesser, T., Zamponi, F., Uschmann, I., and Förster, E., "Microfocus Cu K_{α} source for femtosecond x-ray science," *Opt. Lett.* **30**, 1737–1739 (Jul 2005).
- [13] Brunel, F., "Not-so-resonant, resonant absorption," *Phys. Rev. Lett.* **59**, 52–55 (Jul 1987).
- [14] Zamponi, F., Ansari, Z., von Korff Schmising, C., Rothhardt, P., Zhavoronkov, N., Woerner, M., Elsaesser, T., Bargheer, M., Trobitzsch-Ryll, T., and Haschke, M., "Femtosecond hard x-ray plasma sources with a kilohertz repetition rate," *Applied Physics A: Materials Science & Processing* **96**, 51–58 (July 2009).
- [15] Zamponi, F., Ansari, Z., Woerner, M., and Elsaesser, T., "Femtosecond powder diffraction with a laser-driven hard x-ray source," *Opt. Express* **18**, 947–961 (Jan 2010).
- [16] Kiel, M., Mitzscherling, S., Leitenberger, W., Santer, S., Tiersch, B., Sievers, T. K., Möhwald, H., and Bargheer, M., "Structural characterization of a spin-assisted colloid-polyelectrolyte assembly: Stratified multilayer thin films," *Langmuir* **26**(23), 18499–18502 (2010).
- [17] von Korff Schmising, C., Bargheer, M., Kiel, M., Zhavoronkov, N., Woerner, M., Elsaesser, T., Vrejoiu, I., Hesse, D., and Alexe, M., "Accurate time delay determination for femtosecond x-ray diffraction experiments," *Applied Physics B: Lasers and Optics* **88**(1), 1–4 (2007).

Paper II

Normalization schemes for ultrafast x-ray diffraction using a table-top laser-driven plasma source.

D. Schick, A. Bojahr, M. Herzog, C. von Korff Schmising, R. Shayduk, W. Leitenberger, P. Gaal, and M. Bargheer

Rev. Sci. Instrum. 83, 2 (2012)

Normalization schemes for ultrafast x-ray diffraction using a table-top laser-driven plasma source

D. Schick,¹ A. Bojahr,¹ M. Herzog,¹ C. von Korff Schmising,² R. Shayduk,³ W. Leitenberger,³ P. Gaal,³ and M. Bargheer^{3,a)}

¹*Institut für Physik & Astronomie, Universität Potsdam, Karl-Liebknecht-Str. 24-25, 14476 Potsdam, Germany*

²*Institut für Optik und Atomare Physik, Technische Universität Berlin, Straße des 17. Juni 135, 10623 Berlin, Germany*

³*Helmholtz Zentrum Berlin, Albert-Einstein-Strasse 15, 12489 Berlin, Germany*

(Received 1 November 2011; accepted 10 January 2012; published online 7 February 2012)

We present an experimental setup of a laser-driven x-ray plasma source for femtosecond x-ray diffraction. Different normalization schemes accounting for x-ray source intensity fluctuations are discussed in detail. We apply these schemes to measure the temporal evolution of Bragg peak intensities of perovskite superlattices after ultrafast laser excitation. © 2012 American Institute of Physics. [doi:10.1063/1.3681254]

I. INTRODUCTION

Ultrafast x-ray diffraction (UXRD) allows for tracking atomic motion on its specific time scale in various physical, chemical, and biological processes.^{1–3} In most UXRD experiments the pump-probe scheme is employed, in which the sample is excited repetitively by an ultrafast stimulus, e.g., a fs laser pulse, and is probed subsequently at different time delays between pump and probe pulses.

Besides accelerator-based x-ray sources with fs time resolution,^{4–7} laser-driven plasma x-ray sources (PXS) proved to be a practical alternative for UXRD experiments with no beamtime limitation, relatively low costs for build-up and maintenance as well as an intrinsic synchronization between the optical pump and x-ray probe pulses.⁸ In conventional x-ray tubes electrons are accelerated onto a metal target to generate characteristic line emission (K-shell ionization and recombination) and a broad bremsstrahlung background. This process can also be driven efficiently by focusing an intense laser pulse of more than 10^{16} W cm⁻² onto a metal target. Under proper conditions free electrons are generated and instantaneously accelerated back into the metal by the next half-cycle of the laser's electric field.^{9–15} The released x-ray pulses typically have a duration of a few hundred fs which is generally determined by the interaction time of the electrons with the metallic target.

Even though sources working at kilohertz repetition rate offer a relatively high flux of up to 3×10^6 ph/s on the sample using x-ray optics^{16,17} long integration times are necessary to acquire a sufficient signal-to-noise ratio (SNR) in most UXRD experiments. Moreover, large intensity fluctuations of PXS sources, compared to conventional x-ray tubes, call for advanced normalization schemes.

In this review we present a brief description of the new UXRD setup at the University of Potsdam. On the example of ultrafast Bragg peak intensity oscillations of two perovskite superlattices we discuss different normalization approaches and their experimental applicability. In particular, we intro-

duce a rapid scanning technique adapted from all-optical experiments as well as a scheme which utilizes the single reflection of a Montel x-ray optic to measure the incoming x-ray flux directly.

II. SYSTEM CHARACTERISTICS

In recent years, different designs of laser-driven plasma x-ray sources have been successfully applied to numerous UXRD experiments.^{18–21} The PXS setup at the University of Potsdam is a further development of the system introduced in Ref. 22. In addition to its excellent degree of automation and stability as well as its high standard of radiation safety, the setup can be employed in various x-ray diffraction and reflection geometries.^{23–25}

The PXS is driven by a two-stage Ti:sapphire amplifier (Legend Duo, COHERENT) working at 1 kHz repetition rate with a center wavelength of 800 nm and a pulse energy of 8 mJ compressed into a pulse duration of 40 fs. The laser beam is split into a main part of 80% for the x-ray generation and the remaining pulse energy is guided via a motorized mechanical delay line to excite the sample at a defined time before the probing x-ray pulse. The laser plasma is generated on a copper tape running in an evacuated interaction chamber, which can be moved within the fixed focal plane of the laser, perpendicular to the spooling direction of the tape. Thereby one can write multiple tracks onto one tape prolonging the measurement time up to 10 h. Both the entrance and exit window of the vacuum chamber are protected by plastic tapes which catch most of the copper debris that is ejected by the laser plasma. The generated x-ray pulses (dominantly characteristic Cu K_α and K_β lines) are collected, focused, and monochromatized to only Cu K_α energies by a Montel multilayer optic (INCOATEC) with a convergence of 0.3° and a focal spot size of only 200–300 μm FWHM at a distance $d = 1000$ mm from the source. The selected x-ray optic is adapted to the experimental needs which specify the energy bandwidth, angular distribution, and spot size of the x-rays at the sample. In most of our experiments

^{a)}Electronic mail: bargheer@uni-potsdam.de.

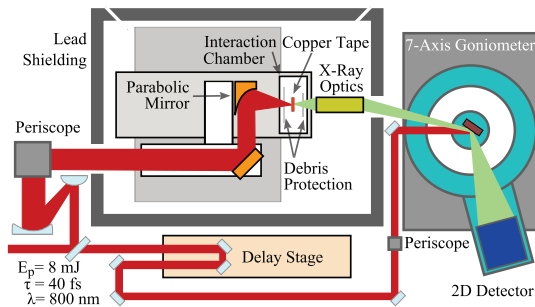


FIG. 1. (Color online) The laser is focused onto a copper tape inside a vacuum chamber to generate fs x-ray pulses. Both copper tape and plastic debris-protection tapes run perpendicular to the plane of drawing. To write new tracks on the copper band, the entire vacuum chamber is translated. The x-rays are collected, monochromatized, and focused onto the sample by a multilayer Montel optic. The diffracted x-rays are detected by a fast read-out CMOS 2D camera.

on epitaxial thin films and multilayers a symmetric θ - 2θ geometry is applied. Here, the sample is placed in the x-ray focal plane to reduce time smearing effects due to a generally inevitable non-collinearity between laser pump and x-ray probe beam and to probe a homogeneously excited part of the sample. The x-ray detector can be easily exchanged, but we commonly use a fast read-out CMOS 2D camera (Pilatus 100 k, DECTRIS) to record diffracted x-ray photons. The complete setup is sketched in Fig. 1.

The performance of the PXS can be characterized by three main parameters: pulse length, photon flux, and intensity stability. Since there is no detector that is fast enough to measure the duration of ultrashort x-ray pulses directly we rely on several successful experiments in our and other groups^{21,25} which evidence the sub-ps temporal resolution of PXS machines.

The x-ray flux can be improved by an increase of the laser intensity on the metal target, but only up to a certain saturation limit.^{10,12} From there on a further increase of the x-ray flux can be achieved by a larger interaction volume of the laser-produced electrons with the target, e.g., by larger foci, which will increase the x-ray source size in return. At very high laser intensities in the relativistic limit the efficiency rises again, however, at the expense of a high background of high energetic radiation. For our setup we achieved nearly 10^{11} ph/s with Cu K_{α} energy in the full solid angle of 4π under optimal conditions. Only 5×10^5 ph/s of the total flux are focused onto the sample using the Montel x-ray optic at a normal performance. Thus, the number of diffracted photons per pulse for a typical Bragg peak with 1% peak reflectivity is well below ten for our system. Consequently, we are within the single photon counting regime for each detector pixel, because the divergence of the diffracted x-rays yields 10–100 illuminated pixels on the detector area depending on the exact sample-detector-position.

Of course, the optimal performance of the PXS requires extensive tuning of all mechanical and optical components. Although we benefit heavily from the engineering knowledge and skills which are included in the commercial and semi-commercial components of our setup, we cannot avoid all me-

chanical and optical instabilities which cause x-ray intensity fluctuations on several time scales. In general, we distinguish short-term fluctuations and long term drifts. The latter ones occur within minutes up to hours and can be explained by contamination of the PXS interaction chamber by copper debris, side shifts of the copper tape, and also by the increasing roughness of the copper tape after writing multiple tracks with the laser onto it. These long-term drifts can result in intensity changes and jumps of up to 50% and are not periodic in time.

Short-term fluctuations include all intensity instabilities typically within a few seconds down to pulse-to-pulse fluctuations. They are caused by the driving laser, unstable optical components but mainly by the position instabilities of the spooled copper tape with respect to the laser focus as well as target material inhomogeneities. Under certain conditions (which we usually avoid) very large intensity bursts can be observed in the integrated energy range from 1–100 keV, which may be assigned to electron beam generation²⁶ and the subsequent bremsstrahlung creation in the surrounding aluminium and lead walls of the vacuum chamber. These fluctuations can be easily suppressed by any type of monochromator in the setup, such as a Montel optic.

III. NORMALIZATION SCHEMES

As already described above only a few photons per pulse are diffracted in a typical UXR experiment. In order to measure temporal intensity changes of only a few percent with a sufficient SNR it is necessary to accumulate thousands up to millions of diffracted x-ray pulses over minutes and hours of measurement time. In general, the short-term fluctuations of the incoming x-ray flux increase the statistical error of the recorded signal. A reliable normalization technique can help to cancel the contribution of the intensity fluctuations to the signal and to minimize the necessary averaging time. Normalization is definitely mandatory in case of long-term drifts, which describe the changing mean value of the fluctuating x-ray intensity over absolute measurement time t . Because of the non-periodic behaviour in time of these drifts it is not easy to average them out. Hence, the measured signal would mainly represent the intensity drift of the source rather than the response of the sample under investigation if no normalization is applied.

We choose two superlattice (SL) samples in order to evaluate different normalization approaches. These artificial heterostructures consist of N_{SL} epitaxially grown double layers made of a metallic and insulating perovskite material. The spatial period $d_{SL} = d_{metal} + d_{insulator}$ of a double layer leads to SL Bragg peaks at multiple integers of the reciprocal SL vector $g_{SL} = 2\pi/d_{SL}$ where we adapt the enumeration of the SL peaks from Ref. 27. In the UXR experiments an 800 nm fs-pulse excites the sample, but is only absorbed in the metallic layers of the SL and thus induces a periodic stress profile.^{28,29} As a result, a coherent longitudinal phonon mode is excited which corresponds to an anti-phase oscillation of the individual layer thicknesses in each double layer. These structural dynamics lead to a periodic intensity change of most SL Bragg peaks. For many superlattice peaks the intensity of the x-ray Bragg reflection is proportional to the

amplitude of the superlattice phonon (i.e., expansion of the metallic layers and compression of the dielectric layers in between), since the contribution of the two layer materials to the structure factor of the reflections is varied linearly. In some cases this x-ray interference leads to additional modulation as for the peak SL+1 in Figs. 5 and 7 making the response even faster.³⁰ For both samples studied in this paper, the signal can be well approximated by a cosine-like oscillation due to the quasi-instantaneous stress. The oscillations are exponentially damped as the energy stored in the superlattice phonons propagates into the substrate.²⁹ Since in the current paper we only use the fast response for a demonstration of the setup, we refrain from further discussion of the physics and settle for observing the good applicability of the fit function. The according oscillation period of the coherent phonon mode is given by the double layer period d_{SL} and the material-specific sound velocities and is only a few ps for the considered samples. Thus, we can prove the sub-ps temporal resolution of the PXS. In order to observe the coherent phonon oscillation of the SL the integrated intensity of the diffracted x-rays $R(\tau)$ from a single SL Bragg peak has to be measured for different time delays τ . In analogy to all-optical pump-probe experiments we refer to $R(\tau)$ as transient x-ray reflectivity.

In the experiment the measured signal $S(\tau, t)$ also depends on the absolute time t because of the fluctuations and drifts of the incoming intensity $I(t)$:

$$S(\tau, t) = R(\tau) I(t).$$

In order to extract the reflectivity $R(\tau)$ from the real signal a normalization scheme must provide a measure which is proportional to $I(t)$ and at the same time independent of the delay τ . Obviously, this can be achieved by an additional detector that monitors only $I(t)$. For the observation of structure factor changes of a Bragg reflection we are only interested in the relative reflectivity change

$$\frac{S(\tau, t) - S_0(t)}{S_0(t)} = \frac{[R(\tau) - R_0] I(t)}{R_0 I(t)} = \frac{\Delta R(\tau)}{R_0},$$

where $R_0 = R(\tau < 0)$ denotes the unpumped reflectivity and $S_0(t) = S(\tau < 0, t)$ the measured unpumped signal. Here the incoming intensity $I(t)$ cancels out if $S(\tau, t)$ and $S_0(t)$ can be measured simultaneously or within a sufficiently small time interval Δt in which $I(t)$ can be assumed to be constant, e.g., for Δt smaller than long-term drifts of the x-ray source, and hence a direct measure of $I(t)$ is not necessary.

However, the applicability of a certain normalization method can be limited by various factors such as the x-ray diffraction geometry or the investigated sample itself. In the upcoming paragraphs we describe general approaches for normalization and give examples of their implementation from our and other groups.

A. Low-repetition rate normalization

The first SL sample consists of 11 double layers made of 7.9 nm metallic SrRuO₃ (SRO) and 14.9 nm dielectric SrTiO₃ (STO) epitaxially grown on a SRO buffer layer and a STO substrate by pulsed laser deposition.³¹ This sample was already studied intensively^{29,32,33} and has a SL phonon

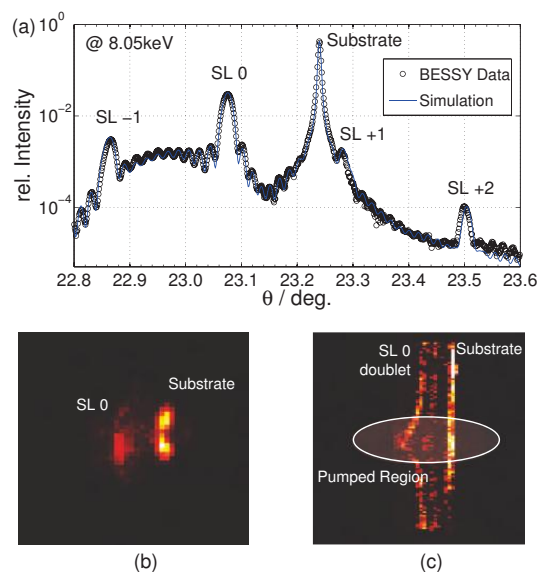


FIG. 2. (Color online) (a) The θ - 2θ diffraction scan of the STO/SRO SL features the sharp and intense STO substrate Bragg peak as well as several SL Bragg peaks. The experimental 2D diffraction patterns of the 0th SL Bragg peak are shown in two configurations. (b) The sample is placed in the focus of the Montel x-ray optic. (c) The sample is illuminated by the direct PXS emission without x-ray optics. The 0th SL Bragg peak appears as a $K_{\alpha 1, \alpha 2}$ doublet. The $K_{\alpha 2}$ Bragg reflection of the substrate is not within the divergence of the x-rays on the sample.

oscillation period of 3.2 ps, which can be derived most easily from the transient reflectivity change of the 0th SL Bragg peak. The θ - 2θ diffraction curve of the STO/SRO SL is shown in Fig. 2(a). It was measured at the energy-dispersive reflectometry (EDR) beamline of the storage ring BESSY II of the Helmholtz-Zentrum Berlin at a photon energy of 8.82 keV. For better comparison with the PXS data the θ -axis of the diffraction curve was rescaled for the Cu K_{α} energy of 8.05 keV.

PXS driven UXRD experiments generally feature a rather large angular distribution of the incoming x-ray beam because of the used focussing x-ray optics or, in case of no optics, because of the divergence of the nearly point-like x-ray emission from the laser plasma. Thus, it is favourable to use 2D x-ray cameras, or at least 1D arrays, in order to record the available angular information of the diffracted photons. In case of a diode-like point detector angular information or even the total information of the diffracted intensity, which misses the angular acceptance of the detector, is lost. Unfortunately, typical CCD x-ray cameras have a very low frame rate because of their long dead-time up to several seconds, which is mainly due to their long read-out time. Accordingly, the integration time for a single diffraction image should be well above 1 min in order to have a sufficiently high duty cycle of the detector. Otherwise a large fraction of the precious diffracted x-ray photons cannot be detected. The drawback of slow frame rates can be balanced by taking advantage of the large number of CCD pixels in order to record simultaneously the signal and normalization with the same CCD camera.²¹

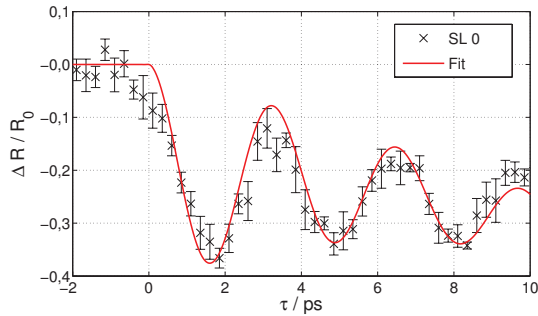


FIG. 3. (Color online) The relative reflectivity $\Delta R/R_0$ of the 0th SL Bragg peak of the SRO/STO SL was measured with the substrate normalization scheme. The error bars are determined by averaging 10 independent delay scan.

As it can be seen from Fig. 2(a) the angular separation between the 0th SL peak and the STO substrate peak is smaller than 0.3° . Thus, it is possible to record both peaks simultaneously within the convergence of our Montel optic, see Fig. 2(b). The same situation can be achieved without the use of an x-ray optics, where the divergence on the sample depends on its distance to the x-ray source. In the latter case, see Fig. 2(c), the sample is completely illuminated by the direct PXS emission. Within the collected angular range the 0th SL peak is visible as a $K_{\alpha 1, \alpha 2}$ doublet, whereas the $K_{\alpha 2}$ contribution of the strong substrate is cut off by the finite size of the sample.

The dielectric STO substrate is not optically excited by the 800 nm pump pulse. For delays larger than the time for sound propagation through the thin SL layers (in our case $\tau > 35$ ps) propagating sound waves originating from within the SL influence the structure of the STO substrate.^{29,34} Within this defined delay window the substrate peak reflectivity R_{sub} is constant. Consequently, the recorded signal of the substrate peak $S_{\text{sub}}(t)$ only depends on the absolute time t and can thus be utilized as a measure of the incoming intensity $I(t)$. Here we directly benefit from the large detector area, since no additional hardware is required to employ this normalization scheme. The data shown in Fig. 3 were obtained with this substrate normalization scheme while the sample was placed in the direct emission of the PXS without x-ray optics. Due to the repetition of the complete delay scan for several times we are able to plot also statistical error bars. The substrate normalization scheme strongly depends on the sample and the available angular distribution of the incoming x-rays. Furthermore, this method cannot be applied for large delays because of the transient change of the substrate reflectivity.

A more generally applicable normalization scheme is already indicated in Fig. 2(c) where the sample is placed in the direct PXS emission without x-ray optics. For a sufficiently large x-ray spot size on the sample also each point in the diffraction pattern originates from a different position on the sample. If the pumped region is smaller than the probe area on the sample also the diffraction pattern will contain a pumped and unpumped region. This situation can also be achieved with x-ray optics, but here the sample should be placed out of the x-ray focal plane in order to superimpose both areas more

easily. In this pumped-unpumped normalization scheme the transient signal $S(\tau, t)$ and the unpumped signal $S_0(t)$ can be measured simultaneously with the same CCD camera. We can apply this scheme as a normalization to determine the transient reflectivity change $\Delta R(\tau)/R_0$ for any crystalline sample.

However, a large fraction of the photons diffracted by the 0th SL Bragg peak does not contribute to the transient reflectivity $R(\tau)$. Moreover, the excitation on the sample is very inhomogeneous, as it is indicated by the curvature of the SL peak in Fig. 2(c). Another drawback of this scheme is the rather large x-ray footprint on the sample, which gives rise to an undesired time smearing and also maps different positions of the sample at once, which may be problematic for low-quality samples that lack lateral homogeneity.

For this specific STO/SRO SL sample the substrate normalization scheme is preferable compared to the pumped-unpumped method, because the SNR mainly depends on the total number of recorded photons, meaning the sum of photons contributing to the signal and to the normalization. This number is much higher for the intense substrate reflection. However, both normalization schemes can be applied in the so-called low-repetition rate regime for slow detectors without the need of additional hardware. It is even possible to apply both methods with or without x-ray optics, although one should prefer the use of the Montel x-ray optic because of the higher flux on the sample and the smaller x-ray energy bandwidth.

B. High-repetition rate normalization

The following normalization schemes are applied to a similar SL sample. This SL is made of 15 double layers of which each consist of 7.3 nm metallic $(\text{La}_{0.7}\text{Sr}_{0.3})\text{MnO}_3$ (LSMO) and 13.7 nm ferroelectric $(\text{Ba}_{0.7}\text{Sr}_{0.3})\text{TiO}_3$ (BST). Again the SL is grown epitaxially on a STO substrate. The θ - 2θ diffraction curve is shown in Fig. 4 and was again measured at the EDR beamline of the storage ring BESSY II of the Helmholtz-Zentrum Berlin.³⁵ The ultrafast response of this SL to an 800 nm fs pump pulse is very similar to the STO/SRO SL discussed above but with a slightly different period of the coherent SL phonon oscillation of 3.8 ps.

A common procedure to reduce statistical errors in a pump-probe experiment is increasing the repetition rate of the measurement. A well-known high-repetition rate

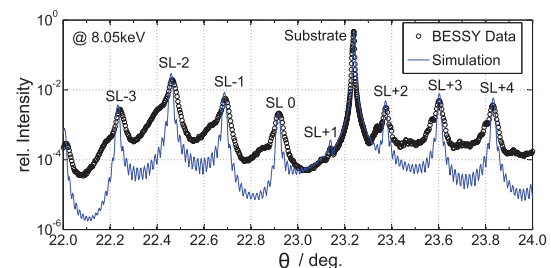


FIG. 4. (Color online) Several orders of SL Bragg peaks as well as an intense substrate Bragg peak are observable in the θ - 2θ scan of the LSMO/BST SL sample.

normalization scheme from all-optical experiments is chopping. Here the pump beam is periodically blocked in order to record the signal $S(\tau, t)$ and the unpumped signal $S_0(t)$ subsequently within a short time interval $\Delta t = 1/f_{\text{chop}}$ where f_{chop} is the chopping frequency. In this case half of the diffracted photons contribute to the signal and the other half to the normalization. If Δt is shorter than the time scale of long term drifts we can assume $I(t) = I(t + \Delta t)$ to be constant within this interval neglecting short-term fluctuations. Hence, we can apply this scheme to measure the relative reflectivity change $\Delta R(\tau)/R_0$. If Δt is even shorter than most of the characteristic short-term fluctuations of the PXS, chopping can also drastically reduce these sources of noise. Ideally, this requires a shot-to-shot temporal resolution of the x-ray camera. Because area detectors with kHz readout frequencies are just becoming available we have not implemented the chopping scheme, yet.

A very elegant way of normalization is again adapted from all-optical experiments and referred to as the rapid scanning method.³⁶ As the name suggests the complete delay range of interest of a pump-probe experiment is scanned very rapidly within a time interval Δt in which the incoming intensity $I(t)$ can again assumed to be constant. Thus, a single scan has to be faster than the time scale on which long-term drifts occur. It is not possible to scan the complete delay in a time shorter than all short-term fluctuations ($\Delta t < 5$ ms). Several of these fast delay scans are averaged to decrease the statistical errors caused by the fluctuations of the incoming intensity. With the rapid scanning method all diffracted photons contribute directly to the signal and no intensity is lost for normalization.

Similar to the chopping technique, the performance of rapid scanning is mainly limited by the frame rate of the x-ray detector and additionally by the speed of the delay stage. A complete delay scan has to be faster than the long-term drifts of the PXS which occur typically on the time scale of minutes. Hence, we do not have to utilize the Pilatus' full frame rate of up to 200 Hz but can work within a more easily controllable regime of ~ 1 Hz frame rate in order to scan a typical number of 50 delays well within 1 min of scan time.

A measurement of reflectivity oscillation for different SL Bragg peaks of the LSMO/BST SL is depicted in Fig. 5. The data were recorded with a frame rate of 2 Hz of the Pilatus camera and the complete scan was repeated up to 40 times.

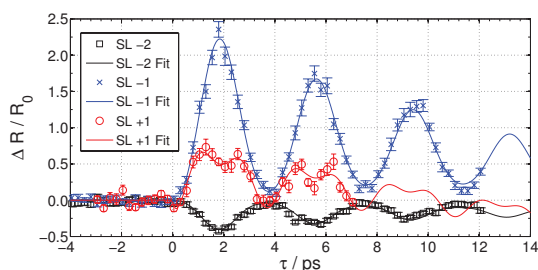


FIG. 5. (Color online) The rapid scanning technique was applied to measure the relative reflectivity $\Delta R/R_0$ of the SL-2, SL-1, and SL+1 Bragg peaks of the LSMO/BST SL. The data for each SL peak was accumulated within ~ 20 min per curve averaging over 40 complete delay scans with a frame rate of 2 Hz.

The total integration time per curve was ~ 20 min and we achieved an average relative error for all data points of 5.3%.

Rapid scanning provides a normalization without measuring the incoming intensity $I(t)$ directly. It is not capable of reducing short-term fluctuations in our implementation but can only average them out. This normalization technique is universally applicable. However, fast read-out x-ray detectors are the key part of this high-repetition normalization scheme, since one complete delay scan must be finished faster than the time scale of long-term fluctuations.

C. Direct normalization

In order to provide a sample-independent and direct measure of the incoming intensity $I(t)$ an additional detector is required. This detector then has to measure the PXS flux between source and sample ideally with the same frame rate as the x-ray camera records the diffraction signal. X-ray sensitive diodes are generally fast enough for this purpose and have a sufficiently high quantum efficiency to record also low x-ray intensities. Since the integrated intensity over the whole PXS spectrum is not proportional to the intensity of the characteristic x-ray emission lines used in the diffraction experiments, it is necessary to monitor the x-ray flux behind a monochromator or with an according energy-dispersive detector.³⁷ One usually has to bypass some fraction of the incoming x-ray beam onto the normalization detector which will reduce the flux on the sample accordingly. Such direct normalization schemes were already implemented, e.g., by placing an ionization chamber³⁸ or a thin diamond beam splitter²⁴ into the incoming x-ray beam.

In our setup the Montel x-ray optic acts as a monochromator since it transmits only the Cu K_α energies which are then diffracted from the sample. A detailed description of Montel optics can be found in the literature.^{16,39} The divergent emission of the source is focused in two dimensions by two sequential reflections from elliptically bent multilayer mirrors. The transmission profile of the optic shown in the inset of Fig. 6 reveals that in addition to this monochromatic focal region F there are two regions S which are produced by x-rays undergoing only a single reflection from one multilayer mirror. This radiation is monochromatic as well, and we can assume a linear relation between the intensity in the S regions and in the focus F. In a typical diffraction experiment the two S-beams do not hit the sample and are therefore useless. In our case we use an x-ray diode (CRYSTAL PHOTONICS) to monitor the x-ray flux in one of the S regions to have a direct and proportional measure of the monochromatic incoming intensity $I(t)$.

In order to verify the applicability of this normalization scheme we measured the direct intensity of the Montel focus F with the Pilatus camera in single-photon-counting mode and the intensity of a single reflection S with the x-ray diode simultaneously. The ratio of the diode and the Pilatus signal shown as red line in Fig. 6 proves the linear relation between the two signals. Accordingly, the normalized signal contains much less short-term fluctuations as compared to the original intensity which improves the SNR for UXRD experiments drastically. For very large fluctuations and drifts of about 50%

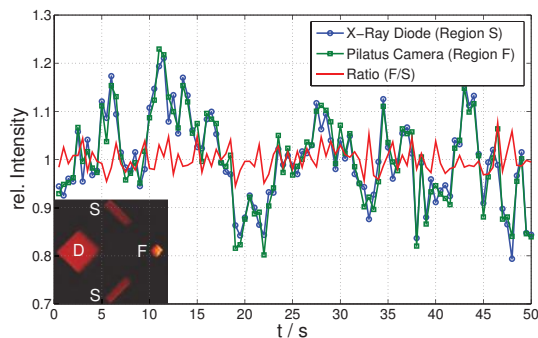


FIG. 6. (Color online) The focus F of the Montel optic was measured with the Pilatus camera (green square) simultaneously with the intensity of a single reflection S of the Montel optic by an x-ray diode (blue circle). The ratio of the Pilatus and diode signal (red line) features much less fluctuations than the original data. The transmission profile of the Montel optic is shown in the inset, where the direct transmission of the Montel optic is labelled as D.

of the PXS intensity a slight nonlinearity of the x-ray diode signal causes deviations of the normalized signal. This nonlinearity is most likely caused by an electronic offset of the diode itself and may be reduced by a suitable calibration routine. The direct normalization scheme reduces short-term fluctuations but cannot completely cancel large long-term drifts because of the diode's nonlinearity. Therefore, we combine this method with the rapid scanning technique to improve the SNR even further.

We apply this combination of diode-normalization and rapid scanning again for the measurement of SL Bragg peak oscillations of the LSMO/BST SL (Fig. 7). In comparison with the data shown in Fig. 5 the average relative error for each data point is further reduced to 4.6% although the total integration time per curve is reduced to only 10 min. This normalization scheme requires extensive technical efforts such as high-repetition x-ray cameras and an additional x-ray diode as well as an x-ray optic. On the other hand, this combined normalization technique is independent of the investigated sample and does not decrease the number of photons which account for the diffraction signal.

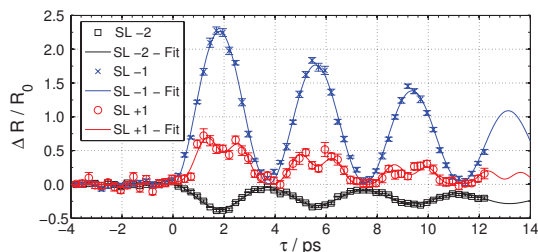


FIG. 7. (Color online) The reflectivity oscillations of three different SL Bragg peaks of a LSMO/BST SL were measured with a combination of the x-ray diode normalization and rapid scanning. The frame rate of the Pilatus was 1 Hz and each curve was obtained within a total integration time of ~ 10 min.

IV. CONCLUSIONS AND OUTLOOK

Even though PXS sources operated at kHz repetition rate are easy to use and feature high stability, advanced normalization schemes are necessary to achieve a sufficient SNR in UXRD experiments. Here we presented a detailed overview of low- and high-repetition rate normalization techniques as well as a diode-based direct normalization scheme utilizing the specific transmission profile of a Montel x-ray optic. With the combination of the direct intensity normalization and the rapid scanning we could drastically reduce short-term fluctuations and cancel long term drifts of the PXS, respectively. With the diode normalization scheme it is also possible to record time-resolved $\theta-2\theta$ scans over an angular range much larger than the divergence of the x-ray optics. Thereby not only peak intensity but also the position, width and shape of a Bragg peak can be precisely observed on an ultrafast time scale.

ACKNOWLEDGMENTS

We gratefully acknowledge the financial support by the BMBF via Grant No. 03WK03A and the Deutsche Forschungsgemeinschaft (DFG) (Grant No. BA2281/3-1). We thank Dr. Ionela Vrejoiu for fruitful discussions and for providing the samples experimentally investigated.

- ¹A. Rousse, C. Rischel, and J.-C. Gauthier, *Rev. Mod. Phys.* **73**, 17 (2001).
- ²M. Bargheer, N. Zhavoronkov, M. Woerner, and T. Elsaesser, *ChemPhysChem* **7**, 783 (2006).
- ³M. Chergui and A. H. Zewail, *ChemPhysChem* **10**, 28 (2009).
- ⁴R. W. Schoenlein, S. Chattopadhyay, H. H. W. Chong, T. E. Glover, P. A. Heimann, C. V. Shank, A. A. Zholents, and M. S. Zolotarev, *Science* **287**, 2237 (2000).
- ⁵K. Hollmack, S. Khan, R. Mitzner, and T. Quast, *Phys. Rev. Lett.* **96**, 054801 (2006).
- ⁶P. Beaud, S. L. Johnson, A. Streun, R. Abela, D. Abramsohn, D. Grolimund, F. S. Krasniqi, T. Schmidt, V. Schlott, and G. Ingold, *Phys. Rev. Lett.* **99**, 174801 (2007).
- ⁷B. McNeil, *Nat. Photonics* **3**, 375 (2009).
- ⁸A. L. Cavalieri, D. M. Fritz, S. H. Lee, P. H. Bucksbaum, D. A. Reis, J. Rudati, D. M. Mills, P. H. Fuoss, G. B. Stephenson, C. C. Kao, D. P. Siddons, D. P. Lowney, A. G. MacPhee, D. Weinstein, R. W. Falcone, R. Pahl, J. Als-Nielsen, C. Blome, S. Düsterer, R. Ischebeck, H. Schlarb, H. Schulte-Schrepping, T. Tschentscher, J. Schneider, O. Hignette, F. Sette, and K. Sokolowski-Tinten, *Phys. Rev. Lett.* **94**, 114801 (2005).
- ⁹F. Brunel, *Phys. Rev. Lett.* **59**, 52 (1987).
- ¹⁰C. Reich, P. Gibbon, I. Uschmann, and E. Förster, *Phys. Rev. Lett.* **84**, 4846 (2000).
- ¹¹A. Cavalleri, C. W. Siders, F. L.H. Brown, D. M. Leitner, C. Tóth, J. A. Squier, C. P. J. Barty, K. R. Wilson, K. Sokolowski-Tinten, M. Horn von Hoegen, D. von der Linde, and M. Kammler, *Phys. Rev. Lett.* **85**, 586 (2000).
- ¹²F. Ewald, H. Schwoerer, and R. Sauerbrey, *Europhys. Lett.* **60**, 710 (2002).
- ¹³W. Krueer, *The Physics of Laserplasma Interactions* (Westview, New York, 2003).
- ¹⁴W. Lu, M. Nicoul, U. Shymanovich, A. Tarasevitch, P. Zhou, K. Sokolowski-Tinten, D. von der Linde, M. Mašek, P. Gibbon, and U. Teubner, *Phys. Rev. E* **80**, 026404 (2009).
- ¹⁵M. Nicoul, U. Shymanovich, A. Tarasevitch, D. von der Linde, and K. Sokolowski-Tinten, *Appl. Phys. Lett.* **98**, 191902 (2011).
- ¹⁶M. Bargheer, N. Zhavoronkov, R. Bruch, H. Legall, H. Stiel, M. Woerner, and T. Elsaesser, *App. Phys. B: Lasers Opt.* **80**, 715 (2005).
- ¹⁷N. Zhavoronkov, Y. Gritsai, M. Bargheer, M. Woerner, T. Elsaesser, F. Zamponi, I. Uschmann, and E. Förster, *Opt. Lett.* **30**, 1737 (2005).
- ¹⁸C. Rose-Petrucci, R. Jimenez, T. Guo, A. Cavalleri, C. W. Siders, F. Rksi, J. A. Squier, B. C. Walker, K. R. Wilson, and C. P. J. Barty, *Nature (London)* **398**, 310 (1999).

- ¹⁹K. Sokolowski-Tinten, C. Blome, J. Blums, A. Cavalleri, C. Dietrich, A. Tarasevitch, I. Uschmann, E. Förster, M. Kammler, M. Horn-von Hoegen, and D. von der Linde, *Nature (London)* **422**, 287 (2003).
- ²⁰C. von Korff Schmising, M. Bargheer, M. Kiel, N. Zhavoronkov, M. Woerner, T. Elsaesser, I. Vrejoiu, D. Hesse, and M. Alexe, *Phys. Rev. Lett.* **98**, 257601 (2007).
- ²¹M. Bargheer, N. Zhavoronkov, Y. Gritsai, J. C. Woo, D. S. Kim, M. Woerner, and T. Elsaesser, *Science* **306**, 1771 (2004).
- ²²F. Zamponi, Z. Ansari, C. von Korff Schmising, P. Rothhardt, N. Zhavoronkov, M. Woerner, T. Elsaesser, M. Bargheer, T. Trobitzsch-Ryll, and M. Haschke, *Appl. Phys. A: Mater. Sci. Process.* **96**, 51 (2009).
- ²³*Time-Resolved X-Ray Scattering*, edited by K.-T. Tsen, J.-J. Song, M. Betz, and A. Y. Elezzabi (SPIE, Bellingham, Washington, 2011), Vol. 7937.
- ²⁴B. Freyer, J. Stingl, F. Zamponi, M. Woerner, and T. Elsaesser, *Opt. Express* **19**, 15506 (2011).
- ²⁵F. Zamponi, Z. Ansari, M. Woerner, and T. Elsaesser, *Opt. Express* **18**, 947 (2010).
- ²⁶J. Uhlig, C. G. Wahlström, M. Walczak, V. Sundström, and W. Fullagar, *Laser Part. Beams* **29**, 415 (2011).
- ²⁷G. Bauer, *Optical Characterization of Epitaxial Semiconductor Layers* (Springer-Verlag, Berlin, 1996).
- ²⁸M. Woerner, C. von Korff Schmising, M. Bargheer, N. Zhavoronkov, I. Vrejoiu, D. Hesse, M. Alexe, and T. Elsaesser, *Appl. Phys. A: Mater. Sci. Process.* **96**, 83 (2009).
- ²⁹M. Herzog, D. Schick, P. Gaal, R. Shayduk, C. von Korff Schmising, and M. Bargheer, *Appl. Phys. A* **1** (2011).
- ³⁰M. Herzog, D. Schick, W. Leitenberger, R. Shayduk, R. M. van der Veen, C. J. Milne, S. L. Johnson, I. Vrejoiu, and M. Bargheer, *New J. Phys.* **14**, 013004 (2012).
- ³¹I. Vrejoiu, G. Le Rhun, L. Pintilie, D. Hesse, M. Alexe, and U. Gösele, *Adv. Mater.* **18**, 1657 (2006).
- ³²C. von Korff Schmising, M. Bargheer, M. Kiel, N. Zhavoronkov, M. Woerner, T. Elsaesser, I. Vrejoiu, D. Hesse, and M. Alexe, *Appl. Phys. B* **88**, 1 (2007).
- ³³M. Herzog, W. Leitenberger, R. Shayduk, R. van der Veen, C. J. Milne, S. L. Johnson, I. Vrejoiu, M. Alexe, and D. Hesse, *Appl. Phys. Lett.* **96**, 161906 (2010).
- ³⁴C. von Korff Schmising, M. Bargheer, M. Kiel, N. Zhavoronkov, M. Woerner, T. Elsaesser, I. Vrejoiu, D. Hesse, and M. Alexe, *Phys. Rev. B* **73**, 212202 (2006).
- ³⁵In the simulation we assume a perfect sample structure. Accordingly, only the positions and amplitudes of the SL Bragg peaks are predicted correctly.
- ³⁶G. C. Cho, W. Kütt, and H. Kurz, *Phys. Rev. Lett.* **65**, 764 (1990).
- ³⁷M. Silies, H. Witte, S. Linden, J. Kutzner, I. Uschmann, E. Förster, and H. Zacharias, *Appl. Phys. A: Mater. Sci. Process.* **96**, 59 (2009).
- ³⁸K. Sokolowski-Tinten, private communication (2011).
- ³⁹U. Shymanovich, M. Nicoul, K. Sokolowski-Tinten, A. Tarasevitch, C. Michaelsen, and D. von der Linde, *Appl. Phys. B: Lasers Opt.* **92**, 493 (2008).

Paper III

Ultrafast reciprocal-space mapping with a convergent beam

D. Schick, R. Shayduk, A. Bojahr, M. Herzog, C. von Korff Schmising, P. Gaal, and M. Bargheer

J. Appl. Cryst. 46, 5 (2013)



Journal of
**Applied
Crystallography**
ISSN 0021-8898

Ultrafast reciprocal-space mapping with a convergent beam

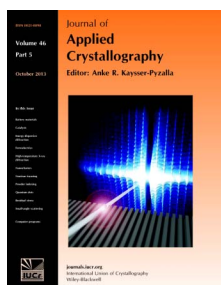
Daniel Schick, Roman Shayduk, André Bojahr, Marc Herzog, Clemens von Korff Schmising, Peter Gaal and Matias Bargheer

J. Appl. Cryst. (2013). **46**, 1372–1377

Copyright © International Union of Crystallography

Author(s) of this paper may load this reprint on their own web site or institutional repository provided that this cover page is retained. Reproduction of this article or its storage in electronic databases other than as specified above is not permitted without prior permission in writing from the IUCr.

For further information see <http://journals.iucr.org/services/authorrights.html>



Journal of Applied Crystallography covers a wide range of crystallographic topics from the viewpoints of both techniques and theory. The journal presents papers on the application of crystallographic techniques and on the related apparatus and computer software. For many years, the *Journal of Applied Crystallography* has been the main vehicle for the publication of small-angle scattering papers and powder diffraction techniques. The journal is the primary place where crystallographic computer program information is published.

Crystallography Journals **Online** is available from journals.iucr.org

research papers

Journal of
Applied
Crystallography

ISSN 0021-8898

Received 24 May 2013

Accepted 19 July 2013

Ultrafast reciprocal-space mapping with a convergent beam

Daniel Schick,^a Roman Shayduk,^d André Bojahr,^a Marc Herzog,^{a,b} Clemens von Korff Schmising,^c Peter Gaal^d and Matias Bargheer^{a,d,*}

^aInstitut für Physik and Astronomie, Universität Potsdam, Karl-Liebknecht-Strasse 24–25, 14476 Potsdam, Germany, ^bAbteilung Physikalische Chemie, Fritz-Haber-Institut der Max-Planck-Gesellschaft, Faradayweg 4–6, 14195 Berlin, Germany, ^cHelmholtz-Zentrum Berlin für Materialien und Energie GmbH, Wilhelm-Conrad-Röntgen Campus, BESSY II, Albert-Einstein-Strasse 15, 12489 Berlin, Germany, and ^dInstitut für Optik und Atomare Physik, Technische Universität Berlin, Strasse des 17 Juni 135, 10623 Berlin, Germany. Correspondence e-mail: bargheer@uni-potsdam.de

A diffractometer setup is presented, based on a laser-driven plasma X-ray source for reciprocal-space mapping with femtosecond temporal resolution. In order to map out the reciprocal space, an X-ray optic with a convergent beam is used with an X-ray area detector to detect symmetrically and asymmetrically diffracted X-ray photons simultaneously. The setup is particularly suited for measuring thin films or imperfect bulk samples with broad rocking curves. For quasi-perfect crystalline samples with insignificant in-plane Bragg peak broadening, the measured reciprocal-space maps can be corrected for the known resolution function of the diffractometer in order to achieve high-resolution rocking curves with improved data quality. In this case, the resolution of the diffractometer is not limited by the convergence of the incoming X-ray beam but is solely determined by its energy bandwidth.

© 2013 International Union of Crystallography
Printed in Singapore – all rights reserved

1. Introduction

Reciprocal-space mapping (RSM) has been established as a powerful tool for the nondestructive structural analysis of thin films and heterostructures (Bauer *et al.*, 1995; Fewster, 1997; Bowen & Tanner, 1998; Holy *et al.*, 1999). In addition to the intense specular Bragg reflections, the surrounding diffuse scattering covered by RSM gives access to microscopic information on strain states, dislocations and mosaicity, as well as the shape and size of the coherently scattering domain. The common drawback of RSM experiments is the need for time-consuming mesh scans in order to map out the reciprocal space in two or even three dimensions.

So far, high-resolution RSM has been precluded from time-resolved diffractometry such as *in situ* or pump–probe X-ray diffraction (XRD), either because of the too long integration time for a single reciprocal-space map or because of the required long-term stability, respectively. Owing to the availability of modern position-sensitive X-ray detectors (PSDs) with low noise and large dynamic range, several new diffractometer setups for RSM have been implemented (Kinne *et al.*, 1998; Mudie *et al.*, 2004; Masson *et al.*, 2005; Mariager *et al.*, 2009). In these high-speed RSM setups, the analysing part of the diffractometer has been replaced by a PSD in order to record symmetrically and asymmetrically diffracted X-rays simultaneously, resulting in a considerable decrease in the total measurement time. Compared with a conventional high-resolution diffractometer, the resolution in reciprocal space of the above-mentioned high-speed RSM

setups is limited by the PSD used, which defines the analyser acceptance by its pixel size and distance from the sample, while the monochromator settings are unchanged. Recent high-speed *in situ* RSM experiments during molecular beam epitaxy by Hu *et al.* (2012) proved the power of this new method.

In this contribution, we present a detailed characterization of a diffractometer for time-resolved RSM utilizing a laser-driven plasma X-ray source (PXS) providing femtosecond (fs) temporal resolution in a pump–probe scheme. The low photon flux at such exceptionally short pulse sources requires the collection of as many photons as possible. Accordingly, the resolution function of the PXS diffractometer is dominated by the convergent incoming X-rays, including Cu $K\alpha_1$ and $K\alpha_2$ energies, in contrast with other high-speed RSM setups.

In the first part, we will derive the resolution function of the ultrafast reciprocal-space mapping (URSM) setup in order to prove its applicability for the multidimensional structural analysis of thin films and heterostructures. As an example of a time-resolved URSM experiment, we present data from a double-layer structure made up of a ferroelectric $\text{PbZr}_{0.2}\text{Ti}_{0.8}\text{O}_3$ (PZT) layer grown on a metallic SrRuO_3 (SRO) layer on top of a dielectric SrTiO_3 (STO) substrate, which exhibits in- and out-of-plane lattice dynamics on a picosecond (ps) timescale after photo-excitation (Schick *et al.*, 2013). For laterally nearly perfect samples, the resolution function of the URSM setup dominates the in-plane broadening of the reciprocal lattice points (RLPs), and no lateral structural infor-

mation is resolvable by RSM. In order to access only the out-of-plane structural information we can correct the URSM data for the known resolution function of the setup, in order to collect one-dimensional time-resolved XRD data with high resolution and increased data quality compared with conventional XRD. The resolution of such rocking curves is no longer limited by the convergence of the incoming X-ray beam but solely by its energy bandwidth.

2. Experimental setup

The hardware constituting the experimental setup of the PXS has been described recently (Zamponi *et al.*, 2009; Schick *et al.*, 2012). In short, we use a two-stage Ti:sapphire amplifier operating at a repetition rate of 1 kHz with a centre wavelength of 800 nm and a pulse energy of 8 mJ compressed into a pulse of 40 fs duration to generate X-ray pulses (predominantly characteristic Cu $K\alpha$ and $K\beta$ lines) by focusing the main part (80%) of the laser light onto a moving copper tape in a vacuum chamber. The emitted X-ray bursts are further collected, focused and monochromated to only Cu $K\alpha$ energies ($E_{K\alpha_1} = 8047$ eV, $E_{K\alpha_2} = 8027$ eV, $\Delta E/E \simeq 0.25\%$) by a Montel multilayer optic with a convergence of $\Delta\omega = 0.3^\circ$ (full width at half-maximum, FWHM) in both dimensions and a focal spot size of only 200–300 μm (FWHM) at a distance $d = 1000$ mm from the source. From the maximum X-ray flux of approximately 5×10^5 photons s^{-1} , the brilliance B of the X-ray focus can be estimated as

$$B = 1.1 \times 10^5 \frac{\text{photons}}{\text{s mm}^2 \text{ mrad}^2 0.1\% \text{ BW}}, \quad (1)$$

which is much lower than for standard X-ray tubes (BW denotes bandwidth). However, considering the PXS pulse length of only 200 fs, the resulting peak brilliance per pulse becomes

$$B_{\text{peak}} = 5.7 \times 10^{14} \frac{\text{photons}}{\text{s mm}^2 \text{ mrad}^2 0.1\% \text{ BW}}. \quad (2)$$

Owing to the limited photon flux of the PXS, it is not reasonable to increase the brilliance of the source by additional monochromators and/or collimators since time-resolved experiments require high counting statistics.

The remaining 20% of the optical laser light is used to excite the sample. The relative timing of the optical pump pulses to the X-ray probe pulses is set by a mechanical delay stage and is inherently jitter free. The temporal information is extracted by performing XRD scans for different delays between optical pump pulses and X-ray probe pulses.

The sample is mounted in the centre of a two-circle goniometer which is placed in the focal plane of the X-ray optics. Thus, the X-ray footprint on the sample is minimized in order to reduce time-smearing effects due to the inevitable non-collinearity between laser pump and X-ray probe beam, and in order to probe a homogeneously excited part of the sample. The fast read-out CMOS (complementary metal-oxide semiconductor) two-dimensional X-ray detector is mounted on the outer circle of the goniometer at a distance of approximately

700 mm from the centre. The pixel size of the detector is approximately 200 μm in both dimensions, resulting in an angular acceptance in the scattering plane for each pixel of $\Delta\theta = 0.016^\circ$.

In order to account for both long- and short-term fluctuations, the PXS intensity is monitored directly by recording the unused intensity of a single reflection of our Montel X-ray optic with an integrating fast X-ray diode (Schick *et al.*, 2012). The nonlinear dependence between the diode response and the number of X-ray photons at the focus have been calibrated to determine the absolute number of X-ray photons per second at the focus during real experiments. Accordingly, the recorded rocking scans/RSM reflect the absolute diffracted intensity of the investigated sample.

3. Resolution area

Here, we discuss the resolution of the URSM setup, which is given by the smallest volume element in reciprocal space that is resolved by the X-ray diffractometer. Since we are carrying out only two-dimensional RSM, this volume element is reduced to an area and we can integrate the diffracted intensity on the two-dimensional detector along the dimension that is normal to the diffraction plane during the actual XRD scans. Accordingly, it would be sufficient to use a one-dimensional pixel array with a large pixel height to detect the diffracted X-rays. Knowledge of the resolution area is essential for the applicability of the diffractometer setup, since it determines the structural details of a sample which can be identified by RSM.

We carried out an $\omega/2\theta$ scan with the area detector in order to measure symmetric Bragg reflections with the URSM setup (see Fig. 1). The $\omega/2\theta$ scan ($\omega = \theta$) corresponds to a scan along q_z in reciprocal space (inset in Fig. 1). However, the PSD records symmetrically and asymmetrically diffracted photons at the same time, which corresponds to a scan of the detector angle θ at a fixed incoming angle ω (2θ scan). Accordingly, we can assign an angle θ to each individual pixel column of the PSD for a fixed ω , if the centre column of the region of interest (ROI) on the PSD is always at $\theta = \omega$. The angles of the surrounding pixel columns at position x (positive integer) follow from

$$\theta(x) = \Delta\theta(x - x_c) + \omega, \quad (3)$$

where x_c is the position of the central pixel column in the ROI and $\Delta\theta$ is the angular acceptance of each pixel column.

The diffracted intensities measured in (ω, θ) space can be converted into q space by the following coordinate transformation (Holy *et al.*, 1999):

$$\mathbf{q} = \begin{pmatrix} q_x \\ q_z \end{pmatrix} = k \begin{pmatrix} \cos\theta - \cos\omega \\ \sin\omega + \sin\theta \end{pmatrix}, \quad (4)$$

where $k = 2\pi/\lambda$ is the magnitude of the incoming and outgoing X-ray wavevectors, since only elastic diffraction is considered; λ is the wavelength of the radiation. The resolution area of the diffractometer depends on various parameters but we discuss only the most prominent ones here. We can neglect any

research papers

broadening on the reciprocal-space map due to a finite X-ray spot size on the sample, since we use a convergent beam with the sample in the focus of the X-ray beam path, and hence the X-ray footprint is comparable to the size of the individual pixels of the PSD. We consider the convergence of the incoming X-rays $\Delta\omega$, the acceptance of the detector pixels $\Delta\theta$ and the wavevector spread due to the energy bandwidth of the X-ray photons $\Delta k/k = \Delta E/E$ as sources of instrumental broadening. As a linear approximation, both the magnitude and direction of the instrumental broadening in q space can be determined by the partial derivative of \mathbf{q} multiplied by the change in the deviating parameter:

$$\Delta\mathbf{q}_\omega = \frac{\partial\mathbf{q}}{\partial\omega} \Delta\omega = \begin{pmatrix} \sin\omega \\ \cos\omega \end{pmatrix} k \omega \Delta\omega, \quad (5)$$

$$\Delta\mathbf{q}_\theta = \frac{\partial\mathbf{q}}{\partial\theta} \Delta\theta = \begin{pmatrix} -\sin\theta \\ \cos\theta \end{pmatrix} k \theta \Delta\theta, \quad (6)$$

$$\Delta\mathbf{q}_k = \frac{\partial\mathbf{q}}{\partial k} \Delta k = \begin{pmatrix} \cos\theta - \cos\omega \\ \sin\omega + \sin\theta \end{pmatrix} \Delta k. \quad (7)$$

For a symmetric Bragg reflection, the inclination of $\Delta\mathbf{q}_\omega$ with respect to the q_z axis is ω . This is referred to as the monochromator streak (Holy *et al.*, 1999). The so-called analyser

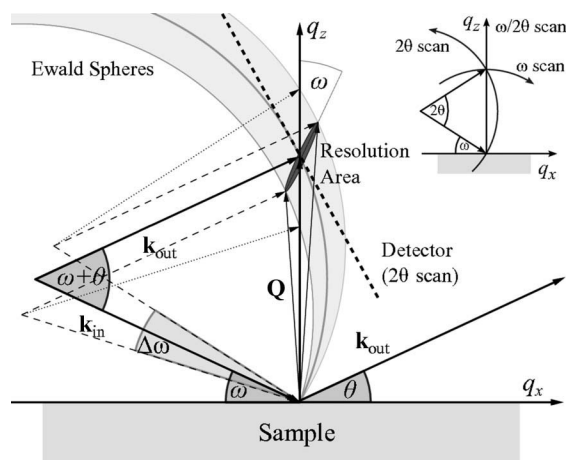


Figure 1

The reciprocal-space coordinate system (q_x, q_z) of the sample. The angles between the sample surface and the incoming and outgoing X-rays, \mathbf{k}_{in} and \mathbf{k}_{out} , are denoted ω and θ , respectively. Owing to the convergence $\Delta\omega$ of \mathbf{k}_{in} , a range of nonconcentric Ewald circles is illuminated simultaneously (dotted lines). The angle-resolving detector is represented as a tangent at the intersection of an Ewald circle and the q_z axis (thick dashed line). The resolution is dominated by the convergence $\Delta\omega$ and we neglect the acceptance of the detector pixels $\Delta\theta \rightarrow 0$ here (see text). A pixel at a fixed angle θ then integrates over the resolution area, which is inclined by ω with respect to the q_z axis. The thin dashed lines are parallel to \mathbf{k}_{out} (fixed θ) but originate at different \mathbf{k}_{in} vectors, determined by the convergence $\Delta\omega$. The energy spread leads to a broadening along q_z . The resolution area is approximated as an ellipsoid, assuming a Gaussian distribution of $\Delta\omega$ and ΔE . The inset shows the different scan types for RSM: the $\omega/2\theta$ scan goes along the q_z axis, the ω scan is approximately parallel to the q_x axis and the 2θ scan goes along the Ewald circle.

streak originates from $\Delta\mathbf{q}_\theta$ and is inclined by $\omega \simeq \theta$ in the opposite direction. Since the magnitude of $\Delta\mathbf{q}_\omega$ is approximately 20 times larger than the magnitude of $\Delta\mathbf{q}_\theta$ for the URSM setup, we neglect the latter in the following discussion. Fig. 1 shows the graphical analogue of the theoretical derivation of the instrumental broadening of the URSM setup. Owing to the convergence $\Delta\omega$ of the incoming X-rays \mathbf{k}_{in} , a distribution of nonconcentric Ewald circles is illuminated in reciprocal space. A single detector pixel at a fixed angle θ with an infinitesimally small acceptance $\Delta\theta \rightarrow 0$ integrates the diffracted intensity along the vector $|\Delta\mathbf{q}_\omega|$, which is constructed by a parallel translation of \mathbf{k}_{out} to the origins of all incident \mathbf{k}_{in} (thin dashed lines in Fig. 1). This resolution streak is inclined by ω with respect to the q_z axis (monochromator streak). The energy spread of the incoming X-rays leads to an additional broadening along q_z , which is approximated as an ellipsoidal resolution area in Fig. 1 for a Gaussian distribution of $\Delta\omega$ and ΔE .

The resolution function of the URSM setup can be determined experimentally by measuring the reciprocal-space map around an RLP of an almost perfect bulk crystal. The measured data correspond to a convolution of the resolution function with the RLP, which can be approximated as a δ function for the case of a perfect bulk crystal. Fig. 2(a) shows the experimental reciprocal-space map of the (002) Bragg

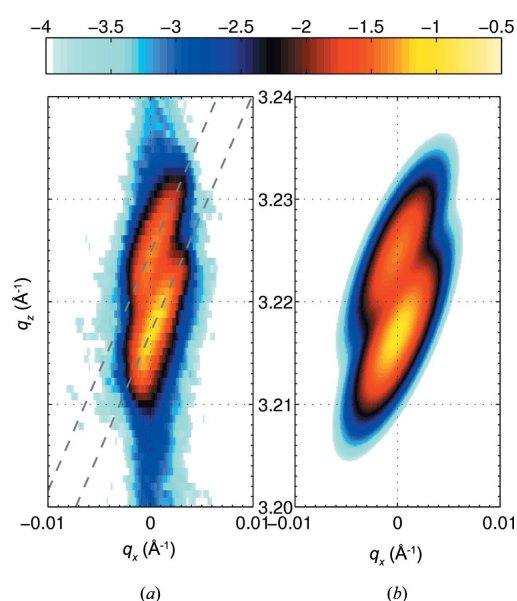


Figure 2

(a) The measured reciprocal-space map of the (002) Bragg reflection of a nearly perfect STO substrate. The data are plotted with equidistant axes and reveal the resolution area of the time-resolved RSM setup. The inclination of the resolution area with respect to the q_z axis is ω and is represented by the grey dashed lines. The peak doubling and the broadening along q_z are caused by the Cu $K\alpha$ doublet and the natural line width of each $K\alpha$ line, respectively. (b) The theoretical resolution area at $\omega = 23.23^\circ$ is plotted, accounting for the convergence $\Delta\omega$ and the energy bandwidth of the incoming X-rays \mathbf{k}_{in} . Broadening due to the finite acceptance of the detector is neglected here.

reflection of a nearly perfect STO substrate. The inclination of the resolution area with respect to the q_z axis can be determined as $\omega = 23.23^\circ$, which is represented by the grey dashed lines. The doubling of the RLP originates from the Cu $K\alpha$ doublet and corresponds to a separation of approximately $\Delta q_z = k\Delta E/E \simeq 0.01 \text{ \AA}^{-1}$. The broadening along q_z is caused by the natural line width of each $K\alpha$ line, which is approximately 2 eV (Krause & Oliver, 1979). The diffuse background along the q_z axis indicates the crystal truncation rod of the substrate. In Fig. 2(b), the theoretical resolution area of the URSM setup is plotted, which is derived from equations (5)–(7). The resolution area is approximated as two two-dimensional Gaussian functions with one main axis along $\Delta \mathbf{q}_\omega$. The intensities are normalized to the maximum of the experimental data shown in Fig. 2(a), and the ratio of the maxima of the two Gaussians equals the intensity ratio of the Cu $K\alpha_1$ and $K\alpha_2$ lines. The good agreement between the experimentally determined and theoretically derived resolution functions of the URSM setup allows one to distinguish between instrumental and structural broadening of RLPs in actual time-resolved RSM experiments. Furthermore, neglecting additional sources of instrumental broadening proved to be valid.

4. Time-resolved reciprocal-space mapping

In order to prove the applicability of the diffractometer setup for time-resolved RSM, we have chosen an epitaxial thin-film

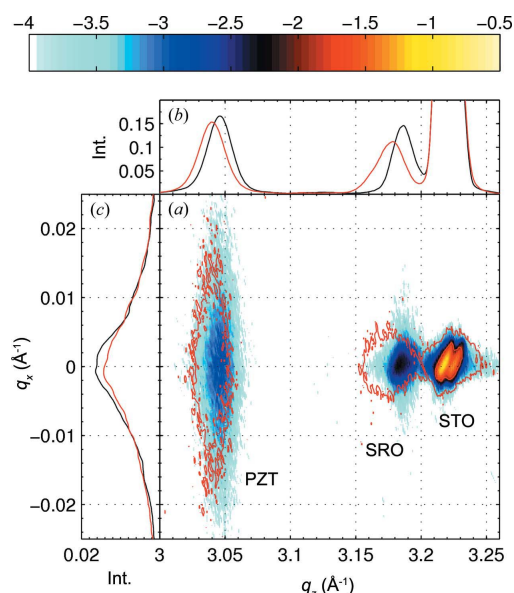


Figure 3 (a) The measured reciprocal-space map of the (002) Bragg reflections of the PZT/SRO double layer on an STO substrate. The red contour lines (constant reflectivity of $10^{-3.5}$) and the red lines in parts (b) and (c) indicate the changed RSM at a delay of $t = 75$ ps after excitation of the sample with an 800 nm femtosecond laser pulse. (b), (c) Integrated reciprocal-space maps over the q_x and q_z dimension, respectively. In (c), the integration is carried out only over the q_z range of the PZT peak.

sample that consists of a ferroelectric PZT layer and a metallic SRO transducer layer which were grown onto an STO substrate by pulsed laser deposition (Vrejoiu *et al.*, 2006). From the detailed characterization of the sample by transmission electron microscopy (TEM) and static XRD, we derived layer thicknesses of $d_{\text{PZT}} = 207$ nm and $d_{\text{SRO}} = 147$ nm, and average lattice constants normal to the sample surface of $c_{\text{PZT}} = 4.130 \text{ \AA}$, $c_{\text{SRO}} = 3.948 \text{ \AA}$ and $c_{\text{STO}} = 3.905 \text{ \AA}$ (Schick *et al.*, 2013). The ferroelectric PZT layer exhibits large defects such as threading and misfit dislocations, due to the intrinsic domain formation of this material. This gives rise to structural in-plane broadening of the corresponding RLP.

The resulting time-resolved reciprocal-space map is depicted in Fig. 3 and features the dominant broadening of the PZT RLP along q_x . The broadening of the SRO and STO RLPs is dominated by the resolution area of the diffractometer, which is indicated by their size and inclination. The SRO RLP also features a slight diffuse broadening in the q_x dimension due to its lower crystal quality compared with the STO substrate. The adoption of the high-speed RSM technique allows one to measure a time-resolved reciprocal-space map within minutes, providing good photon statistics. For the femtosecond variant of RSM at PXS machines this is particularly important, because the reciprocal-space maps for different time delays after excitation have to be compared, and long-term drifts of the setup are often inevitable. The unpumped data set shown in Fig. 3 was recorded within 30 min. The red contour lines at a constant reflectivity of $10^{-3.5}$ in Fig. 3(a), and the red lines in Figs. 3(b) and 3(c), show the result of the RSM probing 75 ps after excitation of the sample with an 800 nm femtosecond laser pulse. The changes in the positions and widths of the material-specific Bragg peaks in the reciprocal-space map can be analysed in order to study the photoinduced in- and out-of-plane lattice dynamics with femtosecond temporal resolution (Schick *et al.*, 2013).

5. Rocking scans

For laterally nearly perfect crystalline samples, the structural Bragg peak broadening in-plane is well below the resolution of our URSM setup. As an example, we show the URSM data of a superlattice (SL) in Fig. 4(a). The SL is composed of 15 double layers, each consisting of 7.3 nm metallic ($\text{La}_{0.7}\text{Sr}_{0.3}\text{MnO}_3$ (LSMO) and 13.7 nm ferroelectric ($\text{Ba}_{0.7}\text{Sr}_{0.3}\text{TiO}_3$ (BST)). The SL is grown epitaxially on an STO substrate with very high crystalline quality. Here, we wish to derive a means of benefitting from the URSM setup for such highly perfect crystalline samples. Since we cannot resolve the in-plane Bragg peak broadening for this sample, we are limited to out-of-plane structural information, which can be achieved by standard rocking scans ($\omega/2\theta$ scan for symmetric Bragg reflection). Thus, it would be sufficient to use a one-dimensional point detector in the diffractometer setup. The corresponding rocking curve for a point detector with a large acceptance $\Delta\theta \gg \Delta\omega$ is plotted in Fig. 4(c) as a red line (the data are imitated by integrating the original data from the PSD detector along the scattering plane). The rocking curve

research papers

exhibits good statistics, since nearly all diffracted photons are collected by the detector, but the resolution of the individual Bragg peaks is very low because $\Delta\mathbf{q}_\theta$ can no longer be neglected. Accordingly, all peaks are broadened and no Cu $K\alpha$ doublet is observed.

If we use a point detector with the same acceptance $\Delta\theta$ as for a single pixel of the PSD, *e.g.* by the use of slits, we obtain a much higher resolution of the rocking curve, shown as a blue line in Fig. 4(c). This plot is equivalent to a cut along q_x of the data shown in Fig. 4(a). However, since we discriminate all asymmetrically diffracted X-ray photons with this slit setup, the counting statistic of the resulting rocking curve is approximately 14% that of the large-aperture detector (red line) and is thus not applicable for time-resolved experiments with PXS machines.

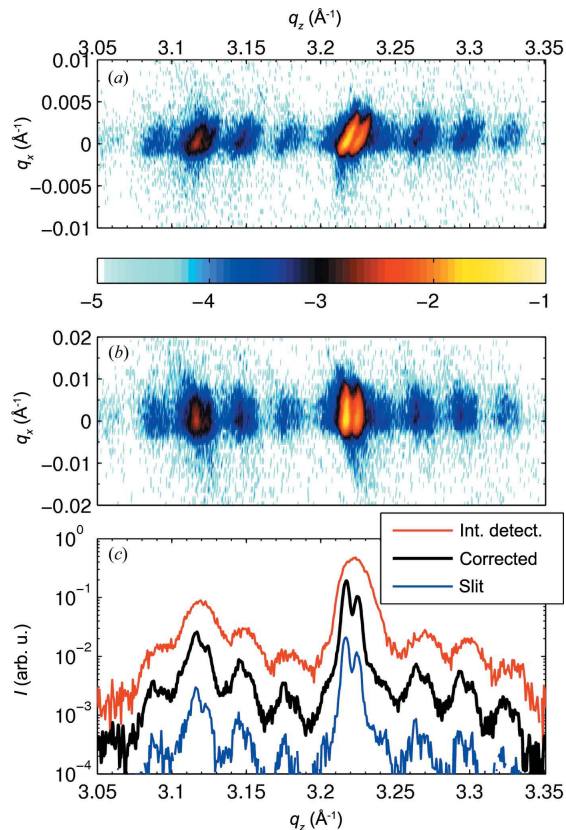


Figure 4 (a) (Original) reciprocal-space map for the BST/LSMO SL on an STO substrate, revealing several SL reflections and the most intense STO substrate (002) reflection. (b) (Corrected) reciprocal-space map after translational/rotational transformation. (c) The red curve imitates a measurement using a large point detector with an acceptance $\Delta\theta$ much larger than the convergence $\Delta\omega$. The blue curve imitates the use of a slit in front of a point detector $\Delta\theta \rightarrow 0$, *i.e.* a cut at $q_x = 0$ from (a). The black curve is the integration over the complete q_x range of the corrected data shown in (b). The curves are offset in intensity for better visualization.

Since we know that the broadening of the RLP for such highly perfect samples originates primarily from the resolution function of the URSM setup, we can correct the data accordingly. By rotating each ellipsoidal RLP that intersects the q_z axis at $q_z = 2k \sin \omega$ by an angle of $\gamma = (90^\circ - \omega)$, we can assign all asymmetrically diffracted X-ray photons to the correct q_z value of the symmetric RLP by integrating over the q_x axis. The coordinate transformation is derived in Appendix A and the result is shown in Fig. 4(b), where all RLPs are now aligned parallel to the q_x axis. The integration of these corrected data along q_x is shown as a black curve in Fig. 4(c) and combines the high resolution of the slit-like blue curve and the good statistics of the large-aperture-like red curve.

6. Conclusions

The implementation of the high-speed RSM technique using position-sensitive X-ray detectors allows the implementation of time-resolved RSM at PXS setups. The instrumental and structural broadening of the URSM can be distinguished by the inclination and width of the measured RLPs. The method has been applied to study the in- and out-of-plane lattice dynamics in a ferroelectric thin film after photoexcitation on a picosecond timescale (Schick *et al.*, 2013). For nearly perfect crystalline samples, the experimental routine can be applied with an adapted data-processing routine in order to correct the measured RLPs for the known resolution function of the diffractometer. This procedure allows for the recording of high-resolution rocking curves without discriminating diffracted X-rays, since the resolution is no longer limited by the convergence of the incoming X-ray beam, but solely by its energy bandwidth.

APPENDIX A
Resolution area correction

Fig. 5 sketches the RLP in the reciprocal-space map for a highly perfect crystalline sample, so the RLP is primarily broadened by the resolution area of the URSM setup. As was derived in §3, the ellipsoidal RLP is inclined by ω with respect

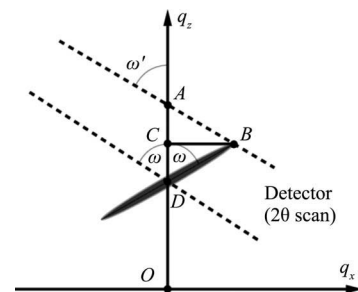


Figure 5 The ellipsoidal RLP is inclined by ω and intersects the q_z axis at point D . The intensity along the ellipsoidal RLP, *e.g.* at point B , is recorded for an incoming angle ω' at a pixel at $\theta' \neq \omega'$.

to the q_z axis when the intersection of the RLP with the q_z axis is at the point $D = (0, 2k \sin \omega)$. In order to correct the data for the resolution function of the diffractometer, one has to rotate the ellipsoidal RLP around the point D by an angle of $\gamma = (90^\circ - \omega)$. For any point B along the RLP, this is done by translating point B by the vector $-\mathbf{OD}$, in order subsequently to rotate B counterclockwise by γ around the origin O of the coordinate system, and translating it back by the vector \mathbf{OD} .

However, the intensity at point B is measured at an incoming angle ω' with a pixel at an angle $\theta' \neq \omega'$. Thus, it is nontrivial to determine the coordinates of the corresponding intersection point $D(\omega)$ from the point $B(\omega', \theta')$. If $\omega' \simeq \omega$, which holds for a small convergence $\Delta\omega$, one can approximate that $\overline{DC} = \overline{CA}$ and one can derive the q_z coordinate of point D as

$$D_z = \overline{OA} - 2\overline{CA} = 2(B_z - k \sin \omega'), \quad (8)$$

where B_z is the q_z coordinate of the point $B(\omega', \theta')$ given by the general transformation $\mathbf{q}(\omega, \theta)$ into q space, cf. equation (4).

The complete coordinate transformation for the correction of the URSM data for laterally nearly perfect samples can then be written in matrix form as a combination of translation and rotation:

$$\begin{aligned} \mathbf{q}_c &= \mathbf{R} \cdot [\mathbf{q}(\omega, \theta) - \mathbf{OD}] + \mathbf{OD} \\ &= \begin{pmatrix} \cos \gamma & -\sin \gamma \\ \sin \gamma & \cos \gamma \end{pmatrix} \cdot \left[\mathbf{q}(\omega, \theta) - \begin{pmatrix} 0 \\ D_z \end{pmatrix} \right] + \begin{pmatrix} 0 \\ D_z \end{pmatrix}, \quad (9) \end{aligned}$$

where \mathbf{R} is a rotation matrix.

The authors gratefully acknowledge financial support by the BMBF via grant No. 03WKPO3A and by the Leibniz Graduate

School 'Dynamics in New Light' (DinL). We thank Dr Ionela Vrejoiu for fruitful discussions and for providing the experimental samples.

References

- Bauer, G., Li, J. & Koppensteiner, E. (1995). *J. Cryst. Growth*, **157**, 61–67.
- Bowen, D. K. & Tanner, B. K. (1998). *High-resolution X-ray Diffractometry and Topography*. London: Taylor and Francis.
- Fewster, P. F. (1997). *Crit. Rev. Solid State Mater. Sci.* **22**, 69–110.
- Holy, V., Pietsch, U. & Baumbach, T. (1999). *High-resolution X-ray Scattering from Thin Films and Multilayers*. Springer Tracts in Modern Physics, Vol. 149. Heidelberg: Springer.
- Hu, W., Suzuki, H., Sasaki, T., Kozu, M. & Takahasi, M. (2012). *J. Appl. Cryst.* **45**, 1046–1053.
- Kinne, A., Thoms, M., Röss, H. R., Gerhard, T., Ehinger, M., Faschinger, W. & Landwehr, G. (1998). *J. Appl. Cryst.* **31**, 446–452.
- Krause, M. O. & Oliver, J. H. (1979). *J. Phys. Chem. Ref. Data*, **8**, 329–338.
- Mariager, S. O., Lauridsen, S. L., Dohn, A., Bovet, N., Sørensen, C. B., Schlepütz, C. M., Willmott, P. R. & Feidenhans'l, R. (2009). *J. Appl. Cryst.* **42**, 369–375.
- Masson, O., Boule, A., Guinebretière, R., Lecomte, A. & Dauger, A. (2005). *Rev. Sci. Instrum.* **76**, 063912.
- Mudie, S. T., Pavlov, K. M., Morgan, M. J., Hester, J. R., Tabuchi, M. & Takeda, Y. (2004). *J. Synchrotron Rad.* **11**, 406–413.
- Schick, D., Bojahr, A., Herzog, M., Gaal, P., Vrejoiu, I. & Bargheer, M. (2013). *Phys. Rev. Lett.* **110**, 095502.
- Schick, D., Bojahr, A., Herzog, M., von Korff Schmising, C., Shayduk, R., Leitenberger, W., Gaal, P. & Bargheer, M. (2012). *Rev. Sci. Instrum.* **83**, 025104.
- Vrejoiu, I., Le Rhun, G., Zakharov, N. D., Hesse, D., Pintilie, L. & Alexe, M. (2006). *Philos. Mag.* **86**, 4477–4486.
- Zamponi, F., Ansari, Z., von Korff Schmising, C., Rothhardt, P., Zhavoronkov, N., Woerner, M., Elsaesser, T., Bargheer, M., Trobitzsch-Ryll, T. & Haschke, M. (2009). *Appl. Phys. A*, **96**, 51–58.

Paper IV

Ultrafast x-ray diffraction studies of photoexcited coherent phonons in SrRuO₃ thin films

D. Schick, P. Gaal, A. Bojahr, W. Leitenberger, R. Shayduk, A. Hertwig, I. Vrejoiu, M. Herzog, and M. Bargheer

arxiv 1301.3324, (2013)

Ultrafast x-ray diffraction studies of photoexcited coherent phonons in SrRuO₃ thin films

D. Schick,¹ P. Gaal,² A. Bojahr,¹ W. Leitenberger,¹ R. Shayduk,²
A. Hertwig,³ I. Vrejoiu,⁴ M. Herzog,^{1,*} and M. Bargheer^{1,2}

¹*Institut für Physik und Astronomie, Universität Potsdam,
Karl-Liebknecht-Str. 24-25, 14476 Potsdam, Germany*

²*Helmholtz-Zentrum Berlin für Materialien und Energie GmbH,*

Wilhelm-Conrad-Röntgen Campus, BESSY II, Albert-Einstein-Str. 15, 12489 Berlin Germany

³*Bundesanstalt für Materialforschung und -prüfung, Unter den Eichen 87, 12205 Berlin, Germany*

⁴*Max-Planck-Institut für Mikrostrukturphysik, Weinberg 2, 06120 Halle, Germany*

(Dated: January 16, 2013)

We present ultrafast x-ray diffraction experiments on thin films of metallic SrRuO₃ (SRO) after their excitation with ultrashort intense laser pulses. Depending on the layer thickness, the data exhibit a transient splitting of the (002) SRO Bragg peak evidencing the generation and propagation of sharp acoustic strain waves. These distinct structural dynamics are due to the exceptionally fast electron-phonon relaxation that gives rise to a quasi-instantaneous thermal stress in SRO. The interpretation is corroborated by numerical simulations which show excellent agreement with the experimental findings. Despite the qualitatively different lattice dynamics for different SRO layer thicknesses, we identify a universal evolution of the transient average layer strain. The inferred discrepancy of the thermal stress profile from the excitation profile may hint toward a temperature-dependent effective Grüneisen parameter of SRO.

Keywords: Ultrafast, X-ray diffraction, Thin films, Lattice dynamics

I. INTRODUCTION

In general, the internal energy of condensed matter is spread over various degrees of freedom such as electrons, lattice, magnetization and polarization. Intense and ultrashort laser pulses can directly excite one or more of these degrees of freedom within a given material. The subsequent dynamics of the individual subsystems and thus the entire system are then governed by the coupling strengths of the different degrees of freedom. For instance, structural dynamics of a crystalline lattice can be induced directly by infrared/THz absorption¹ and Brillouin/Raman scattering^{2,3} or indirectly by an initial electronic excitation (interband or intraband^{4,5}) and subsequent electron-phonon coupling^{5,6}. Depending on the material of interest, the electronic and phononic subsystems may also be coupled to other degrees of freedom such as polarization^{6,7}, magnetization^{8–11} or charge and/or orbital order^{11–14}. The understanding of these complex physical processes for a given material is of fundamental interest and, moreover, promises technological advances in the fields of signal processing, data storage and sensors as well as novel x-ray optics for ultrafast studies^{15–17}. In particular, the coupling of various degrees of freedom is often mediated by the lattice. This triggered an enormous interest in time-resolved scattering techniques during the last two decades in order to monitor the laser-induced changes of the structural properties^{4,18–21}.

A material of particular interest is the “bad metal” SrRuO₃ (SRO) due to its various complex physical properties such as itinerant ferromagnetism^{22,23}, ultrafast magnetostriction and electron-phonon coupling^{9,24}, neg-

ative spin polarization²⁵, orbital ordering²⁶ and non-Fermi liquid behaviour^{27,28}. This material can be epitaxially grown on single-crystal substrates (such as dielectric SrTiO₃ [STO]) with high structural perfection²⁹. In combination with a fast electron-phonon relaxation of 200 fs or less^{9,24} and a very high damage threshold³⁰, SRO is perfectly suited as transducer material for the generation of coherent longitudinal acoustic (LA) phonons³¹.

This report focuses on the structural dynamics of layered crystalline solids induced by ultrashort laser pulses. In particular, we discuss the generation and evolution of acoustic deformations of SRO thin films on a supporting STO substrate. We utilize the experimental method of ultrafast x-ray diffraction (UXRD). This technique employs the pump-probe scheme in which the laser-induced structural dynamics are probed by an ultrashort hard x-ray pulse at different time delays τ after the arrival of the excitation (pump) pulse. After a brief introduction of the theoretical framework which describes the ultrafast build-up of laser-induced thermal stress in SRO, we present results of UXRD experiments on two thin films with thicknesses smaller and larger than the optical penetration depth of the 800 nm pump light. The transient changes in the UXRD data readily evidence a complex formation and propagation of LA phonon wavepackets. However, qualitatively different features appear for the two different samples. In particular, the thicker SRO layer exhibits a splitting of the Bragg peak as opposed to a continuous shift in case of the thinner film. The experimental data can be precisely simulated by means of numerical models for the photoinduced structural dynamics³² and the dynamical diffraction of x-rays from these transient crystal structures³⁰. The universal

features of the lattice dynamics are analyzed in detail by considering the spatiotemporal strain fields and the potential and kinetic energy of the photoexcited thin film as well as the substrate.

II. HEATING OF SRO THIN FILMS BY ULTRASHORT LASER PULSES

The topic of laser-induced heating and transport properties of elemental metals (or metal layers) is a fairly well understood process²² and has been discussed many times in literature^{33–36}. In the following we want to give a brief summary and apply the standard theoretical models to the case of thin films of SRO on a STO substrate.

The standard model for describing the transient processes in laser-heated metals is the two-temperature model (TTM) proposed by Anisimov *et al.*³³. It assumes that the optical energy of the laser pulse is entirely absorbed by the conduction band electrons in the metal. The electronic system then rapidly thermalizes towards an elevated electron temperature via electron-electron scattering processes. The temperature of the electronic system T_e then differs from the temperature of the lattice T_l (phononic system) and subsequent electron-phonon collisions transfer energy from electrons to phonons until the two subsystems reach thermal equilibrium. Due to lattice anharmonicities the incoherently excited phonons produce thermal stress which eventually leads to the thermal expansion of the metal. For most metals the electron relaxation time τ_e is on the order of a few tens of femtoseconds (fs)³⁶ and is thus shorter than the typical timescales of laser pulse durations and all other dynamical processes involved. In particular, this assumption holds for SRO which exhibits a very short electron relaxation time of $\tau_e \approx 4.2$ fs at 145 K^{27,37}. This validates the consideration of an electron temperature at all times and restricts the electronic heat transport to be diffusive. Typically, the linear dimensions of the excitation and probe area on the sample surface is much larger than the penetration depth or the film thickness of the metal. Under these circumstances the differential equations of the TTM can be restricted to one spatial dimension and read as follows:

$$C_e(T_e) \frac{\partial T_e}{\partial t} = \frac{\partial}{\partial x} \left(k_e(T_e, T_l) \frac{\partial T_e}{\partial x} \right) - G[T_e - T_l] + S(x, t) \quad (1)$$

$$C_l(T_l) \frac{\partial T_l}{\partial t} = \frac{\partial}{\partial x} \left(k_l(T_e, T_l) \frac{\partial T_l}{\partial x} \right) + G[T_e - T_l] \quad (2)$$

where $C_{e/l}$ and $k_{e/l}$ are the electronic/lattice heat capacity and conductivity, respectively, G is the electron-phonon coupling factor and $S(x, t)$ is the heat source determined by the laser pump pulse^{34,35}. The usual considerations of the TTM for elemental metals employ the fact that the heat is dominantly conducted by the conduction band electrons and that the phononic heat conductivity

is comparably small. This allows the omission of the first term in (2)^{33–36}. In SRO, however, the heat is carried by the electrons and lattice in approximately equal parts^{38,39} which is why we keep this term in (2).

As motivated above, the electron-electron scattering rate is very large in SRO²⁷. The electrons are thus not able to ballistically transport energy out of the excited region into deeper parts of the sample. In addition, SRO is known to have a very fast electron-phonon relaxation time (i.e. large G) on the order of a few hundred femtosecond^{9,24} which is also much faster than any diffusion processes of electrons and phonons. When considering the structural dynamics in thin SRO films on the timescale of a few tens of picoseconds, we can thus disregard the diffusion terms in (1) and (2). This simplifies the problem considerably and the eventual expansion profile (caused by the thermal stress profile) in SRO is proportional to the exponentially decaying profile of the deposited energy density where the proportionality constant is given by the Grüneisen parameter γ ⁴⁰. The energy density profile is given by the derivative of Lambert-Beer's law and thus defined by the optical penetration depth ξ_{opt} of the pump laser light at 800 nm wavelength.

An implication of the very fast electron-phonon coupling in SRO is the fact that the thermal stress is built up quasi-instantaneously which launches coherent LA phonons up to very high frequencies^{9,17,24,30–32}. Similar to the temperature considerations above the structural dynamics are reduced to one spatial dimension. The coherent longitudinal (plane) strain waves traverse the excited metal layer until the entire coherent vibrational energy has left into the substrate and a quasi-statically thermally expanded layer is left. In the following sections we show that the coherent phonon dynamics inside the excited SRO thin film and the underlying STO substrate can be accurately monitored by UXRd experiments. For the later analysis we define the characteristic timescale of sound propagation through a thin film by $T_{\text{sound}} = d/v_{\text{sound}}$ where d is the film thickness and v_{sound} is the longitudinal sound velocity perpendicular to the sample surface.

III. EXPERIMENTAL RESULTS

The UXRd experiments presented and discussed in the following were conducted on thin SRO films of different thickness epitaxially grown on a STO substrate. The samples were excited by ultrashort optical laser pulses at 800 nm wavelength and the triggered structural dynamics within the first few tens of picoseconds were observed by UXRd employing the Plasma X-Ray Source (PXS) at the University of Potsdam, Germany⁴¹. This laser-based x-ray source utilizes hard x-ray pulses at the characteristic Cu $K_{\alpha 1}$ and $K_{\alpha 2}$ line ($E_{\text{PXS}}^{(1)} = 8.048$ keV and $E_{\text{PXS}}^{(1)} = 8.028$ keV) with a pulse duration of ≈ 200 fs. The PXS thus provides the temporal and spatial resolution required for studying coherent acoustic phonon dy-

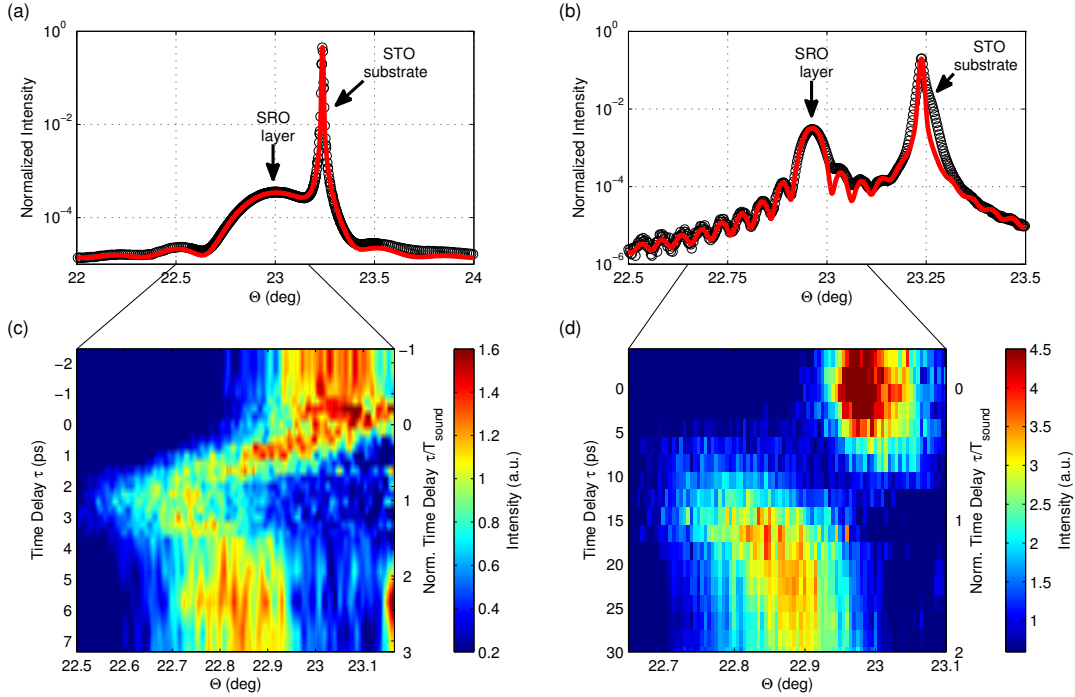


FIG. 1. Static XRD curves (symbols) and dynamical XRD simulation of a (a) 15.4 nm and a (b) 94.8 nm SRO layer on STO around the (002) reflections. The data were recorded at the ESRF ($E_{\text{ESRF}} = 12.0$ keV) and at BESSY II ($E_{\text{BESSY}} = 8.66$ keV), respectively, at x-ray photon energies differing from the characteristic Cu $K_{\alpha 1}$ line ($E_{\text{PXS}} = 8.048$ keV) generated by the PXS. The Bragg angle axes in panel (a) and (b) were thus converted to an artificial x-ray photon energy E_{PXS} to be comparable to the plots (c) and (d). The lower panels present the UXRD data recorded with the PXS on the SRO Bragg peak of the (c) thinner and (d) thicker SRO thin film. The excitation fluences of the 800 nm pump pulses are 30 mJ/cm^2 and 20 mJ/cm^2 , respectively.

namics in thin crystalline films with a thickness below a few hundred nanometer.

The SRO thin film samples were pre-characterized by static x-ray diffraction (XRD) at synchrotron-based x-ray sources. The results of the static Θ - 2Θ scans around the respective (002) reflections are represented by the symbols in Fig. 1(a) and (b). As expected, the thicker SRO film exhibits a narrow and intense Bragg reflection whereas the Bragg peak of the thinner SRO film is much broader and weaker. The solid lines are results of dynamical XRD simulations used for the determination of the layer thickness and c -axis lattice parameter. The simulations revealed a thickness $d_1 = 15.4$ nm and an out-of-plane lattice parameter of $c_1 = 3.9525 \text{ \AA}$ for the thinner SRO layer (Fig. 1(a)) and $d_2 = 94.8$ nm and $c_2 = 3.9493 \text{ \AA}$ (Fig. 1(b)) for the thicker layer. The different lattice parameters are consistent if one considers the epitaxy with the cubic STO substrate ($c_{\text{sub}} = 3.905 \text{ \AA}$) and the relaxation of the substrate-induced tetragonally distorted SRO unit cell as the layer thickness increases. Employing the longitudinal sound velocity of

SRO, $v_{\text{sound}} = 6.312 \text{ nm/ps}$ (Ref. 42), the derived layer thicknesses imply sound transit times of $T_{\text{sound}}^{(1)} = 2.45$ ps and $T_{\text{sound}}^{(2)} = 15.0$ ps for the thinner and thicker SRO layer, respectively. The two samples are chosen in order to represent the limiting cases of layers with thickness smaller and larger than the literature value of the optical penetration depth at 800 nm, $\xi_{\text{opt}}^{\text{lit}} \approx 52 \text{ nm}$ (Ref. 27), respectively.

The UXRD data recorded at the PXS on the thinner and thicker SRO layer using a pump fluence of 30 and 20 mJ/cm^2 are shown in Fig. 1(c) and (d), respectively. Due to the limited signal-to-noise ratio and angle-resolution of the PXS the UXRD data quality is poorer for the thinner SRO layer and the respective SRO Bragg peak of the unexcited sample is not clearly separated from the substrate peak. Nevertheless, the data can be unambiguously analyzed in terms of transient SRO Bragg peak shifts by proper substrate subtraction and thus allow for a clear understanding of the coherent and incoherent phonon dynamics in the photoexcited SRO layers.

The UXRD data exhibit transient changes of the SRO

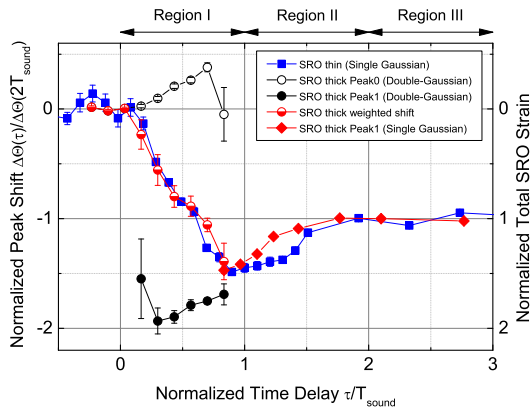


FIG. 2. Normalized transient shift and splitting of the SRO Bragg peak extracted from the UXRd data shown in Fig. 1(c) and (d). The continuous shift observed in the thinner SRO layer is represented by the blue squares (single-Gaussian fitting). The empty and solid black bullets show the transient Bragg angles of the decaying initial and the rising shifted peak for the thicker SRO layer (double-Gaussian fitting). For $\tau/T_{\text{sound}} > 1$ the red diamonds indicate the continuous backshift of the thicker SRO layer (single-Gaussian fitting). The intensity-weighted shift for the thin SRO layer is shown by the red half-filled bullets. The error bars represent the 68% confidence interval of the fitting parameter and lines are a guide to the eye.

Bragg peak positions just after the laser excitation at $\tau = 0$. This directly implies that the quasi-instantaneous heating of the SRO lattice triggers certain structural dynamics inside the SRO layers. At first sight, these dynamics appear to be qualitatively different. In case of the thinner SRO layer we observe a continuous shift of the Bragg peak towards lower angles for $0 < \tau < T_{\text{sound}}$ (region I), followed by a slight continuous backshift for $T_{\text{sound}} < \tau < 2T_{\text{sound}}$ (region II) until it reaches a new quasi-stationary position for $\tau > 2T_{\text{sound}}$ (region III). This quasi-stationary expansion represents the thermal expansion of SRO due to the absorbed energy of the exciting laser pulse. In contrast, the thicker SRO layer does not exhibit a continuous shift for $0 < \tau < T_{\text{sound}}$ (region I). Instead, we find a splitting of the initial Bragg peak into two distinct reflections at intermediate times until the initial peak has disappeared. Similar Bragg peak splittings have been previously observed in photoexcited bulk crystals and thin films^{4,43,44}, however, either the signatures were relatively weak compared to the bulk reflection or a thorough description of the underlying structural dynamics is missing. The comparison of the experimental results in Fig. 1(c) and (d) rises the question whether the structural dynamics responsible for the observed features are indeed qualitatively different. This issue is addressed in the subsequent sections.

We extracted the transient Bragg angles of the mea-

sured SRO peaks by fitting the data with single and double-Gaussian functions. The obtained peak positions are displayed in Fig. 2 where we plot the Bragg angle change normalized to the quasi-stationary value after $2T_{\text{sound}}$, $\Delta\theta(\tau)/\Delta\theta(2T_{\text{sound}})$, versus time delay in units of T_{sound} . Since the angle changes are fairly small they are proportional to the average strain variations of the SRO layer. This is indicated by the secondary y-axis in Fig. 2 presenting the normalized total SRO strain. The plot verifies the features visible in the contour plots in Fig. 1(c) and (d). The thinner sample exhibits a continuous shift of a single SRO peak (blue squares). In contrast, the SRO peak in the thicker sample for normalized time delays up to T_{sound} (region I) shows a peculiar splitting. The Bragg angles of the initial and displaced peaks are represented by the black empty and solid bullets in Fig. 2, respectively. In addition, we observe that both individual peaks shift to higher Bragg angles as they decay and rise. Despite the unequal behaviour of the respective SRO peaks in region I, the normalized transient shifts in region II and III ($\tau > T_{\text{sound}}$) appear to be comparable in both SRO layers. In addition, we evaluate the intensity-weighted transient shift of the thicker SRO layer in region I which is shown by the red half-filled bullets in Fig. 2. This curve represents the sum of the individual shifts weighted by the intensity of the respective Bragg peak at each time step. We find that this curve coincides with the transient peak shift of the thinner SRO layer. This immediately implies that the time-evolution of the average strain is identical in both layers as will be discussed below in more detail.

IV. DISCUSSION

A. Splitting versus Shifting of Bragg Peaks

In this section we focus on the time region I ($0 < \tau < T_{\text{sound}}$) where we observe a splitting of the SRO Bragg peak for the thicker sample. We perform numerical lattice-dynamics calculations and use the results in order to simulate the transient XRD response of the SRO layer.

It has recently been shown that a linear-chain model of masses and springs is well-suited to calculate the lattice dynamics triggered by the quasi-instantaneous thermal stress in SRO³². Moreover, the results of these calculations can be easily used to accurately simulate the transient x-ray response of such photoexcited nanolayered samples employing dynamical XRD theory³⁰. We therefore apply this toolbox to the present case of laser-excited SRO layers of different thickness in order to elucidate the general features of the structural dynamics.

The details of the linear-chain model simulations for the calculation of the photoinduced lattice dynamics of a thin SRO film on a STO substrate are given elsewhere³². The essential ingredient is the assumption of an instantaneous rise of an isotropic thermal stress in SRO due

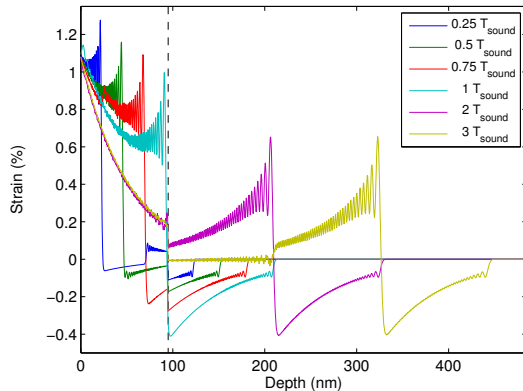


FIG. 3. Calculated photoinduced strain field of the thicker SRO layer on STO for selected time delays. The laser excitation at $\tau = 0$ launches coherent LA phonons which form sharp strain waves propagating through the layer and the substrate.

to incoherently excited phonons at $\tau = 0$. In a recent UXRd study on hexagonal LuMnO₃ anisotropic elastic properties had to be accounted for which are due to the lower crystal symmetry compared to SRO⁴³. However, the SRO unit cell only slightly deviates from cubic symmetry (pseudocubic) implying rather isotropic elastic properties⁴². The fact that the thermal stress in SRO builds up quasi-instantaneously has been proven to be valid by several UXRd experiments on a few-ps timescale^{30–32}. In fact, very tiny phase shifts of photoexcited coherent phonons modes in superlattices have been observed which evidence a crossover from a finite rise time (≈ 200 fs) to an instantaneous onset of the displacive thermal stress²⁴. Nonetheless, as we discuss below, the assumption of an instantaneous driving force is sufficiently good for the dynamics considered in this report. In Section II we mention that the very fast electron-phonon relaxation in SRO implies a thermal stress profile given by the exponential absorption of the pump light. Accordingly, we start our calculations by assuming an exponential thermal stress profile with a $1/e$ decay length defined by the optical penetration depth of SRO, $\xi_{\text{th}} = \xi_{\text{opt}}^{\text{lit}} = 52$ nm²⁷.

The spatio-temporal strain field for the thicker SRO layer on STO resulting from the lattice dynamics calculations is shown in Fig. 3. The laser-induced thermal stress sets in at $\tau = 0$. The instantaneous rise of this driving force coherently excites LA phonon modes up to very high frequencies. In total, the superposition of all coherent phonons results in propagating strain wave fronts starting at the air-SRO and SRO-STO interfaces where the thermal stress is not balanced and exhibits large gradients. In case of the 94.8 nm SRO layer whose thickness is almost twice the optical penetration depth of 800 nm light, $\xi_{\text{opt}}^{\text{lit}}$, the dominating strain front is an expansion

wave launched at the surface. The expansion wave starting at the SRO-STO interface has much lower amplitude but is still visible (blue line in Fig. 3). Thus the essential feature inferred from the calculations for the thicker SRO layer is the generation of a propagating wave front dividing the SRO layer into an expanded sublayer near the surface whereas the remaining sublayer gets slightly compressed in total for $0 < \tau < T_{\text{sound}}$ (green and red line in Fig. 3). The thickness of these sublayers is gradually increasing and decreasing with time, respectively. The slight compression of the decreasing sublayer is addressed in more detail below. At later times the coherent strain waves have propagated into the substrate forming a bipolar strain pulse⁴⁵ leaving a stationarily expanded SRO layer. A very small acoustic mismatch of SRO and STO results in a negligible reflection coefficient of acoustic waves at the SRO-STO interface⁴⁶. That is, the strain waves do not travel back and forth several times inside the SRO layer which would lead to a breathing mode of this layer as observed in other material combinations or in free-standing films^{47,48}.

A closer look at the transient strain fields in Fig. 3 reveals that the propagating wavepackets are superimposed by a peculiar fine structure which is most pronounced for the tensile component of the bipolar strain pulse. Since we solve the differential equations of the linear chain analytically these features are no numerical artifacts³². In fact, these high-frequency oscillations are a characteristic feature of a discretized linear chain and do not occur in elastic continuum models⁴⁵. They are a result of the fact that the motion on the linear chain is essentially initiated at the surface and interface due to the large gradients of the thermal stress at these points. In addition to the initial displacement of the outermost masses on the linear chain an oscillatory motion of these is launched⁴⁹. A thorough description of this high-frequency component is out of the scope of this report and shall be given elsewhere. Note that these high-frequency modes require a very fast build-up of the thermal stress to be efficiently excited, i.e. a sufficiently short pump pulse and a fast electron-phonon relaxation. However, in real SRO and STO crystals at room temperature the lifetime of acoustic phonons of such high frequency is expected to be very short due to anharmonic phonon-phonon scattering^{31,50,51}.

In order to correlate the identified transient features of the photoinduced lattice dynamics to the transient signals in UXRd experiments we calculate the diffraction curves of the sample at each time step utilizing the transient lattice deformations presented in Fig. 3. Figure 4(a) compares the numerical results with experimental data similar to the data shown in Fig. 1(d) but at a higher pump fluence of 30 mJ/cm² and without substrate subtraction. The presented simulation accounts for the instrument function of the PXS and assumes a decay length of the thermal stress profile of $\xi_{\text{th}} = 44$ nm to obtain a good match. This deviation from the optical penetration length $\xi_{\text{opt}}^{\text{lit}}$ is addressed below. The simula-

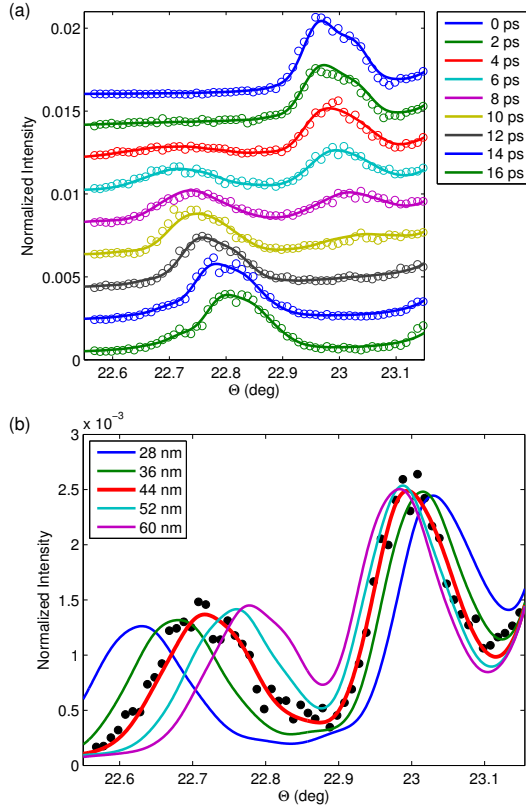


FIG. 4. (a) Comparison of the transient diffraction curves measured on the thicker SRO layer at the PXS (symbols) with simulations (solid lines). The experimental data were recorded at a pump fluence of 30 mJ/cm^2 . Time delay increases from top to bottom and the curves are displaced for clarity. The simulations employ an exponential thermal stress profile with decay length $\xi_{th} = 44 \text{ nm} < \xi_{opt}^{lit}$. (b) Transient diffraction curve at $\tau = 6 \text{ ps}$ (symbols) and simulations assuming different ξ_{th} .

tion reproduces the UXRD data very precisely. In particular, the splitting of the SRO Bragg peak and the individual shifts as the peaks decay and grow are in perfect agreement. We can now correlate the features revealed by the UXRD data to the structural dynamics obtained by the numerical lattice-dynamics calculations (Fig. 3). The initial rocking curve at $\tau = 0$ represents the unexcited SRO layer. As discussed above, the photoinduced thermal stress essentially launches a strain wave front at the surface which generates a gradually growing expanded sublayer. This rather thin expanded layer gives rise to the appearance of the broad and weak extra peak at lower angles. The peak grows as time delay increases since the thickness of this expanded sublayer increases. Simultaneously, the slightly negatively strained sublayer

decreases in thickness leading to the gradual disappearance and broadening of the initial SRO peak. This observation immediately verifies the very fast generation of the thermal stress which is required for the sharp division into differently strained sublayers⁵².

The UXRD data also show a slight shifting of the individual peaks to higher angles as they rise and fall. As evidenced in Fig. 4(a), the simulation also accurately reproduces this behaviour. The reason of the transient shifts of both peaks can also be found in the calculated lattice dynamics and is related to the exponential profile of the thermal stress and of the resulting layer expansion. As can be inferred from Fig. 3, the expansion wave launched at the surface gradually imprints an exponential expansion profile into the SRO film. The average strain of the expanded sublayer thus decreases as time increases. Accordingly, the angular displacement of the related rising Bragg peak is largest just after time zero and slowly decreases as time increases. The reason for the slight shift of the initial peak is a little more subtle. In simple words one may say that at early times the strongly expanding near-surface region of the SRO layer increasingly squeezes the less expanding near-interface region until the entire layer is expanded. In general, a gradient in the (instantaneous) thermal stress profile launches acoustic sound waves. In the considered case, the most dominant gradients appear at the surface and interface where the sharp strain waves are triggered. However, also the exponentially varying negative gradient inside the SRO film is responsible for a compressive strain wave component propagating towards the substrate. This compressive strain component is dominant over the tiny tensile strain wave from the SRO-STO interface (green and red line in Fig. 3). Hence it causes an increasing compression of the corresponding sublayer as time increases which is represented by the slight shift of the initial SRO Bragg peak towards higher angles. At later times it turns out that the exponential gradient is also responsible for the corresponding shape of the bipolar strain pulse in the substrate (magenta and yellow line in Fig. 3).

The above explanations rely on the exponential dependence of the thermal stress and thus expansion profile which suggest that the particular shifting behaviour of the two peaks is sensitive to, e.g., the decay length ξ_{th} of these profiles. To verify this we performed simulations with different values of this decay length. The final strain of the SRO layer and thus the Bragg angle of the SRO peak at late times is held constant. A comparison of the transient rocking curve at $\tau = 6 \text{ ps}$ with these simulations is shown in Fig. 4(b). Indeed, the shorter the decay length the more shifted is the rising (decaying) peak due to a relatively larger average expansion (compression) of the near-surface (near-interface) sublayer at early times. Surprisingly, the best fit of the UXRD data shown in Fig. 4(a) is achieved assuming a decay length of $\xi_{th} = 44 \text{ nm}$. As discussed in Section II, the extraordinary fast electron-phonon relaxation in SRO should generate a thermal stress and expansion profile having a de-

cay length ξ_{th} equal to the optical absorption length $\xi_{\text{opt}}^{\text{lit}}$. However, the decay length deduced from the UXR data is significantly lower than the expected 52 nm. Even if one allowed for any ballistic or diffusive thermal transport before the energy is coupled into the lattice this result could not be explained since these processes tend to flatten out any gradients resulting in a longer decay length.

There are two effects which could cause the unexpected steepness of the observed expansion profile. First, the optical penetration depth could possibly be different in the considered thin films as compared to the bulk material due to finite size effects and/or variations of the optical constants by stationary strains that are induced by epitaxy^{53,54}. We performed spectroscopic ellipsometry measurements on the thick SRO layer and found an optical penetration depth of $\xi_{\text{opt}}^{\text{exp}} = 48$ nm at a wavelength of 800 nm. This value is indeed slightly smaller than the literature bulk value of 52 nm²⁷ but still significantly larger than the lengthscale of the expansion profile deduced from the UXR data.

The second possible effect which could cause a steeper expansion profile is a weak temperature dependence of the Grüneisen parameter γ describing the ratio of thermal expansion and deposited energy. In general, this parameter is nearly material-independent and shows almost no temperature dependence, however, a slight increase of γ with temperature can be observed in several materials⁵⁵. An increase of γ with T would cause a larger expansion of the near-surface regions of the SRO layer relative to the deposited energy density profile which would result in a steeper expansion profile as revealed by the UXR data.

In the following we briefly turn to the lattice dynamics of the thinner SRO layer whose thickness is much smaller than the optical penetration length of the 800 nm pump light. Here, we can extend the concept of differently strained sublayers. Since the deposited energy density is comparable near the surface and interface, respectively, the launched strain wave fronts are also similar in amplitude. Accordingly, one finds three sublayers of different strains which should in principle cause a more complicated splitting of the layer Bragg peak. However, due to the small thickness of the SRO layer the corresponding Bragg peak is very broad and thus prevents any splitting from being observed. The required strain amplitudes to observe a splitting for the very thin film would be too large. This complex splitting of Bragg peaks could possibly be visible on thicker layers of materials having an accordingly larger optical penetration depth.

B. Universal Features of Lattice Dynamics in SRO Thin Films

In the previous section we discussed the qualitatively different UXR signatures while the coherent strain waves pass through the layer once ($0 < \tau < T_{\text{sound}}$).

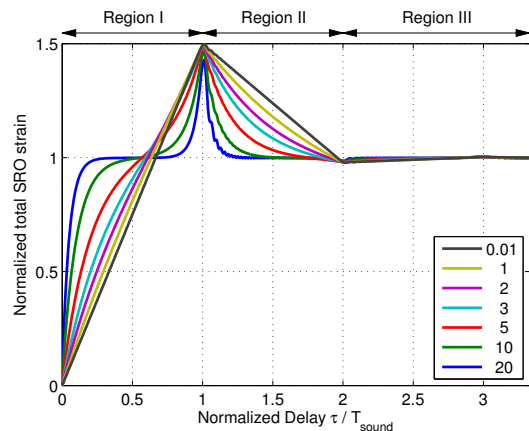


FIG. 5. Transient average SRO strain for different ratios d/ξ_{th} .

As already mentioned in section III, the transient shifts appear very similar for the two thin films with different thicknesses at times later than T_{sound} (region II and III). Moreover, the transient weighted shifts (average strain) are almost identical for all times. In the following we thus address the evolution of the average layer strain and how it depends on the ratio of the layer thickness d and the decay length of the thermal stress ξ_{th} .

In order to investigate the effect of a varying ratio d/ξ_{th} , we calculate the spatio-temporal strain fields for the thick SRO layer (d fixed) at various values of ξ_{th} . We then extract the transient average SRO strain normalized to the final strain at $\tau > 2T_{\text{sound}}$ and plot the results versus normalized time delay τ/T_{sound} in Fig. 5. We identify three regions of qualitatively different lattice dynamics which, however, show universal behaviour independent of the ratio d/ξ_{th} . In region I ($0 < \tau < T_{\text{sound}}$) the coherent strain waves cause the average SRO strain to monotonically increase to 150% of the final thermal expansion. This value of maximum strain does not depend on the ratio d/ξ_{th} , however, the precise evolution of the total SRO strain is influenced by the ratio. It changes from linear to jump-like as the ratio decreases. Similar observations hold for region II ($T_{\text{sound}} < \tau < 2T_{\text{sound}}$) but here we find a monotonically decreasing strain until it reaches the final value determined by the pure thermal expansion due to the increased SRO temperature. In region III ($\tau > 2T_{\text{sound}}$) the SRO strain remains quasi-constant until it relaxes back to zero via heat diffusion into the substrate on a nanosecond timescale (not included in the model and not shown).

The quantitative difference of the total SRO strain evolution is simply explained by the different shapes of the strain waves launched at the surface and/or interface. In case of $d/\xi_{\text{th}} \ll 1$ (grey line in Fig. 5) square-like strain pulses are launched at the surface and interface with com-

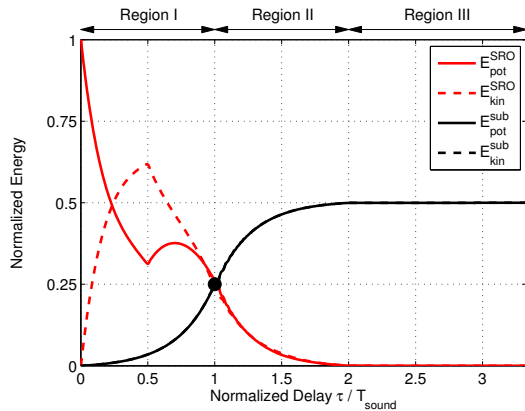


FIG. 6. Transient normalized potential (solid lines) and kinetic energy (dashed lines) of the coherent strain waves inside the SRO layer (red) and the STO substrate (black). The energies were derived from the calculation presented in Fig. 3. Note that the potential and kinetic energy in the substrate are identical and thus the respective curves are overlaid. The black bullet indicates the point at which all normalized energies are identical. This point is independent of ξ_{th}

parable amplitudes which results in the piecewise linear evolution of the total strain. In contrast, if $d/\xi_{th} \gg 1$ (blue line in Fig. 5) only a small portion underneath the surface of the SRO layer is excited which then rapidly expands just after time zero. Moreover, a rather localized bipolar strain pulse is launched⁴⁵ which has a vanishing integral strain as we discuss below. Around $\tau = T_{sound}$ the bipolar strain pulse leaves the SRO layer and causes the spike-like transient increase of the total SRO strain. Altogether, Figure 5 evidences that the calculations precisely predict the average SRO strain dynamics derived from the transient (weighted) shift of the SRO Bragg peaks shown in Fig. 2. In particular, the slight differences of the red and blue data in Fig. 2 (SRO layers of different thickness) can thus mainly be attributed to the different ratios d/ξ_{th} .

The striking feature in Fig. 5 is that the normalized total strain in the SRO layer at $\tau = T_{sound}$ and for $\tau > 2T_{sound}$ (region III) is independent of the ratio d/ξ_{th} . In particular, the maximum strain due to the coherent phonon dynamics is always 50% larger than the steady-state strain after $2T_{sound}$ due to incoherent phonons (i.e. heat). To give an explanation we employ the potential and kinetic energy of the coherent strain waves inside the SRO layer and the STO substrate, respectively, which are shown in Fig. 6. At $\tau = 0$ the thermal stress is generated quasi-instantaneously by the absorption of the laser pulse which increases the equilibrium distance of atoms in the lattice. Therefore, the thermal stress gives rise to an initial potential energy since the SRO layer is now compressed relative to the new equilibrium state. The kinetic energy is zero since no atomic motion has started

at this point. As explained in section IV A, the thermal stress launches propagating strain waves inside the SRO layer which is evidenced by the increasing kinetic and decreasing potential energy of SRO. The increase in both kinetic and potential energy inside the STO substrate is due to the corresponding strain pulse launched from the interface into the substrate (cf. Fig. 3). At $\tau = T_{sound}$ all energies are identical and the key point is that this observation is independent of the ratio d/ξ_{th} (not shown) which is indicated by the black bullet. In particular, the substrate-related energies reached half of their maximum values since the compressive part of the bipolar strain pulse has entered the substrate while the tensile part still remains in the SRO layer. This implies that the integral strain of the two individual parts of the bipolar strain pulse (tensile and compressive) is equal but has opposite signs. In contrast to the initially ($\tau = 0$) compressed state of the SRO layer relative to the new equilibrium state after $2T_{sound}$, the coherent superposition of the longitudinal strain waves at $\tau = T_{sound}$ results in a tensile state relative to the new equilibrium (cf. Fig. 3). At this point in time the potential energy of the SRO layer dropped to 1/4 of its initial value. Since the potential energy generally is proportional to the square of the strain we conclude that the relative expansion at $\tau = T_{sound}$ is 1/2 of the initial relative compression. Hence the maximum absolute strain relative to the unexcited state at $\tau = T_{sound}$ has to be 150% of the equilibrium (thermal) strain after $2T_{sound}$.

As mentioned in section IV A the perfect acoustic matching of SRO and STO prevents the coherent strain waves from being (partially) reflected back into the SRO layer. If there is a significant acoustic mismatch the strain waves would travel back and forth until all vibrational energy has been transferred to the substrate. This would result in an oscillatory behaviour of the total SRO strain as was observed by UXRD in a photoexcited Gold layer on a Mica substrate⁴⁷. The limiting case of such an acoustic breathing of a metal film is represented by free-standing films where the amplitude decay of the acoustic waves is merely given by internal damping effects. Such breathing of free-standing Al films has been studied by femtosecond electron diffraction⁴⁸. Ideally, the maximum strain at $\tau = T_{sound}$ due to the coherent structural dynamics in an acoustically decoupled photoexcited thin film is 100% above the steady-state thermal expansion which is related to the dispersive nature of the excitation mechanism^{18,56}. Any type of energy loss—be it coherent by transmission losses into the substrate or incoherent by internal damping and/or scattering—leads to a decrease of the maximum coherent strain at $\tau = T_{sound}$. In the present case of a semi-infinite substrate with perfect acoustic matching the coherent strain maximum of the metal layer is reduced by a factor of 2 since a part of the initial potential energy is transferred to the substrate in form of the compressive half of a bipolar strain pulse.

V. CONCLUSION

In this report we address the issue of the one-dimensional coherent structural dynamics in thin films of metallic SrRuO₃ (SRO) on a dielectric substrate SrTiO₃ which are triggered by the absorption of ultrafast optical laser pulses. We show experimental results of UXR experiments which probe the photoexcited coherent lattice dynamics of two SRO layers with different thickness. The observed changes of the respective SRO Bragg peaks exhibit qualitatively different features. In particular, the Bragg peak of the thicker SRO layer shows a transient splitting into two separated reflections which evidences the propagation of sharp longitudinal strain waves through the metal layer. These coherent wavepackets are caused by the exceptionally fast electron-phonon relaxation previously identified in SRO^{9,24}. Numerical models accounting for the photoinduced structural dynamics and dynamical XRD show excellent agreement assuming a surprisingly small decay length of the thermal stress profile of 44 nm. This deviation from the measured optical

penetration depth in these thin films may be attributed to a temperature-dependent Grüneisen parameter. Finally, we analyze the UXR-calibrated coherent phonon dynamics in detail using the numerical simulations. The UXR features can unambiguously be related to the precise structural dynamics. We discuss the features specific to the layers of different thickness (Bragg peak splitting versus continuous shift) and identify a universal evolution of the total strain of a photoexcited thin metal film of arbitrary thickness on a semi-infinite substrate. Our work gives a very precise and UXR-calibrated picture of the acoustic deformation of laser-heated metal layers on a supporting substrate and carefully relates the transient structural features to UXR signatures. We believe that this work is very valuable for the quantitative interpretation of time-resolved scattering experiments on the complex photoinduced structural dynamics of crystalline nanolayered structures such as thin films, multilayers and superlattices.

We thank the BMBF for funding the project via grant No. 05K10IP1 and the DFG via grant No. BA2281/3-1.

-
- * marc.herzog@uni-potsdam.de
- ¹ M. Forst, C. Manzoni, S. Kaiser, Y. Tomioka, Y. Tokura, R. Merlin, and A. Cavalleri, *Nat. Phys.* **7**, 854 (2011), 10.1038/nphys2055.
 - ² A. Bartels, T. Dekorsy, H. Kurz, and K. Köhler, *Phys. Rev. Lett.* **82**, 1044 (1999).
 - ³ T. E. Stevens, J. Kuhl, and R. Merlin, *Phys. Rev. B* **65**, 144304 (2002).
 - ⁴ C. Rose-Petruck, R. Jimenez, T. Guo, A. Cavalleri, C. W. Siders, F. Rksi, J. A. Squier, B. C. Walker, K. R. Wilson, and C. P. J. Barty, *Nature* **398**, 310 (1999), 10.1038/18631.
 - ⁵ J. Hohlfeld, S. S. Wellershoff, J. Güdde, U. Conrad, V. Jähnke, and E. Matthias, *Chem. Phys.* **251**, 237 (2000).
 - ⁶ C. von Korff Schmising, M. Bargheer, M. Kiel, N. Zhavoronkov, M. Woerner, T. Elsaesser, I. Vrejoiu, D. Hesse, and M. Alexe, *Phys. Rev. Lett.* **98**, 257601 (2007).
 - ⁷ D. Daranciang, M. J. Highland, H. Wen, S. M. Young, N. C. Brandt, H. Y. Hwang, M. Vattilana, M. Nicoul, F. Quirin, J. Goodfellow, T. Qi, I. Grinberg, D. M. Fritz, M. Cammarata, D. Zhu, H. T. Lemke, D. A. Walko, E. M. Dufresne, Y. Li, J. Larsson, D. A. Reis, K. Sokolowski-Tinten, K. A. Nelson, A. M. Rappe, P. H. Fuoss, G. B. Stephenson, and A. M. Lindenberg, *Phys. Rev. Lett.* **108**, 087601 (2012).
 - ⁸ A. V. Kimel, A. Kirilyuk, P. A. Usachev, R. V. Pisarev, A. M. Balbashov, and T. Rasing, *Nature* **435**, 655 (2005), 10.1038/nature03564.
 - ⁹ C. von Korff Schmising, A. Harpoeth, N. Zhavoronkov, Z. Ansari, C. Aku-Leh, M. Woerner, T. Elsaesser, M. Bargheer, M. Schmidbauer, I. Vrejoiu, D. Hesse, and M. Alexe, *Phys. Rev. B* **78**, 060404 (2008).
 - ¹⁰ A. Kirilyuk, A. V. Kimel, and T. Rasing, *Rev. Mod. Phys.* **82**, 2731 (2010).
 - ¹¹ H. Ehrke, R. I. Tobey, S. Wall, S. A. Cavill, M. Först, V. Khanna, T. Garl, N. Stojanovic, D. Prabhakaran, A. T. Boothroyd, M. Gensch, A. Mirone, P. Reuter, A. Revcolevschi, S. S. Dhesi, and A. Cavalleri, *Phys. Rev. Lett.* **106**, 217401 (2011).
 - ¹² D. Lim, V. K. Thorsmølle, R. D. Averitt, Q. X. Jia, K. H. Ahn, M. J. Graf, S. A. Trugman, and A. J. Taylor, *Phys. Rev. B* **71**, 134403 (2005).
 - ¹³ P. Beaud, S. L. Johnson, E. Vorobeve, U. Staub, R. A. D. Souza, C. J. Milne, Q. X. Jia, and G. Ingold, *Phys. Rev. Lett.* **103**, 155702 (2009).
 - ¹⁴ H. Ichikawa, S. Nozawa, T. Sato, A. Tomita, K. Ichiyanagi, M. Chollet, L. Guerin, N. Dean, A. Cavalleri, S.-i. Adachi, T. Arima, H. Sawa, Y. Ogimoto, M. Nakamura, R. Tamaki, K. Miyano, and S.-y. Koshihara, *Nat. Materials* **10**, 101 (2011), 10.1038/nmat2929.
 - ¹⁵ M. Dawber, K. M. Rabe, and J. F. Scott, *Rev. Mod. Phys.* **77**, 1083 (2005).
 - ¹⁶ W. Eerenstein, N. D. Mathur, and J. F. Scott, *Nature* **442**, 759 (2006), 10.1038/nature05023.
 - ¹⁷ M. Herzog, W. Leitenberger, R. Shayduk, R. van der Veen, C. J. Milne, S. L. Johnson, I. Vrejoiu, M. Alexe, D. Hesse, and M. Bargheer, *Appl. Phys. Lett.* **96**, 161906 (2010).
 - ¹⁸ M. Bargheer, N. Zhavoronkov, Y. Gritsai, J. C. Woo, D. S. Kim, M. Woerner, and T. Elsaesser, *Science* **306**, 1771 (2004), <http://www.sciencemag.org/cgi/reprint/306/5702/1771.pdf>.
 - ¹⁹ D. M. Fritz, D. A. Reis, B. Adams, R. A. Akre, J. Arthur, C. Blome, P. H. Bucksbaum, A. Cavalleri, S. Engemann, S. Fahy, R. W. Falcone, P. H. Fuoss, K. J. Gaffney, M. J. George, J. Hajdu, M. P. Hertlein, P. B. Hillyard, M. Horn-von Hoegen, M. Kammler, J. Kaspar, R. Kienberger, P. Krejčík, S. H. Lee, A. M. Lindenberg, B. McFarland, D. Meyer, T. Montagne, É. D. Murray, A. J. Nelson, M. Nicoul, R. Pahl, J. Rudati, H. Schlarb, D. P. Sidons, K. Sokolowski-Tinten, T. Tschentscher, D. von der Linde, and J. B. Hastings, *Science* **315**, 633 (2007),

- <http://www.sciencemag.org/content/315/5812/633.full.pdf>.
- ²⁰ B. J. Siwick, J. R. Dwyer, R. E. Jordan, and R. J. D. Miller, *Science* **302**, 1382 (2003), <http://www.sciencemag.org/content/302/5649/1382.full.pdf>.
- ²¹ M. Eichberger, H. Schafer, M. Krumova, M. Beyer, J. Dem-sar, H. Berger, G. Moriena, G. Sciaini, and R. J. D. Miller, *Nature* **468**, 799 (2010).
- ²² L. Klein, J. S. Dodge, C. H. Ahn, G. J. Snyder, T. H. Geballe, M. R. Beasley, and A. Kapitulnik, *Phys. Rev. Lett.* **77**, 2774 (1996).
- ²³ M. Ziese, I. Vrejoiu, and D. Hesse, *Phys. Rev. B* **81**, 184418 (2010).
- ²⁴ A. Bojahr, D. Schick, L. Maerten, M. Herzog, I. Vrejoiu, C. von Korff Schmising, C. J. Milne, S. L. Johnson, and M. Bargheer, *Phys. Rev. B* **85**, 224302 (2012).
- ²⁵ D. C. Worledge and T. H. Geballe, *Phys. Rev. Lett.* **85**, 5182 (2000).
- ²⁶ H.-T. Jeng, S.-H. Lin, and C.-S. Hsue, *Phys. Rev. Lett.* **97**, 067002 (2006).
- ²⁷ P. Kostic, Y. Okada, N. C. Collins, Z. Schlesinger, J. W. Reiner, L. Klein, A. Kapitulnik, T. H. Geballe, and M. R. Beasley, *Phys. Rev. Lett.* **81**, 2498 (1998).
- ²⁸ G. Cao, O. Korneta, S. Chikara, L. E. DeLong, and P. Schlottmann, *Solid State Commun.* **148**, 305 (2008).
- ²⁹ I. Vrejoiu, G. Le Rhun, L. Pintilie, D. Hesse, M. Alexe, and U. Gösele, *Adv. Mater.* **18**, 1657 (2006).
- ³⁰ M. Herzog, D. Schick, W. Leitenberger, R. Shayduk, R. M. van der Veen, C. J. Milne, S. L. Johnson, I. Vrejoiu, and M. Bargheer, *New J. Phys.* **14**, 013004 (2012).
- ³¹ M. Herzog, A. Bojahr, J. Goldshteyn, W. Leitenberger, I. Vrejoiu, D. Khakhulin, M. Wulff, R. Shayduk, P. Gaal, and M. Bargheer, *Appl. Phys. Lett.* **100**, 094101 (2012).
- ³² M. Herzog, D. Schick, P. Gaal, R. Shayduk, C. v. Korff Schmising, and M. Bargheer, *Appl. Phys. A* **106**, 489 (2012).
- ³³ S. I. Anisimov, B. L. Kapeliovich, and T. L. Perel'man, *Sov. Phys. JETP* **39**, 375 (1974).
- ³⁴ T. Q. Qiu and C. L. Tien, *Int. J. Heat Mass Transfer* **37**, 2789 (1994).
- ³⁵ P. M. Norris, A. P. Caffrey, R. J. Stevens, J. M. Klopff, J. James T. McLeskey, and A. N. Smith, *Rev. Sci. Instrum.* **74**, 400 (2003).
- ³⁶ J. K. Chen, D. Y. Tzou, and J. E. Beraun, *Int. J. Heat Mass Transfer* **49**, 307 (2006).
- ³⁷ At higher temperatures the electron-electron collisions become more frequent^{35,37} which results in an even smaller electron relaxation time at room temperature.
- ³⁸ M. Shepard, P. F. Henning, G. Cao, and J. E. Crow, *J. Appl. Phys.* **83**, 6989 (1998).
- ³⁹ T. Maekawa, K. Kurosaki, H. Muta, M. Uno, and S. Yamanaka, *J. Alloys Compd.* **387**, 56 (2005).
- ⁴⁰ N. D. Ashcroft and N. W. Mermin, *Solid state physics*, 1st ed. (Saunders College, Fort Worth, 1976).
- ⁴¹ D. Schick, A. Bojahr, M. Herzog, C. von Korff Schmising, R. Shayduk, W. Leitenberger, P. Gaal, and M. Bargheer, *Rev. Sci. Instrum.* **83**, 025104 (2012).
- ⁴² S. Yamanaka, T. Maekawa, H. Muta, T. Matsuda, S. Kobayashi, and K. Kurosaki, *J. Solid State Chem.* **177**, 3484 (2004).
- ⁴³ H. J. Lee, J. Workman, J. S. Wark, R. D. Averitt, A. J. Taylor, J. Roberts, Q. McCulloch, D. E. Hof, N. Hur, S.-W. Cheong, and D. J. Funk, *Phys. Rev. B* **77**, 132301 (2008).
- ⁴⁴ F. Quirin, M. Vattilana, U. Shymanovich, A.-E. El-Kamhawy, A. Tarasevitch, J. Hohlfeld, D. von der Linde, and K. Sokolowski-Tinten, *Phys. Rev. B* **85**, 020103 (2012).
- ⁴⁵ C. Thomsen, H. T. Grahn, H. J. Maris, and J. Tauc, *Phys. Rev. B* **34**, 4129 (1986).
- ⁴⁶ L. D. Landau and E. M. Lifshitz, *Course of Theoretical Physics Vol. 6 - Fluid mechanics*, 2nd ed. (Pergamon Pr., Oxford, 1987).
- ⁴⁷ M. Nicoul, U. Shymanovich, A. Tarasevitch, D. von der Linde, and K. Sokolowski-Tinten, *Appl. Phys. Lett.* **98**, 191902 (2011).
- ⁴⁸ J. Li, R. Clinite, X. Wang, and J. Cao, *Phys. Rev. B* **80**, 014304 (2009).
- ⁴⁹ Note, that the frequency of these oscillations actually depends on the particular discretization of the linear chain. The presented simulations assume one mass on the linear chain per unit cell of SRO and STO. If one refines the linear chain to include one mass per lattice plane (i.e. two masses per perovskite unit cell along [001]) the frequency will double.
- ⁵⁰ A. Koreeda, T. Nagano, S. Ohno, and S. Saikan, *Phys. Rev. B* **73**, 024303 (2006).
- ⁵¹ C. Klieber, E. Peronne, K. Katayama, J. Choi, M. Yamaguchi, T. Pezeril, and K. A. Nelson, *Appl. Phys. Lett.* **98**, 211908 (2011).
- ⁵² The clear splitting implies a rise time of the thermal stress much faster than the characteristic timescale of layer expansion, T_{sound} . However, an exact determination of the rise time is not possible with such a sample structure (cf. Ref. 24).
- ⁵³ H. L. Liu, K. S. Lu, M. X. Kuo, L. Uba, S. Uba, L. M. Wang, and H. T. Jeng, *J. Appl. Phys.* **99**, 043908 (2006).
- ⁵⁴ M. Veis, Š. Višňovský, P. Lecoeur, A.-M. Haghiri-Gosnet, J.-P. Renard, P. Beauvillain, W. Prel-lier, B. Mercey, J. Mistrík, and T. Yamaguchi, *J. Phys. D: Appl. Phys.* **42**, 195002 (2009).
- ⁵⁵ C. Kittel, *Introduction to solid state physics*, 7th ed. (Wiley, New York, 1996).
- ⁵⁶ M. Bargheer, J. C. Woo, N. Zhavoronkov, D. S. Kim, M. Woerner, and T. Elsaesser, *phys. stat. sol. (b)* **243**, 2389 (2006).
- ⁵⁷ A. N. Smith and P. M. Norris, *Appl. Phys. Lett.* **78**, 1240 (2001).

Paper V

Comparing the oscillation phase in optical pump-probe spectra to ultrafast x-ray diffraction in the metal-dielectric SrRuO₃/SrTiO₃ superlattice

A. Bojahr, **D. Schick**, L. Maerten, M. Herzog, I. Vrejoiu, C. von Korff Schmising, C. J. Milne, S. L. Johnson, and M. Bargheer

Phys. Rev. B 85, 22 (2012)

Comparing the oscillation phase in optical pump-probe spectra to ultrafast x-ray diffraction in the metal-dielectric SrRuO₃/SrTiO₃ superlattice

André Bojhr,¹ Daniel Schick,¹ Lena Maerten,¹ Marc Herzog,¹ Ionela Vrejoiu,² Clemens von Korff Schmising,³ Chris Milne,⁴ Steven L. Johnson,⁵ and Matias Bargheer^{1,6,*}

¹*Institute of Physics and Astronomy, University of Potsdam, Karl-Liebknecht-Strasse 24-25, 14476 Potsdam, Germany*

²*Max-Planck-Institut für Mikrostrukturphysik, Weinberg 2, 06120 Halle, Germany*

³*Institut für Optik und Atomare Physik, TU Berlin, Strasse des 17. Juni 135, 10623 Berlin*

⁴*Swiss Light Source, Paul Scherrer Institut, 5232 Villigen PSI, Switzerland and Laboratoire de Spectroscopie Ultrarapide, Ecole Polytechnique Federale de Lausanne, 1015 Lausanne, Switzerland*

⁵*Institute for Quantum Electronics, ETH Zurich, Wolfgang-Pauli-Strasse 16, 8093 Zurich, Switzerland*

⁶*Helmholtz Zentrum Berlin, Albert-Einstein-Strasse 15, 12489 Berlin, Germany*

(Received 6 April 2012; revised manuscript received 16 May 2012; published 19 June 2012)

We measured the ultrafast optical response of metal-dielectric superlattices by broadband all-optical pump-probe spectroscopy. The observed phase of the superlattice mode depends on the probe wavelength, making assignments of the excitation mechanism difficult. Ultrafast x-ray diffraction data reveal the true oscillation phase of the lattice which changes as a function of the excitation fluence. This result is confirmed by the fluence dependence of optical transients. We set up a linear chain model of the lattice dynamics and successfully simulated the broadband optical reflection by unit-cell resolved calculation of the strain-dependent dielectric functions of the constituting materials.

DOI: 10.1103/PhysRevB.85.224302

PACS number(s): 63.20.Ry, 42.65.Es

I. INTRODUCTION

Optical femtosecond spectroscopy is an established tool to infer ultrafast dynamics in molecules and solids. Time constants such as the exponential decay or the oscillation period can often be directly ascribed to microscopic processes such as relaxation or vibration. A detailed modeling of the ultrafast optical response requires the quantum-chemical modeling of molecular potentials in the case of molecular systems or calculation of the dielectric function of solids. With the broader accessibility of various experimental setups for ultrafast x-ray diffraction (UXRD), the findings from all-optical experiments can be cross-checked by directly looking at the lattice motion, including a real time measurement of the absolute atomic amplitudes. In the case of bulk semiconductors UXRD allowed conclusions to be drawn on modifications of the strain fronts induced by the fast diffusion of hot carriers.¹⁻³ For bulk bismuth UXRD in combination with *ab initio* simulations revealed how the lattice potential changes with the time-dependent carrier density.⁴ UXRD and ultrafast electron-diffraction studies show that, for increasing excitation fluence, electronic pressure gains importance versus phonon pressure in metallic systems.^{5,6} All these processes influence the oscillation phase of the excited phonons. In reverse, measuring the oscillation phase elucidates the excitation mechanisms.

The influence of Raman excitation has been discussed in bulk systems, superlattices, and multilayers.⁷ Under strictly nonresonant conditions this excitation causes a sine-like phase of the lattice motion. In contrast the so-called dispersive excitation of coherent phonons (DECP)⁸ results in a cosine-like lattice motion.⁹ DECP is exclusively observed in opaque materials and can be described by the imaginary part of the Raman tensor.¹⁰ Additional excitation mechanisms which show a displaced equilibrium of the lattice oscillation

are surface charge screening, the photo Demer effect, or heating of the lattice by rapid electron-phonon scattering.¹¹ In many cases the oscillation phase was measured by all-optical techniques and ascribed to the phase of the lattice motion. Raman scattering with real and imaginary tensor contributions is held responsible for the excitation of coherent phonons in metallic systems (Cd, Zn, Zr) as well.^{12,13} In the most intensively investigated material, the semimetal Bi, the microscopic interpretation of the excitation is developed in detail. Theory predicts the time-dependent change of the interatomic potential during the relaxation of photoexcited carriers.^{4,14} A similarly detailed interpretation of the excitation in terms of quasiparticle generation is exemplified for Si.¹⁵ UXRD would yield direct experimental information on the lattice motion in this case. However, there is only a single UXRD experiment that measures lattice dynamics (polaritons) induced by nonresonant Raman excitation.¹⁶

Several all-optical studies measured a fluence dependent phase of oscillations, which was ascribed to the simultaneous action of DECP and Raman mechanisms.¹⁷ Superlattices exhibit phonon modes which are very well suited for fundamental tests, as their periods can be tuned via the layer thickness. Especially for UXRD experiments they yield high signal-to-noise ratio of the experimental signal. The nanosized layers support zone folded acoustic phonons¹⁸ with few-picosecond oscillation periods, well suited for distinguishing tiny phase differences. Optical excitation of the opaque constituent of a superlattice yields a standing strain wave where the opaque material is periodically expanded while the transparent material is compressed. For GaAs/AlGaAs superlattices a UXRD study under high fluence conditions revealed a dominant DECP mechanism¹⁹ whereas all-optical measurements under low-fluence conditions suggest the Raman mechanism.⁷ Although it is well established to use such ultrafast structural techniques, the problem of determining the arrival time of the x-ray or

electron pulses with high precision relative to the pump pulse persists. A direct and detailed comparison of ultrafast optical response over a broad spectral range with the actual lattice motion determined by ultrafast diffraction techniques under identical excitation conditions is lacking.

In this contribution we revisit the metal-dielectric superlattice (SL) composed of SrRuO₃ (SRO) and SrTiO₃ (STO), for which it was shown by UXRd measurements that there are at least two contributing mechanisms for photoexcited lattice dynamics: thermal expansion by electron-phonon and phonon-phonon interaction and ultrafast magnetostriction.²¹ We present a fluence-dependent UXRd study which shows a relative phase shift of about 130 fs of the lattice motion, indicating that for high fluence the photon energy is coupled more rapidly to the expansion. At high fluences the measured phase of the lattice motion is consistent with an instantaneous DECP mechanism within the experimental error. In broadband optical reflectivity measurements we find that the oscillation phase of the all-optical signal strongly depends on the probe wavelength; however, we can confirm the relative shift of the oscillation phase with fluence. To determine the absolute phase of the lattice oscillation we perform a combined optical pump-probe and UXRd experiment without moving any components.

In order to better understand the broadband optical response, the lattice dynamics are calculated in a masses-and-springs model and calibrated in phase and amplitude using the UXRd data. The calculated spatiotemporal strain pattern is used to simulate the optical response by using the strain-dependent dielectric functions of SRO and STO, where the dependence $\partial N_{\text{SRO}}/\partial \eta$ of the complex refractive index N_{SRO} on the strain η is the only freely adjustable parameter. The agreement of these x-ray calibrated simulations with the optical response is very good. These data directly show that all-optical pump-probe data can exhibit nearly arbitrary oscillation phases, even if the lattice dynamics are fixed.

II. SETUP AND EXPERIMENTAL RESULTS

The sample consists of 10 double layers of STO/SRO (13 nm/7.5 nm) deposited by pulsed laser deposition on an STO substrate.²² In all experiments presented in this manuscript we use pump pulses with a wavelength of $\lambda_{\text{pump}} = 800$ nm. Figure 1(a) presents fluence-dependent UXRd data recorded at the MicroXAS-FEMTO beamline of the Swiss Light Source (SLS).²³ The amplitude of the oscillation has been analyzed²⁴ and discussed previously.²⁰ The according strain amplitude is reproduced in Fig. 1(b). Panel 1(c) shows the delay t_0^{osc} of the oscillation phase extracted from fitting the data in panel 1(a) to an analytical function [Eq. (1)] describing the sample response, which will be further discussed in Sec. IV. In short, the symmetric superlattice-phonon mode of the metallic/insulating superlattice is excited by expanding the metal layers. For the highest fluence the oscillation starts approximately 130 fs earlier. Figure 2(a) shows the transient optical reflectivity of the sample at $\lambda_{\text{probe}} = 670$ nm. The rapid rise of the reflectivity originates from quasi-instantaneous heating of the metal electrons. The rising edge determines the arrival time of the optical pump pulse. The slanted arrows indicate the delay of the oscillation for lower pump fluence. For

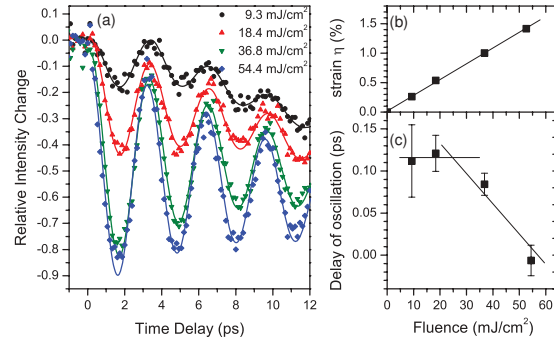


FIG. 1. (Color online) (a) UXRd measurements of the (00 116) reflection of the SRO/STO SL recorded at the SLS $\lambda_{\text{pump}} = 800$ nm for different fluences. (b) Strain amplitude derived from the data in panel (a) by comparison to a dynamical x-ray diffraction simulation (Ref. 20). (c) Oscillation phase extracted from the measured data using the fit function of eq. 1. The error bars correspond to a 68% confidence interval from fitting the relative phase. The absolute phase is obtained by comparison to the experiments at the laser-based plasma source discussed in Fig. 4.

an accurate evaluation we subtract the incoherent background (dotted line) and fit oscillations to the data. The resulting linear fluence dependence of the amplitude is shown in Fig. 2(b). The phase delay is plotted in Fig. 2(c) and compared to the UXRd result. The excellent agreement suggests that indeed for low fluence the oscillation is delayed by about 130 fs due to a finite electron-phonon coupling time as the expansion is dominated by phonon-phonon interaction. In contrast, for high fluence the

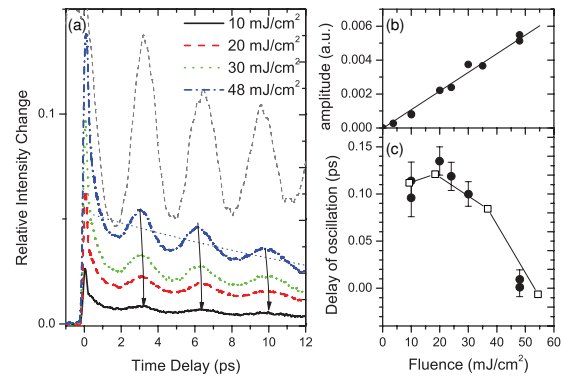


FIG. 2. (Color online) (a) Measured optical reflectivity $\lambda_{\text{probe}} = 670$ nm for different fluences. The dotted line indicates the incoherent background contribution which is subtracted from each transient to fit the oscillations and to plot Fig. 3(a). The thin dashed line shows the UXRd measurement for comparison. (b) Oscillation amplitude as a function of the fluence. (c) Comparison of the relative oscillation phase of the optical signal (solid circles) to the phase determined by UXRd [open squares reproduced from Fig. 1(c)]. The error bars of the relative phase are determined from the maximum deviation of phases in two measurement series. The absolute phase is shifted to agree with the UXRd data.

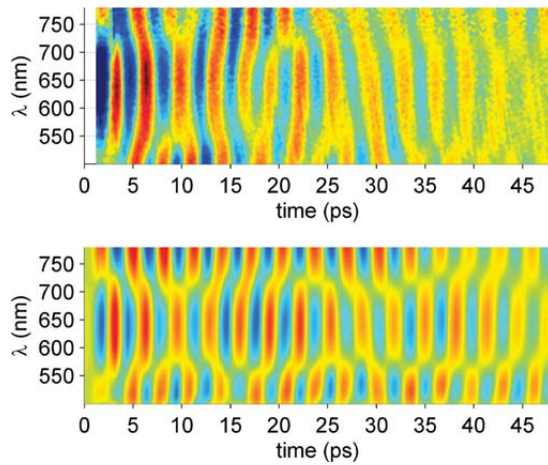


FIG. 3. (Color) (a) Experimentally measured change of the optical reflectivity from $\lambda_{\text{probe}} = 500$ to 780 nm at normal incidence after exciting the sample at $\lambda_{\text{pump}} = 800$ nm as a function of time delay. The electronic response and a slowly varying signal contribution have been subtracted as exemplified in Fig. 2(a). (b) Results from the simulation described in the text. The slowly varying background has been subtracted as well. The simulations show that the spectral position of the phase change at 560 and 720 nm is given by an interference of light reflected from the surface and the interface to the substrate.

time for coupling the energy into the expansion mode is so fast that we cannot distinguish it from an instantaneous response.

Our broadband optical pump-probe setup is similar to those reported in the literature,^{25,26} where a white-light continuum serves as the probe pulse. Hence, we not only measure the data at 670 nm (Fig. 2) but over the full visible range. The analysis teaches us to interpret all-optical data with great care. After subtraction of the slowly varying background for each wavelength as exemplified by the dotted line in Fig. 2(a), the broadband data exhibit complex dependence of the phase on the probe wavelength [Fig. 3(a)].

A general problem in UXRD experiments is the precise determination of the time zero. For all-optical pump-probe data we cross-checked that the rising edge of the signal corresponds to $t = 0$ by sum-frequency generation of pump and probe in a beta-Barium-Borate (BBO) crystal. To calibrate the time origin of the UXRD data, we repeated the UXRD experiment at the laser-based femtosecond diffractometer at the University of Potsdam.²⁷ We removed the x-ray optic which is used for the standard operation of the diffractometer.^{27,28} The Bragg condition selects a small angular range of the generated x-ray pulses which are diffracted from the sample (hatched beam in the schematic in Fig. 4). We introduce slits along this x-ray beam to ensure that, after removing the copper tape for x-ray generation, only laser photons propagating along this x-ray probe path impinge on the sample, now as optical probe pulses.

To switch between optical and x-ray probes, only the copper band and a $10 \mu\text{m}$ thick plastic film are removed from the beam path. The optical probe pulse and the x-ray probe-pulse have

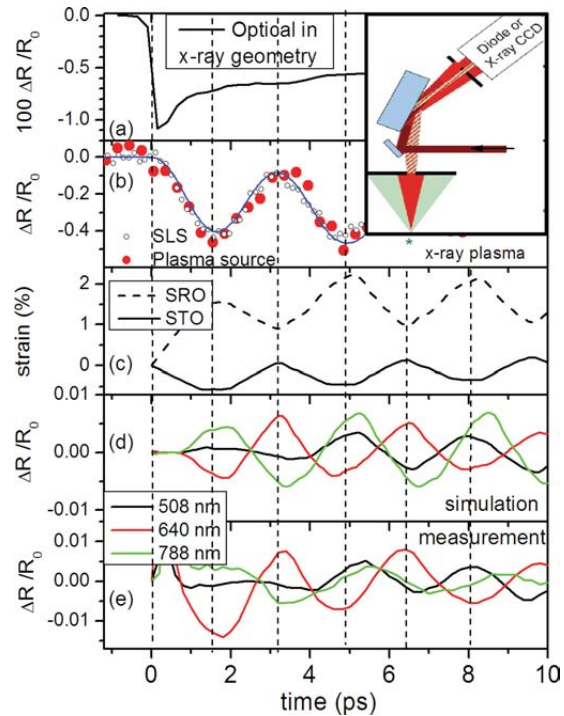


FIG. 4. (Color) (a) All-optical response measured in the same configuration for $\lambda_{\text{pump}} = 800$ nm and $\lambda_{\text{probe}} = 800$ nm. The schematic shows the combined optical/x-ray pump-probe geometry. Optical (red) and x-ray (green) probe pulses collinearly propagate through a slit towards the sample. Both emerge from the laser focus on the copper tape which generates the x-ray pulses and which is removed for optical probing. (b) UXRD data from the laser-based plasma source (red dots) with removed x-ray optics to precisely determine the zero time delay. The signal is shifted by 250 fs to earlier times with respect to the data as measured, according to the analysis described in the text. For comparison we show the UXRD data measured at the SLS [open circles, reproduced from Fig. 1(a)]. The blue line is the simulated UXRD signal based on the calculated lattice dynamics. (c) Simulated average strain in STO (solid) and SRO (dashed) pattern which is consistent with the observed x-ray diffraction signal. (d) Simulated optical reflectivity for three selected probe wavelengths. (e) Corresponding color-coded horizontal cuts through Fig. 3(a).

the same geometric path. The optical path is different due to the decreased group velocities c^* in air for x rays ($c_{\text{xray}}^* - c$)/ $c < 10^{-6}$ and 800 nm light pulses ($c_{\text{opt}}^* - c$)/ $c = 3 \times 10^{-4}$. The 300 mm path in air behind the laser focus makes the x rays arrive 300 fs earlier than the laser pulse traveling the same path in the all-optical experiment. In addition the laser passes through 5 cm of vacuum before the focus in the x-ray experiment, which is replaced by an air path in the optical experiment, adding another 50 fs to the time delay. A contribution in the opposite direction is the additional time delay of the x-ray pulses due to the propagation of electrons in the metal target before the x-ray production. This leads to a temporally extended x-ray

pulse with a duration in the 100–200 fs range²⁹ as compared to the 40 fs laser pulses. In essence this delays the x-ray pulse by about 100 fs, since the leading edge of the x-ray pulse must coincide with the optical excitation pulse as the first generated x rays travel at the speed of light, and the trailing edge is delayed by the x-ray pulse duration which is given by the hot electrons moving through the copper target.³⁰

In short, the time axis of the UXR D experiment must be shifted by 250 fs with respect to the all-optical experiment. Time zero is determined by the steepest slope due to the electronic heating in SRO detected in the all-optical experiment [Fig. 4(a)], which is consistent with the time overlap determined in a thin BBO crystal for second-harmonic generation. Now the UXR D signal is measured in exactly the same configuration and plotted in Fig. 4(b) already shifted as discussed above. For comparison the data from Fig. 1(a) measured at the SLS are shown as well. Panel 4(c) compares this to simulations discussed below, which also predict the optical response for three selected wavelengths [panel 4(d)], which are in excellent agreement with the measured data at these wavelengths [panel 4(e)]. The pump fluence in both the UXR D and the optical experiment was approximately 20 mJ/cm². In total, Fig. 4 summarizes how time zero is compared in all-optical and UXR D experiments and how both data sets are linked to the simulation of lattice dynamics discussed in the next section.

Earlier UXR D measurements on the very same STO/SRO SL reported an additional delay of approximately 500 fs for weak excitation.^{21,31,32} Very careful analysis of all experiments shows that this discrepancy can be partly ascribed to a modified oscillation phase for the higher pump fluence and partly to the group-velocity delay of the optical pulses and x-ray pulses in air which was neglected at that time.

III. SIMULATIONS

As a theoretical support of our interpretations, we have set up a linear chain model of the superlattice in which instantaneous stress is generated by optically induced heating of the lattice. The elastic constants are known and the spatio-temporal strain pattern has been previously calculated.³³ On the timescale $t < 10$ ps heat diffusion can be neglected and it is not relevant for the stress generation.³⁴ In the optical signal it gives rise to a slowly varying background that is subtracted before considering the oscillations. The average strain in the SRO and STO layers resulting from this calculation is given in Fig. 4(c). The simulated strain map with unit-cell resolution is the common starting point to predict both the UXR D signal [panel 4(b)] and the all-optical signal [panel 4(d)]. The simulated solid line in panel 4(b) is obtained from using the calculated spatio-temporal strain pattern³³ in a dynamical x-ray diffraction simulation.²⁰

To calculate the optical response we specify the complex index of refraction $N(z, t) = n + i\kappa$ for each unit cell along growth direction of the superlattice for each timestep and calculate the optical reflectivity in a standard optical matrix formalism. For STO both the wavelength-dependent index of refraction $n_{\text{STO}}(\lambda)$ and its derivative $dn_{\text{STO}}/d\eta = 0.5$ with respect to strain η are taken from the literature.^{35–37} The complex refractive index $N_{\text{SRO}}(\lambda) = n_{\text{SRO}}(\lambda) + i\kappa_{\text{SRO}}(\lambda)$ of SRO

is derived from the literature.³⁸ The derivatives for SRO are unknown and hence we use $dn_{\text{SRO}}/d\eta$ and $d\kappa_{\text{SRO}}/d\eta$ as fitting parameters to match the observed data simultaneously for all probe wavelengths. We already obtain a reasonable agreement [compare Figs. 3(a) and 3(b) and Figs. 4(d) and 4(e)] if we assume $dn_{\text{SRO}}/d\eta = dn_{\text{STO}}/d\eta = 0.5$ and $d\kappa_{\text{SRO}}/d\eta = 1.5$ independent of wavelength. Additional variations of the optical constants with the wavelength could yield even more accurate agreement. However, already at the current level of simulation the agreement of the optical broadband data with simulations presented in Fig. 3(b) gives us confidence in our interpretation. From an experimental point of view the validation via UXR D is a preferable cross-check.

IV. DISCUSSION

For $t > 0$ the UXR D signals can be well fitted by the following function:

$$S(t) = -A \sin\left(\pi \frac{t - t_0^{\text{osc}}}{T_{\text{osc}}}\right)^2 \exp\left(-\frac{t - t_0^{\text{osc}}}{T_{\text{dec}}}\right) - m(t - t_0^{\text{lin}}). \quad (1)$$

The shape of this fitting function is uniquely determined by the physics contained in the simulation. The oscillatory part originates from the excitation of a single zone-folded LA phonon mode which modulates the x-ray diffraction structure factor of the superlattice reflection, and the decay is essentially due to the propagation of the excitation into the substrate.²⁰ The linear slope on the signal is explained by the shift of the Bragg reflection due to the average heat expansion of the superlattice.

Such a simple fitting function does not exist for the all-optical counterpart. Figure 3 illustrates that the optical signals suffer from a beating due to the interference of probe pulses reflected from the interfaces, from the phonons in the SL, and from the propagating sound wave. Despite this complicated situation, the straightforward simulation yields excellent agreement.

Now we turn to the discussion of the phase shift observed in both experiments. From the carefully determined time zero of the UXR D signal with an accuracy of about ± 100 fs, we can directly conclude that the assumption of an instantaneous stress generation in our simulation is very good, since the phase of the signal at the highest fluence corresponds to a perfect cosine, i.e., to a displacive excitation without considerable additional delay due to electron-phonon coupling. The phase of the lattice motion in the simulation is in good agreement with by the UXR D measurement.

The fluence dependent study in Fig. 1 shows that for lower fluence the lattice stress starts about 130 fs later, yielding an estimate of the electron-phonon coupling time. Although the absolute determination of the time zero is only accurate within ± 100 fs, the relative phase delay of 130 ± 50 fs is determined with sufficient accuracy. The same clear trend is observed in the oscillation phase of the all-optical signal at 670 nm [Fig. 2(c)]. Below a fluence of about 20 mJ/cm² the electronic pressure is likely negligible compared to the lattice contribution to the expansion. Hence, below this fluence the phase is set by the electron-phonon coupling time in SRO. In the simplest models for metals, the electronic heat capacity rises linearly with the temperature and the lattice contribution

saturates to the Dulong-Petit limit. However, calculations based on the electronic density of states (DOS) show that for most metals this is not true under strong nonequilibrium conditions.³⁹ Since for the case of the bad metal SRO with strong electron correlations, simulations of the DOS strongly depend on the method used,⁴⁰ and we do not attempt to predict the electronic stress contributions.

In the semiconducting material InSb a phase shift of the oscillations towards earlier times was observed for higher fluence.² This was attributed to a decreasing lattice heating time for strong excitation, essentially because the reduced lifetime of LO phonons⁴¹ limits the carrier-lattice thermalization dynamics.⁴² Similar arguments could apply in the case of SRO. Specifically, the observation of an oscillation starting earlier for higher fluence is in contrast to the observation of electronic pressure in elementary metallic systems such as aluminum and gold.^{5,6} In these metals a larger electron-phonon coupling time leads to larger effect size in the opposite direction, namely because the electron-lattice heat transfer takes longer for high fluence. We cannot rule out that contributions from impulsive Raman scattering play a role in the phase shift; however, all processes in question—Raman, electronic pressure, lattice heat expansion—scale linearly with the pump fluence in the simplest models and would not explain a fluence dependence

of the phase. Therefore we think that time- and temperature-dependent modification of the electron-phonon interaction must be responsible for the observed phase delay.

In conclusion, we have presented ultrafast x-ray diffraction (UXRD) and all-optical pump-probe experiments on the metal-dielectric superlattice STO/SRO. Only the combination of both methods allows one to experimentally deduce the absolute phase of the optically induced lattice motion. From fluence-dependent UXRD we extract a relative shift of the oscillation phase of the lattice which is readily ascribed to electronic pressure. The same fluence dependence of the phase is observed in all-optical experiments. However, the complex wavelength dependence of the broadband data highlight that the oscillation phase of all-optical experiments must be interpreted with care. Our x-ray calibrated simulations of the all-optical data validates the detailed interpretation.

ACKNOWLEDGMENTS

We thank R. van der Veen for her valuable experimental support at the MicroXAS-FEMTO beamline. We gratefully acknowledge the financial support by the BMBF via Grant No. 03WKP03A and the Deutsche Forschungsgemeinschaft (DFG) (Grant No. BA2281/3-1).

*bargheer@uni-potsdam.de

¹A. Morak, T. Kaempfer, I. Uschmann, A. Luebecke, E. Foerster, and R. Sauerbrey, *Phys. Status Solidi B* **243**, 2728 (2006).

²F. S. Krasniqi, S. L. Johnson, P. Beaud, M. Kaiser, D. Grolimund, and G. Ingold, *Phys. Rev. B* **78**, 174302 (2008).

³P. Sondhauss, O. Synnergren, T. N. Hansen, S. E. Canton, H. Enquist, A. Srivastava, and J. Larsson, *Phys. Rev. B* **78**, 115202 (2008).

⁴D. M. Fritz, D. A. Reis, B. Adams, R. A. Akre, J. Arthur, C. Blome, P. H. Bucksbaum, A. L. Cavalieri, S. Engemann, S. Fahy *et al.*, *Science* **315**, 633 (2007).

⁵J. Li, R. Clinite, X. Wang, and J. Cao, *Phys. Rev. B* **80**, 014304 (2009).

⁶M. Nicoul, U. Shymanovich, A. Tarasevitch, D. von der Linde, and K. Sokolowski-Tinten, *Appl. Phys. Lett.* **98**, 191902 (2011).

⁷A. Bartels, T. Dekorsy, H. Kurz, and K. Köhler, *Phys. Rev. Lett.* **82**, 1044 (1999).

⁸H. J. Zeiger, J. Vidal, T. K. Cheng, E. P. Ippen, G. Dresselhaus, and M. S. Dresselhaus, *Phys. Rev. B* **45**, 768 (1992).

⁹C.-K. Sun, J.-C. Liang, and X.-Y. Yu, *Phys. Rev. Lett.* **84**, 179 (2000).

¹⁰T. E. Stevens, J. Kuhl, and R. Merlin, *Phys. Rev. B* **65**, 144304 (2002).

¹¹T. Dekorsy, G. Cho, and H. Kurz, in *Light Scattering in Solids VIII*, Vol. 76 of *Topics in Applied Physics*, edited by M. Cardona and G. Güntherodt (Springer, Berlin, 2000), pp. 169–209.

¹²V. V. Kruglyak, R. J. Hicken, G. P. Srivastava, M. Ali, B. J. Hickey, A. T. G. Pym, and B. K. Tanner, *Phys. Rev. B* **76**, 012301 (2007).

¹³M. Hase, K. Ishioka, J. Demsar, K. Ushida, and M. Kitajima, *Phys. Rev. B* **71**, 184301 (2005).

¹⁴S. L. Johnson, P. Beaud, C. J. Milne, F. S. Krasniqi, E. S. Zijlstra, M. E. Garcia, M. Kaiser, D. Grolimund, R. Abela, and G. Ingold, *Phys. Rev. Lett.* **100**, 155501 (2008).

¹⁵M. Hase, M. Kitajima, A. Constantinescu, and H. Petek, *Nature (London)* **426**, 51 (2003).

¹⁶A. Cavalleri, S. Wall, C. Simpson, E. Statz, D. W. Ward, K. A. Nelson, M. Rini, and R. W. Schoenlein, *Nature (London)* **442**, 664 (2006).

¹⁷K. J. Yee, Y. S. Lim, T. Dekorsy, and D. S. Kim, *Phys. Rev. Lett.* **86**, 1630 (2001).

¹⁸C. Colvard, T. A. Gant, M. V. Klein, R. Merlin, R. Fischer, H. Morkoc, and A. C. Gossard, *Phys. Rev. B* **31**, 2080 (1985).

¹⁹M. Bargheer, N. Zhavoronkov, Y. Gritsai, J. C. Woo, D. S. Kim, M. Woerner, and T. Elsaesser, *Science* **306**, 1771 (2004).

²⁰M. Herzog, D. Schick, W. Leitenberger, R. Shayduk, R. M. van der Veen, C. J. Milne, S. L. Johnson, I. Vrejoiu, and M. Bargheer, *New J. Phys.* **14**, 013004 (2012).

²¹C. von Korff Schmising, A. Harpoeth, N. Zhavoronkov, Z. Ansari, C. Aku-Leh, M. Woerner, T. Elsaesser, M. Bargheer, M. Schmidbauer, I. Vrejoiu *et al.*, *Phys. Rev. B* **78**, 060404 (2008).

²²M. Herzog, W. Leitenberger, R. Shayduk, R. van der Veen, C. J. Milne, S. L. Johnson, I. Vrejoiu, M. Alexe, D. Hesse, and M. Bargheer, *Appl. Phys. Lett.* **96**, 161906 (2010).

²³P. Beaud, S. L. Johnson, A. Streun, R. Abela, D. Abramsohn, D. Grolimund, F. S. Krasniqi, T. Schmidt, V. Schlott, and G. Ingold, *Phys. Rev. Lett.* **99**, 174801 (2007).

²⁴The strain amplitude is derived by comparing the model and experimental data in the inset of Fig. 3(a) in Ref. 20. Since the agreement is nearly perfect, the mapping of fluence on strain yields

- the linear function presented in Fig. 1(b). We do not attempt to discuss the tiny deviations, as we focus here on the phase of the oscillations.
- ²⁵I. Bozovic, M. Schneider, Y. Xu, R. Sobolewski, Y. H. Ren, G. Lüpke, J. Demsar, A. J. Taylor, and M. Onellion, *Phys. Rev. B* **69**, 132503 (2004).
- ²⁶S. Brivio, D. Polli, A. Crespi, R. Osellame, G. Cerullo, and R. Bertacco, *Appl. Phys. Lett.* **98**, 211907 (2011).
- ²⁷D. Schick, A. Bojahr, M. Herzog, C. von Korff Schmising, R. Shayduk, W. Leitenberger, P. Gaal, and M. Bargheer, *Rev. Sci. Instrum.* **83**, 025104 (2012).
- ²⁸F. Zamponi, Z. Ansari, C. von Korff Schmising, P. Rothardt, N. Zhavoronkov, M. Woerner, T. Elsaesser, M. Bargheer, T. Trobitzsch-Ryll, and M. Haschke, *Appl. Phys. A* **96**, 51 (2009).
- ²⁹F. Zamponi, Z. Ansari, M. Woerner, and T. Elsaesser, *Opt. Express* **18**, 947 (2010).
- ³⁰C. Reich, P. Gibbon, I. Uschmann, and E. Förster, *Phys. Rev. Lett.* **84**, 4846 (2000).
- ³¹C. von Korff Schmising, M. Bargheer, M. Kiel, N. Zhavoronkov, M. Woerner, T. Elsaesser, I. Vrejoiu, D. Hesse, and M. Alexe, *Appl. Phys. B* **88**, 1 (2007).
- ³²M. Woerner, C. von Korff Schmising, M. Bargheer, N. Zhavoronkov, I. Vrejoiu, D. Hesse, M. Alexe, and T. Elsaesser, *Appl. Phys. A* **96**, 83 (2009).
- ³³M. Herzog, D. Schick, P. Gaal, R. Shayduk, C. von Korff Schmising, and M. Bargheer, *Appl. Phys. A* **106**, 489 (2012).
- ³⁴R. Shayduk, H. A. Navirian, W. Leitenberger, J. Goldshteyn, I. Vrejoiu, M. Weinelt, P. Gaal, M. Herzog, C. von Korff Schmising, and M. Bargheer, *New J. Phys.* **13**, 093032 (2011).
- ³⁵M. Cardona, *Phys. Rev.* **140**, A651 (1965).
- ³⁶A. Giardini, *J. Opt. Soc. Am.* **47**, 726 (1957).
- ³⁷M. L. Hassel Ledbetter and S. Kim, *Phase Transitions* **23**, 61 (1990).
- ³⁸P. Kostic, Y. Okada, N. C. Collins, Z. Schlesinger, J. W. Reiner, L. Klein, A. Kapitulnik, T. H. Geballe, and M. R. Beasley, *Phys. Rev. Lett.* **81**, 2498 (1998).
- ³⁹Z. Lin, L. V. Zhigilei, and V. Celli, *Phys. Rev. B* **77**, 075133 (2008).
- ⁴⁰H.-T. Jeng, S.-H. Lin, and C.-S. Hsue, *Phys. Rev. Lett.* **97**, 067002 (2006).
- ⁴¹K. T. Tsen, J. G. Kiang, D. K. Ferry, and H. Morkoc, *Appl. Phys. Lett.* **89** (2006).
- ⁴²A. H. Chin, R. W. Schoenlein, T. E. Glover, P. Balling, W. P. Leemans, and C. V. Shank, *Phys. Rev. Lett.* **83**, 336 (1999).

Paper VI

udkm1Dsim - A Simulation Toolkit for 1D Ultrafast Dynamics in Condensed Matter

D. Schick, A. Bojahr, M. Herzog, R. Shayduk, C. von Korff Schmising, and M. Bargheer
Comput. Phys. Commun. in press, (2013)

UDKM1DSIM - A Simulation Toolkit for 1D Ultrafast Dynamics in Condensed Matter

D. Schick^{a,*}, A. Bojahr^a, M. Herzog^{a,b}, R. Shayduk^c, C. von Korff Schmising^d, M. Bargheer^{a,c}^a*Institut für Physik & Astronomie, Universität Potsdam, Karl-Liebknecht-Straße 24-25, 14476 Potsdam, Germany*^b*Abteilung Physikalische Chemie, Fritz-Haber-Institut der Max-Planck-Gesellschaft, Faradayweg 4-6, 14195 Berlin, Germany*^c*Helmholtz-Zentrum Berlin für Materialien und Energie GmbH, Wilhelm-Conrad-Röntgen Campus, BESSY II, Albert-Einstein-Straße 15, 12489 Berlin, Germany*^d*Institut für Optik und Atomare Physik, Technische Universität Berlin, Straße des 17. Juni 135, 10623 Berlin, Germany***Abstract**

The UDKM1DSIM toolbox is a collection of MATLAB (MathWorks Inc.) classes and routines to simulate the structural dynamics and the according X-ray diffraction response in one-dimensional crystalline sample structures upon an arbitrary time-dependent external stimulus, e.g. an ultrashort laser pulse. The toolbox provides the capabilities to define arbitrary layered structures on the atomic level including a rich database of corresponding element-specific physical properties. The excitation of ultrafast dynamics is represented by an N -temperature model which is commonly applied for ultrafast optical excitations. Structural dynamics due to thermal stress are calculated by a linear-chain model of masses and springs. The resulting X-ray diffraction response is computed by dynamical X-ray theory. The UDKM1DSIM toolbox is highly modular and allows for introducing user-defined results at any step in the simulation procedure.

Keywords: ultrafast dynamics, heat diffusion, N -temperature model, coherent phonons, incoherent phonons, thermoelasticity, dynamical X-ray theory

PROGRAM SUMMARY

Manuscript Title: UDKM1DSIM - A Simulation Toolkit for 1D Ultrafast Dynamics in Condensed Matter

Authors: D. Schick, A. Bojahr, M. Herzog, R. Shayduk, C. von Korff Schmising, M. Bargheer

Program Title: UDKM1DSIM

Journal Reference:

Catalogue identifier:

Licensing provisions: BSD

Programming language: MATLAB (MathWorks Inc.)

Computer: PC/Workstation

Operating system: running MATLAB installation required (tested on MS Win XP - 7, Ubuntu Linux 11.04-13.04)

RAM: MATLAB's typical RAM requirement of 196MB is sufficient for most simulations

Has the code been vectorized or parallelized?: parallelization for dynamical XRD computations

Number of processors used: 1-12 for MATLAB Parallel Computing Toolbox; 1- ∞ for MATLAB Distributed Computing Toolbox

Keywords: ultrafast dynamics, heat diffusion, N -temperature model, coherent phonons, incoherent phonons, thermoelasticity, dynamical X-ray theory

Classification: 7.8 Structure and Lattice Dynamics, 7.9 Transport Properties, 8 Crystallography

External routines/libraries:

optional:

MATLAB Parallel Computing Toolbox, MATLAB Distributed Computing Toolbox

Required (included in the package):

MTIMESX Fast Matrix Multiply for MATLAB by James Tursa, XML_IO_TOOLS by Jaroslaw Tuszynski, TEXTPROGRESSBAR by Paul Proteus

Nature of problem:

Simulate the lattice dynamics of 1D crystalline sample structures due to an ultrafast excitation including thermal transport and compute the corresponding transient X-ray diffraction pattern.

Solution method:

The program provides an object-oriented toolbox for building arbitrary layered 1D crystalline sample structures including a rich database of element-specific parameters. The excitation, thermal transport and lattice dynamics are simulated utilizing MATLAB's ODE solver. Alternatively, the lattice dynamics can also be calculated analytically utilizing MATLAB eigenproblem solver. The dynamical X-ray diffraction is computed in a parallelized matrix formalism.

Restrictions:

The program is restricted to 1D sample structures and is further limited to longitudinal acoustic phonon modes and symmetrical X-ray diffraction geometries.

Unusual features:

The program is highly modular and allows to include user-defined inputs at any time of the simulation procedure.

Running time:

The running time is highly dependent on the number of unit cells in the sample structure and other simulation parameters such as time span or angular grid for X-ray diffraction computations. However, the example files are computed in approx. 1-5 min. each on a 8 Core Processor with 16GB RAM available.

*Corresponding author

Email address: daniel.schick@uni-potsdam.de (D. Schick)

URL: <http://www.udkm.physik.uni-potsdam.de> (M. Bargheer)

1. Introduction

Physics on the ultrafast time scales and nanometer length scales has received enormous attention during the last decade. Ultrafast X-ray diffraction (UXRD) techniques allow for directly studying structural dynamics on the atomic length and time scales. The knowledge of the time-resolved structural response to an ultrafast optical stimulus is essential for the understanding of various condensed matter phenomena.[1–4]

The UDKM1DSIM toolbox is a collection of classes and routines to model 1D crystalline sample structures on the atomic level and to simulate incoherent (heat diffusion) as well as coherent lattice dynamics (acoustic phonons) by semi-coupled equations of thermoelasticity.[5, 6] The resulting transient X-ray diffraction response for the 1D sample structure is computed by dynamical X-ray theory.[7, 8] Due to the high modularity of the toolbox it is easy to introduce user-defined procedures in between the simulation steps. The complete package is written in the MATLAB programming language and requires the installation of the MATLAB software environment. In order to use the multi-core capabilities of MATLAB the Parallel Computing has to be installed but is not required for UDKM1DSIM to work. As a convention for this document, all files and directories are formatted without serifs (`./path/file.ext`) and all MATLAB code is written in typewriter format (`code = [1 10]`). Furthermore, all physical quantities have to be input in SI units and the same applies for all output variables.¹ The latest UDKM1DSIM package files can be downloaded from www.udkm.physik.uni-potsdam.de/udkm1dsim including a detailed documentation and example files. It is highly recommended to be familiar with the basics of MATLAB programming as well as with fundamental object-orientated programming schemes. Please refer to the rich MATLAB documentation on these topics for further help.

In the following, we introduce the implementation and common workflow of the UDKM1DSIM toolbox as well as the underlying physical concepts. Please refer to the specific class documentations in the `./documentation/` folder of the toolbox for detailed information on all available methods and properties. Finally, we provide examples of the UDKM1DSIM package which are compared with selected ultrafast experiments on nano-layered thin film samples.

2. Implementation & Workflow

The UDKM1DSIM package is developed as MATLAB toolbox with a command-line/script-based user-interface. The backbone of the fully object-orientated toolbox is a collection of classes in the `./classes/` folder which hold the complete logic for building 1D sample structures and to

¹A helper class `units` is provided to easily convert physical quantities.

calculate the ultrafast dynamics in these structures. Additional helper routines (`./helpers/`) and material parameter files (`./parameters/`) are included to improve the user experience.

2.1. Structure Generation

The common workflow of a simulation procedure is to create a crystalline sample structure at the beginning. This 1D structure is build of atoms which form unit cells. Unit cells are then grouped to layers/sub-structures which can be further nested, e.g. to build multilayer structures. All physical properties which are necessary for the later simulations are stored in this structural objects. The involved files are `atomBase.m`, `atomMixed.m`, `unitCell.m` and `structure.m`.

2.1.1. Atoms

The smallest building block for a structure is an atom, which is represented by the `atomBase` class. Atomic properties are automatically loaded on construction of each `atomBase` instance from the given parameter files, by providing the correct symbol of the desired chemical element:

```
C = atomBase('C');
H = atomBase('H');
```

By executing the command `C.display()` all properties of the corresponding `atomBase` object are displayed. Solid solutions, i.e. stoichiometric atomic substitutions, can be modelled by the `atomMixed` class. Here, `atomBase` objects can be added with an according relative amount to the solution:

```
ZrTi = atomMixed('0.2 Zirconium/0.8 Titanium');
ZrTi.addAtom(atomBase('Zr'), 0.2);
ZrTi.addAtom(atomBase('Ti'), 0.8);
```

The resulting mixed atomic properties are the weighted average of the constituent's properties.

2.1.2. Unit Cells

The `unitCell` class holds most of the physical properties which are necessary for the further simulations. In addition to structural information, i.e. the position of atoms in the unit cell, thermal and mechanical properties are stored here. The only required parameters on initialization of a `unitCell` instance are a unique identifier (ID), name, and the *c*-axis (lattice parameter normal to the sample surface) of the unit cell. All other properties can be optionally handed over within a parameter struct on construction, or can be added/modified later:

```
cAxis          = 3.95e-10; % [m]
prop.soundVel  = 5100;    % [m/s]
.
.
prop.heatCapacity = 465; % [J/kg K]
% SrRuO3 - Perovskite
SRO = unitCell('SRO', 'SRO', cAxis, prop);
```


After the construction of a `unitCell` object, one can add `atomBase` or `atomMixed` object at relative positions in the 1D unit cell, e.g. for the cubic SrRuO_3 (SRO) perovskite unit cell:

```
SRO.addAtom(Sr, 0 );
SRO.addAtom(O , 0 );
SRO.addAtom(Ru, 0.5);
SRO.addAtom(O , 0.5);
SRO.addAtom(O , 0.5);
```

All available unit cell properties can be easily displayed by executing the command `SRO.disp()`. The position of atoms in the unit cell can be visualized by executing `SRO.visualize()`.

2.1.3. Structures

The final 1D crystalline samples are represented by the `structure` class which only requires a name on initialization. One can add any number of `unitCell` objects to a structure, as well as nested substructures. An example of a $\text{SrRuO}_3/\text{SrTiO}_3$ superlattice with 10 periods on a SrTiO_3 (STO) substrate is shown in the listing below:

```
DL = structure('Double Layer');
% add 13 SRO and 25 STO unit cells to the DL
DL.addSubStructure(SRO,13);
DL.addSubStructure(STO,25);

S = structure('Superlattice Sample');
% add 10 DLs to the sample
S.addSubStructure(DL,10);
% add 1000 STO unit cells to the sample
S.addSubStructure(STO,1000);
```

In order to simplify the sample structure creation, all of the above mentioned steps can be included in an external XML file which holds all information on atoms, unit cells and on the structure itself. Hence, it is easy to store structures outside of MATLAB in a unified and open standard. An example XML file is provided in the `./example/` folder of the toolbox. In order to load the data from the XML file into the MATLAB workspace one needs to execute the following command providing the relative or absolute path to the XML file:

```
S = structure('void', './structure.xml');
```

Again, the structure properties can be displayed with the command `S.disp()` and the structure can be visualized by `S.visualize()`.

2.2. Simulation Classes

Besides the 1D sample structures, also all simulations are programmed as classes and inherit from the super-class `simulation`. All `simulation`-inherited classes provide fundamental properties and methods for storing and loading of simulation results from a so-called `/cache/` folder. The `UDKM1DSIM` toolbox can decide independently by comparing a unique hash of all simulation input parameters

whether a simulation result (once calculated) can be loaded from the cache folder or needs to be (re-)calculated. The hash algorithm decides also which parameter changes are relevant for a simulation model, e.g. a change of the sound velocity of a unit cell does not change the result of the heat diffusion calculation, however it does change the result of the lattice dynamics simulation. Further functionalities of the `simulation` class are to enable/disable any command-line messages during the simulations, e.g. to display the elapsed time for a simulation step, and to change the mode of progress displaying.

In order to calculate the time-dependent X-ray diffraction response of a 1D crystalline sample structure to an ultrafast stimulus the following three simulation steps are necessary:

1. The excitation is described as temperature changes in an N -temperature model with optional heat diffusion which determines the temperature evolution in the N coupled subsystems.
2. The resulting lattice dynamics due to thermal stress possibly generated by any of the N subsystems are calculated by a 1D linear-chain model.
3. Dynamical X-ray theory is applied to calculate the UXRD response to the lattice dynamics.

These three steps are encapsulated in the simulation classes `heat`, `phonon`, and `XRD` which all require a `structure` object on initialization.

It is important to note, that each of the simulation steps listed above may be executed independently with user-defined inputs. Thus it is not necessary to execute the heat and phonon simulations if the user needs to calculate the X-ray diffraction result e.g. for artificial or externally calculated lattice dynamics.

2.3. Thermal Excitation & Diffusion

The `UDKM1DSIM` toolbox allows for different excitation scenarios and optional thermal transport. The most general model is an N -temperature model (NTM) which is described in section 2.3.1.[9] However, for various experimental cases it is convenient to simplify the simulation procedure in order to save computational time.

In all cases it is assumed that the sample structure is excited by a light pulse which is absorbed following Lambert-Beer's law:

$$I(z) = I_0 e^{-z/\zeta} \quad , \quad (1)$$

with ζ as optical penetration depth of the material for the considered wavelength. Accordingly, one can define the transmission and absorption in the material as follows:

$$\tau = \frac{I(z)}{I_0} = e^{-z/\zeta} \quad , \quad \alpha = 1 - \tau \quad . \quad (2)$$

The deposited optical energy is then given by the spatial derivative of the absorption:

$$\frac{\partial \alpha}{\partial z} = \frac{1}{\zeta} e^{-z/\zeta} \quad . \quad (3)$$

The most simplified excitation scenario is represented by an instantaneous temperature jump of the excited sample structures (infinitely short laser pulse). This assumption is generally valid if the excitation and thermal equilibration between all N subsystems happen much faster than the subsequent thermal and/or lattice dynamics. The instantaneous temperature jump at depth z can be calculated from the energy absorbed by the corresponding unit cell via:

$$\Delta E(z) = \int_{T_1}^{T_2} m c [T(z)] dT(z) \quad , \quad (4)$$

where T_1 is the initial and T_2 is the final temperature of the unit cell, m is the unit cell mass, and $c(T)$ is the temperature-dependent specific heat capacity. In order to calculate the absorbed energy per unit cell at the depth z in the sample structure one can linearize Eq. 3 for small Δz in terms of energy instead of intensity to get

$$\Delta E = \frac{\partial \alpha}{\partial z} E_0 \Delta z \quad , \quad (5)$$

where Δz is the size of the according unit cell. The initial energy E_0 which is incident on the first unit cell can be derived from the incident absorbed fluence $F = E_0/A$, where A is the area of a single unit cell. Hence, one has to minimize the following modulus in order to obtain the final temperature T_2 of a unit cell after optical excitation:

$$\left| \int_{T_1}^{T_2} m c [T(z)] dT(z) - \frac{E_0}{\zeta} e^{-z/\zeta} \Delta z \right| \stackrel{!}{=} 0 \quad . \quad (6)$$

In order to solve the above minimization problem it is necessary that the heat capacity $c(T)$ is input as a polynomial of any order, thus enabling MATLAB to integrate $c(T)$ algebraically with respect to the temperature T .

The temperature jump resulting from the optical excitation at $t = 0$ can be further used as initial condition for solving the 1D heat diffusion equation:

$$c [T(z, t)] \rho \frac{\partial T(z, t)}{\partial t} = \frac{\partial}{\partial z} \left(k [T(z, t)] \frac{\partial T(z, t)}{\partial z} \right) \quad (7)$$

including the thermal conductivity $k(T)$ and mass density ρ of the individual unit cells. The UDKM1DSIM toolbox is capable of calculating the optical excitation and thermal dynamics independently for a given sample structure, thermal parameters, and excitation scenario. The corresponding code listing for an excitation at $t_0 = 0$ with a fluence of $F = 5$ mJ/cm² including heat diffusion for a given sample structure `s` might look as follows:

```
% initialization of heat simulation
H = heat(S, forceRecalc);
% S - structure object
% forceRecalc - boolean
% enable heat diffusion
H.heatDiffusion = true;
% introduces SI units
u = units;
```

```
% temporal grid for heat simulations
time = (-20:0.1:200)*u.ps;
% initial temperature of the structure
initTemp = 300*u.K;
% define the excitation
F = 5*u.mJ/u.cm^2;
% the temperature profile is calculated:
[tempMap, deltaTempMap] = ...
H.getTempMap(time, F, initTemp);
```

Here, `initTemp` is the initial temperature of the sample, which can be defined globally or per unit cell and the vector `time` defines the time grid of the calculation. The actual numerical calculation is executed by the last command in the above listing and requires no further insight into the involved mathematics. The UDKM1DSIM toolbox allows for more sophisticated excitation scenarios, such as optical pulse sequences with arbitrary temporal pulse separations and durations as well as user-defined pulse energy distributions. Please refer to the corresponding examples for further details on this topic.

2.3.1. N -Temperature Model

The so-called N -temperature model (NTM)[9] is a very general model for laser heating of metals and semiconductors. In the NTM materials are described by N thermal subsystems having individual temperatures $T_j(z, t)$, heat capacities $c_j(T_j)$, thermal conductivities $k_j(T_j)$ and coupling terms $G_j(T_1, \dots, T_N)$. The subsystems might be represented by e.g. electrons, lattice, or spins of the according material:

$$\begin{aligned} c_1(T_1) \frac{\partial T_1}{\partial t} &= \frac{\partial}{\partial z} \left(k_1(T_1) \frac{\partial T_1}{\partial z} \right) \\ &\quad + G_1(T_1, \dots, T_N) + S(z, t) \\ &\quad \vdots \\ c_N(T_N) \frac{\partial T_N}{\partial t} &= \frac{\partial}{\partial z} \left(k_N(T_N) \frac{\partial T_N}{\partial z} \right) \\ &\quad + G_N(T_1, \dots, T_N) \quad . \end{aligned} \quad (8)$$

The UDKM1DSIM toolbox limits the excitation of a structure with N subsystem to happen exclusively in the first subsystem. The excitation can be either given as an initial condition due to an instantaneous temperature jump (see above) or by a spatially and temporally varying source term $S(z, t)$. This source term is the energy flux per volume and time

$$S(z, t) = \frac{\partial^2 E}{A \partial z \partial t} \quad , \quad (9)$$

where A is again the unit cell area. The spatial profile of $S(z, t)$ is given by the absorbed energy density from Eq. 3 and the temporal profile is limited to a Gaussian function, which states as

$$\frac{\partial^2 E}{\partial z \partial t} = \frac{d\alpha}{dz} E_0 \sigma(t) \quad , \quad (10)$$

with $\sigma(t)$ as a normalized Gaussian function in time [s⁻¹] and E_0 as the initial energy incident on the first unit cell.

The resulting source term reads as follows:

$$S(z, t) = \frac{d\alpha}{dz} F \sigma(t) \quad . \quad (11)$$

In order to enable the evaluation of the NTM it is necessary to input all material properties in the structure as N -dimensional cell arrays. Each element of the cell array can be either a constant value for the according property or an anonymous function of the j^{th} subsystem temperature T_j . In contrast to simple heat simulations with only a single subsystem one needs to define the additional `unitCell` property `subSystemCoupling` which represents the term $G(T)$ in Eq. 9.

As it is necessary to solve the heat diffusion equation the `UDKM1DSIM` toolbox allows to define boundary conditions of each subsystem, such as isolating boundaries, constant temperature, or constant heat flux on either side of the sample structure. Details on the broad capabilities of the `UDKM1DSIM` toolbox for thermal simulations are given in the example files `heatExample.m`, `heatNTmodelExample.m`, and `heatExcitationExample.m`.

2.4. Lattice Dynamics

The optically induced temperature change usually induce thermal stress in laser-heated materials. This thermal stress eventually relaxes via thermal expansion which is quantified by the linear thermal expansion coefficient:

$$\alpha(T) = \frac{1}{L} \frac{dL}{dT} \quad . \quad (12)$$

Since the temperature change $\Delta T(z, t)$ for each unit cell at each time step is known one can calculate the actual thermal expansion of each unit cell by

$$l = \Delta L = L_1 \left(e^{[A(T_2) - A(T_1)]} - 1 \right) \quad , \quad (13)$$

where L_1 is the initial length (c -axis of the unit cell), $A(T)$ is the integral of $\alpha(T)$, T_1 and T_2 denote the initial and final temperatures of each unit cell, respectively. It is again necessary to define $\alpha(T)$ as a polynomial of any order of the temperature T to enable MATLAB for simple and fast algebraic integration.

The thermally expanded unit cells are only the final state of the laser-excited crystal. In order to calculate the transient lattice dynamics (including only longitudinal acoustic phonons) towards this final state, we set up a model of a linear chain of masses and springs in which each unit cell represents a mass m_i that is coupled to its neighbors via springs with the spring constant $k_i = m_i v_i^2 / c_i^2$ (c_i - lattice c -axis, v_i - longitudinal sound velocity):[10]

$$m_i \ddot{x}_i = -k_i(x_i - x_{i-1}) - k_{i+1}(x_i - x_{i+1}) + m_i \gamma_i (\dot{x}_i - \dot{x}_{i-1}) + F_i^{\text{heat}}(t) \quad . \quad (14)$$

Here $x_i(t) = z_i(t) - z_i^0$ denotes the shift of each unit cell from its initial position. Furthermore, we introduce an empirical damping term $F_i^{\text{damp}} = \gamma_i(\dot{x}_i - \dot{x}_{i-1})$ and the

external force (thermal stress) $F_i^{\text{heat}}(t)$. In order to solve this system of coupled differential equations for each of the $i = 1 \dots N$ unit cells the `UDKM1DSIM` toolbox provides an analytical (`phononAna`) and a numerical model (`phononNum`) which are described in detail below. Examples for both models are given in the example files `phononExample.m`, and `phononAnharmonicExample.m`.

2.4.1. Analytical Solution

To obtain an analytical solution of Eq. 14 we neglect the damping term $F_i^{\text{damp}}(t)$ and derive the homogeneous differential equation in matrix form

$$\frac{d^2}{dt^2} \mathbf{X} = \mathbf{K} \mathbf{X} \quad . \quad (15)$$

Here $\mathbf{X} = (x_1 \dots x_N)$ and \mathbf{K} is the tri-diagonal force matrix.[10] The matrix \mathbf{K} can be diagonalized to obtain the eigenvectors Ξ_j and eigenfrequencies ω_j in order to find the general solution

$$\mathbf{X}(t) = \sum_j \Xi_j (A_j \cos(\omega_j t) + B_j \sin(\omega_j t)) \quad (16)$$

Mathematical details on the analytical model are given in Ref. [10] and in the documentation of the `phononAna` class. Generally, we use MATLAB's capability to solve the eigenproblem for \mathbf{K} in order to get the results for $\mathbf{X}(t)$ for each time step. One can implement the thermal stress as new equilibrium position $x_i^\infty(t)$ /initial conditions for the general solution Eq. 16 by doing an according coordinate transformation. The thermal stress [$F_i^{\text{heat}}(t)$] can be modeled as spacer sticks l_i in between the unit cells which are calculated from Eq. 13.

As an example listing of the analytical solution of the coherent phonon dynamics we continue the above code, having the structure `S`, `time` and the results of the heat simulation (`tempMap`, `deltaTempMap`) in memory.

```
% initialization of analytical phonon simulation
P = phononAna(S, forceRecalc);
% the strain profile is calculated:
strainMap = ...
P.getStrainMap(time, tempMap, deltaTempMap);
```

The matrix `deltaTempMap` is the temporal derivative of the temperature profile `tempMap`. The analytical model has the advantage that once the eigenproblem is solved for a fixed \mathbf{K} (fixed sample structure) the strain profile can be easily solved for any excitation profile at any time. In the case of a quasi-instantaneous excitation without heat diffusion this results in an extremely fast calculation since the initial conditions $\mathbf{X}(0)$ change only once for the excitation. However, the analytical model becomes rather slow for time-dependent thermal stress, because of the recalculation of these initial conditions for each time step. Accordingly, the temporal variation of the thermal stress due to damping has not been implemented in this model. The main disadvantage of the analytical model is the limitation to purely harmonic inter-atomic potentials which is

overcome by the numerical model, described below. The numerical model is generally also faster in the total computational time and further accounts for phonon scattering and damping effects.

2.4.2. Numerical Solution

Mathematical details on the numerical model for the coherent phonon dynamics can be found in the documentation of the `phononNum` class and in Ref. [11]. Generally, we use MATLAB's ODE solver to calculate the results for Eq. 14 which can be simplified to

$$m_i \ddot{x}_i = F_i^{\text{spring}} + F_i^{\text{damp}} + F_i^{\text{heat}} .$$

Here $F_i^{\text{spring}} = -k_i(x_i - x_{i-1}) - k_{i+1}(x_i - x_{i+1})$ is the force acting on each mass due to the relative shifts in respect to the left and right neighboring masses. The numerical solution also allows for non-harmonic inter-atomic potentials of up to the order M . Accordingly, $k_i = (k_i^{(1)} \dots k_i^{(M-1)})$ can be a vector accounting for higher orders of the potential which is purely quadratic ($k_i = k_i^{(1)}$) in the harmonic case. Thus we can introduce the following term into F_i^{spring} :

$$k_i(x_i - x_{i-1}) = \sum_{j=1}^{M-1} k_i^{(j)}(x_i - x_{i-1})^j , \quad (17)$$

which accounts for the anharmonic interaction. In order to calculate anharmonic phonon propagation, including damping, one needs to set the according properties of the `unitCell` object. For the example of the SRO unit cell defined in Sec. 2.1.2 one has to write

```
SRO.phononDamping = 1e-12;           % [kg/s]
SRO.setHOSpringConstants([-7e12]); % [kg/m s^2]
```

which sets the damping constant to $\gamma_{\text{SRO}} = 10^{-12}$ kg/s and the second-order of the spring constant to $k_{\text{SRO}}^{(2)} = -7 \times 10^{12}$ kg / m s². The actual numerical calculation for the coherent phonon dynamics is similar to the analytical model expect for the initialization of the `phononNum` object at the beginning:

```
% initialization of numerical phonon simulation
P = phononNum(S, forceRecalc);
% the strain profile is calculated:
strainMap = ...
    P.getStrainMap(time, tempMap, deltaTempMap);
```

We want to highlight, that the analytical and numerical lattice dynamics calculations share the same syntax in order to calculate the strain profile after optical excitations. In addition, the user can input any temperature profile for the thermal stresses and is not limited to the results of the heat simulations. In accordance to the NTM described in Sec. 2.3.1, the thermal stresses can account for multiple thermodynamic subsystems in the sample by introducing different `unitCell` linear thermal expansion coefficients $\alpha_j(T_j)$ for the j^{th} subsystem.

2.5. X-Ray Diffraction

In order to probe transient lattice dynamics with atomic resolution, time-resolved XRD techniques have emerged as an appropriate method in experimental physics. The `UDKM1DSIM` toolbox provides methods to simulate the static and transient XRD response of crystalline sample structures. Due to the limitation to 1D sample structures only symmetrical X-ray diffraction in co-planar geometry is implemented. For the calculation of static XRD curves (rocking curves) for homogeneously strained layers two different theoretical approaches are provided: kinematical and dynamical XRD. In kinematical XRD theory (`XRDkin`) the incident X-ray beam is unaffected by the crystal, since absorption and multiple reflections are neglected.[12] In the `XRDkin` class no refraction correction has been implemented so far. However, the kinematical theory is a rather fast analytical approach for thin crystal layers, ideally imperfect mosaic crystals, and rocking curves at the wings of Bragg peaks. For high quality crystals, thick crystals, and rocking curves close to the maximum of strong Bragg peaks, so-called dynamical XRD theory (`XRDdyn`) should be considered.[8] Dynamical XRD theory accounts for absorption, refraction, scattering, and multiple reflections (extinction) of the incident beam. In comparison to kinematical theory, dynamical XRD is generally slower to calculate due to its complex matrix formalism. However, in order to calculate the transient XRD response of a 1D sample structure due to ultrafast lattice dynamics only dynamical theory is implemented in the `UDKM1DSIM` toolbox, since here its matrix formalism has no disadvantages against the kinematical theory in terms of computational time. Examples on the applications and limitations of the two models are given in the example file `XRDexample.m`.

For both theories the smallest scatterers in each structure are the individual atoms, whose scattering cross sections are given by the atomic form factor f . [8] Generally, these atomic form factors dependent on the energy E and scattering vector $q_z = 2k \sin(\theta)$ of the incident X-ray beam, where $k = 2\pi/\lambda$ is the X-ray wave number and θ is the incidence angle:[8]

$$f(q_z, E) = f_{CM}(q_z) + \delta f_1(E) - i f_2(E) . \quad (18)$$

The dispersion corrections $\delta f_1(E)$ and absorption correction $f_2(E)$ have been experimentally determined[13] whereas the angle-dependence $f_{CM}(q_z)$ is a theoretical correction from Hartree-Fock calculations.[14] The values of $f(q_z, E)$ are automatically loaded and calculated from the according parameter files by the `UDKM1DSIM` toolbox for each atom/ion for a given E and q_z and the reader may refer to the documentation of the `atomBase` class for further details. In order to account for the polarization of the X-rays one has to introduce a θ -dependent polarization factor $P(\theta)$ in kinematical and dynamical XRD calculations

given by:[8]

$$P(\theta) = \begin{cases} 1 & \text{s-polarized} \\ \cos(2\theta) & \text{p-polarized} \\ \frac{1+\cos(2\theta)}{2} & \text{unpolarized} \end{cases} \quad (19)$$

2.5.1. Kinematical XRD

For the calculation of rocking curves using kinematical theory one further introduces the structure factor of a unit cell

$$S(q_z, E, \epsilon) = \sum_i^N f_i e^{-i q_z z_i(\epsilon)} \quad (20)$$

The structure factor $S(q_z, E, \epsilon)$ is the summation of all atomic form factors $f_i(q_z, E)$ in a specific unit cell and also depends on the lattice strain ϵ by the position $z_i(\epsilon)$ of the individual atoms in the unit cell. From Ref. [12] one can now calculate the diffracted wave field amplitude at the detector from a single layer of similar unit cells as follows:

$$E_p = \frac{i}{\epsilon_0 m_e c_0^2} \frac{P(\theta) S(q_z, E, \epsilon)}{A q_z} \quad (21)$$

with e as electron charge, m_e as electron mass, c_0 as vacuum light velocity, ϵ_0 as vacuum permittivity, and A as area of the unit cell in the plane normal to q_z . For the case of N similar planes of unit cells one can then write:

$$E_p^N = \sum_{n=0}^{N-1} E_p e^{i q_z z n} \quad (22)$$

where z is the distance between the planes (c -axis of the unit cells). The above equation can be simplified to

$$E_p^N = E_p \psi(q_z, z, N) \quad (23)$$

introducing the interference function

$$\psi(q_z, z, N) = \sum_{n=0}^{N-1} e^{i q_z z n} = \frac{1 - e^{i q_z z N}}{1 - e^{i q_z z}} \quad (24)$$

The total reflected wave field E_p^t of all $i = 1 \dots M$ homogeneous layers is the summation of the individual wave fields $E_p^{N,i}$:

$$E_p^t = \sum_{i=1}^M E_p^{N,i} e^{i q_z Z_i} \quad (25)$$

where $Z_i = \sum_{j=1}^{i-1} (N_j z_j)$ is the distance of the i^{th} layer from the surface. Finally, the actual reflectivity of the sample structure is calculated by $R = E_p^t (E_p^t)^*$.

In order to obtain the static kinematical rocking curve of a given sample structure s one can follow the code listing below:

```
% set the simulation parameters
E = 8047*u.eV; % X-ray energy
pol = 0.5; % mixed X-ray polarization
```

```
theta = (22:0.001:24)*u.deg; % angular range
% initialization of XRDkin simulation
K = XRDkin(S,forceRecalc,E,pol);
% set the qz-range by a theta-vector
K.setQzByTheta(theta);
% calculate the static rocking curve:
Rs = K.homogeneousReflectivity();
```

2.5.2. Dynamical XRD

In dynamical XRD theory a complex matrix formalism is applied to calculate the reflection and transmission of X-rays by individual atomic layers forming the sample structure.[8] The basic building blocks for this formalism are the reflection-transmission matrices of the atomic planes

$$H = \frac{1}{\tau} \begin{pmatrix} (\tau^2 - \rho^2) & \rho \\ -\rho & 1 \end{pmatrix} \quad (26)$$

and propagation matrices

$$L = \begin{pmatrix} \exp(i\phi) & 0 \\ 0 & \exp(-i\phi) \end{pmatrix} \quad (27)$$

The matrix elements are defined as follows:

$$\rho = -i \frac{4 \pi r_e f(q_z, E) P(\theta) e^{-M}}{q_z A} \quad (28)$$

$$\tau = 1 - i \frac{4 \pi r_e f(0, E) e^{-M}}{q_z A} \quad (29)$$

$$\phi = \frac{q_z d}{2} \quad (30)$$

where r_e is the classical electron radius, $M = (\text{dbf } q_z)^2/2$ with $\text{dbf}^2 = \langle u^2 \rangle$ as average thermal vibration of the atoms (Debye-Waller factor), and d is the distance between two layers of scattering objects.

In order to obtain the final reflectivity of the sample structure one has to carry out the according matrix multiplications of the H and L matrices. The reflectivity-transmission matrix (RTM) of a single unit cell M_{RT} is calculated from the individual H_i of each atom and the propagation matrices between the atoms L_i :

$$M_{RT} = \prod_i H_i L_i \quad (31)$$

For N identical layers of unit cells one can calculate the N^{th} power of the unit cell's RTM $(M_{RT})^N$ instead of carrying out N matrix multiplications in order to save computational time. The RTM for the homogeneous sample $M_{RT}^{\text{hom,tot}}$ consisting of K homogeneous substructures then becomes:

$$M_{RT}^{\text{hom,tot}} = \prod_{k=1}^K (M_{RT}^{(k)})^{N_k} \quad (32)$$

For the case of an inhomogeneously strained sample one has to carry out the matrix multiplication for each individually strained unit cell. Thus, the RTM of the inhomogeneous sample $M_{RT}^{\text{inhom,tot}}$ containing $m = 1 \dots M$

unit cells is calculated by:

$$M_{RT}^{\text{inhom,tot}} = \prod_{m=1}^M M_{RT}^{(m)}, \quad (33)$$

which is a rather expensive calculation since it has to be carried out for all differently strained types of unit cells, for all θ or q_z , and for all time steps. The final reflectivity R of the sample is the calculated from the matrix elements of the 2×2 RTM matrix as follows:

$$R = \left| M_{RT(1,2)}^{\text{tot}} / M_{RT(2,2)}^{\text{tot}} \right|^2. \quad (34)$$

In the following code listing we refer again to the results of the `heat` and `phonon` simulations for the given sample structure S introduced above. For the static case the syntax for kinematical and dynamical XRD is similar. However, the simulation of UXRD from transient lattice dynamics which inevitable involves inhomogeneously strained layers is only implemented in the `XRDdyn` class.

```
% initialization of XRDkin simulation
D = XRDdyn(S,forceRecalc,E,pol);
% set the qz-range by a theta-vector
D.setQzByTheta(theta);
% calculate the static rocking curve in 1 line
Rh = D.homogeneousReflectivity();
% calculate a reduced number of strains per unique
% unit cell in order to save computational time
strainVectors = ...
    P.getReducedStrainsPerUniqueUnitCell(strainMap);
% calculate the transient XRD:
R = D.getInhomogeneousReflectivity(...
    strainMap,strainVectors);
```

2.5.3. Parallel Computing

As mentioned before, the calculation of the transient XRD result is very expensive in computational time, since heavy matrix multiplications for all individually strained unit cells in the sample, for all angles θ and time steps have to be carried out. In order to speed up this calculations the `UDKM1DSIM` toolbox uses MATLAB's parallel computing capabilities. The `Parallel Computing Toolbox` has to be installed to enable this feature. In this parallel mode the dynamical XRD results for the individual time steps are calculated parallel, e.g. on a multi-core system or computer-cluster², since the results at different angles and time steps are independent. The user can individually decide how to calculate the inhomogeneous reflectivity by adding a third input parameter `type` to the function call. The value of the `type` parameter can be `'parallel'` (default), `'distributed'`, or `'sequential'`, whereas the latter case does not require additional licenses for the MATLAB Parallel or Distributed Computing Toolbox:

²Cluster calculations require a MATLAB Distributed Computing Server license.

```
type = 'sequential';
R = D.getInhomogeneousReflectivity(...
    strainMap,strainVectors,type);
```

3. Examples

In this section we want to provide physical examples for the application of the `UDKM1DSIM` toolbox. The complete example code can be found in the `./examples/` folder.

3.1. Bragg-Peak Splitting Evidences Inhomogeneous Expansion

Here we consider a 95 nm metallic SRO thin film on a dielectric STO substrate which is photoexcited by an ultrashort laser pulse. The excitation is modeled as instantaneous temperature jump and we further neglect heat diffusion. The temperature change at $t = 0$ is shown in Fig. 1 a) and features an exponential decay in the absorbing SRO layer in accordance with Eq. 1. Subsequent coherent phonon dynamics are calculated by the `phononNum` class and the resulting spatio-temporal strain profile is depicted in Fig. 1 b).

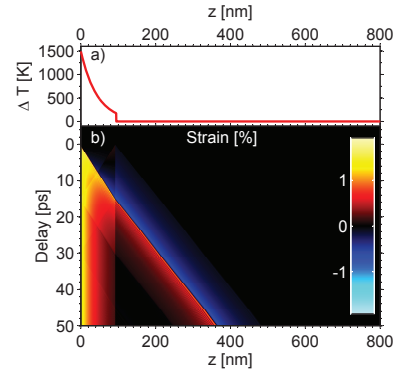


Figure 1: (Color online) a) Temperature change in the SRO thin film after excitation at $t = 0$. b) Spatio-temporal strain profile due to optical excitation of the SRO film. The SRO/STO interface is at $z = 95$ nm.

Using the result of the `phononNum` simulation as input for the dynamical XRD calculations (`XRDdyn`) we obtain the UXRD response of the ultrafast excitation of the SRO layer which is shown in Fig. 2 as a waterfall plot. Here, the SRO Bragg peak splits up due to the excited lattice dynamics and does not continuously shift. Details for this example simulation and comparison to experimental data can be found in Ref. [15].

3.2. Superlattice Oscillations

In this example a superlattice (SL) structure is excited by an ultrashort laser pulse. The SL consists of 11 double layers (DL) each of which is composed of 20 unit cells

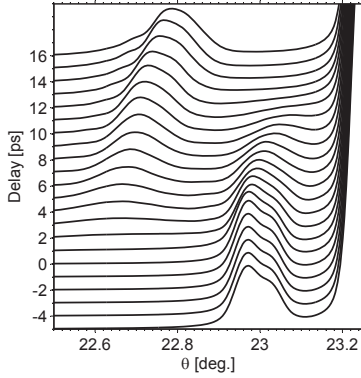


Figure 2: Waterfall plot of the SRO Bragg peak reflectivity for different delays after excitation of the thin film. The SRO peak splits up into two peaks instead of continuously shifting into its new position.

of SRO and 38 unit cells of STO. The SL is grown on an STO substrate. The excitation is again modeled as instantaneous temperature jump at $t = 0$ neglecting thermal transport. The temperature profile after excitation is shown in Fig. 3 a). The comb-like temperature profile originates from the alternating metallic and dielectric layers in the SL and exhibits an exponential decay towards the substrate. Due to the excitation profile, a longitudinal optical SL phonon mode, also known as zone-folded longitudinal acoustic phonon (ZFLAP), is excited which results in the complex spatio-temporal strain pattern shown in Fig. 3 b). Here, the strain oscillation directly indicates the frequency of the optical phonon mode.

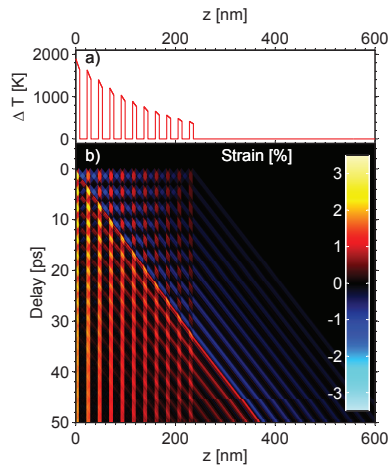


Figure 3: (Color online) a) Temperature change in the SL after excitation at $t = 0$. b) Spatio-temporal strain profile due to optical excitation of the SL film. The SL/Substrate interface is at $z = 235$ nm.

The SL structure also results in complex static XRD signatures as can be seen in Fig. 4. This static rocking curve is calculated by the `XRDdyn` class which allows to access also the individual rocking curves of the repeated substructures. The equidistant Bragg peaks originate from the SL structure and are numerated as SLi . The most intense Bragg peak is the STO substrate reflection.

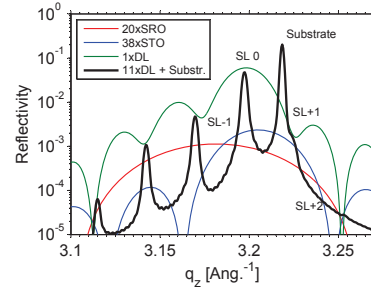


Figure 4: (Color online) The static rocking curve of the sample structure is convoluted with a Pseudo-Voigt function in order to account for instrumental broadening. The Bragg peaks of the SL are numerated as SLi . The colored lines represent the rocking curves of the nested substructures in the sample.

The transient X-Ray diffraction calculations using the coherent phonon result as input feature intensity oscillations of the SL Bragg peaks due to the excited longitudinal optical SL phonon. The integrated intensities of the $SL0$ and $SL+2$ Bragg peaks are plotted as transients in Fig. 5. For the $SL+2$ peak a non-linear X-ray response is observed. Details on this simulation and a comparison to UXRD experiments are given in Ref. [16].

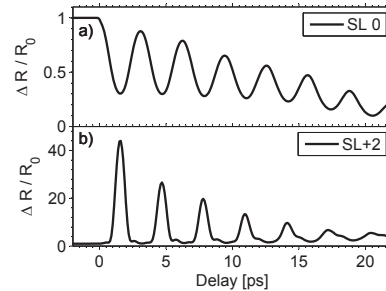


Figure 5: The integrated intensity modulation of the $SL0$ and $SL+2$ Bragg peak are plotted over the pump-probe delay. The X-ray response of the $SL+2$ shows even non-linear behavior.

3.3. Quasi-Monochromatic Phonon Wave Packet

In the last example a thin 15 nm SRO layer on an STO substrate is excited by a pulse sequence of 8 ultra-short laser pulses with a pulse separation of 7.2 ps in order to generate a coherent quasi-monochromatic phonon wave packet in the substrate. The average temperature

in the SRO layer is plotted in inset of Fig. 6, where the excitation is again modeled as instantaneous temperature jump without heat diffusion. The corresponding transient strain pattern is calculated by the `phononNum` class including damping in the STO substrate. The waterfall plot in Fig. 6 shows the subsequent generation of bi-polar strain pulses in the substrate after each laser excitation.

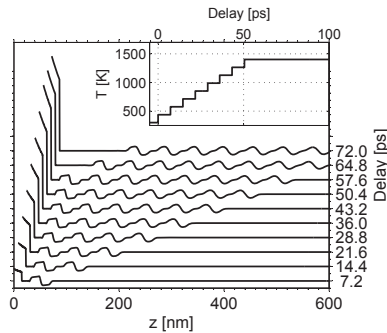


Figure 6: The strain profile for different pump-probe delays are plotted as waterfall diagram. For better visualization, the graphs are also shift along the x -axis. The amplitude of the thermal strain in the SRO layer has a maximum of approx. 1 % and the amplitude of the phonon wave packet is approx. 0.05 %. The inset shows the average temperature in the SRO layer due to the multipulse excitation of the sample.

From this strain pattern we can compute the according transient X-ray reflectivity using the `XRDdyn` class. Fig. 7 depicts the side bands of the STO substrate Bragg reflection for different pump-probe delays. The rise of the first-order side band at $q_z = 3.229 \text{ \AA}^{-1}$ and a second-order side band at $q_z = 3.240 \text{ \AA}^{-1}$ become stronger after each excitation of the sample. Details on this simulation and comparison to experimental data can be found in Ref. [17] and [18].

4. Conclusions

The `UDKM1DSIM` toolbox enables the user to easily build 1D crystalline structures on the atomic-level using a rich database of element-specific physical parameters. The excitation and thermal transport in such 1D structures is calculated within the frame of an N -temperature model. The results are then plugged into an analytical or numerical model for evaluating the dynamics of coherent longitudinal acoustic phonon in the structure. Kinematical and dynamical XRD theory are provided to further calculate the static rocking curves of the structures for symmetrical Bragg reflections in coplanar diffraction geometry. The transient XRD response of the structures due to coherent phonon dynamics is evaluated exclusively by dynamical XRD theory.

The `UDKM1DSIM` toolbox is programmed fully object-orientated and highly modular in order to allow for user-defined inputs at any step of the simulation procedure.

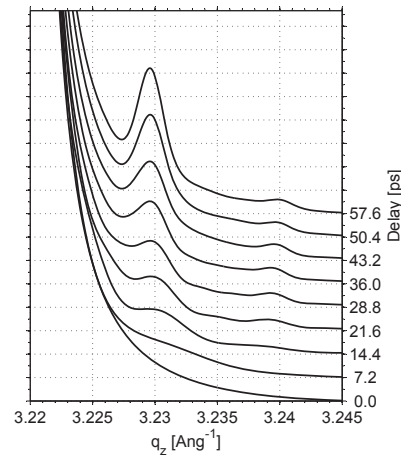


Figure 7: The side bands of the STO substrate Bragg peak are plotted for different pump-probe delays as waterfall diagram. The rise of the 1st order side band at $q_z = 3.229 \text{ \AA}^{-1}$ and even a second order at $q_z = 3.240 \text{ \AA}^{-1}$ of the excited phonon wave packet becomes stronger after each pump event.

Hence the toolbox is not only applicable for the comparison of experimental UXRD data to the introduced theoretical models but also as an educational/theoretical test ground for students and researchers in the scientific field of ultrafast structural dynamics and ultrafast XRD.

- [1] C. Rose-Petruck, R. Jimenez, T. Guo, A. Cavalleri, C. W. Siders, F. Rksi, J. A. Squier, B. C. Walker, K. R. Wilson, C. P. J. Barty, Picosecond-milliångström lattice dynamics measured by ultrafast X-ray diffraction, *Nature* 398 (6725) (1999) 310–312. doi:10.1038/18631.
- [2] K. Sokolowski-Tinten, C. Blome, J. Blums, A. Cavalleri, C. Di- etrich, A. Tarasevitch, I. Uschmann, E. Förster, M. Kamm- ler, M. Horn-von Hoegen, D. von der Linde, Femtosecond X-ray measurement of coherent lattice vibrations near the Lindemann stability limit., *Nature* 422 (6929) (2003) 287–9. doi:10.1038/nature01490.
- [3] M. Bargheer, N. Zhavoronkov, Y. Gritsai, J. C. Woo, D. S. Kim, M. Woerner, T. Elsaesser, Coherent atomic motions in a nanostructure studied by femtosecond X-ray diffraction., *Science* 306 (5702) (2004) 1771–3. doi:10.1126/science.1104739.
- [4] C. Korff Schmising, M. Bargheer, M. Kiel, N. Zhavoronkov, M. Woerner, T. Elsaesser, I. Vrejoiu, D. Hesse, M. Alexe, Cou- pled Ultrafast Lattice and Polarization Dynamics in Ferroelectric Nanolayers, *Physical Review Letters* 98 (25) (2007) 257601. doi:10.1103/PhysRevLett.98.257601.
- [5] I. A. Veres, T. Berer, P. Burgholzer, Numerical modeling of thermoelastic generation of ultrasound by laser irradiation in the coupled thermoelasticity., *Ultrasonics* 53 (1) (2013) 141–149. doi:10.1016/j.ultras.2012.05.001.
- [6] D. Y. Tzou, J. K. Chen, J. E. Beraun, Recent Development of Ultrafast Thermoelasticity, *Journal of Thermal Stresses* 28 (6-7) (2005) 563–594. doi:10.1080/01495730590929359.
- [7] S. Stepanov, E. Kondrashkina, R. Köhler, D. Novikov, G. Materlik, S. Durbin, Dynamical x-ray diffraction of mul- tilayers and superlattices: Recursion matrix extension to grazing angles, *Physical Review B* 57 (8) (1998) 4829–4841. doi:10.1103/PhysRevB.57.4829.
- [8] J. Als-Nielsen, D. McMorrow, *Elements of Modern X-Ray Physics*, John Wiley & Sons, Ltd., New York, 2001. doi:10.1002/9781119998365.

-
- [9] S. I. Anisimov, B. Kapeliovich, T. Perel'man, Electron emission from metal surfaces exposed to ultrashort laser pulses, *Sov. Phys. JETP* 39 (2) (1975) 375–377.
- [10] M. Herzog, D. Schick, P. Gaal, R. Shayduk, C. von Korff Schmising, M. Bargheer, Analysis of ultrafast X-ray diffraction data in a linear-chain model of the lattice dynamics, *Applied Physics A* 106 (3) (2011) 489–499. doi:10.1007/s00339-011-6719-z.
- [11] A. Bojahr, M. Herzog, D. Schick, I. Vrejoiu, M. Bargheer, Calibrated real-time detection of nonlinearly propagating strain waves, *Physical Review B* 86 (14) (2012) 144306. doi:10.1103/PhysRevB.86.144306.
- [12] B. E. Warren, X-ray diffraction, 2nd Edition, Dover Publications, New York, 1990.
- [13] B. Henke, E. Gullikson, J. Davis, X-Ray Interactions: Photoabsorption, Scattering, Transmission, and Reflection at $E = 50\text{--}30,000$ eV, $Z = 1\text{--}92$, Atomic Data and Nuclear Data Tables 54 (2) (1993) 181–342. doi:10.1006/adnd.1993.1013.
- [14] D. T. Cromer, J. B. Mann, X-ray scattering factors computed from numerical HartreeFock wave functions, *Acta Crystallographica Section A* 24 (2) (1968) 321–324. doi:10.1107/S0567739468000550.
- [15] D. Schick, P. Gaal, A. Bojahr, W. Leitenberger, R. Shayduk, A. Hertwig, I. Vrejoiu, M. Herzog, M. Bargheer, Ultrafast x-ray diffraction studies of photoexcited coherent phonons in SrRuO₃ thin films, Submitted.
- [16] M. Herzog, D. Schick, W. Leitenberger, R. Shayduk, R. M. van der Veen, C. J. Milne, S. L. Johnson, I. Vrejoiu, M. Bargheer, Tailoring interference and nonlinear manipulation of femtosecond x-rays, *New Journal of Physics* 14 (1) (2012) 13004. doi:10.1088/1367-2630/14/1/013004.
- [17] M. Herzog, A. Bojahr, J. Goldshteyn, W. Leitenberger, I. Vrejoiu, D. Khakhulin, M. Wulff, R. Shayduk, P. Gaal, M. Bargheer, Detecting optically synthesized quasimonochromatic sub-terahertz phonon wavepackets by ultrafast x-ray diffraction, *Applied Physics Letters* 100 (9) (2012) 94101. doi:10.1063/1.3688492.
- [18] A. Bojahr, M. Herzog, S. Mitzscherling, L. Maerten, D. Schick, W. Leitenberger, R. Shayduk, P. Gaal, M. Bargheer, Brillouin scattering of visible and hard X-ray photons from optically synthesized phonon wavepackets, *Opt. Lett.* submitted.

Paper VII

Localized excited charge carriers generate ultrafast inhomogeneous strain in the multiferroic BiFeO₃

D. Schick, M. Herzog, H. Wen, P. Chen, C. Adamo, P. Gaal, D. G. Schlom, P. G. Evans, Y. Li, and M. Bargheer

Phys. Rev. Lett. under review, (2013)

Localized excited charge carriers generate ultrafast inhomogeneous strain in the multiferroic BiFeO₃

Daniel Schick,¹ Marc Herzog,^{1,2} Haidan Wen,³ Pice Chen,⁴ Carolina Adamo,^{5,6} Peter Gaal,⁷ Darrell G. Schlom,^{5,8} Paul G. Evans,⁴ Yuelin Li,³ and Matias Bargheer^{1,7,*}

¹*Institut für Physik & Astronomie, Universität Potsdam, Karl-Liebknecht-Str. 24-25, 14476 Potsdam, Germany*

²*Abteilung Physikalische Chemie, Fritz-Haber-Institut der Max-Planck-Gesellschaft, Faradayweg 4-6, 14195 Berlin, Germany*

³*X-ray Science Division, Argonne National Laboratory, Argonne, Illinois 60439, USA*

⁴*Department of Materials Science and Engineering and Materials Science Program, University of Wisconsin-Madison, Madison, Wisconsin 53706, USA*

⁵*Department of Material Science and Engineering, Cornell University, Ithaca, New York 14853, USA*

⁶*Department of Applied Physics, Stanford University, Stanford, CA 94305-4045, USA*

⁷*Helmholtz-Zentrum Berlin für Materialien und Energie GmbH,*

Wilhelm-Conrad-Röntgen Campus, BESSY II, Albert-Einstein-Str. 15, 12489 Berlin, Germany

⁸*Kavli Institute at Cornell for Nanoscale Science, Ithaca, New York 14853, USA*

(Dated: August 1, 2013)

We apply ultrafast X-ray diffraction with femtosecond temporal resolution to monitor the lattice dynamics in a thin film of multiferroic BiFeO₃ after above-bandgap photoexcitation. The sound-velocity limited evolution of the observed lattice strains indicates a quasi-instantaneous photoinduced stress which decays on a nanosecond time scale. This stress exhibits an inhomogeneous spatial profile evidenced by the broadening of the Bragg peak. These new data require substantial modification of existing models of photogenerated stresses in BiFeO₃: the relevant excited charge carriers must remain localized to be consistent with the data.

Multiferroics have a great potential for application due to their possible coupling of ferroelectricity and magnetism [1–3]. BiFeO₃ (BFO) is one of the few room temperature multiferroics today [4–8] and of these the only one that is a stable phase. Its relatively small bandgap of approx. 2.7 eV [13] renders BFO an ideal candidate for applications in spintronics and memory devices [5] with a perspective for ultrafast optical switching similar to purely ferroelectric [14] or magnetic materials [15]. The photovoltaic effect in this complex material and the underlying ultrafast carrier dynamics after above-bandgap femtosecond (fs) optical excitation have been studied thoroughly [16–18]. All-optical experiments showed that the rapid photoinduced mechanical stress excites coherent phonons [22, 23]. The dynamics of photoinduced strains were directly and quantitatively measured in a recent synchrotron-based ultrafast X-ray diffraction (UXRD) study with a temporal resolution of 100 ps [24]. Combined optical measurements revealed a linear dependence of the transient strain and the number of excited carriers over several nanoseconds (ns). This led to the conclusion that depolarization field screening (DFS) including macroscopic transport of the carriers to the surface and interface could be the dominant stress generating process, although the effect of excited antibonding orbitals was not ruled out [24].

In this letter we report complementing UXRD experiments at a laser-driven plasma X-ray source (PXS) in order to monitor the coherent and incoherent lattice dynamics in a BFO thin film sample with subpicosecond (ps) temporal resolution after above-bandgap

excitation. We observe a sound-velocity limited evolution of the structural response within 10 ps indicating a quasi-instantaneous stress. The substantial Bragg peak broadening is a direct evidence of an inhomogeneous spatial strain profile. It appears quasi-instantaneously and decays on nanosecond time scales as reconfirmed by new synchrotron-based UXRD data recorded at the Advanced Photon Source (APS). We obtain quantitative agreement of the transient peak shift and broadening measured with both setups and can firmly conclude that the photogenerated stress driving the film expansion has a strongly inhomogeneous spatial profile in the 35 nm thick film. We rule out a dominant thermal contribution since the peak broadening after 1 ns is incompatible with the equilibration of temperature within a 35 nm thick film, irrespective of potential interface thermal resistance.

We propose a model of local charge carrier displacement within the BFO unit cells after above-bandgap excitation resulting in a lattice distortion possibly due to the inverse piezoelectric effect which drives the expansion instantaneously together with stress contributions resulting from the population of antibonding orbitals. Subsequent fast trapping of the excited charge carriers in the film maintains the stress according to the optical excitation profile over several ns until they decay radiatively [16]. Our experimental study provides an important benchmark for simulations of the photovoltaic response of ferroelectric oxide materials [25, 26], which will have to predict strongly inhomogeneous ultrafast and long lived charge carriers.

We investigate the very same sample which was stud-

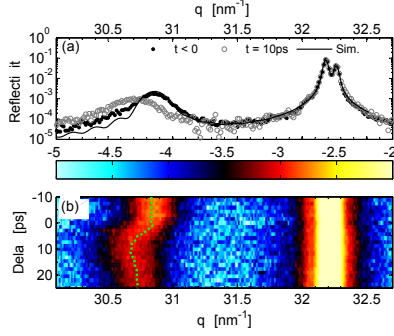


FIG. 1. (Color online) (a) Rocking curves of the 002 pseudocubic Bragg reflections from the BFO layer and STO substrate measured by the PXS. The solid black line is a simulation of the static rocking curve. (b) Measured transient rocking curves (diffracted intensity in logarithmic scale). The green dashed line indicates the extracted center of the BFO peak.

ied in Ref. 24. The sample is composed of a $d = 35$ nm thick pseudocubic (001) BFO film epitaxially grown on a (001) STO substrate. The ferroelectric polarization points along the [111] pseudocubic direction of BFO and exhibits a four-fold symmetry with most of the polarization pointing towards the surface [27]. The direct bandgap of this sample has been determined to 2.6 eV [24]. At the excitation wavelength of $\lambda = 400$ nm the optical penetration $\zeta = 32$ nm [30] determines the excitation profile following Lambert-Beer's law.

The UXRD setups at the PXS and the APS have been described elsewhere [31–33]. The PXS provides a temporal resolution below 200 fs at an X-ray photon energy of 8.047 keV (Cu K_{α}) and is operated in a convergence-correction mode [34]. The X-ray and UV footprints on the sample have diameters of approx. 300 μm and 1 mm (FWHM), respectively. The UV pump beam is p -polarized and incidents under 40° from the surface. The synchrotron based setup provides much higher stability for long term measurements in the ns range, while excitation and probing conditions are very similar [24].

Figure 1 (a) shows the static rocking curve of the 002 pseudocubic Bragg peaks of the BFO and STO substrate as measured by the PXS together with a transient rocking curve at $t = 10$ ps delay. The high crystalline quality of the film is evidenced by the the static rocking curve which coincides with the dynamical X-ray simulation for a $d = 35$ nm thick perfect BFO film on STO including the instrumental resolution. Figure 1 (b) shows the transient rocking curves for the early delays from -10 ps to 25 ps with the photoexcitation occurring at $t = 0$. The peak shift of the BFO 002 pseudocubic reflection measures the average out-of-plane strain (z -direction) in the layer: $-\Delta q_z(t) \propto \langle \epsilon(z, t) \rangle_z$. The observed shift to smaller q_z

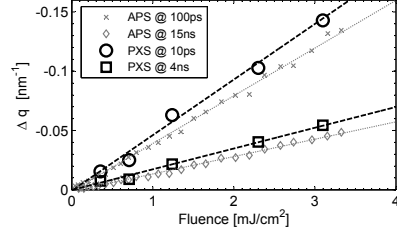


FIG. 2. Shift Δq_z of the 002 pseudocubic BFO Bragg peak measured as a function of fluence at different delays. The dashed and dotted lines represent linear fits.

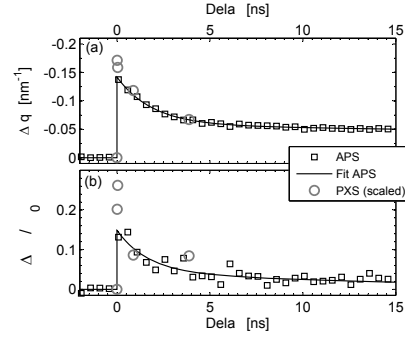


FIG. 3. The transient shift Δq_z (a) and the relative change of the width $\Delta w/w_0$ (b) of the 002 pseudocubic BFO Bragg peak. The APS data was measured at an excitation fluence of $F = 3.47$ mJ/cm² and the PXS data was scaled according to the fluence calibration. The black solid line represents an exponential fit of the APS data.

corresponds to an ultrafast expansion $\Delta c/c \approx 5 \times 10^{-3}$ of the BFO film along the surface normal without any contraction features which were observed for the ferroelectric material PbTiO_3 (PTO) [25].

Figure 2 shows the linear dependence of the transient peak shift on the absorbed fluence for selected delays ranging from $t = 0.01$ ns to 15 ns and confirms that data from the PXS and APS setups quantitatively agree within a reasonable 50 % recalibration of fluences between the two laboratories. The linear fluence dependence suggests that the origin of stress is the same for early (ps) and late (ns) delays.

The transient BFO peak shift and width are plotted in Fig. 3. The smaller peak shift of the APS data within the first 50 ps originates from the limited temporal resolution (100 ps) of the synchrotron-based experiments. The decay of the shift is fitted by an exponential function with a time constant ($\tau_{\text{decay}}^{\text{shift}} \approx 2.29 \pm 0.14$ ns).

The width w inversely depends on the number of scattering atomic layers (size broadening) and on the inhomogeneous strain-fields within the film (strain-broadening)

[36, 37]. We can neglect mosaic-broadening for the high-quality BFO film [38] and for the synchrotron-based APS experiments instrumental broadening is negligible, too.

Although the link of the peak profile to the spatial strain profile is non-trivial, we can assume that the change of the width Δw depends linearly on the variation $\Delta\epsilon(z, t)$ of the strain: $\Delta w(t) \propto \Delta\epsilon(z, t)$. If the layer is homogeneously strained ($\Delta\epsilon = 0$) no additional peak broadening is observed ($\Delta w = 0$). The transient width Δw reveals a significant inhomogeneous strain profile in the BFO layer over the whole observed time scale. The exponential fit in Fig. 3 (b) results in comparable decay times for the width and shift: $\tau_{\text{decay}}^{\text{width}} \approx 2.31 \pm 0.92$ ns. This directly indicates that the spatial strain profile does not equilibrate within the thermal relaxation time $\tau_{\text{th}} = d^2 \rho c / \kappa = 850$ ps of the $d = 35$ nm thick BFO layer [39].

For delays $t \gg 20$ ps larger than the time it takes strain waves to travel twice through the thin film at the speed of longitudinal sound $v_{\text{BFO}} = 3.5$ nm/ps [23], the observed shift Δq_z is not only proportional to the average strain but also to the transient stress according Hook's law $\Delta q_z \propto \epsilon(z, t) \propto \sigma(z, t)$. The similarity of the decay times for the shift and broadening moreover suggests that the transient stress $\sigma(z, t)$ can be approximated by a time-invariant spatial stress profile $f(z)$ that decays in amplitude $A(t)$, i.e. no transport processes are relevant to the driving stress: $\sigma(z, t) = A(t) \times f(z)$. We can then directly link the peak shift $\Delta q_z(t)$ to the amplitude $A(t)$ by: $\Delta q_z(t) \propto \langle \sigma(z, t) \rangle_z \propto A(t) \times \langle f(z) \rangle_z$, as well as the peak width by: $\Delta w(t) \propto A(t) \times \Delta f(z)$.

To elucidate the origin of the photoinduced stress at very early delays ($t \leq 20$ ps), where the stresses cannot be calculated via Hook's law, we simulate the BFO peak shift from a 1D lattice dynamics simulation [40, 41] of the strain profile $\epsilon(z, t)$ for the given stress

$$\sigma(z, t) \propto A(t) \times f(z) = H(t) \left(1 - \gamma e^{-t/\tau_{\text{rise}}} \right) \times e^{-z/\zeta}.$$

We explicitly use the optical penetration depth $\zeta = 32$ nm and assume a time-dependent rise $A(t)$ of the stress which includes a quasi-instantaneous stress approximated by the Heaviside step function $H(t)$ and an additional stress component growing with the time constant τ_{rise} . The transient stress is plotted in Fig. 4 (a) for several relative strengths γ of the instantaneous and delayed stress components [42]. We apply dynamical X-ray theory to calculate the according rocking curves from the simulated $\epsilon(z, t)$ in order to extract the transient peak shift. We clearly obtain the best fit to the experimental peak shift for $\gamma = 0$. In the examples shown in Fig. 4 we used the timescale $\tau_{\text{rise}} = 2$ ps, however, we have cross-checked this statement with additional simulations using longer timescales τ_{rise} for the delayed stress and also for different spatial stress profiles. In essence this proves that the dominant contribution to the stress is instantaneous

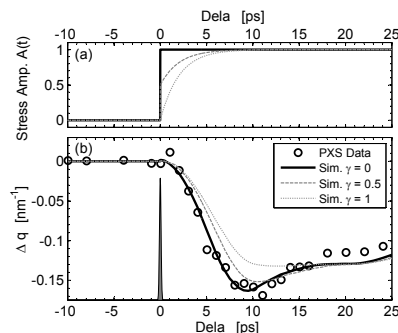


FIG. 4. The black circles in (b) show the transient shift of the 002 pseudocubic BFO Bragg peak extracted from the data shown in Fig. 1 (b). The black solid line represent the simulated peak shift for an instantaneous stress. The simulated peak shift for a semi-instantaneous stress (gray dashed line) and a fully diffusive-like stress (gray dotted line) both with a time constant $\tau_{\text{rise}} = 2$ ps, see text. The corresponding stress amplitudes $A(t)$ are plotted in panel (a). The gray Gaussian at $t = 0$ in panel (b) indicates the temporal resolution of 200 fs of the PXS setup.

and spatially inhomogeneous.

We want to emphasize the importance of several key parameters entering the simulation:

- i. The temporal overlap of X-ray probe and UV pump pulses ($t = 0$) was determined independently with an accuracy of approx. ± 100 fs [35].
- ii. The film thickness was determined experimentally by XRD measurements to $d = 35$ nm.
- iii. We determined the longitudinal acoustic sound velocity $v_{\text{BFO}} = 3.5$ nm/ps independently by an oscillation of the layer thickness after photoexcitation [42] (not shown) with good agreement to literature values [23].

The DFS model proposed as origin of the fast lattice expansion in BFO [24] and in ferroelectric PTO [25] requires free charge carriers to travel from within the bulk material to the interfaces of the layer to screen the depolarization fields. The ferroelectric polarization increases while the carriers drift with velocity v_d . The inverse piezoelectric effect would thus yield a finite stress rise time τ_c which is required for the carriers to propagate across the film. The typical charge carrier mobility in ferroelectrics is between $\mu = 0.1 - 3.0$ cm^2/Vs [43] and typical internal electric fields are in the range of $E \approx 200$ kV/cm [9]. Even for a high charge carrier mobility of $\mu < 3$ cm^2/Vs this leads to $\tau_c = d/\mu E > 5$ ps for the BFO sample which contradicts the quasi-instantaneous stress that is required to drive the ultrafast lattice dynamics, c.f. Fig. 4. We would further expect a spatially homogeneous stress profile from the DFS model due to the capacitor-like geometry in the film, which is incompatible with the significant long-lived peak

broadening shown in Fig. 3 (b). We conclude that the depolarization field screening due to diffusion of charge carriers cannot be a dominant process in BFO.

Unfortunately, the fluence dependent study (Fig. 2) cannot differentiate between alternative stress mechanisms, since all of them essentially depend linearly on the fluence. In the DFS model this is only true for low fluence, since the process saturates when the depolarization field is fully screened [44]. For PTO [25] the saturation occurs at excitation fluences of approx. 1 mJ/cm^2 . In our experiment the strain in BFO remains linear up to fluences of more than 4 mJ/cm^2 (Fig. 2) with comparable strain levels. At even higher fluences the BFO film starts to degrade. Since only a very small number of the excited carriers is sufficient to drive the stress in the DFS model [24], the absence of strain saturation effect disfavors the DFS model as well.

The thermal contribution to the stress can be quantitatively estimated: The electrons in the BFO film exhibit an excess energy of approx. 0.5 eV in the conduction band when they are excited with 3.1 eV photons. This excess energy is transferred rapidly to the lattice via electron-phonon coupling within 1 ps [16, 24] resulting in a fast temperature increase of the lattice. We calculate this temperature jump as $\Delta T = 44 \text{ K}$ averaged over the BFO film thickness for an excitation fluence of $F = 3.47 \text{ mJ/cm}^2$ taking into account the internal refraction of the pump light in the BFO layer. This corresponds to a maximum thermal strain of $\epsilon = 44 \text{ K} \times 1.84 \times 10^{-5} \text{ K}^{-1} = 0.8 \times 10^{-3}$ which accounts only for a small fraction of the peak shift [Fig. 3 (a)]. A numerical simulation [41] of the heat diffusion assuming bulk values [24] yields the timescale 5 ns for reducing the average BFO temperature rise to 6 K . Even the artificial introduction of very large thermal interface resistance [45] keeping the heat in the BFO layer would only explain about half of the observed shift for $t > 10 \text{ ns}$. More importantly the long-lasting peak broadening shows that a different mechanism must be in action.

The dominant mechanism right after excitation which is still important after 10 ns must be driven by a strongly inhomogeneous charge carrier distribution in the 35 nm thin film. After excitation electrons may occupy antibonding orbitals driving an expansion of the film. Since the charge distribution in the excited orbitals is different, this shift of electron density on a unit cell length scale will influence the local ferroelectric polarization and trigger stress via the inverse piezoelectric effect. The subtle distinction between the two processes can currently be given by theory and experiments reported in the literature corroborating our suggestion: UV pump pulses generate p - d charge transfer (CT) excitonic states in BFO [16, 46]. The strong absorption edge smearing of the 2.6 – 2.8 eV band [30, 47] and an additional weak 2.4 eV band superimposed on its tail, measured by static spectroscopy, point to a CT instability as well as self-trapping of p - d CT

excitons and the nucleation of electron-hole droplets [46]. The ultrafast CT after UV excitation strongly affects the local ferroelectric polarization [46] as evidenced by THz emission [19, 20] and leads to a quasi-instantaneous piezoelectric stress in the BFO unit cells. Due to the rapid trapping of the CT excitonic states the initial spatial excitation profile is maintained and the temporal dependence of the lattice strains is solely determined by electronic recombination and not by additional diffusion processes. Transient absorption data [24] and photoluminescence experiments [16] support this picture.

In conclusion, we applied UXRd experiments with sub-ps temporal resolution to monitor transient lattice dynamics in a multiferroic BFO thin film after above-bandgap photoexcitation. The peak shift reveals a rapid expansion that is only limited by the sound velocity, indicating a quasi-instantaneous photoinduced stress. The peak broadening indicates a strongly inhomogeneous spatial stress profile for ps up to ns delays, excluding thermal stresses as the dominant process. We propose a model of a local charge carrier displacement within the BFO unit cell after photoexcitation leading to an instantaneous stress due to the inverse piezoelectric effect. The fast trapping of the involved charge carriers maintains the spatial excitation profile until they decay radiatively on a ns time scale. We believe that this information is essential for testing theoretical models that can also predict the contribution of the deformation potential from antibonding orbital. The subtle distinction between these processes could in principle be given by more nontrivial UXRd experiments where an additional (e.g. electronic) control over the polarization is implemented.

The work at Argonne was supported by the U.S. Department of Energy, Office of Science, Office of Basic Energy Sciences, under Contract No. DE-AC02-06CH11357. Work at Cornell University was supported by the Army Research Office through Agreement No. W911NF-08-2-0032. We acknowledge the financial support for the work at Potsdam by the BMBF via grant No. 03WKP03A.

* bargheer@uni-potsdam.de; www.udkm.physik.uni-potsdam.de

- [1] W. Eerenstein, N. D. Mathur, and J. F. Scott, *Nature* **442**, 759 (2006).
- [2] R. Ramesh and N. A. Spaldin, *Nat. Mater.* **6**, 21 (2007).
- [3] L. W. Martin, S. P. Crane, Y.-H. Chu, M. B. Holcomb, M. Gajek, M. Huijben, C.-H. Yang, N. Balke, and R. Ramesh, *J. Phys.: Condens. Matter* **20**, 434220 (2008).
- [4] N. A. Hill, *J. Phys. Chem. B* **104**, 6694 (2000).
- [5] G. Catalan and J. F. Scott, *Adv. Mater.* **21**, 2463 (2009).
- [6] A. A. Belik, S. Iikubo, K. Kodama, N. Igawa, S.-i. Shamoto, S. Niitaka, M. Azuma, Y. Shimakawa, M. Takano, F. Izumi, and E. Takayama-Muromachi,

- Chem. Mater. **18**, 798 (2006).
- [7] M.-r. Li, U. Adem, S. R. C. McMitchell, Z. Xu, C. I. Thomas, J. E. Warren, D. V. Giap, H. Niu, X. Wan, R. G. Palgrave, F. Schiffrmann, F. Cora, B. Slater, T. L. Burnett, M. G. Cain, A. M. Abakumov, G. van Tendeloo, M. F. Thomas, M. J. Rosseinsky, and J. B. Claridge, *J. Am. Chem. Soc.* **134**, 3737 (2012).
- [8] W. Wang, J. Zhao, W. Wang, Z. Gai, N. Balke, M. Chi, H. N. Lee, W. Tian, L. Zhu, X. Cheng, D. J. Keavney, J. Yi, T. Z. Ward, P. C. Snijders, H. M. Christen, W. Wu, J. Shen, and X. Xu, *Phys. Rev. Lett.* **110**, 237601 (2013).
- [9] J. Wang, J. B. Neaton, H. Zheng, V. Nagarajan, S. B. Ogale, B. Liu, D. Viehland, V. Vaithyanathan, D. G. Schlom, U. V. Waghmare, N. A. Spaldin, K. M. Rabe, M. Wuttig, and R. Ramesh, *Science* **299**, 1719 (2003).
- [10] D. H. Kim, H. N. Lee, M. D. Biegalski, and H. M. Christen, *Appl. Phys. Lett.* **92**, 012911 (2008).
- [11] D. Lebeugle, D. Colson, A. Forget, M. Viret, a. M. Bataille, and A. Gukasov, *Phys. Rev. Lett.* **100**, 227602 (2008).
- [12] T. Zhao, A. Scholl, F. Zavaliche, K. Lee, M. Barry, A. Doran, M. P. Cruz, Y. H. Chu, C. Ederer, N. a. Spaldin, R. R. Das, D. M. Kim, S. H. Baek, C. B. Eom, and R. Ramesh, *Nat. Mater.* **5**, 823 (2006).
- [13] V. Železný, D. Chvostová, L. Pajasová, I. Vrejoiu, and M. Alexe, *Appl. Phys. A* **100**, 1217 (2010).
- [14] C. von Korff Schmising, M. Bargheer, M. Kiel, N. Zhavoronkov, M. Woerner, T. Elsaesser, I. Vrejoiu, D. Hesse, and M. Alexe, *Phys. Rev. Lett.* **98**, 257601 (2007).
- [15] C. Stanciu, F. Hansteen, A. Kimel, A. Kirilyuk, A. Tsukamoto, A. Itoh, and T. Rasing, *Phys. Rev. Lett.* **99**, 047601 (2007).
- [16] Y. M. Sheu, S. a. Trugman, Y.-S. Park, S. Lee, H. T. Yi, S.-W. Cheong, Q. X. Jia, a. J. Taylor, and R. P. Prasankumar, *Appl. Phys. Lett.* **100**, 242904 (2012).
- [17] T. Choi, S. Lee, Y. J. Choi, V. Kiryukhin, and S.-W. Cheong, *Science* **324**, 63 (2009).
- [18] S. Y. Yang, L. W. Martin, S. J. Byrnes, T. E. Conry, S. R. Basu, D. Paran, L. Reichertz, J. Ihlefeld, C. Adamo, A. Melville, Y.-H. Chu, C.-H. Yang, J. L. Musfeldt, D. G. Schlom, J. W. Ager, and R. Ramesh, *Appl. Phys. Lett.* **95**, 062909 (2009).
- [19] K. Takahashi, N. Kida, and M. Tonouchi, *Phys. Rev. Lett.* **96**, 117402 (2006).
- [20] D. S. Rana, I. Kawayama, K. Mavani, K. Takahashi, H. Murakami, and M. Tonouchi, *Adv. Mater.* **21**, 2881 (2009).
- [21] B. Kundys, M. Viret, D. Colson, and D. O. Kundys, *Nat. Mater.* **9**, 803 (2010).
- [22] L. Y. Chen, J. C. Yang, C. W. Luo, C. W. Laing, K. H. Wu, J.-Y. Lin, T. M. Uen, J. Y. Juang, Y. H. Chu, and T. Kobayashi, *Appl. Phys. Lett.* **101**, 041902 (2012).
- [23] P. Ruello, T. Pezeril, S. Avanesyan, G. Vaudel, V. Gusev, I. C. Infante, and B. Dkhil, *Appl. Phys. Lett.* **100**, 212906 (2012).
- [24] H. Wen, P. Chen, M. Cosgriff, D. Walko, J. Lee, C. Adamo, R. Schaller, J. Ihlefeld, E. Dufresne, D. Schlom, P. Evans, J. Freeland, and Y. Li, *Phys. Rev. Lett.* **110**, 037601 (2013).
- [25] D. Daranciang, M. Highland, H. Wen, S. Young, N. Brandt, H. Hwang, M. Vattilana, M. Nicoul, F. Quirin, J. Goodfellow, T. Qi, I. Grimberg, D. Fritz, M. Cammarata, D. Zhu, H. Lemke, D. Walko, E. Dufresne, Y. Li, J. Larsson, D. Reis, K. Sokolowski-Tinten, K. Nelson, A. Rappe, P. Fuooss, G. Stephenson, and A. Lindenberg, *Phys. Rev. Lett.* **108**, 087601 (2012).
- [26] S. M. Young and A. M. Rappe, *Phys. Rev. Lett.* **109**, 116601 (2012).
- [27] F. Johann, A. Morelli, D. Biggemann, M. Arredondo, and I. Vrejoiu, *Phys. Rev. B* **84**, 094105 (2011).
- [28] J. F. Ihlefeld, N. J. Podraza, Z. K. Liu, R. C. Rai, X. Xu, T. Heeg, Y. B. Chen, J. Li, R. W. Collins, J. L. Musfeldt, X. Q. Pan, J. Schubert, R. Ramesh, and D. G. Schlom, *Appl. Phys. Lett.* **92**, 142908 (2008).
- [29] A. Kumar, R. C. Rai, N. J. Podraza, S. Denev, M. Ramirez, Y.-H. Chu, L. W. Martin, J. Ihlefeld, T. Heeg, J. Schubert, D. G. Schlom, J. Orenstein, R. Ramesh, R. W. Collins, J. L. Musfeldt, and V. Gopalan, *Appl. Phys. Lett.* **92**, 121915 (2008).
- [30] S. R. Basu, L. W. Martin, Y. H. Chu, M. Gajek, R. Ramesh, R. C. Rai, X. Xu, and J. L. Musfeldt, *Appl. Phys. Lett.* **92**, 091905 (2008).
- [31] F. Zamponi, Z. Ansari, C. von Korff Schmising, P. Rothhardt, N. Zhavoronkov, M. Woerner, T. Elsaesser, M. Bargheer, T. Trobitzsch-Ryll, and M. Haschke, *Appl. Phys. A* **96**, 51 (2009).
- [32] D. Schick, A. Bojahr, M. Herzog, C. von Korff Schmising, R. Shayduk, W. Leitenberger, P. Gaal, and M. Bargheer, *Rev. Sci. Instrum.* **83**, 25104 (2012).
- [33] E. M. Dufresne, B. Adams, M. Chollet, R. Harder, Y. Li, H. Wen, S. J. Leake, L. Beitra, X. Huang, and I. K. Robinson, *Nucl. Instrum. Meth. A* **649**, 191 (2011).
- [34] D. Schick, R. Shayduk, A. Bojahr, M. Herzog, C. von Korff Schmising, and M. Bargheer, *J. Appl. Cryst.* **accepted** (2013).
- [35] A. Bojahr, D. Schick, L. Maerten, M. Herzog, I. Vrejoiu, C. von Korff Schmising, C. J. Milne, S. L. Johnson, and M. Bargheer, *Phys. Rev. B* **85**, 224302 (2012).
- [36] B. E. Warren and B. L. Averbach, *J. Appl. Phys.* **21**, 595 (1950).
- [37] G. Williamson and W. Hall, *Acta Metall. Mater.* **1**, 22 (1953).
- [38] D. Schick, A. Bojahr, M. Herzog, P. Gaal, I. Vrejoiu, and M. Bargheer, *Phys. Rev. Lett.* **110**, 095502 (2013).
- [39] Thermal conductivity $\kappa_{\text{BFO}} = 3 \text{ W}/(\text{mK})$, density $\rho_{\text{BFO}} = 8.34 \text{ g}/\text{cm}^3$, specific heat $c_{\text{BFO}} = 0.3 \text{ J}/(\text{gK})$. Values taken from the supplement of Ref. 24.
- [40] M. Herzog, D. Schick, P. Gaal, R. Shayduk, C. von Korff Schmising, and M. Bargheer, *Appl. Phys. A* **106**, 489 (2011).
- [41] D. Schick, A. Bojahr, M. Herzog, C. von Korff Schmising, R. Shayduk, and M. Bargheer, *Comput. Phys. Commun.* **under review**, 1 (2013).
- [42] M. Nicoul, U. Shymanovich, A. Tarasevitch, D. von der Linde, and K. Sokolowski-Tinten, *Appl. Phys. Lett.* **98**, 191902 (2011).
- [43] J. F. Scott, *Science* **315**, 954 (2007).
- [44] J. T. Darrow, X.-C. Zhang, and D. H. Auston, *Appl. Phys. Lett.* **58**, 25 (1991).
- [45] D. a. Walko, Y.-M. Sheu, M. Trigo, and D. a. Reis, *J. Appl. Phys.* **110**, 102203 (2011).
- [46] R. Pisarev, A. Moskvin, A. Kalashnikova, and T. Rasing, *Phys. Rev. B* **79**, 235128 (2009).
- [47] A. J. Hauser, J. Zhang, L. Mier, R. a. Ricciardo, P. M. Woodward, T. L. Gustafson, L. J. Brillson, and F. Y. Yang, *Appl. Phys. Lett.* **92**, 222901 (2008).

Paper VIII

Following Strain-Induced Mosaicity Changes of Ferroelectric Thin Films by Ultrafast Reciprocal Space Mapping

D. Schick, A. Bojahr, M. Herzog, P. Gaal, I. Vrejoiu, and M. Bargheer

Phys. Rev. Lett. 110, 9 (2013)

Following Strain-Induced Mosaicity Changes of Ferroelectric Thin Films by Ultrafast Reciprocal Space Mapping

D. Schick,¹ A. Bojahr,¹ M. Herzog,¹ P. Gaal,² I. Vrejoiu,³ and M. Bargheer^{1,2,*}

¹*Institut für Physik und Astronomie, Universität Potsdam, Karl-Liebknecht-Straße 24-25, 14476 Potsdam, Germany*

²*Helmholtz-Zentrum Berlin für Materialien und Energie GmbH, Wilhelm-Conrad-Röntgen Campus, BESSY II, Albert-Einstein-Straße 15, 12489 Berlin, Germany*

³*Max-Planck-Institut für Mikrostrukturphysik, Weinberg 2, 06120 Halle, Germany*

(Received 24 October 2012; revised manuscript received 14 January 2013; published 26 February 2013)

We investigate coherent phonon propagation in a thin film of ferroelectric $\text{PbZr}_{0.2}\text{Ti}_{0.8}\text{O}_3$ (PZT) by ultrafast x-ray diffraction experiments, which are analyzed as time-resolved reciprocal space mapping in order to observe the in- and out-of-plane structural dynamics, simultaneously. The mosaic structure of the PZT leads to a coupling of the excited out-of-plane expansion to in-plane lattice dynamics on a picosecond time scale, which is not observed for out-of-plane compression.

DOI: 10.1103/PhysRevLett.110.095502

PACS numbers: 61.72.Hh, 07.85.Jy, 61.05.cp, 63.22.Np

Oxides are attractive constituents of future nanoelectronic devices because of their broad spectrum of outstanding physical properties, such as ferroelectricity and ferromagnetism, and owing to the progress made in the fabrication of high quality epitaxial heterostructures [1]. Epitaxial strain engineering and the careful choice of mechanical and electrical boundary conditions enable a direct influence on these functionalities [2–6]. Structural defects and nanoscale inhomogeneities, such as dislocations and domains, typically affect the properties of functional oxides and have been extensively studied by experiment and theory [7,8]. Ultrafast x-ray diffraction (UXRD) emerged as a powerful tool to observe lattice motion in real time [9–11] and has provided a deeper insight in the structure-property relations of functional oxides on ultrashort time scales. Recent femtosecond x-ray scattering experiments on ferroelectric oxides showed that electron screening induces an ultrafast piezoelectric response of the lattice [12] and that in turn, the deformation leads to a change of the polarization [13]. However, these experiments were conducted on rather perfect epitaxial crystals. The influence of nanodomains has been considered in experiments on transient phases [14], but the role of static structural defects remained unexplored on such an ultrafast time scale.

Here, we exemplify how ultrafast reciprocal space mapping (URSM) using a laser-based plasma x-ray source yields direct additional information on the reversible in-plane structure dynamics in a ferroelectric perovskite $\text{PbZr}_{0.2}\text{Ti}_{0.8}\text{O}_3$ (PZT) film which is solely induced by the existence of dislocations typical of such materials. In particular, the width of the PZT Bragg reflection reports that tensile out-of-plane strain leads to drastically increased damping. The energy dissipates into in-plane strain which is evidenced by the in-plane component of the reciprocal space map. Our results indicate that in mismatched epitaxial films of oxide materials, with their high

susceptibility to the formation of domains and dislocations, in-plane phenomena emerge on a hundred picosecond time scale. URSM yields the relevant information on lateral lattice dynamics in such materials in which nanoscale inhomogeneities inherently broaden the peaks in reciprocal space. It is important to realize that such inhomogeneities are a natural paradigm in oxides originating from competing phases with similar free energy rather than a result of imperfect crystal growth [7]. A better understanding of such time-domain effects in novel functional oxide materials will be important for studying the influence of structural defects on the ultrafast response of collective phenomena, such as piezoelectricity.

As a typical structure, we grew a ferroelectric layer of PZT and a metallic SrRuO_3 (SRO) electrode layer onto an SrTiO_3 (STO) substrate by pulsed laser deposition (PLD) [15]. The transmission electron micrograph (TEM) image [Fig. 1(a)] shows layer thicknesses of $d_{\text{PZT}} = 207$ nm and $d_{\text{SRO}} = 147$ nm, respectively. The average lattice

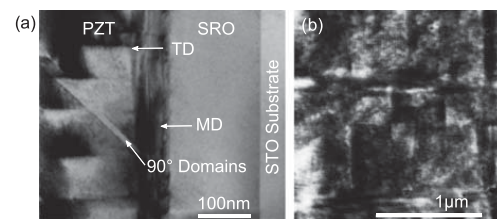


FIG. 1. TEM and AFM images of the PZT-SRO double layer grown onto an STO substrate by PLD. (a) The cross section TEM micrograph reveals that a minority of 90° a -domains are embedded in the matrix of the c -axis grown tetragonal PZT film, as proved by the AFM topography image in (b) as well. Misfit dislocations (MD) and threading dislocations (TD) formed at the SRO-PZT interface and across the PZT film account for the lateral inhomogeneity on a sub-100 nm length scale.

constants normal to the sample surface derived from static x-ray diffraction are $c_{\text{PZT}} = 4.130 \text{ \AA}$ and $c_{\text{SRO}} = 3.948 \text{ \AA}$. The TEM image [Fig. 1(a)] features only a few a -domains in the PZT layer, which are domains with a polarization vector pointing normal to the c -axis of the layer [15]. Accordingly, out-of-plane polarized domains are called c -domains. The small amount of a -domains is confirmed by the very weak scattering observed around 3.12 \AA^{-1} in the static and transient rocking curves in Figs. 2(a)–2(c). We neglect these ferroelastic domains and the switching between the 90° polarizations states in the further discussion. Due to stress relaxation in the mismatched epitaxial PZT film, misfit dislocations (MD) at the SRO interface

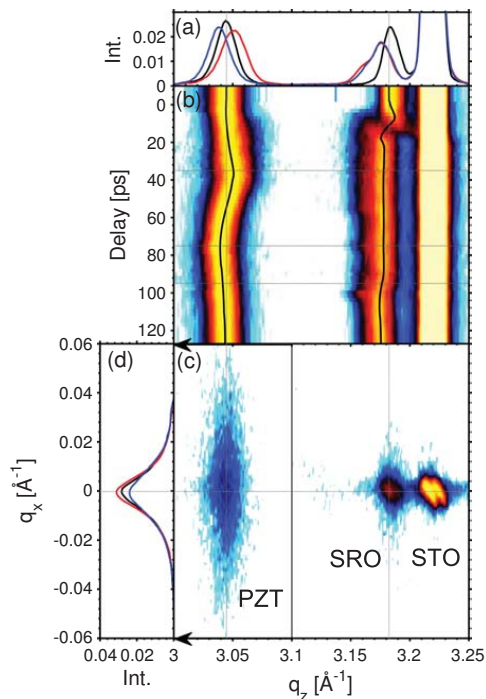


FIG. 2 (color). Transient x-ray diffraction measurements and static reciprocal space map of the PZT-SRO sample. (a) θ - 2θ scans of the structure around the (0 0 2) Bragg reflections of PZT, SRO, and STO before excitation (black) and at delays of maximum peak shift s_z of PZT, at $t = 35$ ps (red) and $t = 75$ ps (blue). (b) Transient θ - 2θ scans for continuous variation of $-10 < t < 125$ ps. The horizontal dashed lines indicate the delays of the selected plots shown in panels (a) and (d). The solid black lines indicate the center of the Bragg peaks. (c) The reciprocal space map of the PZT-SRO double layer sample before excitation features a rather broad PZT peak in q_x direction. All peaks widths suffer from an additional broadening due to the convergence and energy bandwidth of the incident x-rays. (d) Intensity of the PZT peak integrated over the q_z dimension before excitation (black) and at delays of change of peak width w_x of PZT, at $t = 35$ ps (red) and $t = 95$ ps (blue).

and threading dislocations (TD) expanding through the entire layer are visible in Fig. 1(a) [15]. As a result, lateral regions below 100 nm size are observable in PZT, whereas the SRO layer is free of such inhomogeneities. Nevertheless, the AFM topography in Fig. 1(b) reveals that the mean roughness of the PZT surface is below 2 \AA .

In order to characterize the response of the PZT film to ultrashort stress pulses, we excited the SRO electrode with near-infrared (800 nm) femtosecond light pulses with a pulse duration of $\tau_{\text{opt}} = 40$ fs and monitored the induced lattice dynamics by UXRd experiments at a laser-driven plasma x-ray source (PXS) [16,17] in a pump-probe scheme. The generated hard x-ray pulses [$E = 8.05$ keV ($\text{Cu } K_\alpha$), $\tau_{x\text{-ray}} = 150$ fs] were collected by a Montel multilayer mirror and focused onto the sample with a convergence of 0.3° . The diffracted photons were accumulated with a CMOS hybrid-pixel area detector in classical θ - 2θ geometry. This allowed for detecting symmetrically and asymmetrically diffracted x-ray photons at the same time, avoiding time-consuming mesh scans in order to measure reciprocal space maps (RSM) around specific Bragg reflections [18–21]. Consequently, we acquired information both on in-plane and out-of-plane structure dynamics utilizing this time-resolved version of RSM. The temporal overlap of the optical pump and x-ray probe pulses was determined in an independent cross correlation experiment [22] and was set to the delay 0 ps.

First, we discuss the conventional x-ray diffraction from lattice planes parallel to the surface. Figure 2(a) shows the θ - 2θ scans for three different time delays between optical pump and x-ray probe pulses. The black line represents the unexcited lattice and we can confirm the lattice constants of the three constituting materials from the respective Bragg angles. The photoinduced dynamics are evident from the changes of the three material specific Bragg reflections, which are shown in Fig. 2(b). By fitting each Bragg reflection for each material with a Gaussian, we can extract the peak width $w_z(t)$ (FWHM) and peak center $c_z(t)$ for each delay t in the q_z dimension. For the later analysis, it is convenient to introduce the peak shift $s_z(t) = c_z(t) - c_z(0)$. The absorption of the pump pulse takes place exclusively in the SRO electrode layer, leading to a quasi-instantaneous temperature rise. The heat expansion of SRO by 0.35% is limited by the speed of sound in the material and proceeds within 24 ps, evidenced by the shift to smaller Bragg angles [23]. On the same time scale, the substrate shows a tiny shoulder at the high-angle side according to the compression of STO adjacent to the expanding metal layer. Similarly, the PZT film is first compressed by the strain imposed from the expanding SRO; however, it expands after the strain wave is reflected from the sample surface [24]. A detailed evaluation and discussion will be given below.

While this evaluation of UXRd signals is straightforward and the example shows the power of the method, we

now discuss how to gain the information on the in-plane dynamics. The RSM before excitation is shown as a contour plot in Fig. 2(c). In general, the size of the reciprocal lattice points in the RSM is inversely proportional to the length scale of coherently scattering regions of the crystal in the according in-plane and out-of-plane directions. The additional broadening due to the instrument function of the x-ray diffraction setup, which is mainly given by the 0.3° convergence and Cu K_α energy bandwidth of the incident x-rays, can be seen in the peak profile of the structurally perfect STO substrate in the RSM. Figure 2(d) shows the diffraction signal integrated over the q_z range of the PZT peak. Similar to the convention above, we define the width (FWHM) and shift for the q_x dimension as $s_x(t)$ and $w_x(t)$. The large static value of w_x^{PZT} is consistent with the average size of the lateral regions in the PZT layer of about 50 nm observed in the TEM image [Fig. 1(a)]. In crystallography, this broadening of w_x can be described by the model of mosaicity [25], assuming the crystal to consist of small mosaic blocks. These blocks are homogeneous in themselves but the x-rays scattered from different blocks do not sum up coherently. The in-plane size of the blocks defines the lateral correlation length which is inversely proportional to the broadening of the RSM in q_x . Tilting of the blocks can give rise to an additional broadening. These two effects may be distinguished by measuring a RSM around an asymmetrical Bragg reflection [18]. Figure 2(d) shows that w_x increases considerably for snapshots recorded after the reflection of the strain wave at the sample surface.

In order to discuss our experimental results, we apply a 1D model of the sample structure to simulate the lattice dynamics by a linear chain model of masses and springs [26]. These simulations are well established to predict the out-of-plane dynamics but do not consider the in-plane dynamics directly. Therefore, we employ the out-of-plane phonon damping as an adjustable parameter to couple energy to in-plane motion. First, we calculate the temperature rise in the SRO after optical excitation [Fig. 3(a)] from the laser fluence, absorption depth, and heat capacity of this metal. The quasi-instantaneous thermal stress excites coherent acoustic phonons (strain waves) which are launched from the interfaces to the PZT layer and STO substrate. Calculated strain profiles for different delays are depicted in Fig. 3(b). Since heat diffusion from the SRO into the PZT layer can be neglected on this short time scale (≈ 100 ps) [27], the PZT lattice dynamics are exclusively determined by the compression wave traveling from the SRO-PZT interface to the PZT-air interface. Here, the strain wave is reflected and converted into an expansion wave traveling back to the SRO layer and further into the STO substrate. Due to the good acoustic impedance matching of the three materials, we neglect reflections at layer interfaces.

From the simulated spatiotemporal strain map, the resulting transient changes of the x-ray diffraction profile

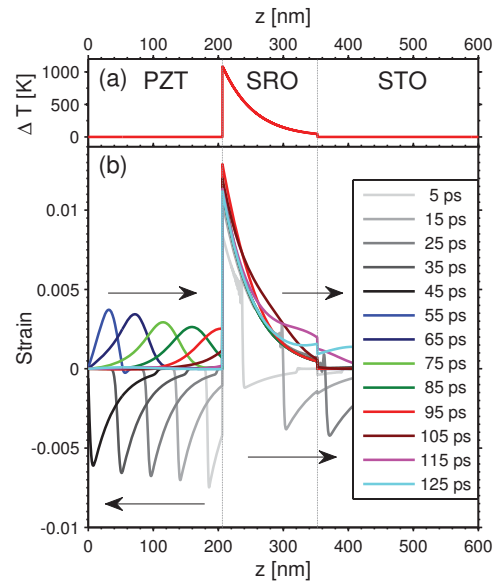


FIG. 3 (color). Simulation results for the temperature gradient and lattice dynamics after optical excitation. (a) The optical pump laser causes a quasi-instantaneous temperature increase only in the metallic SRO layer at delay zero. (b) The excited lattice dynamics are calculated by a 1D linear chain model. The strain profiles show a coherent sound wave with a sharp leading edge traveling from the PZT-SRO interface to the PZT-air interface. It is converted to an expansion wave that undergoes much stronger damping transforming it into a smooth and broad strain profile.

in q_z dimension for the PZT and SRO layers are calculated by dynamical x-ray diffraction theory [28]. Taking the elastic constants of each material, we can use the damping of coherent phonons by impurities and coupling to in-plane motion as adjustable parameters. Figures 4(a), 4(b), 4(d), and 4(e) show the excellent agreement of the simulated x-ray diffraction data with the measured values for s_z and w_z .

The peak shift s_z is a measure of the change of the average c -axis lattice parameter of the PZT and SRO layers, which was qualitatively discussed above. The change of w_z essentially reflects the inhomogeneous strain, which in SRO is given by the short absorption length of the optical pump light leading to a stress exponentially decaying with z . Initially, SRO only expands near the PZT interface. At 12 ps after excitation, the expansion wave has propagated through half the SRO layer, which leads to a maximum w_z^{SRO} [Fig. 4(d)], that in fact reflects a splitting of the SRO Bragg peak [23,26]. Due to the peak splitting, the Gaussian fit indicates a compression of the SRO layer for s_z^{SRO} as long as only a small fraction of SRO is expanded. Similarly to SRO, w_z^{PZT} rises and the peak shifts to larger angles as the compression travels through the PZT

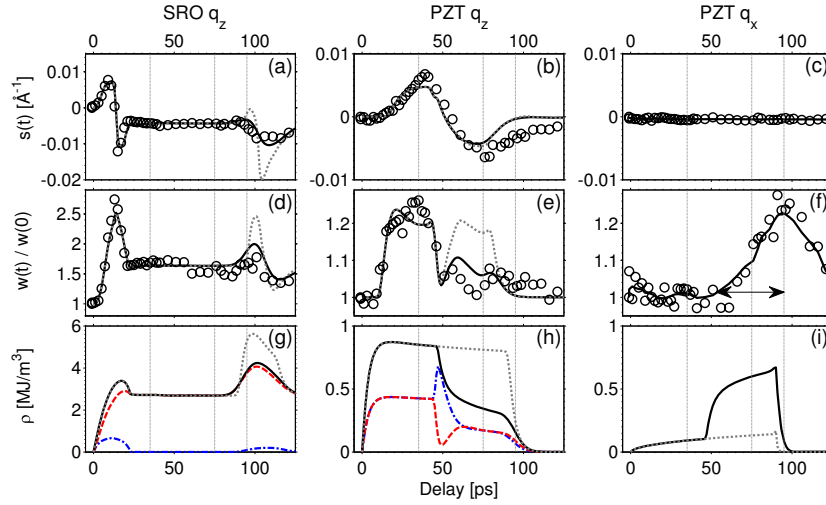


FIG. 4 (color online). (a–f) Comparison of experimental data (circles) with the simulation results (solid black lines). In panels (c) and (f), the solid lines are only guides to the eye. All grey dotted lines are the analogue to the black lines assuming constant damping in PZT. Panels (g) and (h) show the kinetic (dashed-dotted blue), potential (dashed red), and total (solid black) energy density in the according layer. (i) Damped energy density of out-of-plane motion in PZT.

layer [Figs. 4(b) and 4(e)]. Later, s_z^{PZT} becomes negative when the sound wave is reflected at the surface ($t > 50$ ps) and propagates back to the substrate. w_z^{PZT} is much smaller for $t > 50$ ps although the tensile strain during expansion, s_z^{PZT} , has nearly the same magnitude as the preceding compression. This implies that the strain pulse in PZT broadens in space rendering the layer less inhomogeneously strained when the layer expands.

In order to fit these four transient data sets for PZT and SRO [Figs. 4(a), 4(b), 4(d), and 4(e)] simultaneously in our simulations, we have introduced phonon damping in PZT as the only free parameter. The best fit for the four data sets was achieved when the damping factor in PZT is chosen 50 times larger for expansive out-of-plane strain compared to compressive strain of the same magnitude. The according results are plotted as solid black lines in Figs. 4(a), 4(b), 4(d), and 4(e). The grey dotted lines represent the results for a constant damping factor in PZT for expansion and compression. We can exclude pure surface scattering as the reason for the asymmetric damping behavior since this would lead to a much smaller amplitude of s_z^{PZT} in order to achieve the same decrease of w_z^{PZT} for the expansive strain. The increase of the damping in PZT is visualized in Fig. 3(b) where the colored lines ($t > 50$ ps) show a smooth out-of-plane expansion, whereas the greyish lines ($t < 50$ ps) show the inhomogeneous compression before the reflection at the surface changes the sign of the strain wave.

From our lattice dynamics simulations, we can also determine the kinetic (dashed-dotted blue), potential (dashed red), and total (solid black) energy density of the

out-of-plane coherent phonons in each layer [Figs. 4(g) and 4(h)]. We introduced the phonon damping in PZT to couple energy to lateral phonons. This energy is essentially the difference of the total energy of out-of-plane coherent phonons in PZT with and without damping. The result is plotted in Fig. 4(i) where the grey dotted line corresponds again to the case of constant damping. The increase of the lateral energy density in PZT [Fig. 4(i)] goes along with a considerable increase of w_x^{PZT} that reflects a change of the inhomogeneity in-plane, probably because the lateral blocks develop an inhomogeneous in-plane strain that is dynamically coupled to the out-of-plane motion according to the Poisson ratio [Fig. 4(f)]. We do not observe the converse effect during the compression of the PZT layer ($t < 50$ ps). The horizontal arrow in Fig. 4(f) indicates the time scale of the buildup of the lateral strain of approx. 50 ps. We can link this time scale to a lateral length scale of approx. 200 nm via the sound velocity of PZT of 4.6 nm/ps. This time scale agrees well with the in-plane block size observed in the TEM image in Fig. 1(a) and w_x^{PZT} of the static RSM in Fig. 2(c).

The analysis of the measured signal alone already suggests the following interpretation: The expansion of SRO sends a compression wave into PZT. The in-plane mosaicity or nanoinhomogeneity is unchanged during this period. When the strain changes sign upon reflection at the surface, PZT expands and according to Poisson ratio, the mosaicity must now laterally contract. The in-plane inhomogeneity is increased as millions of in-plane contraction waves start at all the lateral dislocations. We conclude that only out-of-plane expansion of PZT couples energy

to in-plane dynamics and that this effect is essentially suppressed for out-of-plane compression since this would have to expand the mosaic blocks, which is sterically forbidden by the adjacent blocks. This compares favorably with our simulations of the out-of-plane lattice dynamics, requiring an increased damping for the expansion wave in the PZT, which can be understood as an increase of the coupling between in-plane and out-of plane lattice motions.

In conclusion, we have demonstrated the first measurement of the lattice dynamics in a structurally imperfect thin film by ultrafast reciprocal space mapping (URSM). We do not only extract the changes of the lattice constants, i.e., the expansion and compression of materials perpendicular to the surface. In addition, we quantify the coupled response in plane, which turns out to be significantly enhanced for out-of-plan expansion, as it provides the in-plane contraction necessary for the atoms to start moving. URSM will be an important method for understanding the ultrafast response of oxide crystals with their natural tendency to form nanoscale inhomogeneities.

We thank B. Birajdar (Max-Planck-Institut für Mikrostrukturphysik, Halle, Germany) for performing the TEM imaging. This work was supported by the Deutsche Forschungsgemeinschaft via Grant No. BA 2281/3-1 and by the German Bundesministerium für Bildung und Forschung via Grants No. 03WKP03A and No. 05K10IP1.

*bargheer@uni-potsdam.de

- [1] D. G. Schlom, L.-Q. Chen, X. Pan, A. Schmehl, and M. A. Zurbuchen, *J. Am. Ceram. Soc.* **91**, 2429 (2008).
- [2] H. Han, Y. Kim, M. Alexe, D. Hesse, and W. Lee, *Adv. Mater.* **23**, 4599 (2011).
- [3] N. Bassiri-Gharb, I. Fujii, E. Hong, S. Trolrier-McKinstry, D. Taylor, and D. Damjanovic, *J. Electroceram.* **19**, 49 (2007).
- [4] Y. Xu, *Ferroelectric Materials and Their Applications* (North-Holland, Amsterdam, 1991).
- [5] C.-L. Jia, K. W. Urban, M. Alexe, D. Hesse, and I. Vrejoiu, *Science* **331**, 1420 (2011).
- [6] K. S. Lee, J. H. Choi, J. Y. Lee, and S. Baik, *J. Appl. Phys.* **90**, 4095 (2001).
- [7] E. Dagotto, *Science* **309**, 257 (2005).
- [8] E. A. Fitzgerald, *Mater. Sci. Rep.* **7**, 87 (1991).
- [9] A. Rousse, C. Rischel, and J.-C. Gauthier, *Rev. Mod. Phys.* **73**, 17 (2001).
- [10] M. Bargheer, N. Zhavoronkov, M. Woerner, and T. Elsaesser, *Chem. Phys. Chem.* **7**, 783 (2006).
- [11] M. Chergui and A. H. Zewail, *Chem. Phys. Chem.* **10**, 28 (2009).
- [12] D. Daranciang *et al.*, *Phys. Rev. Lett.* **108**, 087601 (2012).
- [13] C. von Korff Schmising, M. Bargheer, M. Kiel, N. Zhavoronkov, M. Woerner, T. Elsaesser, I. Vrejoiu, D. Hesse, and M. Alexe, *Phys. Rev. Lett.* **98**, 257601 (2007).
- [14] H. Ichikawa, S. Nozawa, T. Sato, A. Tomita, K. Ichianagi, M. Chollet, L. Guerin, N. Dean, A. Cavalleri, S.-i. Adachi, T.-h. Arima, H. Sawa, Y. Ogimoto, M. Nakamura, R. Tamaki, K. Miyano, and S.-y. Koshihara, *Nat. Mater.* **10**, 101 (2011).
- [15] I. Vrejoiu, G. Le Rhun, N.D. Zakharov, D. Hesse, L. Pintilie, and M. Alexe, *Philos. Mag.* **86**, 4477 (2006).
- [16] F. Zamponi, Z. Ansari, C. von Korff Schmising, P. Rothhardt, N. Zhavoronkov, M. Woerner, T. Elsaesser, M. Bargheer, T. Trobitzsch-Ryll, and M. Haschke, *Appl. Phys. A* **96**, 51 (2009).
- [17] D. Schick, A. Bojahr, M. Herzog, C. von Korff Schmising, R. Shayduk, W. Leitenberger, P. Gaal, and M. Bargheer, *Rev. Sci. Instrum.* **83**, 025104 (2012).
- [18] P.F. Fewster, *Crit. Rev. Solid State Mater. Sci.* **22**, 69 (1997).
- [19] V. Holy, U. Pietsch, and T. Baumbach, *High-Resolution X-Ray Scattering from Thin Films and Multilayers*, Springer Tracts in Modern Physics (Springer, Berlin, 1999).
- [20] J.F. Voitok and A. Kharchenko, *Powder Diffr.* **20**, 125 (2005).
- [21] P.F. Fewster, *J. Appl. Crystallogr.* **37**, 565 (2004).
- [22] A. Bojahr, D. Schick, L. Maerten, M. Herzog, I. Vrejoiu, C. von Korff Schmising, C. Milne, S.L. Johnson, and M. Bargheer, *Phys. Rev. B* **85**, 224302 (2012).
- [23] D. Schick, P. Gaal, A. Bojahr, W. Leitenberger, R. Shayduk, A. Hertwig, I. Vrejoiu, M. Herzog, and M. Bargheer (to be published).
- [24] S.H. Lee, A.L. Cavalleri, D.M. Fritz, M.C. Swan, R.S. Hegde, M. Reason, R.S. Goldman, and D.A. Reis, *Phys. Rev. Lett.* **95**, 246104 (2005).
- [25] J. Als-Nielsen and D. McMorrow, *Elements of Modern X-Ray Physics* (John Wiley & Sons, Ltd., New York, 2001).
- [26] M. Herzog, D. Schick, P. Gaal, R. Shayduk, C. von Korff Schmising, and M. Bargheer, *Appl. Phys. A* **106**, 489 (2012).
- [27] R. Shayduk, H.A. Navirian, W. Leitenberger, J. Goldshteyn, I. Vrejoiu, M. Weinelt, P. Gaal, M. Herzog, C. von Korff Schmising, and M. Bargheer, *New J. Phys.* **13**, 093032 (2011).
- [28] M. Herzog, D. Schick, W. Leitenberger, R. Shayduk, R.M. van der Veen, C. Milne, S.L. Johnson, I. Vrejoiu, and M. Bargheer, *New J. Phys.* **14**, 013004 (2012).

Abbreviations

1D	one-dimensional
APS	Advanced Photon Source
BESSY	Berliner Elektronenspeicherring-Gesellschaft für Synchrotronstrahlung m.b.H.
BFO	BiFeO ₃
BSD	Berkeley Software Distribution
BST	(Ba _{0.7} Sr _{0.3})TiO ₃
DECP	displacive excitation of coherent phonons
DFS	depolarization field screening
ESRF	European Synchrotron Radiation Facility
FEL	free electron laser
IfG	INSTITUTE FOR SCIENTIFIC INSTRUMENTS GMBH
LCM	linear-chain model
LSMO	(La _{0.7} Sr _{0.3})MnO ₃
NTM	<i>N</i> -temperature model
PXS	plasma X-ray source
PZT	Pb(Zr _{0.2} Ti _{0.8})O ₃
RLP	reciprocal lattice point
RSM	reciprocal space mapping
SAXS	small-angle X-ray scattering
SL	superlattice
SLS	Swiss Light Source
SNR	signal-to-noise ratio
SRO	SrRuO ₃

Abbreviations

STO	SrTiO ₃
TTM	two-temperature model
URSM	ultrafast reciprocal space mapping
UXRD	ultrafast X-ray diffraction
WAXS	wide-angle X-ray scattering
XRD	X-ray diffraction
XRR	X-ray reflectivity
ZFLAP	zone-folded longitudinal acoustical phonon

Bibliography

- [1] Y. Xu. *Ferroelectric Materials* (North-Holland, Amsterdam, 1991).
- [2] N. Spalding. *Magnetic Materials* (Cambridge University Press, Cambridge, 2003).
- [3] B. E. Warren. *X-ray diffraction* (Dover Publications, New York, 1990), 2nd edn.
- [4] D. K. Bowen and B. K. Tanner. *High Resolution X-Ray Diffractometry and Topography* (Taylor & Francis, London, 1998).
- [5] M. T. Dove. *Structure and Dynamics* (Oxford University Press, Oxford, 2003).
- [6] K. H. Bennemann. “Ultrafast dynamics in solids”. *J. Phys.: Condens. Matter.* **16**, R995 (2004).
- [7] M. Chergui and A. H. Zewail. “Electron and X-Ray Methods of Ultrafast Structural Dynamics: Advances and Applications”. *ChemPhysChem* **10**, 28 (2009).
- [8] J.-C. Diels and W. Rudolph. *Ultrashort Laser Pulse Phenomena* (Academic Press, Burlington, USA, 2006), 2nd edn.
- [9] J. R. Helliwell and P. M. Rentzepis (Eds.). *Time-resolved Diffraction* (Oxford University Press, Oxford, 1997).
- [10] A. H. Zewail. “4D ultrafast electron diffraction, crystallography, and microscopy.” *Annu. Rev. Phys. Chem.* **57**, 65 (2006).
- [11] A. Rousse, C. Rischel and J.-C. Gauthier. “Femtosecond x-ray crystallography”. *Rev. Mod. Phys.* **73**, 17 (2001).
- [12] M. Bargheer, N. Zhavoronkov, M. Woerner and T. Elsaesser. “Recent Progress in Ultrafast X-ray Diffraction”. *ChemPhysChem* **7**, 783 (2006).
- [13] A. Cavalleri, C. Tóth, C. Siders, J. Squier, F. Ráksi, P. Forget and J. Kieffer. “Femtosecond Structural Dynamics in VO₂ during an Ultrafast Solid-Solid Phase Transition”. *Phys. Rev. Lett.* **87**, 237401 (2001).
- [14] C. von Korff Schmising, M. Bargheer, M. Kiel, N. Zhavoronkov, M. Woerner, T. Elsaesser, I. Vrejoiu, D. Hesse and M. Alexe. “Coupled Ultrafast Lattice and Polarization Dynamics in Ferroelectric Nanolayers”. *Phys. Rev. Lett.* **98**, 257601 (2007).

- [15] P. Beaud, S. Johnson, E. Vorobeva, U. Staub, R. Souza, C. Milne, Q. Jia and G. Ingold. “Ultrafast Structural Phase Transition Driven by Photoinduced Melting of Charge and Orbital Order”. *Phys. Rev. Lett.* **103**, 155702 (2009).
- [16] D. Daranciang, M. Highland, H. Wen, S. Young, N. Brandt, H. Hwang, M. Vattilana, M. Nicoul, F. Quirin, J. Goodfellow, T. Qi, I. Grinberg, D. Fritz, M. Cammarata, D. Zhu, H. Lemke, D. Walko, E. Dufresne, Y. Li, J. Larsson, D. Reis, K. Sokolowski-Tinten, K. Nelson, A. Rappe, P. Fuoss, G. Stephenson and A. Lindenberg. “Ultrafast Photovoltaic Response in Ferroelectric Nanolayers”. *Phys. Rev. Lett.* **108**, 087601 (2012).
- [17] S. de Jong, R. Kukreja, C. Trabant, N. Pontius, C. F. Chang, T. Kachel, M. Beye, F. Sorgenfrei, C. H. Back, B. Bräuer, W. F. Schlotter, J. J. Turner, O. Krupin, M. Doehler, D. Zhu, M. A. Hossain, A. O. Scherz, D. Fausti, F. Novelli, M. Esposito, W. S. Lee, Y. D. Chuang, D. H. Lu, R. G. Moore, M. Yi, M. Trigo, P. Kirchmann, L. Pathey, M. S. Golden, M. Buchholz, P. Metcalf, F. Parmigiani, W. Wurth, A. Föhlisch, C. Schüßler-Langeheine and H. A. Dürr. “Speed limit of the insulator-metal transition in magnetite.” *Nat. Mater.* 1–22 (2013).
- [18] R. W. Schoenlein, W. P. Leemans, A. H. Chin, P. Volfbeyn, T. E. Glover, P. Balling, M. Zolotarev, K.-J. Kim, S. Chattopadhyay and C. V. Shank. “Femtosecond X-ray Pulses at 0.4 Å Generated by 90° Thomson Scattering: A Tool for Probing the Structural Dynamics of Materials”. *Science* **274**, 236 (1996).
- [19] R. W. Schoenlein, S. Chattopadhyay, H. H. W. Chong, T. E. Glover, P. A. Heimann, C. V. Shank, A. A. Zholents and M. S. Zolotarev. “Generation of Femtosecond Pulses of Synchrotron Radiation”. *Science* **287**, 2237 (2000).
- [20] S. Khan, K. Holldack, T. Kachel, R. Mitzner and T. Quast. “Femtosecond Undulator Radiation from Sliced Electron Bunches”. *Phys. Rev. Lett.* **97**, 074801 (2006).
- [21] P. Beaud, S. Johnson, A. Streun, R. Abela, D. Abramsohn, D. Grolimund, F. Krasniqi, T. Schmidt, V. Schlott and G. Ingold. “Spatiotemporal Stability of a Femtosecond Hard-X-Ray Undulator Source Studied by Control of Coherent Optical Phonons”. *Phys. Rev. Lett.* **99**, 174801 (2007).
- [22] B. McNeil. “Free electron lasers: First light from hard X-ray laser”. *Nat. Photonics* **3**, 375 (2009).
- [23] E. Förster, P. Glas, K. Goetz, S. Joks, P. V. Nickles, M. Schnürer and I. Will. “About the sensitivity of in situ diffraction measurements with X-radiation of a laser-produced plasma”. *phys. stat. sol. a* **107**, 85 (1988).
- [24] A. Rousse, P. Audebert, J. Geindre, F. Fallières, J. Gauthier, A. Mysyrowicz, G. Grillon and A. Antonetti. “Efficient K α x-ray source from femtosecond laser-produced plasmas”. *Phys. Rev. E* **50**, 2200 (1994).

-
- [25] N. Zhavoronkov, Y. Gritsai, M. Bargheer, M. Woerner and T. Elsaesser. “Generation of ultrashort K-alpha radiation from quasipoint interaction area of femtosecond pulses with thin foils”. *Appl. Phys. Lett.* **86**, 244107 (2005).
- [26] W. Lu, M. Nicoul, U. Shymanovich, A. Tarasevitch, P. Zhou, K. Sokolowski-Tinten, D. von der Linde, M. Mašek, P. Gibbon and U. Teubner. “Optimized K α x-ray flashes from femtosecond-laser-irradiated foils”. *Phys. Rev. E* **80**, 026404 (2009).
- [27] M. Silies, H. Witte, S. Linden, J. Kutzner, I. Uschmann, E. Förster and H. Zacharias. “Table-top kHz hard X-ray source with ultrashort pulse duration for time-resolved X-ray diffraction”. *Appl. Phys. A* **96**, 59 (2009).
- [28] F. Zamponi, Z. Ansari, C. von Korff Schmising, P. Rothhardt, N. Zhavoronkov, M. Woerner, T. Elsaesser, M. Bargheer, T. Trobitzsch-Ryll and M. Haschke. “Femtosecond hard X-ray plasma sources with a kilohertz repetition rate”. *Appl. Phys. A* **96**, 51 (2009).
- [29] F. Brunel. “Not-so-resonant, resonant absorption”. *Phys. Rev. Lett.* **59**, 52 (1987).
- [30] P. Gibbon and E. Förster. “Short-pulse laser - plasma interactions”. *Plasma Phys. Contr. F.* **38**, 769 (1996).
- [31] C. Rose-Petruck, R. Jimenez, T. Guo, A. Cavalleri, C. W. Siders, F. Rksi, J. A. Squier, B. C. Walker, K. R. Wilson and C. P. J. Barty. “Picosecond–milliångström lattice dynamics measured by ultrafast X-ray diffraction”. *Nature* **398**, 310 (1999).
- [32] A. Rousse, C. Rischel, S. Fourmaux, I. Uschmann, S. Sebban, G. Grillon, P. Balcou, E. Förster, J. P. Geindre, P. Audebert, J. C. Gauthier and D. Hulin. “Non-thermal melting in semiconductors measured at femtosecond resolution.” *Nature* **410**, 65 (2001).
- [33] K. Sokolowski-Tinten, C. Blome, J. Blums, A. Cavalleri, C. Dietrich, A. Tarasevitch, I. Uschmann, E. Förster, M. Kammler, M. Horn-von Hoegen and D. von der Linde. “Femtosecond X-ray measurement of coherent lattice vibrations near the Lindemann stability limit.” *Nature* **422**, 287 (2003).
- [34] M. Bargheer, N. Zhavoronkov, Y. Gritsai, J. C. Woo, D. S. Kim, M. Woerner and T. Elsaesser. “Coherent atomic motions in a nanostructure studied by femtosecond X-ray diffraction.” *Science* **306**, 1771 (2004).
- [35] G. Bauer, J. Li and E. Koppensteiner. “X-ray reciprocal space mapping of heterostructures”. *J. Cryst. Growth* **157**, 61 (1995).
- [36] P. F. Fewster. “Reciprocal space mapping”. *Cr. Rev. Sol. State* **22**, 69 (1997).
- [37] V. Holy, U. Pietsch and T. Baumbach. *High-resolution X-ray scattering from thin films and multilayers* (Springer, Berlin, 1999).

- [38] M. Bargheer, N. Zhavoronkov, R. Bruch, H. Legall, H. Stiel, M. Woerner and T. Elsaesser. “Comparison of focusing optics for femtosecond X-ray diffraction”. *Appl. Phys. B* **80**, 715 (2005).
- [39] E. F. Eikenberry, C. Brönnimann, G. Hülsen, H. Toyokawa, R. Horisberger, B. Schmitt, C. Schulze-Briese and T. Tomizaki. “PILATUS: a two-dimensional X-ray detector for macromolecular crystallography”. *Nucl. Instrum. Meth. A* **501**, 260 (2003).
- [40] C. von Korff Schmising, M. Bargheer, M. Kiel, N. Zhavoronkov, M. Woerner, T. Elsaesser, I. Vrejoiu, D. Hesse and M. Alexe. “Accurate time delay determination for femtosecond X-ray diffraction experiments”. *Appl. Phys. B* **88**, 1 (2007).
- [41] U. Shymanovich, M. Nicoul, W. Lu, S. Kähle, A. Tarasevitch, K. Sokolowski-Tinten and D. von der Linde. “Toward ultrafast time-resolved Debye-Scherrer x-ray diffraction using a laser-plasma source.” *Rev. Sci. Instrum.* **80**, 083102 (2009).
- [42] F. Zamponi, Z. Ansari, M. Woerner and T. Elsaesser. “Femtosecond powder diffraction with a laser-driven hard X-ray source.” *Opt. Express* **18**, 947 (2010).
- [43] B. Freyer, J. Stingl, F. Zamponi, M. Woerner and T. Elsaesser. “The rotating-crystal method in femtosecond X-ray diffraction”. *Opt. Express* **19**, 15506 (2011).
- [44] G. Cho, W. Kütt and H. Kurz. “Subpicosecond time-resolved coherent-phonon oscillations in GaAs”. *Phys. Rev. Lett.* **65**, 764 (1990).
- [45] A. Boulle, O. Masson, R. Guinebretière, A. Lecomte and A. Daurer. “A high-resolution X-ray diffractometer for the study of imperfect materials”. *J. Appl. Cryst.* **35**, 606 (2002).
- [46] A. Kinne, M. Thoms, H. R. Röss, T. Gerhard, M. Ehinger, W. Faschinger and G. Landwehr. “Image Plates as One-Dimensional Detectors in High-Resolution X-ray Diffraction”. *J. Appl. Cryst.* **31**, 446 (1998).
- [47] S. T. Mudie, K. M. Pavlov, M. J. Morgan, J. R. Hester, M. Tabuchi and Y. Takeda. “Collection of reciprocal space maps using imaging plates at the Australian National Beamline Facility at the Photon Factory.” *J. Synchrotron Rad.* **11**, 406 (2004).
- [48] O. Masson, A. Boulle, R. Guinebretière, A. Lecomte and A. Daurer. “On the use of one-dimensional position sensitive detector for x-ray diffraction reciprocal space mapping: Data quality and limitations”. *Rev. Sci. Instrum.* **76**, 063912 (2005).
- [49] S. O. Mariager, S. L. Lauridsen, A. Dohn, N. Bovet, C. B. Sørensen, C. M. Schlepütz, P. R. Willmott and R. Feidenhans'l. “High-resolution three-dimensional reciprocal-space mapping of InAs nanowires”. *J. Appl. Cryst.* **42**, 369 (2009).
- [50] C. M. Schlepütz, S. O. Mariager, S. A. Pauli, R. Feidenhans'l and P. R. Willmott. “Angle calculations for a (2+3)-type diffractometer: focus on area detectors”. *J. Appl. Cryst.* **44**, 73 (2010).

-
- [51] W. Hu, H. Suzuki, T. Sasaki, M. Kozu and M. Takahasi. “High-speed three-dimensional reciprocal-space mapping during molecular beam epitaxy growth of InGaAs”. *J. Appl. Cryst.* **45**, 1046 (2012).
- [52] I. Vrejoiu, M. Alexe, D. Hesse and U. Gösele. “Functional Perovskites - From Epitaxial Films to Nanostructured Arrays”. *Adv. Funct. Mater.* **18**, 3892 (2008).
- [53] D. G. Schlom, L.-Q. Chen, X. Pan, A. Schmehl and M. A. Zurbuchen. “A Thin Film Approach to Engineering Functionality into Oxides”. *J. Am. Chem. Soc.* **91**, 2429 (2008).
- [54] L. Klein, J. Dodge, C. Ahn, G. Snyder, T. Geballe, M. Beasley and A. Kapitulnik. “Anomalous Spin Scattering Effects in the Badly Metallic Itinerant Ferromagnet SrRuO₃”. *Phys. Rev. Lett.* **77**, 2774 (1996).
- [55] M. Ziese, I. Vrejoiu and D. Hesse. “Structural symmetry and magnetocrystalline anisotropy of SrRuO₃ films on SrTiO₃”. *Phys. Rev. B* **81**, 184418 (2010).
- [56] P. Kostic, Y. Okada, N. Collins, Z. Schlesinger, J. Reiner, L. Klein, A. Kapitulnik, T. Geballe and M. Beasley. “Non-Fermi-Liquid Behavior of SrRuO₃: Evidence from Infrared Conductivity”. *Phys. Rev. Lett.* **81**, 2498 (1998).
- [57] M. Ziese, I. Vrejoiu, E. Pippel, P. Esquinazi, D. Hesse, C. Etz, J. Henk, A. Ernst, I. V. Maznichenko, W. Hergert and I. Mertig. “Tailoring Magnetic Interlayer Coupling in La_{0.7}Sr_{0.3}MnO₃/SrRuO₃ Superlattices”. *Phys. Rev. Lett.* **104**, 167203 (2010).
- [58] C. von Korff Schmising, A. Harpoeth, N. Zhavoronkov, Z. Ansari, C. Aku-Leh, M. Woerner, T. Elsaesser, M. Bargheer, M. Schmidbauer, I. Vrejoiu, D. Hesse and M. Alexe. “Ultrafast magnetostriction and phonon-mediated stress in a photoexcited ferromagnet”. *Phys. Rev. B* **78**, 60404 (2008).
- [59] J. Hohlfeld, S.-S. Wellershoff, J. Güdde, U. Conrad, V. Jähnke and E. Matthias. “Electron and lattice dynamics following optical excitation of metals”. *Chem. Phys.* **251**, 237 (2000).
- [60] S. I. Anisimov, B. L. Kapeliovich and T. L. Perel'man. “Electron emission from metal surfaces exposed to ultrashort laser pulses”. *Sov. Phys. JETP* **39**, 375 (1975).
- [61] E. Grüneisen. “Theorie des festen Zustandes einatomiger Elemente”. *Ann. Phys.* **344**, 257 (1912).
- [62] M. Herzog, W. Leitenberger, R. Shayduk, R. M. van der Veen, C. J. Milne, S. L. Johnson, I. Vrejoiu, M. Alexe, D. Hesse and M. Bargheer. “Ultrafast manipulation of hard x-rays by efficient Bragg switches”. *Appl. Phys. Lett.* **96**, 161906 (2010).
- [63] H. Navirian, M. Herzog, J. Goldshteyn, W. Leitenberger, I. Vrejoiu, D. Khakhulin, M. Wulff, R. Shayduk, P. Gaal and M. Bargheer. “Shortening x-ray pulses for pump-probe experiments at synchrotrons”. *J. Appl. Phys.* **109**, 126104 (2011).

- [64] R. Shayduk, H. Navirian, W. Leitenberger, J. Goldshteyn, I. Vrejoiu, M. Weinelt, P. Gaal, M. Herzog, C. von Korff Schmising and M. Bargheer. “Nanoscale heat transport studied by high-resolution time-resolved x-ray diffraction”. *New J. Phys.* **13**, 093032 (2011).
- [65] H. Wen, P. Chen, M. Cosgriff, D. Walko, J. Lee, C. Adamo, R. Schaller, J. Ihlefeld, E. Dufresne, D. Schlom, P. Evans, J. Freeland and Y. Li. “Electronic Origin of Ultrafast Photoinduced Strain in BiFeO₃”. *Phys. Rev. Lett.* **110**, 037601 (2013).
- [66] H. Ichikawa, S. Nozawa, T. Sato, A. Tomita, K. Ichiyanagi, M. Chollet, L. Guerin, N. Dean, A. Cavaliere, S.-i. Adachi, T.-h. Arima, H. Sawa, Y. Ogimoto, M. Nakamura, R. Tamaki, K. Miyano and S.-y. Koshihara. “Transient photoinduced a ‘hidden’ phase in a manganite”. *Nat. Mater.* **10**, 101 (2011).
- [67] W. Eerenstein, N. D. Mathur and J. F. Scott. “Multiferroic and magnetoelectric materials.” *Nature* **442**, 759 (2006).
- [68] R. Ramesh and N. A. Spaldin. “Multiferroics: progress and prospects in thin films.” *Nat. Mater.* **6**, 21 (2007).
- [69] L. W. Martin, S. P. Crane, Y.-H. Chu, M. B. Holcomb, M. Gajek, M. Huijben, C.-H. Yang, N. Balke and R. Ramesh. “Multiferroics and magnetoelectrics: thin films and nanostructures”. *J. Phys.: Condens. Matter* **20**, 434220 (2008).
- [70] N. A. Hill. “Why Are There so Few Magnetic Ferroelectrics?” *J. Phys. Chem. B* **104**, 6694 (2000).
- [71] G. Catalan and J. F. Scott. “Physics and Applications of Bismuth Ferrite”. *Adv. Mater.* **21**, 2463 (2009).
- [72] C. Stanciu, F. Hansteen, A. Kimel, A. Kirilyuk, A. Tsukamoto, A. Itoh and T. Rasing. “All-Optical Magnetic Recording with Circularly Polarized Light”. *Phys. Rev. Lett.* **99**, 047601 (2007).
- [73] Y. M. Sheu, S. A. Trugman, Y.-S. Park, S. Lee, H. T. Yi, S.-W. Cheong, Q. X. Jia, A. J. Taylor and R. P. Prasankumar. “Ultrafast carrier dynamics and radiative recombination in multiferroic BiFeO₃”. *Appl. Phys. Lett.* **100**, 242904 (2012).
- [74] T. Choi, S. Lee, Y. J. Choi, V. Kiryukhin and S.-W. Cheong. “Switchable ferroelectric diode and photovoltaic effect in BiFeO₃.” *Science* **324**, 63 (2009).
- [75] S. Y. Yang, L. W. Martin, S. J. Byrnes, T. E. Conry, S. R. Basu, D. Paran, L. Reichertz, J. Ihlefeld, C. Adamo, A. Melville, Y.-H. Chu, C.-H. Yang, J. L. Musfeldt, D. G. Schlom, J. W. Ager and R. Ramesh. “Photovoltaic effects in BiFeO₃”. *Appl. Phys. Lett.* **95**, 062909 (2009).
- [76] L. Y. Chen, J. C. Yang, C. W. Luo, C. W. Laing, K. H. Wu, J.-Y. Lin, T. M. Uen, J. Y. Juang, Y. H. Chu and T. Kobayashi. “Ultrafast photoinduced mechanical strain in epitaxial BiFeO₃ thin films”. *Appl. Phys. Lett.* **101**, 041902 (2012).

-
- [77] P. Ruello, T. Pezeril, S. Avanesyan, G. Vaudel, V. Gusev, I. C. Infante and B. Dkhil. “Photoexcitation of gigahertz longitudinal and shear acoustic waves in BiFeO₃ multiferroic single crystal”. *Appl. Phys. Lett.* **100**, 212906 (2012).
- [78] R. Pisarev, A. Moskvina, A. Kalashnikova and T. Rasing. “Charge transfer transitions in multiferroic BiFeO₃ and related ferrite insulators”. *Phys. Rev. B* **79**, 235128 (2009).
- [79] S. M. Young and A. M. Rappe. “First Principles Calculation of the Shift Current Photovoltaic Effect in Ferroelectrics”. *Phys. Rev. Lett.* **109**, 116601 (2012).
- [80] I. Vrejoiu, G. Le Rhun, L. Pintilie, D. Hesse, M. Alexe and U. Gösele. “Intrinsic Ferroelectric Properties of Strained Tetragonal PbZr_{0.2}Ti_{0.8}O₃ Obtained on Layer-by-Layer Grown, Defect-Free Single-Crystalline Films”. *Adv. Mater.* **18**, 1657 (2006).
- [81] I. Vrejoiu, G. Le Rhun, N. D. Zakharov, D. Hesse, L. Pintilie and M. Alexe. “Threading dislocations in epitaxial ferroelectric PbZr_{0.2}Ti_{0.8}O₃ films and their effect on polarization backswitching”. *Philos. Mag.* **86**, 4477 (2006).
- [82] E. A. Fitzgerald. “Dislocations in strained-layer epitaxy: theory, experiment, and applications”. *Mater. Sci. Reports* **7**, 87 (1991).
- [83] E. Dagotto. “Complexity in strongly correlated electronic systems.” *Science* **309**, 257 (2005).
- [84] M. Abo-Bakr, J. Feikes, K. Holldack, G. Wüstefeld and H.-W. Hübers. “Steady-State Far-Infrared Coherent Synchrotron Radiation detected at BESSY II”. *Phys. Rev. Lett.* **88**, 254801 (2002).
- [85] C. Thomsen, H. Grahn, H. Maris and J. Tauc. “Surface generation and detection of phonons by picosecond light pulses”. *Phys. Rev. B* **34**, 4129 (1986).
- [86] K. Yee, Y. Lim, T. Dekorsy and D. Kim. “Mechanisms for the Generation of Coherent Longitudinal-Optical Phonons in GaAs /AlGaAs Multiple Quantum Wells”. *Phys. Rev. Lett.* **86**, 1630 (2001).
- [87] M. Herzog, A. Bojahr, J. Goldshteyn, W. Leitenberger, I. Vrejoiu, D. Khakhulin, M. Wulff, R. Shayduk, P. Gaal and M. Bargheer. “Detecting optically synthesized quasi-monochromatic sub-terahertz phonon wavepackets by ultrafast x-ray diffraction”. *Appl. Phys. Lett.* **100**, 94101 (2012).
- [88] P. H. Bucksbaum and R. Merlin. “The phonon Bragg switch: a proposal to generate sub-picosecond X-ray pulses”. *Solid State Commun.* **111**, 535 (1999).
- [89] H. Navirian, R. Shayduk, W. Leitenberger, J. Goldshteyn, P. Gaal and M. Bargheer. “Synchrotron-based ultrafast x-ray diffraction at high repetition rates.” *Rev. Sci. Instrum.* **83**, 63303 (2012).

- [90] K. E. Goodson and Y. S. Ju. “Heat Conduction in Novel Electronic Films”. *Annu. Rev. Mater. Sci.* **29**, 261 (1999).
- [91] D. G. Cahill, W. K. Ford, K. E. Goodson, G. D. Mahan, A. Majumdar, H. J. Maris, R. Merlin and S. R. Phillpot. “Nanoscale thermal transport”. *J. Appl. Phys.* **93**, 793 (2003).
- [92] M. E. Siemens, Q. Li, R. Yang, K. A. Nelson, E. H. Anderson, M. M. Murnane and H. C. Kapteyn. “Quasi-ballistic thermal transport from nanoscale interfaces observed using ultrafast coherent soft X-ray beams.” *Nat. Mater.* **9**, 26 (2010).
- [93] M. N. Luckyanova, J. Garg, K. Esfarjani, A. Jandl, M. T. Bulsara, A. J. Schmidt, A. J. Minnich, S. Chen, M. S. Dresselhaus, Z. Ren, E. A. Fitzgerald and G. Chen. “Coherent Phonon Heat Conduction in Superlattices”. *Science* **338**, 936 (2012).
- [94] D. A. Walko, Y.-M. Sheu, M. Trigo and D. A. Reis. “Thermal transport in thin films measured by time-resolved, grazing incidence x-ray diffraction”. *J. Appl. Phys.* **110**, 102203 (2011).
- [95] W. Fullagar, M. Harbst, S. Canton, J. Uhlig, M. Walczak, C.-G. Wahlström and V. Sundström. “A broadband laser plasma x-ray source for application in ultrafast chemical structure dynamics.” *Rev. Sci. Instrum.* **78**, 115105 (2007).
- [96] M. C. Langner, C. L. S. Kantner, Y. H. Chu, L. M. Martin, P. Yu, R. Ramesh and J. Orenstein. “Effective thermal boundary resistance from thermal decoupling of magnons and phonons in SrRuO₃ thin films”. *Phys. Rev. B* **82**, 054425 (2010).
- [97] R. Venkatasubramanian, E. Siivola, T. Colpitts and B. O’Quinn. “Thin-film thermoelectric devices with high room-temperature figures of merit.” *Nature* **413**, 597 (2001).
- [98] P. Platzman and E. Isaacs. “Resonant inelastic x-ray scattering”. *Phys. Rev. B* **57**, 11107 (1998).
- [99] G. Bauer. *Optical characterization of epitaxial semiconductor layers* (Springer, Berlin, 1996).
- [100] J. Hemberger, A. Krimmel, T. Kurz, H.-A. Krug von Nidda, V. Ivanov, A. Mukhin, A. Balbashov and A. Loidl. “Structural, magnetic, and electrical properties of single-crystalline La_{1-x}Sr_xMnO₃ (0.4 < x < 0.85)”. *Phys. Rev. B* **66**, 094410 (2002).
- [101] V. Shirokov, V. Torgashev, A. Bakirov and V. Lemanov. “Concentration phase diagram of Ba_xSr_{1-x}TiO₃ solid solutions”. *Phys. Rev. B* **73**, 104116 (2006).

Danksagung

Mein Dank gilt in erster Linie Prof. Matias Bargheer, der es mir ermöglicht hat, meine Promotion in einer fantastischen Arbeitsgruppe unter hervorragenden Bedingungen durchführen zu können. Ich möchte ihm auch persönlich für seine erfrischende und motivierende Art danken, mir Physik zu veranschaulichen und bei Problemen zu helfen.

Mein Dank geht weiterhin an die Mitglieder der Arbeitsgruppe ULTRAFAST DYNAMICS IN CONDENSED MATTER an der Universität Potsdam für die freundliche und hilfsbereite Atmosphäre während der gesamten Zeit meiner Promotion. Im Speziellen bedanke ich mich bei Dr. Peter Gaal, Dr. Clemens von Korff Schmising, Dr. Marc Herzog und André Bojahr für ihre tatkräftige Unterstützung meiner Arbeit.

Dem Team vom INSTITUTE FOR SCIENTIFIC INSTRUMENTS GMBH (IfG), bestehend aus Timo Trobitzsch-Ryll, Sebastian Huschka, Markus Oesker und Dr. Wolfgang Mathis, danke ich für die Hilfe beim Aufbau der PXS und der Bewältigung aller kleineren Probleme mit der Hard- und Software des Gerätes. Ebenfalls möchte ich der Physik-Werkstatt der Universität Potsdam danken, im Besonderen Patrick Parnow, für die Herstellung und Bearbeitung vieler technischer Hilfsmittel, ohne die meine Promotionsarbeit nicht in diesem Umfang möglich gewesen wäre. Andreas Pucher möchte ich für seine guten Tipps im Bereich Elektrotechnik danken, die meine Arbeit um einige seltene Lötarbeiten bereichert haben.

Dr. Ionela Vrejoiu und Prof. Darrell Schlom danke ich für die Bereitstellung der hier untersuchten Proben, welche durch ihre außergewöhnliche strukturelle Qualität maßgeblich zum Gelingen meiner Arbeit beigetragen haben.

Am Ende und doch am Wichtigsten möchte ich meiner gesamten Familie danken, die mich bis hierhin immer unterstützt und motiviert hat.

Carmen, danke für die Nachsicht, wenn ich wieder beim Arbeiten die Zeit vergessen habe, und vor allem für das Glück, das Greta und du über mich bringen.

Vielen Dank!

Selbständigkeitserklärung

Hiermit erkläre ich, dass ich die vorliegende Dissertation

Ultrafast Lattice Dynamics in Photoexcited Nanostructures
Femtosecond X-ray Diffraction with Optimized Evaluation Schemes

selbstständig erarbeitet und verfasst habe und alle Hilfsmittel und Hilfen angegeben habe. Ich erkläre, dass ich mich nicht für einen Doktorgrad anderwärts beworben habe und auch einen dementsprechenden Doktorgrad nicht besitze.

Desweiteren erkläre ich, dass ich von der zugrunde liegenden Promotionsordnung Kenntnis genommen habe.

Daniel Schick

Potsdam, den 7. November 2013

A. Appendix

A.1. Additional papers

The following papers are added to the thesis for completeness, although they are not part of the main scope of this work. I contributed to these papers mainly by performing measurements at the PXS, by discussing physics, and by commenting on the manuscripts. For Paper XVI, I also wrote most part of the manuscript by myself. All of my individual contributions to these papers are listed in Chapter 2.

Paper IX

Tailoring interference and nonlinear manipulation of femtosecond x-rays

M. Herzog, **D. Schick**, W. Leitenberger, R. Shayduk, R. M. van der Veen, C. J. Milne, S. L. Johnson, I. Vrejoiu, and M. Bargheer

New J. Phys. 14, 1 (2012)

New Journal of Physics

The open-access journal for physics

Tailoring interference and nonlinear manipulation of femtosecond x-rays

Marc Herzog¹, Daniel Schick¹, Wolfram Leitenberger¹,
Roman Shayduk², Renske M van der Veen^{3,4},
Christopher J Milne^{3,4}, Steven L Johnson³, Ionela Vrejoiu⁵
and Matias Bargheer^{1,2,6}

¹ Institut für Physik und Astronomie, Universität Potsdam, Karl-Liebknecht-Str. 24-25, 14476 Potsdam, Germany

² Helmholtz-Zentrum Berlin für Materialien und Energie GmbH, Hahn-Meitner-Platz 1, 14109 Berlin, Germany

³ Swiss Light Source, Paul Scherrer Institut, 5232 Villigen PSI, Switzerland

⁴ Laboratoire de Spectroscopie Ultrarapide, Ecole Polytechnique Fédérale de Lausanne, 1015 Lausanne, Switzerland

⁵ Max-Planck-Institut für Mikrostrukturphysik, Weinberg 2, 06120 Halle, Germany

E-mail: bargheer@uni-potsdam.de

New Journal of Physics **14** (2012) 013004 (9pp)

Received 14 August 2011

Published 6 January 2012

Online at <http://www.njp.org/>

doi:10.1088/1367-2630/14/1/013004

Abstract. We present ultrafast x-ray diffraction (UXRD) experiments on different photoexcited oxide superlattices. All data are successfully simulated by dynamical x-ray diffraction calculations based on a microscopic model, that accounts for the linear response of phonons to the excitation laser pulse. Some Bragg reflections display a highly nonlinear strain dependence. The origin of linear and two distinct nonlinear response phenomena is discussed in a conceptually simpler model using the interference of envelope functions that describe the diffraction efficiency of the average constituent nanolayers. The combination of both models facilitates rapid and accurate simulations of UXRD experiments.

⁶ Author to whom any correspondence should be addressed.

A large variety of x-ray optics that can be used to monochromatize, focus and analyze the phase of hard x-rays have been invented and realized. Many of them have become standard tools in x-ray science [1] and some more recent developments include e.g. hard-x-ray interferometers with microelectronvolt resolution [2] and nanointerferometers based on refractive lenses [3]. Of particular interest is understanding the manifold physical processes in solids on atomic length and time scales for which hard x-rays providing a subpicosecond time resolution are mandatory [4–8]. Several methods to modify the time structure of x-ray pulses or pulse trains have been reported [9–11]. The concept of exploiting phonons in solid samples generated by femtosecond laser pulses as an ultrafast gateable x-ray mirror [12] has very recently been experimentally implemented using a layered nanostructure composed of the perovskite oxides SrTiO₃ (STO) and SrRuO₃ (SRO) [13]. The authors observed a giant response of a particular Bragg peak showing an intensity increase by a factor of 25 with a gating time of less than 1 ps. The general mechanism was explained as resulting from the expansion of the metallic SRO nanolayers and the concomitant compression of the STO nanolayers that consequently alters the structure factor of the observed Bragg reflection. The artificial spatial layering period was found to set the time scale of the transient gate and the measured diffraction curves could be simulated rather precisely, however, a detailed understanding of the ultrafast x-ray response required for purpose-oriented designing of nanostructures was lacking.

In this paper, we present a detailed analysis of the simulation of transient Θ – 2Θ x-ray diffractograms of periodically layered epitaxial nanostructures, also called superlattices (SL). We show numerical calculations obtained from combined results of (i) a linear-chain model computing the photoexcited lattice dynamics of a given sample [14] and (ii) fully dynamical x-ray diffraction (XRD) calculations. In the following, we refer to these combined linear-chain and dynamical XRD calculations as LCDX. The predicted features of the transient intensities of SL Bragg reflections—including linear and highly nonlinear responses to phonon amplitudes—are interpreted by a conceptually simpler envelope model (EM) that merely considers homogeneous deformations of the single layers. The EM already demonstrates key features that lead to the distinct nonlinear XRD dynamics of such SLs. A comparison to results of ultrafast x-ray diffraction (UXRD) experiments on two different SLs shows the very high degree of precision achieved by the LCDX. The presented analysis will be very valuable for the interpretation of UXRD data in general, and specifically for creating novel devices based on such nonlinear phenomena that utilize the tailorable x-ray interference in artificial nanostructures.

We test our numerical calculations by applying them to two different epitaxial SL samples both composed of metallic and dielectric perovskite oxides. In particular, we consider the previously investigated SL [SRO₂₀/STO₃₈]₁₁ [13] and a SL containing the ferromagnetic metal La_{0.7}Sr_{0.3}MnO₃ (LSMO), namely [LSMO₂₃/STO₃₅]₁₅. The index of each component represents the number of perovskite unit cells per layer, and the overall index gives the number of repeat units of the double layer (DL). This structural characterization of the samples was done by matching Θ – 2Θ diffractograms with simulations utilizing dynamical XRD theory according to the Darwin formalism [15]. Figures 1(a) and 2(a) show the XRD measurements (gray bullets) and the corresponding simulations (red solid line) for SRO/STO and LSMO/STO, respectively, without any laser excitation. In the following, we develop the EM that explains the particular

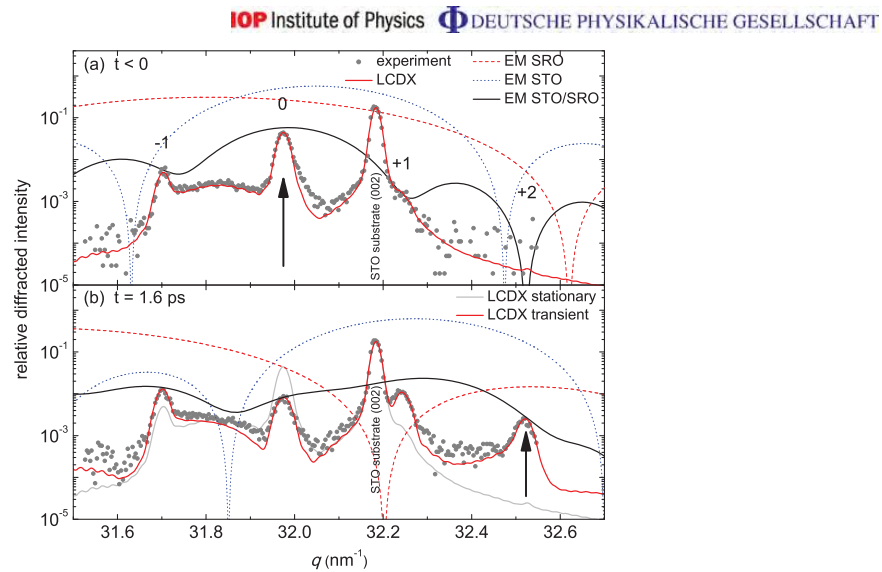


Figure 1. Experimental Θ - 2Θ scans (gray bullets) of the SRO/STO SL. The broken lines show the calculated single-layer envelope functions (scaled for clarity), the black solid line is the DL envelope function (scaled by the number of DL squared), and the red solid line is the resulting SL diffractogram of the LCDX at (a) $t < 0$ and (b) $t = 1.6$ ps after optical excitation with a fluence of 36.8 mJ cm^{-2} . The arrows mark the SL peaks considered in figure 3.

shape of these diffraction curves and provides a fundamental understanding of transient changes upon photoexcitation by femtosecond laser pulses.

As the thickness of the individual layers in both SLs is much smaller than the extinction depth ξ of the x-rays, the corresponding diffractograms are essentially the Fourier transform of their electron densities. Figures 1 and 2 show the square modulus of the diffracted x-ray amplitude $A_M(q)$ ($A_I(q)$) for a single metallic (insulating) layer of the respective sample as a red dashed (blue dotted) line. These curves match a sinc^2 function (the Fourier transform of a homogeneous slab), and we will refer to such curves as envelope functions. The width Δq of such envelope functions is inversely proportional to the real-space thickness d of the respective layer and their center position q_{env} encodes the average strain of that single layer. The envelope of one DL, $|A_{\text{DL}}|^2 = |A_M + A_I|^2$ (black line in figures 1 and 2) accounts for interference of the complex single-layer amplitudes⁷. The DL envelope is scaled by the respective number of DL squared. Clearly, it determines the intensity of the observed SL Bragg reflections since the SL Bragg peaks touch the DL envelope in figures 1(a) and 2(a). In other words, the observed intensity $I(q_{\text{SL}}, t)$ of a particular SL reflection at q_{SL} can be estimated from the relation $I \propto |A_{\text{DL}}|^2$. The SL Bragg peaks thus ‘sample’ the DL envelope at discrete wavevectors that are selected by the Laue condition $q_{\text{SL}} = n \cdot \frac{2\pi}{d_{\text{SL}}} = n \cdot g_{\text{SL}}$, where g_{SL} is the reciprocal lattice vector corresponding to the SL period $d_{\text{SL}} = d_M + d_I$ and $n \in \mathbb{N}$. The single-layer envelope functions themselves have significant intensity only in the q -range around the bulk Laue conditions

⁷ To be precise, one also has to account for the phase shifts due to transmission through the top layer before and after the reflection from the bottom layer. This effect is accounted for in the calculations.

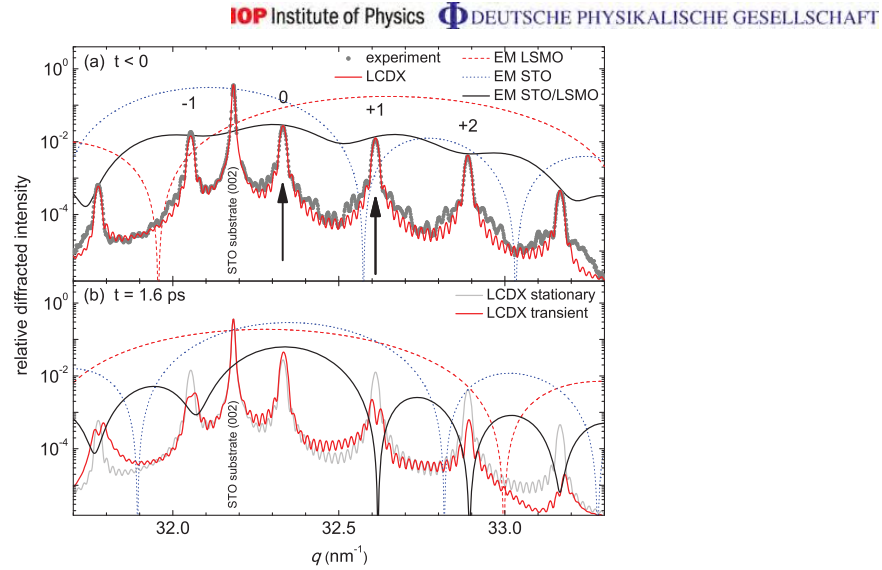


Figure 2. Experimental Θ - 2Θ scans (gray bullets) of the LSMO/STO SL recorded at the EDR-beamline of BESSY II (Helmholtz-Zentrum Berlin). The meaning of the lines and panels is analogous to figure 1, and the arrows mark the SL peaks considered in figure 4.

$q_{M/I} = m \cdot \frac{2\pi}{c_{M/I}}$, where $c_{M/I}$ are the out-of-plane lattice constants of the metal and the insulator, respectively, and $m \in \mathbb{N}$.⁸ For materials with similar c_M and c_I , we number the SL reflections as satellites to the Laue condition $q^{(0)} = \frac{2\pi}{c_{av}} = 2\pi(n_M + n_I)/(n_M c_M + n_I c_I)$ of the so-called zero-order SL peak (ZOP) corresponding to the average lattice constant c_{av} in one DL [16]. Here n_M and n_I correspond to the number of unit cells in the metallic and insulating layers, respectively.

We can now use the above introduced EM to predict the general features of transient changes of diffractograms after laser-pulse excitation such as presented in figure 1. The ultrafast deposition of the excitation energy in the metallic layers of the SL triggers their impulsive expansion [13] which shifts the red dashed envelope to smaller q values. The concomitant compression of STO shifts the blue dotted envelope to larger q values (compare the envelopes in panels (a) and (b) of figures 1 and 2). The magnitude of the envelope shifts is determined by the amplitude of this collective, spatially and temporally periodic lattice motion also referred to as SL phonon mode [14, 17]. As a consequence, the DL envelope function and thus the SL Bragg peak intensities are altered. Eventually, the entire SL will expand within the time $T_{exp} = D/v_{SL}$, where D and v_{SL} are the total SL thickness and the sound velocity in the SL, respectively. For small time delays $t \ll T_{exp}$, however, the SL period remains approximately constant and the SL Bragg peak positions q_{SL} do not change [18]. Here, we exclusively focus on these short-time dynamics.

The UXRD experiments were performed at the FEMTO-slicing beamline of the Swiss Light Source (SLS), providing a time resolution of 140 ± 30 fs [19]. The samples were excited

⁸ In this paper, we exclusively consider the bulk (002) reflections.

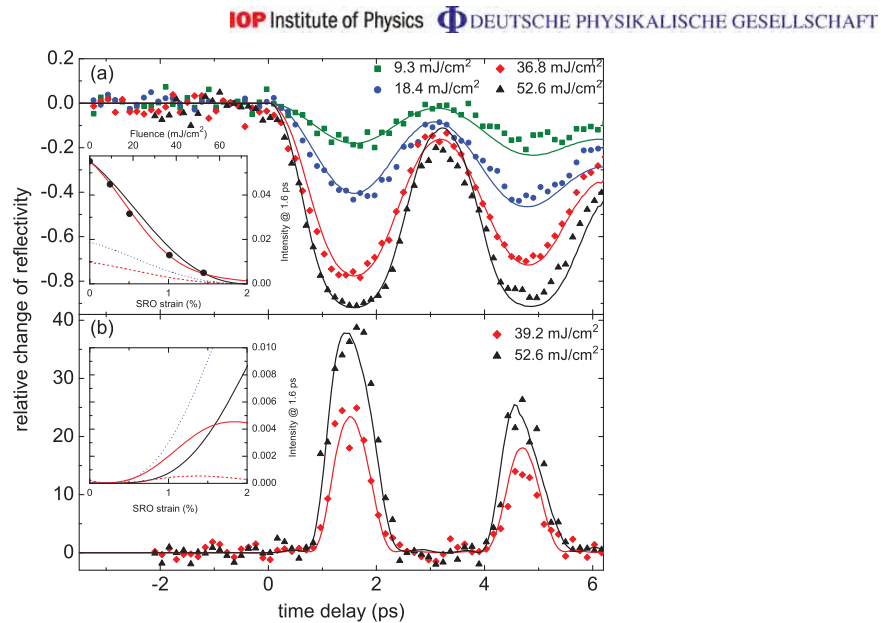


Figure 3. Relative change of Bragg intensity of (a) the ZOP and (b) the +2 SL peak for the SRO/STO SL after optical excitation with different pump fluences. The solid lines represent LCDX calculations. The insets show the calculated SL peak intensities at 1.6 ps according to the EM (black solid line) and LCDX (red solid line). Also, the contributions from individual layers are shown (broken lines). The inset in panel (a) also includes the corresponding experimental data obtained from the transients (bullets).

by ~ 120 fs pump pulses at 800 nm wavelength where the optical penetration depths $\xi_{\text{SRO}} \approx 52$ nm and $\xi_{\text{LSMO}} \approx 90$ nm generate an exponentially decaying stress pattern along the SL stack that is correctly accounted for in the LCDX [14, 20, 21]. As an example, the gray bullets in figures 1(a) and (b) show the measured Θ - 2Θ scans of the STO/SRO SL before and 1.6 ps after excitation, respectively, encompassing four SL reflections (-1 to $+2$). We also recorded the intensity of selected SL Bragg peaks as a function of time delay for different pump fluences. The symbols in figures 3 and 4 illustrate the strong modulations of the relative intensity change $[I(t) - I_0]/I_0$ where $I(t)$ is the measured x-ray intensity at time delay t and I_0 is the measured unpumped signal. Here, it is directly verified that the maximum expansion of the metallic layers of both the SRO/STO and the LSMO/STO SL is reached after 1.6 ps.

In the following, we discuss the simulation of UXR data. We highlight the linear and nonlinear response of distinct Bragg reflections of the two SLs, starting with the ZOP of the SRO/STO SL. The DL envelope of the excited SRO/STO SL in figure 1(b) matches the experimental SL peak intensities very well, if we assume a homogeneous SRO expansion of 1.3% for a laser fluence of 36.8 mJ cm^{-2} . Only the +1 SL peak close to the substrate peak is overestimated by the EM⁹. If we use the LCDX, we are able to properly calculate the x-ray

⁹ The overestimation of the +1 peak remains even if the complete SL including the substrate is simulated according to the EM (see [13]). This discrepancy between the EM and the exact LCDX is thus due to the inhomogeneous excitation density along the SL stack.

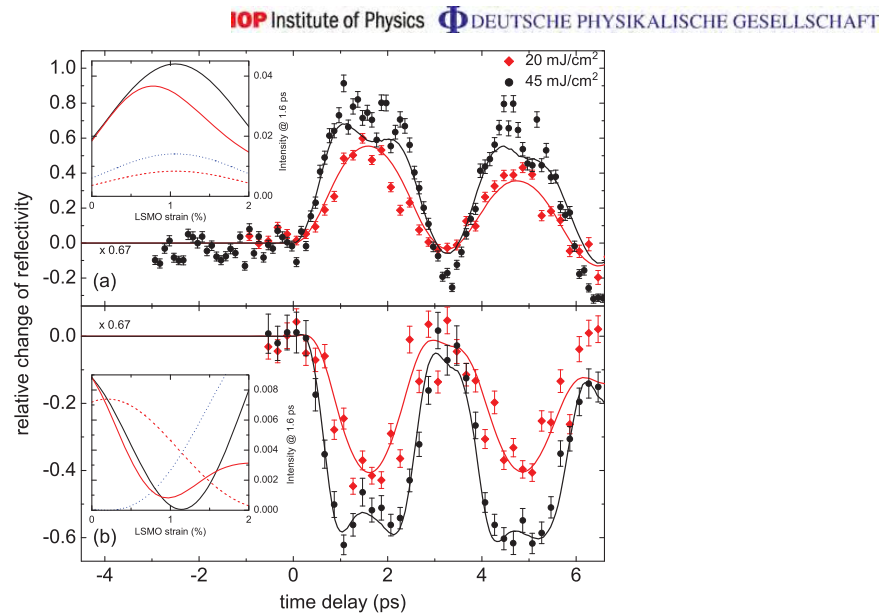


Figure 4. Relative change of the Bragg intensity of (a) the ZOP and (b) the +1 SL peak for the LSMO/STO SL. See figure 3 and the text for plot details.

curve of this particular sample at each point in time and for any strain amplitude. The resulting red line in figure 1(b) shows excellent agreement with the experimental data at 1.6 ps, assuming an average SRO strain of 1.1%.

The photoinduced structure dynamics discussed above lead to a strong decrease of the ZOP intensity with increasing SRO strain, as can be seen in figure 3(a) [13]. According to the EM, this is because the ZOP is governed by the steep flanks of the mutually departing single-layer envelopes. The inset of figure 3(a) compares the ZOP intensity at 1.6 ps as measured (black bullets) and as predicted by the EM (black line) and LCDX (red line). In addition, the contributions of the metallic (red dashed) and insulating (blue dotted) layers are indicated. The EM already yields very good qualitative agreement and illustrates the wide range of linearity up to $\sim 1\%$ average SRO strain. Notably, the LCDX precisely matches the measured ZOP intensity at 1.6 ps (inset). Furthermore, it even accurately reproduces the recorded time scans in figure 3(a). For the highest pump fluence, we deduce an average SRO strain of 1.45% at 1.6 ps.

In the case of SRO/STO ZOP, the linear regime is intrinsically limited because at a certain strain level the ZOP intensity has to vanish, which is indeed the case at about 2% SRO strain. At this point, the first-order minima of both single-layer envelopes approach $q^{(0)}$ (cf inset of figure 3(a)).

In addition to this trivial deviation from linearity, other nonlinear x-ray responses could be identified. As seen in figure 1(a), the +2 SL peak is nearly forbidden in the stationary SL because it is enclosed by the first minima of the SRO and STO layer envelopes [13]. Panel (b) shows that this peak exhibits a strongly enhanced intensity at 1.6 ps due to the structural dynamics. The inset of figure 3(b) indicates the highly nonlinear dependence of this reflection on the SRO

expansion as predicted by the EM (black line). A small strain initially suppresses the peak intensity as it completely shifts the minima of the single-layer envelopes to $q^{(+2)}$. Only above a threshold strain of $\sim 0.5\%$ does this peak attain considerable intensity, mainly due to the increase of the STO envelope function (blue dotted line).

A comparison of the experimental transient intensity of the +2 SL peak with the LCDX calculations presented in figure 3(b) again reveals very good agreement. As the SL phonon amplitude builds up, the intensity first remains unchanged within the signal-to-noise ratio of the experiment up to 800 fs, then rapidly increases to its maximum at about 1.6 ps and subsequently drops back to zero where it again remains for 800 fs. This behavior is repeated for the next periods with lower amplitude according to the energy loss of the SL phonon [14]. This ‘gating’ of x-ray Bragg reflectivity has an FWHM duration of $\lesssim 900$ fs around the maximum at 1.6 ps. Although the EM covers all essential features of the +2 SL peak response (nonlinearity, threshold behavior), the inset of figure 3(b) indicates that the EM predictions quantitatively deviate from the precise LCDX simulations.

As a further test of our models, we present experimental and numerical results for the LSMO/STO SL, including similar linear and nonlinear effects. In addition, however, a transient destructive interference of the diffracted components of the individual layers is identified. The Θ - 2Θ scan of the SL is shown in figure 2. Again, the ZOP of the LSMO/STO SL is located between the individual envelope functions, however this time with interchanged envelope positions of the metallic and insulating layers. According to the EM, this should lead to an increase of the ZOP intensity due to approaching envelope maxima. This is confirmed by the UXRD measurements reported in figure 4(a), which shows the response of the ZOP. The corresponding inset reveals that the EM predicts a linear increase of the ZOP intensity at 1.6 ps up to $\sim 0.5\%$ LSMO strain (black line); at $\sim 1\%$ it reaches a maximum and then even starts to drop again. This non-monotonic dependence can again be understood by the two approaching envelope functions which maximally overlap at an LSMO strain of $\sim 1\%$ where they provide the highest intensity for the ZOP. For higher strain, the ZOP intensity decreases as the envelope maxima separate again. The experimental data at higher pump fluence in figure 4(a) are indeed indicative of this behavior since we observe a clear plateau around 1.6 ps meaning that the turning point has been reached. Once more, the LCDX satisfactorily simulates the data, although the effects are overestimated and thus have to be scaled down to coincide with the experimental data. The reason for this will be discussed below. The inset in figure 4(a) shows that the EM (black line) qualitatively approximates the LCDX (red line).

In the case of other SL peaks, figure 2(b) reveals that the EM yields a crude underestimation of the peak intensities for a homogeneous LSMO strain of 1.15%. We exemplify the underlying mechanism by investigating the +1 SL peak of the LSMO/STO SL at $q^{(+1)} = q^{(0)} + g_{\text{SL}}$ in more detail. Figure 2(b) as well as the inset of figure 4(b) demonstrate that even though both single-layer envelope functions predict a considerable intensity at 1.15% LSMO strain, the DL envelope vanishes. This is caused by the destructive interference of the x-ray waves diffracted from one LSMO and the adjacent STO layer. The experimental data in figure 4(b) indeed show that for high excitation fluence the signal minimum of the transient around 1.6 ps splits up, verifying the destructive interference and the implied non-monotonic dependence on strain. The LCDX (solid lines in figure 4(b)) predicts the relative intensity decrease to be 50% larger compared to what we measured, most likely because the XRD simulations assume a perfect crystal lattice without any kind of disorder or interdiffusion. The simpler EM even predicts a perfect destructive interference of the x-rays which is much less pronounced in the LCDX

calculations since the true strain pattern is taken into account. Thus, it is not surprising that the LCDX still overestimates the effect of the interference. A similar reason holds for the ZOP.

In conclusion, we have presented predictions of combined model calculations simulating the transient strain field dynamics of photoexcited metal/insulator SLs and the induced transient XRD response. We compare these predictions to various UXRD data taken on SRO/STO and LSMO/STO SLs and find excellent agreement for both linear and nonlinear x-ray response to the induced strain. In particular, we have theoretically predicted and experimentally observed a peculiar destructive interference of x-ray waves in an LSMO/STO SL and a highly nonlinear response in an SRO/STO SL. The observations are interpreted by means of a simpler EM connecting the overall x-ray response to the structural dynamics of the individual layers. The EM correctly covers all transient features and often allows quantitative estimations. For precise simulations, the LCDX has to be evaluated. The presented findings emphasize that UXRD experiments can be accurately interpreted to reveal the transient structural dynamics of epitaxial crystals on subpicosecond time scales. They will open paths for simulation-based design of future ultrafast x-ray devices exploiting such nonlinear or interference phenomena that can be tailored into the nanostructures.

Acknowledgments

The time-resolved experiments were performed on the X05LA beamline at the Swiss Light Source, Paul Scherrer Institut, Villigen PSI, Switzerland. We thank the DFG for supporting the project via BA 2281/3-1 and SFB 762.

References

- [1] Authier A 2003 *Dynamical Theory of X-Ray Diffraction* (Oxford: Oxford University Press)
- [2] Shvyd'ko Yu V, Lerche M, Wille H C, Gerdau E, Lucht M, Rüter H D, Alp E E and Khachatryan R 2003 x-ray interferometry with microelectronvolt resolution *Phys. Rev. Lett.* **90** 013904
- [3] Snigirev A, Snigireva I, Kohn V, Yunkin V, Kuznetsov S, Grigoriev M B, Roth T, Vaughan G and Detlefs C 2009 x-ray nanointerferometer based on Si refractive bilenses *Phys. Rev. Lett.* **103** 064801
- [4] Bargheer M, Zhavoronkov N, Woerner M and Elsaesser T 2006 Recent progress in ultrafast x-ray diffraction *Chem. Phys. Chem.* **7** 783–92
- [5] Chergui M and Zewail A H 2009 Electron and x-ray methods of ultrafast structural dynamics: advances and applications *Chem. Phys. Chem.* **10** 28–43
- [6] Johnson S L, Vorobeva E, Beaud P, Milne C J and Ingold G 2009 Full reconstruction of a crystal unit cell structure during coherent femtosecond motion *Phys. Rev. Lett.* **103** 205501
- [7] Lindenberg A M *et al* 2005 Atomic-scale visualization of inertial dynamics *Science* **308** 392–5
- [8] Sokolowski-Tinten K *et al* 2003 Femtosecond x-ray measurement of coherent lattice vibrations near the Lindemann stability limit *Nature* **422** 287–9 (arXiv:10.1038/nature01490)
- [9] Grigoriev A, Dal-Hyun Do, Dong Min Kim, Chang-Beom Eom, Evans P G, Adams B and Dufresne E M 2006 Subnanosecond piezoelectric x-ray switch *Appl. Phys. Lett.* **89** 021109
- [10] Navirian H A, Herzog M, Goldshteyn J, Leitenberger W, Vrejoiu I, Khakhulin D, Wulff M, Shayduk R, Gaal P and Bargheer M 2011 Shortening x-ray pulses for pump-probe experiments at synchrotrons *J. Appl. Phys.* **109** 126104
- [11] Tanaka Y, Hara T, Yamazaki H, Kitamura H and Ishikawa T 2002 Optical switching of x-rays using laser-induced lattice expansion *J. Synchrotron Rad.* **9** 96–8

- [12] Bucksbaum P H and Merlin R 1999 The phonon Bragg switch: a proposal to generate sub-picosecond x-ray pulses *Solid State Commun.* **111** 535
- [13] Herzog M, Leitenberger W, Shayduk R, van der Veen R, Milne C J, Johnson S L, Vrejoiu I, Alexe M and Hesse D 2010 Ultrafast manipulation of hard x-rays by efficient Bragg switches *Appl. Phys. Lett.* **96** 161906
- [14] Herzog M, Schick D, Gaal P, Shayduk R, von Korff Schmising C and Bargheer M 2011 Analysis of ultrafast x-ray diffraction data in a linear-chain model of the lattice dynamics *Appl. Phys. A* **at press**
- [15] Als-Nielsen J and McMorrow D 2001 *Elements of Modern X-Ray Physics* (New York: Wiley)
- [16] Bauer G 1996 *Optical Characterization of Epitaxial Semiconductor Layers* (Berlin: Springer)
- [17] Bargheer M, Zhavoronkov N, Gritsai Y, Woo J C, Kim D S, Woerner M and Elsaesser T 2004 Coherent atomic motions in a nanostructure studied by femtosecond x-ray diffraction *Science* **306** 1771–3
- [18] von Korff Schmising C, Bargheer M, Kiel M, Zhavoronkov N, Woerner M, Elsaesser T, Vrejoiu I, Hesse D and Alexe M 2007 Coupled ultrafast lattice and polarization dynamics in ferroelectric nanolayers *Phys. Rev. Lett.* **98** 257601
- [19] Beaud P, Johnson S L, Streun A, Abela R, Abramsohn D, Grolimund D, Krasniqi F S, Schmidt T, Schlott V and Ingold G 2007 Spatiotemporal stability of a femtosecond hard-x-ray undulator source studied by control of coherent optical phonons *Phys. Rev. Lett.* **99** 174801
- [20] Kostic P, Okada Y, Collins N C, Schlesinger Z, Reiner J W, Klein L, Kapitulnik A, Geballe T H and Beasley M R 1998 Non-fermi-liquid behavior of srro3: evidence from infrared conductivity *Phys. Rev. Lett.* **2009** 2498–501
- [21] Liu H L, Lu K S, Kuo M X, Uba L, Uba S, Wang L M and Jeng H T 2006 Magneto-optical properties of $\text{La}_{0.7}\text{Sr}_{0.3}\text{MnO}_3$ thin films with perpendicular magnetic anisotropy *J. Appl. Phys.* **99** 043908

Paper X

Analysis of ultrafast X-ray diffraction data in a linear-chain model of the lattice dynamics

M. Herzog, **D. Schick**, P. Gaal, R. Shayduk, C. von Korff Schmising, and M. Bargheer
Appl. Phys. A 106, 3 (2011)

Analysis of Ultrafast X-ray Diffraction Data in a Linear-Chain Model of the Lattice Dynamics

M. Herzog¹, D. Schick¹, P. Gaal¹, R. Shayduk², C. v. Korff Schmising³, M. Bargheer^{1,2}

¹ Institute of Physics and Astronomy, University Potsdam, Karl-Liebknecht-Strasse 24-25 14476 Potsdam
 e-mail: bargheer@uni-potsdam.de

² Helmholtz-Zentrum Berlin für Materialien und Energie GmbH, Hahn-Meitner-Platz 1, 14109 Berlin, Germany

³ Atomic Physics Division, Department of Physics, Lund University, P.O. Box 118, 22100 Lund, Sweden

Received: date / Revised version: date

Abstract We present ultrafast x-ray diffraction (UXRD) experiments which sensitively probe impulsively excited acoustic phonons propagating in a SrRuO₃/SrTiO₃ superlattice and further into the substrate. These findings are discussed together with previous UXRD results [1–4] using a normal mode analysis of a linear-chain model of masses and springs, thus identifying them as linear-response phenomena. We point out the direct correspondence of calculated observables with x-ray signals. In this framework the complex lattice motion turns out to result from an interference of vibrational eigenmodes of the coupled system of nanolayers and substrate. UXRD in principle selectively measures the lattice motion occurring with a specific wavevector, however, each Bragg reflection only measures the amplitude of a delocalized phonon mode in a spatially localized region, determined by the nanocomposition of the sample or the extinction depth of x-rays. This leads to a decay of experimental signals although the excited modes survive.

[7]. The resulting standing strain wave was essentially an optical phonon with wavevector $Q = 0$, as it corresponded to the motion of atoms within the super unit cell (one double layer GaAs/AlGaAs) and to a good approximation the substrate could be neglected. No lineshift of the Bragg reflection was observed, evidencing that the size of the super unit cell remained constant on the timescale of the experiment. When the number P of double layers is smaller, e.g. $P = 11$, as was the case in a previously studied oxide SL of SrRuO₃/SrTiO₃ (SRO/STO), the coupling to the substrate leads to a decay of the SL motion.[1–4,8] The timescale of this decay is set by the SL expansion time, corresponding to the time $T = D/v_{\text{SL}} \approx 35$ ps it takes an acoustic phonon to traverse the SL thickness $D = P \cdot d_{\text{SL}} \approx 250$ nm at the average sound velocity v_{SL} . [9,10]

A key advantage of UXRD is the direct correspondence of the real-space periods with the wavevector transfer $\mathbf{q} = \mathbf{k} - \mathbf{k}' = \mathbf{G} \pm \mathbf{Q}$ encoded in a generalized Laue condition, where $G = |\mathbf{G}| = 2\pi/c$ is a reciprocal lattice vector corresponding to the real-space lattice spacing c and \mathbf{Q} is the wavevector of a specific phonon mode. In SLs $G = n \cdot g$ ($n \in \mathbb{N}$) is an integer multiple of the reciprocal SL vector $g = 2\pi/d_{\text{SL}}$. [11] The first achievement of UXRD was to show that coherent acoustic phonons in bulk lattices lead to a temporal modulation of the x-ray diffraction signal at $G \pm Q$ according to the phonon dispersion relation $\omega(Q)$. [12–14] The SL phonon modes exhibit a time dependence according to their frequency $\omega_{\text{SL}} = \omega(Q = 0)$ as an intensity modulation of the SL Bragg peak, as they are optical modes at the mini-Brillouin zone center ($Q = 0$). Exciting a thin Ge film resulted in sidebands to the bulk reflection of a Si substrate at G_{Si} and a continuous shift and broadening of the Ge reflection at G_{Ge} . [15] Experiments on InGaAs/InAlAs SLs also reported shifts of the SL Bragg peaks, and in addition the “unfolding” of the SL phonon with wavevector Q_{SL} into the InP substrate leading to new reflections at $G_{\text{sub}} \pm Q_{\text{SL}}^*$. [16] In all these cases, the excitation of a

1 Introduction

Ultrafast x-ray diffraction (UXRD) is capable of monitoring atomic motion in solids on the atomic length and timescale. It has been applied to the study of optical and acoustic phonons and in particular to zone-folded longitudinal acoustic phonons (ZFLAPs) in superlattices (SLs), which can be viewed as acoustic or optical phonons, from the perspective of the bulk or the SL-mini-Brillouin zone, respectively. [5,6] In theory, the mini-Brillouin zone is defined for an infinite SL. Experimentally, this is approximated by periodically stacking a large number P of epitaxial double layers of two different crystal lattices (e.g. GaAs/AlGaAs) on top of each other. Such a SL with $P = 2000$ and a double layer period d_{SL} was recently investigated after homogeneous excitation with femtosecond laser pulses

broad acoustic phonon spectrum leads to a continuous shift of peaks or the development of a sideband to an existing peak.

In this paper we present UXRd measurements on a photoexcited SRO/STO SL that shows the disappearance of a Bragg reflection at a particular $G = n \cdot g$ and its reappearance at a different $G' = n \cdot g'$ corresponding to an expanded SL without exhibiting a continuous shifting of the rocking curve. In addition, very clear sidebands to the bulk substrate reflection show up. Continuous shifts as well as sidebands of thin film and substrate Bragg peaks have been previously discussed in the context of acoustic sound propagation [12–18]. Here, we focus on analysing such features, including recently published UXRd data on the same SRO/STO SL, within a simple linear-chain model which describes the longitudinal phonon spectrum of the SL on a substrate. We discuss in detail which modes are optically excited and how this gives rise to both propagating and standing waves in the structure. We analyze how the different features of the lattice dynamics can be directly measured and calibrated by UXRd and calculate rocking curves using dynamical x-ray diffraction theory. It turns out that the disappearance and reappearance or rather splitting of the Bragg peak reflects the short-timescale dynamics of the coherent acoustic phonon spectrum within the SL for strong excitation. The sidebands of the substrate peak measure the appearance of this coherent wavepacket distortion in the substrate, whereas the appearance of the $G_{\text{sub}} \pm Q_{\text{SL}}^*$ peaks [16] show the spatial period of the SL phonon after it has propagated (unfolded) into the substrate. All these phenomena are quantitatively predicted by the presented model and therefore identified as a linear response of the sample.

2 Experiments

2.1 Results

Fig. 1 shows the TEM cross section of the SRO/STO SL together with a schematic of the experiment. An optical pump pulse is absorbed by the metallic SRO layers of the sample leading to a quasi-instantaneous spatial stress profile $\Delta(z)$ indicated by the red line. A time-delayed x-ray probe pulse measures the excited sample by diffraction of monochromatic x-ray photons impinging on the sample at different Bragg angles.

We used the laser-based femtosecond x-ray diffractometer at University of Potsdam, which is very similar to the one described recently [19] for measuring a particular SL reflection, whereas transients of the STO substrate peak were recorded at the Femto-slicing beamline of the Swiss Light Source (SLS). [20] The inset of Fig. 2 shows an overview of the sample's diffraction profile around the bulk (0 0 2) reflection of the substrate. The time dependence of the strongest SL peak with the SL-Miller index (0 0 116) has been characterized previously

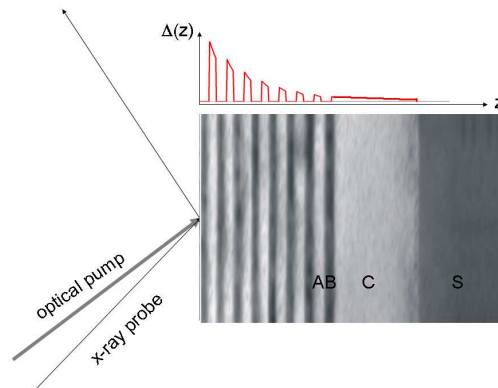


Fig. 1 Schematic of the experiment. An optical laser pulse excites a SL sample with the stacking sequence $(B_n/A_m)_pCS$ (shown here as a TEM image), generating a stress profile $\Delta(z, t = 0)$ (upper panel). In the particular sample shown $A = \text{SRO} = \text{SrRuO}_3$, $B = \text{STO} = \text{SrTiO}_3$, contact layer $C = A$ and substrate $S = B$.

according to its so-called shift within 30 ps and its intensity modulation which shows a period of 3.2 ps due to the SL phonon. [1–4] This modulation decays with a similar time constant of approx. 30 ps.

A new and more detailed set of experimental results on this (0 0 116) reflection is presented in Fig. 2. We measured the time-dependent diffracted x-ray intensity $I(q, t)$ for different wavevector transfers $q = \sin(\theta)4\pi/\lambda$. The Bragg reflectivity is defined by $R(q, t) = I(q, t)/I_0(q)$, where $I_0(q)$ is the x-ray intensity incident on the sample. Fig. 2c) shows the difference spectra $R(q, t) - R_0(q)$, i.e., the changes of the Bragg-reflectivity curve of the sample for a specific time delay t with respect to the spectra averaged over time delays before the excitation pulse $R_0(q) = R(q, t \leq 0)$ (dashed line). This procedure removes a background contribution to the signal (thin black line) which originates from the focusing of x-rays by a multilayer mirror and leads to signals on the x-ray CCD detector at all angles. For comparison, panel b) shows the good agreement to the corresponding difference spectra from the simulation (see theory section) and panel a) shows the calculated spectra directly, clearly representing the disappearance of the right peak and its reappearance to the left. Note, that the appearing peak has strongly shifted components around 31.9 nm^{-1} for early times ($0 < t < 20 \text{ ps}$) and it slightly moves back towards larger angles at later times ($t > 20 \text{ ps}$). The details such as height, position and shape of the peaks in the experimental and calculated difference spectra show excellent agreement. The spectrum for $t = 0$ (thick black line in Fig. 2c) demonstrates that the difference-spectra actually lead to a correct subtraction of the unwanted background as the experimentally measured difference signal is approximately zero.

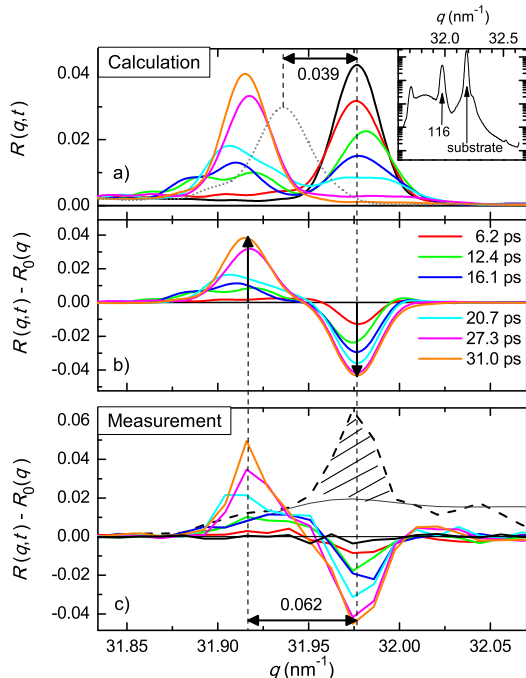


Fig. 2 a) Calculated rocking curves in the vicinity of the (0 0 116) SL reflection as a function of pump-probe time delay. Inset: Extended rocking curve including the (0 0 2) STO substrate peak.[1] b) Derived difference rocking curves with same color code for $t > 0$. c) Measured unpumped rocking curve (dashed line) including background contribution (thin black line). The thick black line shows the difference curve for $t = 0$. Other lines show the measured difference rocking curves with the same color code as in panel a).

Without detailed simulation, the splitting of the SL-Bragg peak for intermediate times can be attributed to two regions of the SL, one having the static spatial SL-period d_{SL} (right peak) and one exhibiting an expanded lattice. The maximum strain of the entire SL occurs at a time delay of approx. 35 ps.

$$\epsilon_{\max} = \frac{D_{\max} - D(0)}{D(0)} = \frac{q_{\max}^{-1} - q(0)^{-1}}{q(0)^{-1}} \quad (1)$$

From Fig. 2 we read $\epsilon_{\max} \approx 0.062/31.975 = 1.9 \cdot 10^{-3}$. This experiment was performed at the femtosecond x-ray diffractometer in Potsdam with laser pulses (≈ 100 fs, 800 nm) at a fluence of approx. 10 mJ/cm^2 .

For a higher angular resolution we recorded shoulders of the STO substrate reflection we performed diffraction experiments with the highly collimated x-rays of the FEMTO-Slicing-beamline at the SLS. The resulting rocking curves recorded under somewhat increased fluence and at 400 nm pump wavelength are presented in Fig. 3. Cross-checks with 800 nm pump pulses show similar results.

From the angular separation of the shoulder from the substrate peak we can estimate the amplitude of the strain wave in the substrate to be $\epsilon_{\text{STO}} = \Delta c/c = 0.04/32.2 \approx 1.24 \cdot 10^{-3}$, which is somewhat smaller than the expansion of the SL observed above.

2.2 Discussion of Results

In the following we discuss how the total optical excitation energy is deposited in the lattice. Using the absorption depth $\zeta_{\text{SRO}} = 52 \text{ nm}$ and the absorbed pump fluence $F = 10 \text{ mJ/cm}^2$, the energy density absorbed by the conduction band electrons of SRO in each layer exponentially decays from $\rho_E^{\text{SRO}} = 1.8 \cdot 10^9 \text{ J/m}^3$ in the first to $\rho_E^{\text{SRO}} = 4.3 \cdot 10^8 \text{ J/m}^3$ in the tenth layer.[1] This energy is then coupled to phonons of SRO on a 100 fs timescale which essentially leads to the expansion of the SL layers.[1–4] We assume that the expansion of the SL is induced exclusively by an expansion of SRO layers with a linear thermal expansion coefficient $\alpha_{\text{SRO}} = 1 \cdot 10^{-5} \text{ K}^{-1}$ and a volumetric heat capacity $C_{\text{SRO}}^{\text{heat}} = 3 \cdot 10^6 \text{ J/(K m}^3)$ of SRO.[9]. The average deposited energy density $\rho_{\text{av}}^{\text{SRO}} = 1.04 \cdot 10^9 \text{ J/m}^3$ in the SRO layers then corresponds to a temperature rise of $\Delta T = \rho_{\text{av}}^{\text{SRO}}/C_{\text{SRO}}^{\text{heat}} = 347 \text{ K}$. The relative expansion of the entire SL due to the exclusive expansion of SRO is $\epsilon(\Delta T) = d_{\text{SRO}}\alpha\Delta T/d_{\text{SL}} = 1.2 \cdot 10^{-3}$ which is similar to ϵ_{\max} .

In a next step, we calculate the energy density transferred to coherent acoustic strain in the SL and later on in the substrate from the measured UXRD data. First, we estimate the amount of energy in the coherent acoustic modes that lead to the observed maximum shift of the SL reflection (Fig. 2). The elastic modulus $E = v_{\text{SL}}^2 \cdot \rho$ is calculated from the averaged longitudinal sound velocity v_{SL} and the mass density ρ of STO and SRO. From the observed maximum strain ϵ_{\max} in the SL with a thickness of $D = 250 \text{ nm}$ we infer the deformation energy density of the SL, i.e. the integrated energy in the longitudinal acoustic modes, to be $\rho_{\text{LA}}^{\text{SL}} = 1/2 E \epsilon_{\max}^2 = 5.3 \cdot 10^5 \text{ J/m}^3$, corresponding to a fraction of approx. $5.2 \cdot 10^{-4}$ of the optically deposited energy density. We will see in the discussion of the theory section that this overestimates the coherent sound energy. In fact, not the maximally shifted curve in Fig. 2a but rather the grey dotted curve shows the peak shift corresponding to the heat expansion $\epsilon_{\text{heat}} = 1.2 \cdot 10^{-3}$ of the sample which—as we will show—also corresponds to the amplitude of the coherent strain wave.

Second, we alternatively consider the observed shoulders of the substrate peak in Fig. 3. As no heat is deposited in the substrate, the lattice deformation indicated by these shoulders must originate from the coherent sound waves propagating into the substrate. In the theory section we will show that in fact both the splitting of the SL peak and the substrate peak shoulders probe

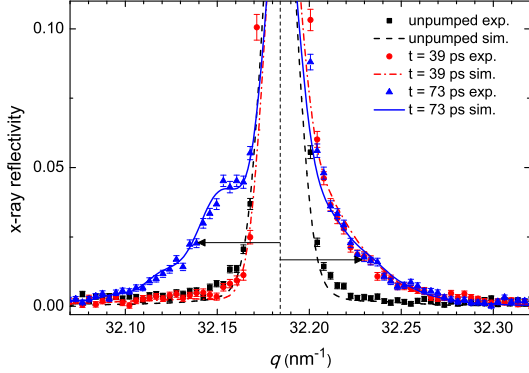


Fig. 3 X-ray diffraction curves in the vicinity of the (0 0 2) STO substrate reflection. Symbols report the measured data, lines correspond to simulations (see text). At 39 ps (73 ps) after the laser-pulse excitation a compression (expansion) wave has entered the substrate, giving rise to the shoulder on the high-angle (low-angle) side. The asymmetry originates from complex interferences of the x-rays from the distorted and undistorted parts of the substrate.

the same superposition of eigenmodes, however, the SL peak probes these delocalized phonons locally within the 250 nm thick SL, whereas the substrate shoulders probe the same modes locally in the first few microns of the substrate. During the propagation into the substrate the ratio of the sound velocities $s = v_{\text{STO}}/v_{\text{SL}} \approx 1.3$ leads to a traveling wave with total length of $l_W = 2sD = 650$ nm (compressive + tensile part). The average compressive and tensile strain ϵ_{STO} inferred from the substrate peak shoulders on the high- q and low- q side, respectively, yields an energy density $\rho_{\text{LA}}^{\text{STO}} = 3.5 \cdot 10^5$ J/m³. Comparing this to $\rho_{\text{LA}}^{\text{SL}}$ one finds that the energy density of the coherent sound is smaller in the substrate, however, the acoustic energy fluence $F_{\text{LA}} = \rho_{\text{LA}}^{\text{STO}} \cdot l_W \approx \rho_{\text{LA}}^{\text{SL}} \cdot D$, i.e., the coherent acoustic energy per excited sample area, is conserved (cf. Fig. 7).

This implies that at the used pump fluence, only a fraction of $F_{\text{LA}}/F = 5 \cdot 10^{-4}$ of the deposited energy is converted into coherent acoustic waves, whereas the rest remains as incoherent phonons, i.e. lattice heat. Note that the energy density ρ_{LA} of the coherent wave is proportional to the square of the strain ϵ^2 , whereas the deposited heat energy $\rho_{\text{av}}^{\text{SRO}}$ is proportional to ϵ according to linear heat expansion. For lower fluences an even smaller fraction of light energy is converted to the coherent sound wave.

3 Theory

In order to analyze the experimental results quantitatively, to visualize the dynamics and to verify that even under such strong excitation the response of the sample is still linear, we set up a linear-chain model of masses

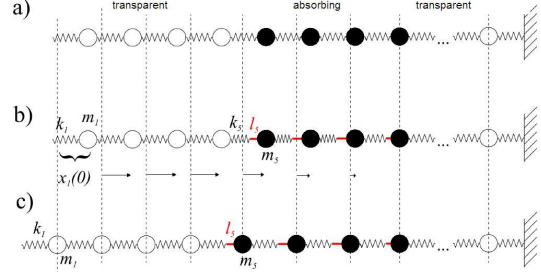


Fig. 4 Schematic of the linear-chain model. a) For $t < 0$ all masses are at rest. b) At $t = 0$ an excitation stress Δ is induced, which is subsequently constant. In the linear-chain schematic it is represented by incompressible sticks, which lead to an instantaneous compression of the springs in the opaque material A . The force constant of the springs remains unchanged. For $t > 0$ masses move according to the new forces. c) Rest positions of masses x_i^∞ for $t \rightarrow \infty$.

and springs. A similar linear-chain model was presented in Ref. [21] for the discussion of ultrafast electron diffraction data on a thin metal film. In the following we describe the extension to superlattices. More importantly we present a normal-mode analysis of this linear-chain model and discuss how this is relevant to the interpretation of diffraction data.

3.1 Linear-chain model

We consider a multilayer with the stacking sequence $(B_n/A_m)_P C S$ composed of m unit cells of an opaque material A and n unit cells of a transparent material B epitaxially grown as a SL with P periods on a virtually infinitely thick and transparent substrate S with a thin contact (electrode) layer C (cf. Fig. 1). The SL is excited with an ultrashort optical light pulse. This heats up the opaque layers A and induces expansive thermal stress $\Delta(z)$ on a timescale τ_Δ short compared to all atomic motions that are of interest in this paper ($\tau_\Delta \ll 1/\omega_{\text{SL}}$). The excitation stress $\Delta(z_A) \sim e^{z_A/\zeta_A}$ varies as a function of penetration depth z_A through opaque layers A and is basically determined by the bulk optical absorption length ζ_A . As a first approximation, we assume that on the timescale of interest, the thermal stress remains constant after the excitation, i.e. $\Delta(z, t) = \Delta(z)H(t)$, where $H(t)$ is a Heaviside step function in time t . In other words, we disregard slow cooling by heat conduction. This assumption is justified by experiments showing that the generated stress is essentially independent of the photon energy [3], and that it is confined within SRO layers for at least 200 ps [2]. We disregard the distinction of electron and phonon contributions to the stress [21] as this should only marginally affect the timing in our experiments.

For the simulation of acoustic waves in the structure we construct a one-dimensional model of N masses and springs along the z -direction (c -axis), where each unit cell is represented by a mass m_A , m_B , m_C and m_S , respectively, which are connected by springs having a force constant $k_i = m_i v_i^2 / c_i^2$. Here v_i is the longitudinal sound velocity, m_i is the mass and c_i is the out-of-plane lattice constant of the i^{th} unit cell ($i = 1, 2, \dots, N$).¹ This model allows the simulation of all longitudinal acoustic modes propagating perpendicular to the surface of the sample. It neglects longitudinal optical modes of the bulk crystals A , B , C and S and all transverse motions. Alternatively, one could follow a continuum-model approach [6], however, here we want to focus on a normal-mode analysis.

To calculate the displacements $x_i(t) = z_i(t) - z_i^0$ from the equilibrium positions z_i^0 in a linear chain of N masses m_i that are connected by springs with force constants k_i and are subject to an additional force $F_i(t)$ (optically induced stress), we have to solve a system of N linear inhomogeneous differential equations

$$m_i \ddot{x}_i = -k_i(x_i - x_{i-1}) - k_{i+1}(x_i - x_{i+1}) + F_i(t) \quad (2)$$

where $i = 1, \dots, N$.

Unlike Ref. [21] we do not solve this set of equations by numerical integration (such as Runge-Kutta methods) but rather find the general solution

$$\mathbf{X}(t) = \sum_{j=1}^N \Xi_j \cdot A_j e^{i\omega_j t}. \quad (3)$$

by diagonalization of the force matrix (see appendix) in terms of eigenvectors Ξ_j to the eigenvalues (eigenfrequencies) ω_j of the system, which in fact represent the acoustic phonon modes of this nanostructure. $\mathbf{X}(t)$ is a vector containing the time-dependent coordinates $x_i(t)$ of all masses. The appropriate boundary condition is depicted in Fig. 4 which shows that at $t = 0$ the springs are quasi-instantaneously compressed (laser induced stress $\Delta(z)$ in SRO) and subsequently evolve towards the configuration for $t \rightarrow \infty$ where all springs attain their original length.

We use the physical insight that the additional time-independent forces proportional to $\Delta(z)$ trigger a “displacive excitation of coherent phonons” (DECP) by displacing the equilibrium position of the masses. Since the essential effect of heating material A is its expansion while keeping the compressibility constant, we can visualize this process by instantaneously inserting incompressible spacer-sticks between the springs and the atoms, which have a length proportional to $\Delta(z)$ (see Fig. 4b). After very long times ($t \rightarrow \infty$), the linear chain would relax into configuration (Fig. 4c) where all springs are at their equilibrium length, which they had before

¹ This corresponds to an elastic modulus $E = \rho v^2$ in a continuum-model approach.

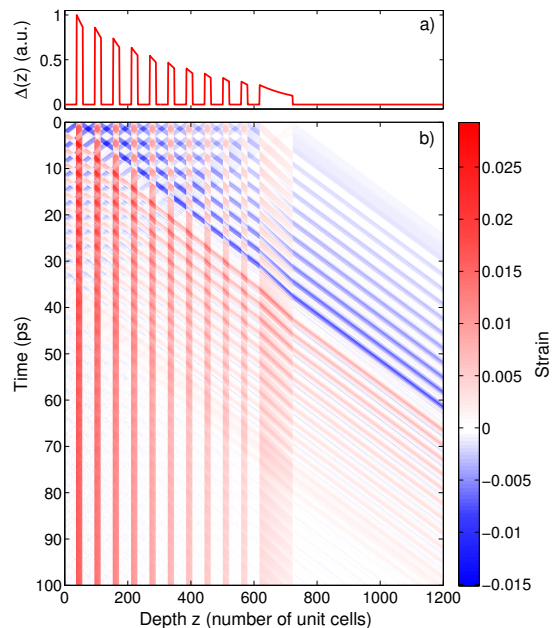


Fig. 5 a) Stress profile $\Delta(z, t = 0)$. b) Contour plot showing the calculated strain in the sample as a function of space and time for the SRO/STO SL investigated experimentally.[1–4]

excitation (Fig. 4a). After solving the equations for all coordinates $x_i(t)$, one can now analytically calculate the relative displacement of the masses $\Delta x_i = x_i - x_{i-1}$ and the corresponding strain $\epsilon_i = [\Delta x_i(t) - \Delta x_i(0)] / \Delta x_i(0)$ for any time t and any given initial stress profile $\Delta(z)$.

This model contains no anharmonic interaction potential and we expect a linear response of the lattice dynamics proportional to the excitation stress $\Delta(z)$. The amplitude of $\Delta(z)$ is the only fitting parameter in this simulation. The lattice parameters, elastic constants, heat capacity etc. are taken from the literature, as well as the absorption length ζ_A . The calibration of the stress amplitude is simply achieved by matching the experimentally observed change of SL-Bragg angle to the average lattice expansion. Fig. 5 shows the result of such a calculation for an SRO/STO SL including the ≈ 42 nm SRO contact layer[1] with an absorption length of the optical excitation light of $\zeta_{\text{SRO}} = 52$ nm.[22] Both standing strain wave contributions with the spatial period of the SL and propagating strain waves can be seen in this contour plot. The slopes of the diagonal stripes directly visualize the local average sound velocity $v_{\text{SL}} = \Delta z / \Delta t$, which is slightly different in the SL, contact layer and substrate.

In order to discuss the significance of eigenmodes in SLs we compare the situation of a few-period SL with $P = 11$ to an infinite SL by imposing periodic boundary conditions. Such an infinite SL was well approximated in the experiments on a GaAs/AlGaAs SL with

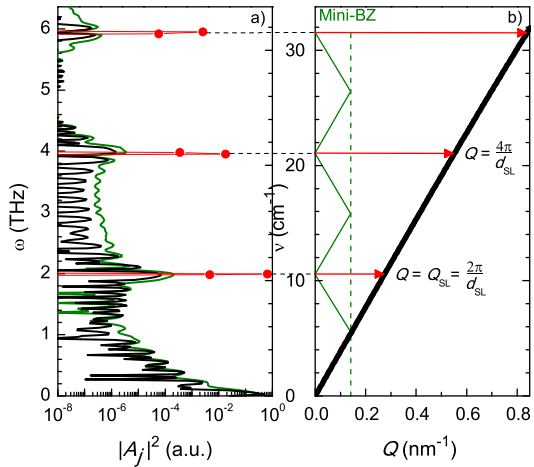


Fig. 6 a) Power spectrum of strain evolution decomposed into amplitudes $|A_j|^2$ of eigenmodes to eigenfrequency ω_j for the infinite SRO/STO SL (periodic boundary condition) with homogeneous excitation ($\zeta_{\text{SRO}} \rightarrow \infty$, red dots) and for the finite SL ($P = 11$) with homogeneous excitation (thin green line) and the experimental optical penetration depth of $\zeta_{\text{SRO}} = 52$ nm (thick black line). Note that for the infinite SL single mode is excited. b) Dispersion relation of a SL from linear-chain model (thick black line) back-folded into the mini-Brillouin-zone (thin blue line).

$P = 2000$. [7, 23] For better comparison, the present calculation is performed for the SRO/STO SL discussed above using periodic boundary conditions. Plotting the eigenfrequencies ω_j as a function of the normal-mode wavevector Q_j visualizes the phonon dispersion relation $\omega(Q)$ (cf. Fig. 6(b)). For a SL it is useful to recall that the dispersion relation can be represented in a smaller mini-Brillouin zone, where the zone boundary is given by π/d_{SL} instead of π/c if d_{SL} is the thickness of one SRO/STO double layer. Fig. 6(a) compares the squared modulus $|A_j|^2$ of the complex amplitudes for the eigenmodes with frequency ω_j (cf. eq. (3)) in an infinite SL with homogeneous excitation ($\zeta \rightarrow \infty$, red dots), in the $P = 11$ SL with homogeneous excitation (thin green line) and in the $P = 11$ SL with the experimental absorption length of $\zeta_{\text{SRO}} = 52$ nm (black). [22] As the spatial symmetry of the excitation pattern $\Delta(z)$ intrinsically mimics the symmetry of the SL, only eigenmodes with a wavevector equal to integer multiples of the reciprocal SL wavevector $Q_{\text{SL}} = g = 2\pi/d_{\text{SL}}$ are selected. For an infinite SL such modes are optical phonons at the zone center of the mini-Brillouin zone scheme (zone-folded dispersion relation plotted in blue in Fig. 6(b)). In this case only few modes are excited. One of them has almost unit probability and we refer to it as the symmetric SL mode with period $T_{\text{SL}} = 2\pi/\omega_{\text{SL}}$, as it corresponds to an expansion of the SRO layers symmetric with respect to the center of the SRO layer. [5] The re-

lated asymmetric mode and all higher harmonics have at least two orders of magnitude less weight. Note that the splitting of the symmetric and asymmetric mode is very small ($\Delta\omega/\omega = 4.5 \cdot 10^{-5}$), indicating an excellent acoustic impedance matching, which is evident also from Fig. 5 where almost the entire soundwave is transmitted to the substrate with essentially zero reflection amplitude.

If we simulate a finite SL, i.e., we do not consider the periodic boundary condition, and add a substrate beneath the SL, the symmetry is broken by both the surface of the SL and the interface to the substrate. Under these conditions, several modes are excited with considerable amplitude (cf. green curve in Fig. 6a). The mode density in the simulation depends on the number of substrate unit cells taken into account, however, clearly the modes in the vicinity of the SL mode and its harmonics still have enhanced weight. Here we chose the substrate approximately three times thicker than the SL, in order to prevent reflections from the backside within the simulated timescale in Fig. 5b). It is the breaking of the symmetry by the surface and the substrate that induces the high occupation of low-frequency modes near $\omega = 0$ indicating a propagating sound wave. If the excitation is changed to the exponentially decaying absorption of energy in the SL, only slight modifications of the power spectrum $|A_j(\omega)|^2$ is observed.

There are several advantages of the normal-mode analysis as compared to a numerical propagation of the differential equation: [21] i) It allows rapid calculation of strain pattern for any time t . ii) Individual modes can be switched off to disentangle complex dynamics. iii) The wavevector Q of each mode predicts where the corresponding time dependence will show up in the UXRD signal. iv) Wavepacket dynamics including the coupling of SL and substrate is interpreted as an interference of waves.

3.2 Comparison to experimental data

We first discuss the coarse findings depicted in Fig. 5. For the SL coupled to the substrate, several eigenmodes in the vicinity of ω_{SL} with approximately equal spatial periodicity are excited, however, they extend into the substrate with similar amplitude as well. According to the mini-BZ scheme, at early times these modes give rise to a standing wave composed of waves with $-Q_{\text{SL}}$ propagating towards the surface and Q_{SL} propagating towards the substrate. This standing wave pattern which is localized in the SL disappears when all waves have propagated into the substrate and hence no time-dependence with frequency ω_{SL} remains in the SL. The waves leave the multilayer as propagating sound waves having the central frequency of the SL mode and the wavevector $Q_{\text{SL}}^* = 2\pi/d_{\text{SL}}^*$, which is determined by the ratio of the substrate sound velocity v_{STO} and the average sound velocity in the SL, i.e., $d_{\text{SL}}^* = v_{\text{STO}}T_{\text{SL}} =$

$d_{\text{SL}} \cdot v_{\text{STO}} / v_{\text{SL}}$. [16] The higher harmonics of the SL mode with frequency $\omega_{\text{SL}} = 2\pi/T_{\text{SL}}$ also show considerable—albeit much smaller—amplitudes and support the spatiotemporal sharpness of the sound features observed in Fig. 5. In previous experiments, these folded acoustic phonons at ω_{SL} were observed as intensity modulations of the SL Bragg reflections. [1–4] In a SL these phonons are backfolded to $Q = 0$ (blue dispersion relation in Fig. 6), and hence they show up in the UXRD measurements at the Bragg angle of stationary SL reflections. When the wavepacket has traveled into the substrate, these modes yield sidebands to the substrate at $G_{\text{STO}} \pm nQ_{\text{SL}}^*$, where n is an integer. [16] The origin of these modes can be seen by the small wavelets that are generated at each interface of the SL.

The surface and the contact layer (interface to the substrate) are the spatial origin of the low-frequency modes [cf. Fig. 5b)]. The reflection of the compressive wavepackets at the surface results in an expansion wave traveling straight through the SL into the substrate with marginal reflection at the interface. The contact layer launches a compression wave into the substrate and another one towards the surface, where it is converted into an expansion wave. Inspection of the average strain per double layer in Fig. 5b) at around 15–20 ps shows that one half of the SL is expanded while the other half has preserved the average lattice constant. This qualitatively explains the experimentally observed disappearance of the original SL peak and the appearance of a shifted peak (Fig. 2). There is no continuous shift of the UXRD curve because there is no region in the SL which has an intermediate strain. The initially larger width of the appearing peak is readily explained by the fact that only a small spatial fraction of the SL contributes at these times ($t < 20$ ps). The very same low-frequency acoustic modes give rise to the sidebands of the substrate peak shown in Fig. 3. In particular, at $t = 39$ ps only the right shoulder exists as the substrate is compressed [blue in Fig. 5b)] and at 73 ps also the expansion wave has entirely entered the substrate [green in Fig. 5b)] inducing the shoulder on the left.

The atomic motion calculated from the linear-chain model also allows to extract information on the energy transport by coherent phonons. We compute the kinetic energy of the atoms from their velocity dx_i/dt and the potential energy from the stress as a function of time for both individual types of SL layers and the substrate. Fig. 7 shows the total energy stored in coherent phonons in a box with a cross section of 1 cm^2 .² At $t = 0$ all energy is quasi-instantaneously stored as potential energy in the SRO layers. As one would expect for a single excited oscillator (phonon mode), the energy is converted

² Here we plot the fraction of total energy in a fixed volume stored in the SL, the contact layer and the substrate. Plotting energy densities would not allow to see the energy conservation for the sum of energies.

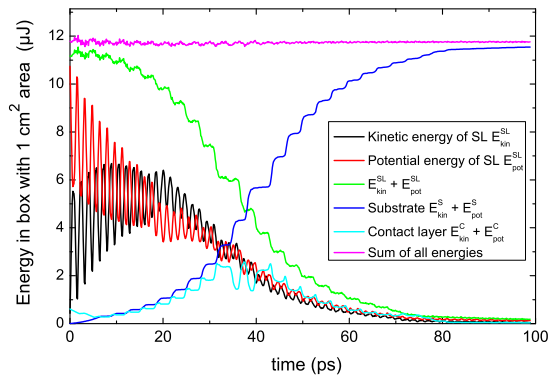


Fig. 7 Energy balance for the finite SL calculated from the linear-chain model. Both the kinetic and potential energy (stress) of the SL have two maxima per period. The energy of the propagating sound wave leaks out of the SL and travels through the contact layer (light blue) into the substrate (dark blue). We assume no considerable heat conduction on this timescale. For an infinite SL the kinetic energy would return to zero after each period (not shown), while in the present case the propagating sound wave always carries kinetic energy.

into kinetic energy and back to potential energy, with two maxima for each type of energy per period. The oscillation period of 3.2 ps is verified by the experimental data. [1–4] On the timescale of sound propagation ($T = D/v_{\text{SL}}$) the vibrational energy leaks into kinetic and potential energy of the substrate. Accordingly, the sum of potential and kinetic energy of the SL decays to half its initial value within 35 ps. The modulation amplitude of the potential energy is reduced by a factor of two faster, namely within 18 ps. This modulation is a direct measure of the energy stored in modes in the vicinity of the superlattice mode ω_{SL} . However, the damping of the signal oscillation amplitude observed in UXRD experiments [1, 4] is underestimated, indicating that additional factors such as anharmonic interaction and dephasing play a role. From the lattice positions $x_i(t)$ we can also calculate the average expansion of the entire SL which reaches a maximum after $T = P \cdot d_{\text{SL}} / v_{\text{SL}} = 35$ ps, in excellent agreement with previous measurements. [4] The maximum wave vector transfer q_{max} observed in Fig. 2 is used to calibrate the maximum average strain in the simulation [eq. (1)].

After $t = 35$ ps already half of the total energy stored in longitudinal acoustic waves has moved from the SL into the contact layer and further into the substrate. It is important to note that this timescale for energy loss is not a coupling time constant, but a timescale describing the interference of the various excited normal modes, which give rise to a propagating sound wave with a particular wave vector. Unless strong differences in the acoustic impedance of the SL and the substrate lead to

substantial reflection of waves at the interface, the expansion wave starting from the surface of the SL reaches the substrate after 35 ps.

In the discussion of UXRd experiments the diffraction of x-ray photons is described as resulting from the scattering by a reciprocal lattice vector and/or a phonon wavevector which describes a delocalized vibration mode. However, the x-ray-diffraction condition probes only particular spatial parts of the sample in which the Bragg condition is fulfilled, even though the vibrational mode is delocalized over the entire crystal.

The loss of modulation amplitude in UXRd signals[1–4] can be explained in our model as resulting from the coupling of the observed part of the sample (SL) to unobserved regions of the sample (substrate). The intensity modulations in the UXRd signal originate from eigenmodes with frequency ω_{SL} . Similarly, the low-frequency acoustic part of the spectrum consists of normal modes which have amplitude in the SL and the substrate. Fig. 2 shows the rapid disappearance of a SL reflection and the appearance of a shifted peak which is completed after 70 ps. The dynamically interfering normal modes subsequently show now time dependence of the SL reflection which only probes the spatial region of the SL. Instead, the observation of the shoulders of the substrate peak in Fig.3 demonstrates that at this time the coherent sound wave is in the substrate.

This implies, that when calculating the coherent wave energy from the transient position of the appearing rocking curve we have to use the value for $t > 70$ ps, as this corresponds to the final state with a tensile and compressive sound wave traveling deeper into the substrate and a quasi-stationary expansion of the SL which is represented in our model by the red spacer sticks (heat expansion) in Fig. 4c). The springs of the SL in this figure are at their equilibrium position, i.e., there is no coherent sound left in the SL. In other words, the coherent wave energy is imposed on the sample by the initial condition which requires the compression of springs in the metallic layers of the SL (Fig. 4b) with respect to the final conditions at $t \rightarrow \infty$ (Fig. 4c). Hence, the expansive strain ϵ_{heat} for $t > 70$ ps, which is approx. 77% of the maximum expansion ϵ_{max} , measures the heat expansion of the SL and consequently the entire coherent sound energy which is encoded in the compressed springs of Fig. 4b) at $t = 0$. For intermediate times the SL peak position is measuring a complex combination of heat expansion and additional expansion and compression due to the coherent sound waves.

Previous experiments have shown pronounced oscillations of the x-ray diffraction efficiency of SL peaks since the structure factor of the SL unit cell is modulated with the frequency ω_{SL} of the SL phonon.[1–4, 7, 8] From the linear-chain model we can deduce the energy contained in the excited modes in the vicinity of ω_{SL} (cf. Fig. 6a). These modes contribute approx. 30% to the total coherent mode energy because the energy per mode

scales as $|A_j|^2 \omega_j^2$. The SL phonon modes itself, however, are neither responsible for the splitting of the appearing peak nor for the shoulders of the substrate. Instead, within the SL they cause the modulation of the peak intensity of SL peaks and within the substrate they give rise to sidebands to the substrate peak at $G_{\text{STO}} \pm n \cdot Q_{\text{SL}}$.

We stress that within our model, at $t = 0$ the delocalized eigenmodes are excited with their respective amplitudes A_j and merely the evolution of the relative phases of the modes leads to the complex pattern of standing and propagating sound waves in the SL and the substrate.

3.3 Quantitative calculation of rocking curves

In order to quantify the comparison of the model calculations and the measurement, the strain profile derived from the linear-chain model is used to calculate the XRD signal according to the Darwin formalism, taking into account the deformation of each unit cell.[24] The x-ray rocking curves $R(q, t)$ resulting from the strain pattern depicted in Fig. 5 are plotted in Fig. 2a). For comparison with experiments (Fig. 2c) we plot the calculated difference spectra $R(q, t) - R_0(q)$ in Fig. 2b).

For large time delay (orange curves in Fig.2) the entire SL peak has changed its position, i.e. the difference signal is maximally negative around the initial position $q(t \leq 0)$ and reaches its positive maximum around the new position q_{max} . For intermediate times, a doublet shows up, indicating that half of the SL has already expanded whereas the remaining part still exhibits an unchanged SL period. Note that the difference of the central positions of the two peaks is larger at early times (green, blue and cyan). This corresponds to the fact that the early expansion of the layers near the surface is larger compared to the later-expanding near-substrate layers which is due to the inhomogeneous excitation profile $\Delta(z)$. This particular feature is also visualized by the dark red color code for large expansion in the strain contour plot (Fig. 5).

While the essential features of the SL Peak would be represented by a kinematic XRD theory as well, the calculation of the substrate peak (Fig. 3) and its shoulders definitely requires the used dynamical diffraction calculations. In particular, we have to add a virtually infinite STO substrate underneath the unit cells of the SL and the substrate used for the coherent phonon simulation, since the extinction length for x-rays is $1 \mu\text{m}$ at the Bragg peak and elsewhere limited by the absorption length of $10 \mu\text{m}$. Fig. 3 again shows very good agreement of simulation and experiment. Not only the effect size and timing is well reproduced, but also details like the smoothly decaying right shoulder as opposed to the decreasing in two steps seen for the left shoulder.

to be time-independent, we can rewrite the inhomogeneous vector equation as:

$$\frac{d^2}{dt^2} \mathbf{X} - \mathbf{K} \mathbf{X} = \Delta \quad (8)$$

$$\Leftrightarrow \frac{d^2}{dt^2} (\mathbf{X} + \mathbf{K}^{-1} \Delta) - \mathbf{K} (\mathbf{X} + \mathbf{K}^{-1} \Delta) = 0 \quad (9)$$

$$\Leftrightarrow \frac{d^2}{dt^2} (\mathbf{X}^\infty) - \mathbf{K} (\mathbf{X}^\infty) = 0 \quad (10)$$

We define the atomic positions z_i^∞ for $t \rightarrow \infty$ as the new equilibrium positions for the new coordinates $\mathbf{X}^\infty = \mathbf{X} - \mathbf{K}^{-1} \Delta$, such that $z_i(t) = z_i^0 + x_i(t) = z_i^\infty + x_i^\infty(t)$. The particular solution of the homogeneous equation for the new coordinates, i.e. the complex coefficients A_j , are found by reading the initial conditions for $t = 0$ from Fig. 4b) and c) and recalling that in $x_i^\infty(t) = z_i^0 - z_i^\infty + x_i(t)$ the relation $x_i(t) = 0$ holds. Hence, we find

$$x_i^\infty(0) = z_i^0 - z_i^\infty = \sum_{j=i+1}^N l_j \quad \text{and} \quad \frac{d}{dt} x_i^\infty(0) = 0 \quad (11)$$

for $i = 1, \dots, N$, where l_j is the length of the j^{th} stick depicting the photoinduced stress which thereby determines the complex coefficients A_j in eq. (3).

References

- M. Herzog, W. Leitenberger, R. Shayduk, R. M. van der Veen, C. J. Milne, S. L. Johnson, I. Vrejoiu, M. Alexe, D. Hesse, and M. Bargheer. Ultrafast manipulation of hard x-rays by efficient Bragg switches. *Appl. Phys. Lett.*, 96:161906, 2010.
- M. Woerner, C. v. Korff Schmising, M. Bargheer, N. Zhavoronkov, I. Vrejoiu, D. Hesse, M. Alexe, and T. Elsaesser. Ultrafast structural dynamics of perovskite superlattices. *Appl. Phys. A*, 96:83, 2009.
- C. v. Korff Schmising, A. Harpoeth, N. Zhavoronkov, Z. Ansari, C. Aku-Leh, M. Woerner, T. Elsaesser, M. Bargheer, M. Schmidbauer, I. Vrejoiu, D. Hesse, and M. Alexe. Ultrafast magnetostriction and phonon-mediated stress in a photoexcited ferromagnet. *Phys. Rev. B*, 78:060404(R), 2008.
- C. v. Korff Schmising, M. Bargheer, M. Kiel, N. Zhavoronkov, M. Woerner, T. Elsaesser, I. Vrejoiu, D. Hesse, and M. Alexe. Accurate time delay determination for femtosecond X-ray diffraction experiments. *Appl. Phys. B*, 88:1, 2007.
- M. Cardona. *Light Scattering in Solids V Superlattices and Other Microstructures (Topics in Applied Physics)*. Springer, 2nd ed. edition, 1989.
- C. Colvard, T. A. Gant, M. V. Klein, R. Merlin, R. Fischer, H. Morkoc, and A. C. Gossard. Folded acoustic and quantized optic phonons in (ga)as superlattices. *Phys. Rev. B*, 31(4):2080, Feb 1985.
- M. Bargheer, N. Zhavoronkov, Y. Gritsai, J. C. Woo, D. S. Kim, M. Woerner, and T. Elsaesser. *Science*, 306:1771, 2004.
- C. v. Korff Schmising, M. Bargheer, M. Kiel, N. Zhavoronkov, M. Woerner, T. Elsaesser, I. Vrejoiu, D. Hesse, and M. Alexe. Coupled Ultrafast Lattice and Polarization Dynamics in Ferroelectric Nanolayers. *Phys. Rev. Lett.*, 98(25):257601, 2007.
- S. Yamanaka, T. Maekawa, H. Muta, T. Matsuda, S. Kobayashi, and K. Kurosaki. Thermophysical properties of SrHfO₃ and SrRuO₃. *J. Solid State Chem.*, 177:3484, 2004.
- Y. H. Ren, M. Trigo, R. Merlin, V. Adyam, and Q. Li. Generation and detection of coherent longitudinal acoustic phonons in the La_{0.67}Sr_{0.33}MnO₃ thin films by femtosecond light pulses. *Appl. Phys. Lett.*, 90:251918, 2007.
- Bauer. *Multilayers*. Springer, 2nd ed. edition, 1998.
- Christoph Rose-Petruck, Ralph Jimenez, Ting Guo, Andrea Cavalleri, Craig W. Siders, Ferenc Rksi, Jeff A. Squier, Barry C. Walker, Kent R. Wilson, and Christopher P. J. Barty. Picosecond-milliangstrom lattice dynamics measured by ultrafast x-ray diffraction. *Nature*, 398(6725):310–312, mar 1999.
- A. M. Lindenberg, I. Kang, S. L. Johnson, T. Missalla, P. A. Heimann, Z. Chang, J. Larsson, P. H. Bucksbaum, H. C. Kapteyn, H. A. Padmore, R. W. Lee, J. S. Wark, and R. W. Falcone. Time-resolved x-ray diffraction from coherent phonons during a laser-induced phase transition. *Phys. Rev. Lett.*, 84(1):111–114, Jan 2000.
- D. A. Reis, M. F. DeCamp, P. H. Bucksbaum, R. Clarke, E. Dufresne, M. Hertlein, R. Merlin, R. Falcone, H. Kapteyn, M. M. Murnane, J. Larsson, T. Missalla, and J. S. Wark. Probing impulsive strain propagation with x-ray pulses. *Phys. Rev. Lett.*, 86(14):3072–3075, Apr 2001.
- K. Sokolowski-Tinten, C. Blome, C. Dietrich, A. Tarasevitch, M. Horn von Hoegen, D. von der Linde, A. Cavalleri, J. Squier, and M. Kammler. Femtosecond x-ray measurement of ultrafast melting and large acoustic transients. *Phys. Rev. Lett.*, 87(22):225701, Nov 2001.
- M. Trigo, Y. M. Sheu, D. A. Arms, J. Chen, S. Ghimire, R. S. Goldman, E. Landahl, R. Merlin, E. Peterson, M. Reason, and D. A. Reis. Probing unfolded acoustic phonons with x-rays. *Phys. Rev. Lett.*, 101(2):025505, 2008.
- A. Cavalleri, C. W. Siders, F. L. H. Brown, D. M. Leitner, C. Tóth, J. A. Squier, C. P. J. Barty, K. R. Wilson, K. Sokolowski-Tinten, M. Horn von Hoegen, D. von der Linde, and M. Kammler. Anharmonic lattice dynamics in germanium measured with ultrafast x-ray diffraction. *Phys. Rev. Lett.*, 85(3):586–589, Jul 2000.
- J. Larsson, A. Allen, P.H. Bucksbaum, R.W. Falcone, A. Lindenberg, G. Naylor, T. Missalla, D.A. Reis, K. Scheidt, A. Sjgren, P. Sondhauss, M. Wulff, and J.S. Wark. Picosecond x-ray diffraction studies of laser-excited acoustic phonons in insb. *Appl. Phys. A*, 75:467–478, 2002.
- F. Zamponi, Z. Ansari, C. v. Korff Schmising, P. Rothhardt, N. Zhavoronkov, M. Woerner, T. Elsaesser, M. Bargheer, T. Trobitzsch-Ryll, and M. Haschke. Femtosecond hard x-ray plasma sources with a kilohertz repetition rate. *Appl. Phys. A*, 96:51, 2009.
- P. Beaud, SL Johnson, A. Streun, R. Abela, D. Abramsohn, D. Grolimund, F. Krasniqi, T. Schmidt, V. Schlott, and G. Ingold. Spatiotemporal Stability of a Femtosec-

- ond Hard-X-Ray Undulator Source Studied by Control of Coherent Optical Phonons. *Phys. Rev. Lett.*, 99(17):174801, 2007.
21. Junjie Li, Rick Clinite, Xuan Wang, and Jianming Cao. Simulation of ultrafast heating induced structural dynamics using a one-dimensional spring model. *Phys. Rev. B*, 80(1):014304, Jul 2009.
 22. P. Kostic, Y. Okada, N. C. Collins, Z. Schlesinger, J. W. Reiner, L. Klein, A. Kapitulnik, T. H. Geballe, and M. R. Beasley. Non-fermi-liquid behavior of srro3: Evidence from infrared conductivity. *Phys. Rev. Lett.*, 81(12):2498, 1998.
 23. M. Bargheer, N. Zhavoronkov, J. C. Woo, D. S. Kim, M. Woerner, and T. Elsaesser. Excitation mechanisms of coherent phonons unravelled by femtosecond x-ray diffraction. *phys. stat. sol. (b)*, 243(10):2389, 2006.
 24. S. A. Stepanov, E. A. Kondrashkina, R. Köhler, D. V. Novikov, G. Materlik, and S. M. Durbin. Dynamical x-ray diffraction of multilayers and superlattices: Recursion matrix extension to grazing angles. *Phys. Rev. B*, 57(8):4829–4841, Feb 1998.
 25. Nuh Gedik, Ding-Shyue Yang, Gennady Logvenov, Ivan Bozovic, and Ahmed H. Zewail. Nonequilibrium Phase Transitions in Cuprates Observed by Ultrafast Electron Crystallography. *Science*, 316(5823):425, 2007.

Paper XI

Calibrated real-time detection of nonlinearly propagating strain waves

A. Bojahr, M. Herzog, **D. Schick**, I. Vrejoiu, and M. Bargheer

Phys. Rev. B 86, 14 (2012)

Calibrated real-time detection of nonlinearly propagating strain waves

André Bojahr,¹ Marc Herzog,¹ Daniel Schick,¹ Ionela Vrejoiu,² and Matias Bargheer^{1,3,*}

¹*Institute of Physics and Astronomy, University of Potsdam, Karl-Liebknecht-Strasse 24-25, 14476 Potsdam, Germany*

²*Max-Planck-Institut für Mikrostrukturphysik, Weinberg 2, 06120 Halle, Germany*

³*Helmholtz Zentrum Berlin, Albert-Einstein-Str. 15, 12489 Berlin, Germany*

(Received 19 July 2012; revised manuscript received 2 October 2012; published 24 October 2012)

Epitaxially grown metallic oxide transducers support the generation of ultrashort strain pulses in SrTiO₃ (STO) with high amplitudes up to 0.5%. The strain amplitudes are calibrated by real-time measurements of the lattice deformation using ultrafast x-ray diffraction. We determine the speed at which the strain fronts propagate by broadband picosecond ultrasonics and conclude that, above a strain level of approx. 0.2%, the compressive and tensile strain components travel at considerably different sound velocities, indicating nonlinear wave behavior. Simulations based on an anharmonic linear-chain model are in excellent accord with the experimental findings and show how the spectrum of coherent phonon modes changes with time.

DOI: 10.1103/PhysRevB.86.144306

PACS number(s): 43.35.+d, 43.25.+y, 61.05.cp, 63.20.kg

Acoustic wave propagation and the deformation of solids are usually analyzed within the approximation of harmonic interatomic potentials leading to the concept of decoupled acoustic phonons including their dispersion relation which is nearly linear for small wave vectors k_p . An anharmonicity must be introduced into the interaction potential in order to describe deformation under very high stress. But also small-phonon-amplitude phenomena are connected to phonon-phonon interaction processes, such as heat expansion and heat conduction.¹ For the material investigated in this paper, SrTiO₃ (STO), all these properties have been studied in detail, since STO is the generic dielectric (quantum paraelectric) perovskite oxide with a variety of interesting properties near its structural phase transition at 105 K. The elastic constants were determined by ultrasound measurements,² the damping of acoustic phonons was investigated by the linewidth of Brillouin scattering³ and apparent deviations of the acoustic dispersion were discussed in the context of picosecond ultrasonics measurements.⁴ Recently ultrafast x-ray diffraction (UXRD) was used to accurately measure the propagation and decay of quasimonochromatic strain pulses in STO.⁵ In general, UXRD data yield unambiguous information on the ultrafast lattice response, which is helpful for the interpretation of optical pump-probe investigations concerning complex problems in solids.^{6–8}

In theory, the changes in the occupation of phonon modes are described as phonon damping due to scattering from defects or anharmonic interaction with thermally activated phonons.^{9–12} For high strain amplitudes also interactions among coherent phonons are possible, which leads to a shape change of coherent phonon pulses. In particular, the self-steepening of strain pulses in sapphire giving rise to N-waves, shock waves, and soliton pulse trains were measured after a long propagation length of more than one hundred microns.^{13–16} These solitons were observed at low temperatures where phonon damping is weak and were discussed by nonlinear wave equations.^{16–18}

In this paper we investigate the nonlinear propagation of giant longitudinal acoustic (LA) bipolar strain pulses in SrTiO₃. We calibrate the strain amplitude by UXRD and show how the mode spectrum constituting the wave changes

as a function of time. Simulations based on an anharmonic linear-chain model yield excellent agreement with ultrashort broadband optical reflectivity measurements and show that compressive strain components propagate faster than tensile strain components. The dependence of the sound velocity on the strain gives rise to a self-steepening of the strain fronts. We analyze the experiments in a linear-chain model with atomic resolution, although for the presented results a continuum model would also be applicable. There are several advantages of this approach and the discussion of sound waves in terms of phonons. First we anticipate experiments for very high wave vectors approaching the Brillouin zone boundary. At a temperature of 110 K, STO undergoes an antiferrodistortive phase transition connected to an optical phonon mode which softens near the zone boundary.¹⁹ For connecting the nonlinear parameters derived in the present paper with the physics near the phase transition our approach will be very helpful. Finally, ultrafast x-ray diffraction naturally supports simulations with unit cell accuracy, and we show in Eq. (1) that in our picosecond ultrasonics experiments the different wavelengths of the reflected photons are sensitive to particular wave vectors of phonons.

We use an epitaxially grown La_{0.7}Sr_{0.3}MnO₃ (LSMO) transducer film on a SrTiO₃ (001) substrate, fabricated by pulsed-laser deposition. The red symbols in Fig. 1(a) show a θ - 2θ scan of the sample recorded at the energy dispersive reflectometer (EDR) beamline of the synchrotron BESSYII of the Helmholtz-Zentrum-Berlin. The bright substrate peak at $\theta = 23.25^\circ$ is cut off to show the less intense layer peak (LSMO) at 23.58° more clearly. The excellent agreement with the simulation (black solid line) confirms the crystalline perfection of the epitaxial film with a thickness of $d_{\text{LSMO}} = 36$ nm, which is very robust against high excitation densities and supports high strain amplitudes. To calibrate the amplitude of the strain wave we measure the expansion of the metallic layer via the shift of the x-ray diffraction signal [Figs. 1(b) and 1(c)] after optical excitation by 50 fs laser pulses around 800 nm wavelength with a fluence of 20 mJ/cm². To probe the structural dynamics we use an x-ray plasma source which provides jitter-free x-ray pulses with a duration of approximately 200 fs.²⁰ The transient angular shift $\Delta\theta$ of the

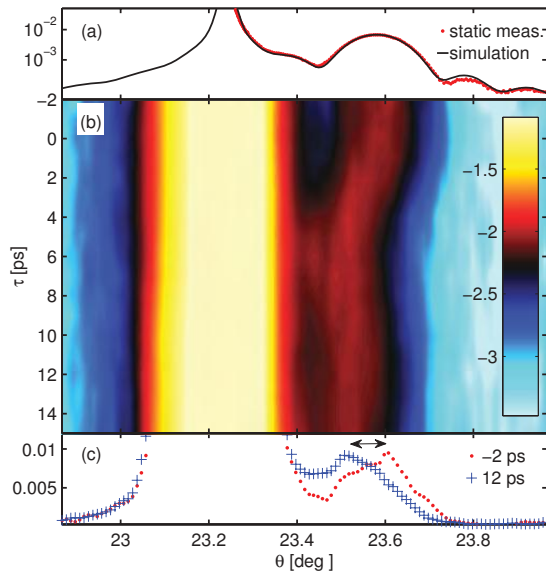


FIG. 1. (Color online) (a) Static θ - 2θ scan of the (002) peaks of the LSMO-STO sample showing a weak and broad layer (LSMO) peak and a much brighter and narrower STO substrate peak. (b) Transient UXRD signal after pumping with a laser pulse. The layer peak shifts to smaller angles indicating the expansion of LSMO within 6 ps (logarithmic color code). (c) Two cuts of panel (b) with pump-probe delays -2 ps (before pumping) and 12 ps (when the strain pulse has left the layer).

LSMO Bragg peak can be read from Fig. 1(b) for time delays up to 15 ps. The shift is connected to the layer strain ϵ by Bragg's law. Figure 1(c) shows the diffraction curve for a time delay of 12 ps yielding an induced LSMO strain of $\epsilon = 0.2\%$.

The observed time dependence of the LSMO Bragg peak can be understood as follows:^{21,22} The absorbed pump pulse induces a quasi-instantaneous thermal stress which is unbalanced at the layer boundaries. This leads to two strain fronts which propagate away from the air-LSMO and LSMO-STO interfaces eventually building up a bipolar strain pulse in the STO substrate.²³ The maximum expansion occurs at $T = d_{\text{LSMO}}/v_{\text{LSMO}} = 6$ ps after the excitation, when the expansion waves starting from the surface and the interface have traveled through the film at the velocity of sound in LSMO, v_{LSMO} .²⁴ After 12 ps the coherent strain wave has completely left the LSMO layer and entered the STO substrate. Reflections of the sound wave at the interface with good acoustic impedance matching can be neglected.^{21,24,25}

In previous experiments we confirmed that the layer strain depends linearly on the excitation fluence²⁶ and that the corresponding bipolar strain wave propagates into the STO substrate.²¹ Hence we conclude a calibration factor of 0.01% LSMO strain per 1 mJ/cm² fluence. The strain amplitude of the bipolar pulse in the STO is half of the LSMO strain after 12 ps weighted with the ratio of the layer and substrate sound

velocities which considers the bipolar pulse stretching in the STO.^{21,24,25}

Having calibrated the amplitude of the lattice response, we follow the propagation of the bipolar strain pulse by optical pump-probe measurements. The setup is very similar to the broadband picosecond ultrasonics setup reported by Pontecorvo *et al.*²⁷ We split the 800 nm laser light into two parts. The intense part is used to pump the sample with fluences ranging from 14 to 47 mJ/cm² and the smaller part is focused into a sapphire plate to generate a white light supercontinuum pulse. This spectrally broad light pulse ranging from 470 to 700 nm is reflected from the sample under an angle $\alpha = 45^\circ$ with respect to the surface normal. We measured the relative transient reflectivity change $\Delta R/R_0$ of the sample for four different fluences at pump-probe delays up to 1 ns with a resolution of 1 ps. Figure 2 shows the response of the sample after correction for the chirp of the white light probe pulse and after subtraction of the slowly varying background which is associated with the transient heat in the LSMO film. Figure 2(a) shows the relative change of reflectivity for the lowest fluence (14 mJ/cm²) and Fig. 2(b) shows the same for the highest fluence (47 mJ/cm²).

All measurements show pronounced oscillations which exhibit a period increasing with the probe wavelength λ . At high fluences we additionally observe a wavelength-dependent beating of these oscillations. The oscillations can be understood as an interference of the light wave reflected by the sample surface with the light wave reflected due to

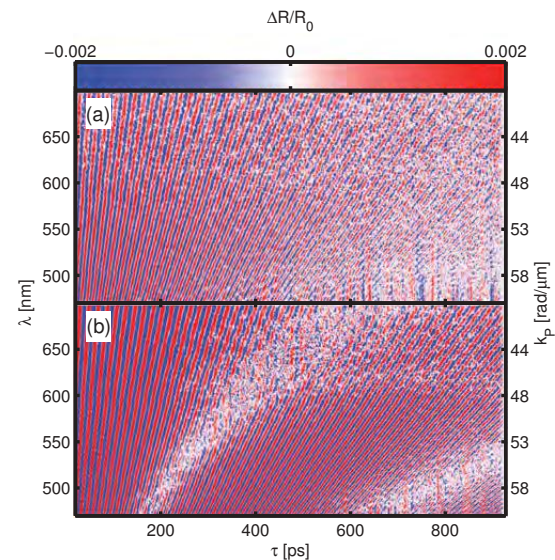


FIG. 2. (Color) Relative optical reflectivity change of the LSMO-STO sample for a pump fluence of (a) 14 mJ/cm² and (b) 47 mJ/cm². The low-frequency background was subtracted by high pass filtering. The probe pulse wavelength is given by λ (left axis). Both measurements show oscillations which are attributed to Brillouin backscattering of a photon from a phonon with wave vector k_p (right axis). For strong excitation conditions (b) we observe a beating in these oscillations.

the refractive index change induced by the propagating strain wave.²³

In order to explain how a photon with wave vector k_L is selectively probing a certain phonon with wave vector k_P , we describe the propagating wave front as a superposition of longitudinal acoustic (LA) phonons with wave vector k_P . Then the “reflection” of the probe light from the strain pulse can be understood as Brillouin backscattering of optical light with wave vector k_L . Therefore, such oscillations are often denoted as “Brillouin oscillations” in the literature.²⁸ The observed frequency ω_P of the signal oscillation corresponds to the eigenfrequency of the LA phonon with wavevector k_P . According to energy and momentum conservation the latter is related to the probe wavelength λ by the Brillouin backscattering condition

$$k_P = 2k_L^\perp = \frac{4\pi}{\lambda}n(\lambda)\cos(\beta), \quad (1)$$

where k_L^\perp is the internal optical wave vector component along the surface normal and $n(\lambda)$ is the refractive index of STO which is taken from the literature.²⁹ The internal angle β is related to α by Snell’s law. Equation (1) implies that the probe wavelength is specific for a certain wave vector of LA phonons. The amplitude of oscillations at each wavelength λ and time interval is a measure of the phonon amplitude of a specific phonon wave vector k_P . The beating observed in Fig. 2(b) is therefore interpreted as a change of the phonon spectrum in time. In particular, the beat node indicates the absence of a certain wave vector k_P at a certain time delay after excitation. This will be discussed in the context of Fig. 4.

Now we discuss how to derive the sound velocity from the measured data shown in Figs. 2(a) and 2(b). The linear dispersion relation of acoustic phonons near the Brillouin zone center is given by $\omega_P(\lambda)/k_P = v_s$ and thus relates the observed oscillation frequency $\omega_P(\lambda)$ to the speed of sound v_s for the LA phonons in STO:

$$v_s = \frac{\omega_P(\lambda)\lambda}{4\pi n(\lambda)\cos(\beta)}. \quad (2)$$

We then calculate the fast Fourier transform $I(\omega_P, \lambda)$ along the time axis for each probe wavelength λ . This yields a relation between λ and the related oscillation frequencies $\omega_P(\lambda)$, which implies a dependence of the sound velocity v_s on the phonon wave vector k_P according to the Brillouin backscattering condition. We use Eq. (2) as a coordinate transformation $v_s(\omega_P(\lambda), \lambda)$ which transforms our Fourier-transformed data into a wavelength-dependent sound velocity distribution $I(v_s, \lambda)$. By integration of the calculated result over all wavelengths we obtain Fig. 3, which shows the measured sound velocity distributions for different photoinduced LSMO strains calibrated by the results of the UXRD measurement. At low strain (0.14%) we observe a single peak around 8 nm/ps which is in a good agreement with the known sound velocity of the LA phonons in STO.²⁵ This peak validates the linear dispersion at low fluence. A nonlinear dispersion (k_P -dependent sound velocity) would lead to a broadened distribution.

However, with increasing strain amplitude we find a splitting in the sound velocity distribution. This implies that, for large strains, the speed of sound depends on the strain

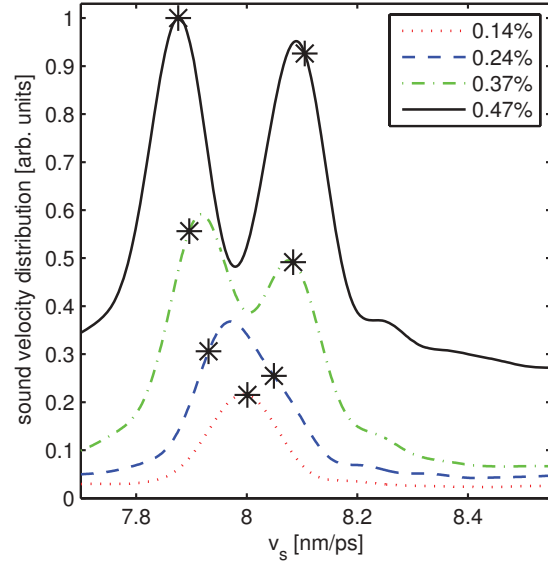


FIG. 3. (Color online) Measured sound velocity distribution of the induced strain pulse in STO. The different pump fluences were calibrated with the UXRD measurement to the resulting induced strains of the LSMO layer which is directly linked to the strain amplitude of the bipolar strain pulse in the STO. The narrow distribution for 0.14% strain implies that the entire strain pulse essentially propagates with a speed around 8 nm/ps. With increasing strain amplitude the sound velocity distribution gets broader and eventually a double-peak distribution is established. At high excitation levels different parts of the strain pulse propagate with different velocities. The stars indicate the sound velocities of the self-steepened sound pulses simulated in Fig. 4(a).

amplitude. The strain amplitude itself modulates the sound velocity of the medium.

To verify these assignments and to understand the underlying excited phonon spectrum, we simulate the lattice dynamics in a linear-chain model which was successfully tested against UXRD data in several cases.^{21,30} In addition to the model proposed in Ref. 21, we introduce an anharmonic potential between adjacent oscillators in order to describe the nonlinear wave propagation. Moreover, we add an empirical phonon damping term proportional to the velocity difference of adjacent oscillators. Mathematically the system is described by N coupled oscillators where each oscillator describes one lattice plane (half unit cell) of the LSMO thin film or the STO substrate. The set of N coupled second-order ordinary differential equations is

$$m_i \ddot{x}_i = k_M(\Delta_i - \Delta_{i-1}) + a_M(\Delta_i^2 - \Delta_{i-1}^2) + m_i \gamma_M(\dot{\Delta}_i - \dot{\Delta}_{i-1}) + F_i(t), \quad (3)$$

where $\Delta_i = x_{i+1} - x_i$ and $i = 2, \dots, N - 1$. The potential is nearly harmonic with a small cubic term. This leads to the linear and parabolic force terms in the coupling force of Eq. (3), where m_i is the mass of the oscillator, k_M is the spring constant, a_M is the anharmonicity parameter, and γ_M is a material specific damping constant.^{31,32} At the interface

of LSMO and STO the differential equation is asymmetric, since k_M , a_M , and γ_M cannot be factored out as in Eq. (3). The first and the last oscillator have no opponent. This defines the boundary condition. We used $N = 48182$ oscillators, i.e., the first $9.4 \mu\text{m}$ of the STO substrate are included in the lattice dynamics simulations.

The elastic properties of LSMO and STO were taken from the literature.^{24,25} For the anharmonicity of STO we made a first approximation from the hydrostatic pressure dependence of the elastic constants, which leads directly to a qualitative agreement.² We then varied the anharmonicity of STO and LSMO to find quantitative agreement of the theory with the experimental data. The final value of the anharmonicity of STO reads $1.8 \times 10^{13} \text{ kg s}^{-2} \text{ m}^{-1}$, which is only 10% smaller than the first guess. The anharmonicity in the LSMO transducer film has only little influence on the dynamics because of the short propagation length. For this we finally used a value of $3 \times 10^{13} \text{ kg s}^{-2} \text{ m}^{-1}$. For the damping parameter γ_i we used a value which yields good agreement for phonon damping in STO observed by UXRD.⁵

$F_i(t)$ describes the driving force of the oscillators due to the optical excitation process. We assume an instantaneous force step $F_i(t)$ at time zero according to the strong electron-phonon coupling in the metallic oxides.⁸ The spatial excitation profile $F_i(t)$ follows an exponential decay determined by the penetration depth of the optical pump light. Accordingly, deeper-lying unit cells exhibit less expansion.²¹

Figure 4(a) shows the simulated strain profile for different times after excitation of the sample with the smallest (black line) and largest (blue line) strain amplitude in the copropagating frame of reference. The center of the bipolar pulse which has a strain level close to zero propagates with the normal speed of sound, which is only valid in the harmonic approximation. In the regions with high amplitude the strain modulates the elastic constants. This nonlinear interaction between the masses changes the shape of the bipolar pulse, in particular leading to a self-steepening pulse front and tail. The tensile part is slower and the compressive part is faster than the sound velocity v_s of the harmonic linear chain. The speed of the pulse front propagation is read from the simulation and indicated in Fig. 3 as stars. The good agreement verifies the interpretation of the measured splitting of the sound velocity distribution.

For further comparison to the measurement and to interpret the impact of the anharmonic interaction on the classical decoupled oscillators called phonons, we analyze the simulated strain profiles in Fig. 4(a) by calculating the Fourier amplitudes $A(k_p, t)$ of sinusoidal waves composing the wave packet for each time delay t . This is essentially an amplitude of phonons (decoupled modes) which describes the wave packet. For better comparison to the experimental observable we plot A/λ in Fig. 4(c), because for a transparent medium the reflectivity modulations scale inversely with λ according to equations (35–38) in the seminal paper of Thomsen *et al.*²³ The distribution of coherently excited phonons rapidly shifts to smaller k_p vectors.

Figure 4(b) shows the amplitude of the measured Brillouin oscillations [Fig. 2(b)], which is proportional to the phonon amplitude of the phonon with wave vector k_p .²³ During the time sequence 240, 320, and 410 ps the first minimum of

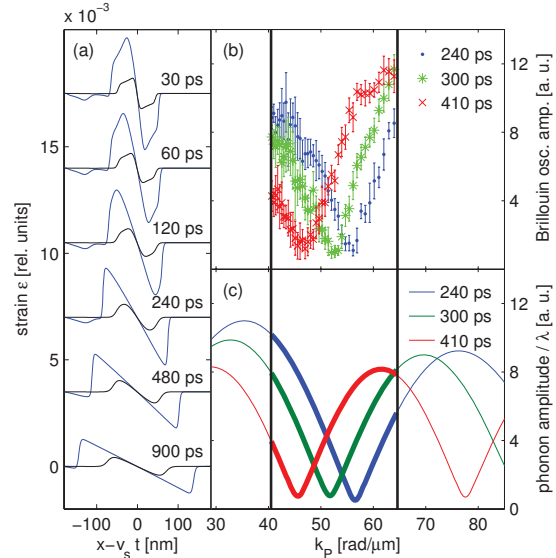


FIG. 4. (Color) (a) Spatial profile of the bipolar strain pulse in the STO for different propagation times in a frame of reference propagating with the speed of sound v_s for high amplitude (blue line, 0.47% strain) and low amplitude (black line, 0.14% strain). For large amplitude, the tensile part of the pulse propagates with subsonic speed and the compressive part propagates with supersonic speed indicated by the stars in Fig. 3. (b) Measured amplitude of oscillations for each wavelength connected to the wave vectors by the Brillouin backscattering condition. The region between the vertical black lines indicates the wave vectors that can be accessed by optical white light. (c) Phonon amplitude divided by the wavelength λ (see text) as a function of wave vector calculated from Fourier transforms of the simulated strain profile, showing good agreement with the measurement in panel (b).

the phonon amplitude is moving through the experimental window of observation given by the Brillouin backscattering condition [Eq. (2)]. These minima represent the fact that, at a certain point in time, these phonons are not occupied. This is the fundamental interpretation of the beating of the measured oscillations. The simulation reproduces also the second measured amplitude minimum [Fig. 2(b)], which moves into the observed wavelength range about 700 ps after excitation (not shown).

We now discuss the physics behind the anharmonic linear-chain model leading to the excellent agreement of theory and experiment. Deformations are only reversible if they are infinitely slow and if the thermodynamic system is in equilibrium at any time. This is not the case for phonons which have a finite oscillation period. The phonon has to damp out because of the intrinsic irreversibility of the oscillation. In other words, the coherent phonon amplitude goes down by dissipating energy to the heat bath.^{5,9–12} In our model we consider this fact by the hydrodynamic damping term γ_M in the second line of Eq. (3).

The force term to second order in strain [a_M in Eq. (3)] is given by the anharmonic interactions of atoms which

contribute only for large strain amplitudes. The set of differential equations [Eq. (3)] can be approximated by a Korteweg–de Vries–Burgers equation (KdVB) if the phonon wavelength is much larger than the lattice constant.³³ This is advantageous to find asymptotic solutions such as solitons. Our approach is useful for the calculation of solutions with certain excitation conditions and for considering acoustic mismatches of different materials. We can account for dispersion higher than third order and compute solutions with phonon wavelengths close to the lattice constant.

In conclusion, we determined the transient phonon spectra of nonlinearly propagating strain pulses in strontium titanate

by transient reflectivity measurements for different fluences, which are experimentally calibrated by time-resolved x-ray diffraction. An anharmonic linear-chain model with phonon damping reproduces the measured spectra in a quantitative way and verifies the interpretation of the transient reflectivity measurements. The anharmonicity thus changes the phonon occupation in time and leads to compressive and tensile strain fronts traveling at 1% faster and slower speed, respectively.

We thank the DFG for supporting the project via BA 2281/3-1 and SFB 762.

*bargheer@uni-potsdam.de

¹N. D. Ashcroft, Neil W. Mermin, *Solid State Physics*, 1st ed. (Saunders College, Fort Worth, 1976).

²A. G. Beattie and G. A. Samara, *J. Appl. Phys.* **42**, 2376 (1971).

³A. Koreeda, T. Nagano, S. Ohno, and S. Saikan, *Phys. Rev. B* **73**, 024303 (2006).

⁴S. Brivio, D. Polli, A. Crespi, R. Osellame, G. Cerullo, and R. Bertacco, *Appl. Phys. Lett.* **98**, 211907 (2011); A. Devos, Y.-C. Wen, P.-A. Mante, and C.-K. Sun, *ibid.* **100**, 206101 (2012); S. Brivio, D. Polli, A. Crespi, R. Osellame, G. Cerullo, and R. Bertacco, *ibid.* **100**, 206102 (2012).

⁵M. Herzog, A. Bojahr, J. Goldshteyn, W. Leitenberger, I. Vrejoiu, D. Khakhulin, M. Wulff, R. Shayduk, P. Gaal, and M. Bargheer, *Appl. Phys. Lett.* **100**, 094101 (2012).

⁶K. G. Nakamura, S. Ishii, S. Ishitsu, M. Shiokawa, H. Takahashi, K. Dharmalingam, J. Irisawa, Y. Hironaka, K. Ishioka, and M. Kitajima, *Appl. Phys. Lett.* **93**, 061905 (2008).

⁷C. von Korff Schmising, A. Harpoeth, N. Zhavoronkov, Z. Ansari, C. Aku-Leh, M. Woerner, T. Elsaesser, M. Bargheer, M. Schmidbauer, I. Vrejoiu *et al.*, *Phys. Rev. B* **78**, 060404 (2008).

⁸A. Bojahr, D. Schick, L. Maerten, M. Herzog, I. Vrejoiu, C. von Korff Schmising, C. J. Milne, S. L. Johnson, and M. Bargheer, *Phys. Rev. B* **85**, 224302 (2012).

⁹A. Akhiezer, *J. Phys. (USSR)* **1**, 277 (1939).

¹⁰H. J. Maris, *Phil. Mag.* **12**, 89 (1965).

¹¹W. Chen, H. J. Maris, Z. R. Wasilewski, and S.-i. Tamura, *Philos. Mag. B* **70**, 687 (1994).

¹²B. C. Daly, K. Kang, Y. Wang, and D. G. Cahill, *Phys. Rev. B* **80**, 174112 (2009).

¹³P. J. S. van Capel and J. I. Dijkhuis, *Appl. Phys. Lett.* **88**, 151910 (2006).

¹⁴P. J. S. van Capel, H. P. Porte, G. van der Star, and J. I. Dijkhuis, *J. Phys.: Conf. Ser.* **92**, 012092 (2007).

¹⁵O. L. Muskens and J. I. Dijkhuis, *Phys. Rev. Lett.* **89**, 285504 (2002).

¹⁶P. J. S. van Capel and J. I. Dijkhuis, *Phys. Rev. B* **81**, 144106 (2010).

¹⁷H. Y. Hao and H. J. Maris, *Phys. Rev. B* **64**, 064302 (2001).

¹⁸H. J. Maris and S. Tamura, *Phys. Rev. B* **84**, 024301 (2011).

¹⁹G. Shirane and Y. Yamada, *Phys. Rev.* **177**, 858 (1969).

²⁰D. Schick, A. Bojahr, M. Herzog, C. von Korff Schmising, R. Shayduk, W. Leitenberger, P. Gaal, and M. Bargheer, *Rev. Sci. Instrum.* **83**, 025104 (2011).

²¹M. Herzog, D. Schick, P. Gaal, R. Shayduk, C. von Korff Schmising, and M. Bargheer, *Appl. Phys. A* **106**, 489 (2012).

²²K. Sokolowski-Tinten, C. Blome, C. Dietrich, A. Tarasevitch, M. Horn von Hoegen, D. von der Linde, A. Cavalleri, J. Squier, and M. Kammler, *Phys. Rev. Lett.* **87**, 225701 (2001).

²³C. Thomsen, H. T. Grahn, H. J. Maris, and J. Tauc, *Phys. Rev. B* **34**, 4129 (1986).

²⁴Y. H. Ren, M. Trigo, R. Merlin, V. Adyam, and Q. Li, *Appl. Phys. Lett.* **90**, 251918 (2007).

²⁵R. O. Bell and G. Rupprecht, *Phys. Rev.* **129**, 90 (1963).

²⁶M. Woerner, C. von Korff Schmising, M. Bargheer, N. Zhavoronkov, I. Vrejoiu, D. Hesse, M. Alexe, and T. Elsaesser, *Appl. Phys. A* **96**, 83 (2009).

²⁷E. Pontecorvo, M. Ortolani, D. Polli, M. Ferretti, G. Ruocco, G. Cerullo, and T. Scopigno, *APPLAB* **98**, 011901 (2011).

²⁸H. Ogi, T. Shagawa, N. Nakamura, M. Hirao, H. Odaka, and N. Kihara, *Phys. Rev. B* **78**, 134204 (2008).

²⁹M. Cardona, *Phys. Rev.* **140**, A651 (1965).

³⁰M. Herzog, D. Schick, W. Leitenberger, R. Shayduk, R. M. van der Veen, C. J. Milne, S. L. Johnson, I. Vrejoiu, and M. Bargheer, *New J. Phys.* **14**, 013004 (2012).

³¹L. D. Landau and E. M. Lifshitz, *Course of Theoretical Physics, Theory of Elasticity* (Pergamon Pr., London, 1986), Vol. 7.

³²E. Arévalo, Y. Gaididei, and F. G. Mertens, *Eur. Phys. J. B* **27**, 63 (2002).

³³E. Arévalo, F. G. Mertens, Y. Gaididei, and A. R. Bishop, *Phys. Rev. E* **67**, 016610 (2003).

Paper XII

Time-domain sampling of x-ray pulses using an ultrafast sample response

P. Gaal, **D. Schick**, M. Herzog, A. Bojahr, R. Shayduk, J. Goldshteyn, H. A. Navirian, W. Leitenberger, I. Vrejoiu, D. Khakhulin, M. Wulff, and M. Bargheer

Appl. Phys. Lett. 101, 24 (2012)



Time-domain sampling of x-ray pulses using an ultrafast sample response

P. Gaal,^{1,a)} D. Schick,² M. Herzog,² A. Bojahr,² R. Shayduk,¹ J. Goldshteyn,²
H. A. Navirian,² W. Leitenberger,² I. Vrejoiu,³ D. Khakhulin,⁴ M. Wulff,⁴ and M. Bargheer^{1,2}

¹Helmholtz-Zentrum Berlin für Materialien und Energie GmbH, Wilhelm-Conrad-Röntgen Campus,
BESSY II, Albert-Einstein-Str. 15, 12489 Berlin, Germany

²Institut für Physik und Astronomie, Universität Potsdam, Karl-Liebknecht-Str. 24-25, 14476 Potsdam,
Germany

³Max-Planck-Institut für Mikrostrukturphysik, Weinberg 2, 06120 Halle, Germany

⁴European Synchrotron Radiation Facility (ESRF), 6 rue Jules Horowitz, 38000 Grenoble, France

(Received 18 September 2012; accepted 19 November 2012; published online 10 December 2012)

We employ the ultrafast response of a 15.4 nm thin SrRuO₃ layer grown epitaxially on a SrTiO₃ substrate to perform time-domain sampling of an x-ray pulse emitted from a synchrotron storage ring. Excitation of the sample with an ultrashort laser pulse triggers coherent expansion and compression waves in the thin layer, which turn the diffraction efficiency on and off at a fixed Bragg angle during 5 ps. This is significantly shorter than the duration of the synchrotron x-ray pulse of 100 ps. Cross-correlation measurements of the ultrafast sample response and the synchrotron x-ray pulse allow to reconstruct the x-ray pulse shape. © 2012 American Institute of Physics. [<http://dx.doi.org/10.1063/1.4769828>]

Ultrafast x-ray diffraction (UXRD) performed at synchrotron sources is an ideal tool for detecting atomic motion in solids, due to the large brilliance and stability of these sources.^{1,2} In particular, the utilization of nanostructured samples, which are excited and measured in a pump-probe scheme, has led to a deeper understanding of the propagation of coherent acoustic sound waves in layered structures.³ In this way, coherent optical superlattice phonons, which correspond to back-folded acoustic phonons have been excited and studied in detail.^{4,5} Such systems show modulations of superlattice Bragg peaks on a picosecond (ps) timescale⁶ and may eventually lead to the development of new devices such as an ultrafast x-ray switch.^{7,8} On a more fundamental level, it has been shown recently that thin layer transducers can be used to excite quasi-monochromatic strain waves, which allow for studying coherent acoustic phonon dynamics.⁹ In typical pump-probe measurements, a sample is excited by an ultrafast laser and subsequently probed by a time-delayed ultrashort probe pulse. For each time delay τ , a snapshot of the sample is recorded. However, the complete dynamics in the sample can only be reconstructed through a series of snapshots if the probe pulses are at least twice as short as the inverse of the highest frequency that is contained in the sample response. In general, a pump-probe signal I_{pp} corresponds to a cross-correlation measurement of the delayed probe pulse $P(t + \tau)$ with the time-dependent response of the sample $S(t)$.¹⁰

$$I_{pp}(\tau) = \int_{-\infty}^{\infty} dt \cdot S(t)P(t + \tau). \quad (1)$$

In the limit of infinitely short probe pulses $P(t) \rightarrow \delta(t)$, the pump-probe signal directly yields the sample response $S(t)$. Therefore, a good knowledge of the temporal structure of the probe pulse is crucial for a correct analysis of the data

obtained in a pump-probe scheme. X-ray pulses generated at synchrotron sources are typically characterized by streak camera measurements, which can provide time-resolutions below 1 ps.^{11,12}

In this letter, we present a cross-correlation measurement of a 100 ps x-ray probe pulse delivered by a synchrotron storage ring and the ultrafast response of a laser excited sample. The idea of the experiment together with the experimental setup is explained in Figures 1(a) and 1(b), respectively. An x-ray probe pulse (black), delivered from the ESRF storage ring is diffracted by a sample (red) exhibiting a dynamic response upon excitation, which is much shorter than the duration of the probe pulse. The sample dynamics is such that it turns the x-ray diffraction (XRD) efficiency on and off on an ultrafast timescale. The transient shown in red in Figure 1(a) is a simulation of the x-ray response of the actual structure that was used in the experiment and which is described below. By delaying the optical excitation pulse against the x-ray probe pulse, different sections of the latter are diffracted. The black transient in Figure 1(a) shows the x-ray probe pulse as determined by streak camera measurements.¹⁴ The ESRF x-ray pulse shows a slight asymmetry. Due to the finite diffraction efficiency of the unexcited sample, a fraction of the x-ray probe pulse is also diffracted when the sample is not excited. We call this fraction the diffraction background. Figure 1(b) shows the experimental setup. Time-resolved measurements were done at the undulator beamline ID09B at ESRF. A general description of the setup can be found in Ref. 13. The storage ring was running in 16-bunch mode¹⁵ delivering monochromatized x-ray pulses at an energy of 12 keV and a duration of 90-120 ps, depending on the charge of the electron bunch. The beamline is equipped with a commercial laser system (Coherent Legend), which yields 800 nm optical pulses with an energy of 1.5 mJ and a duration of 600 fs at a repetition rate of 1 kHz.

In the following, we characterize our sample and explain the nature of the ultrafast response that is later applied to

^{a)}Electronic mail: peter.gaal@helmholtz-berlin.de.

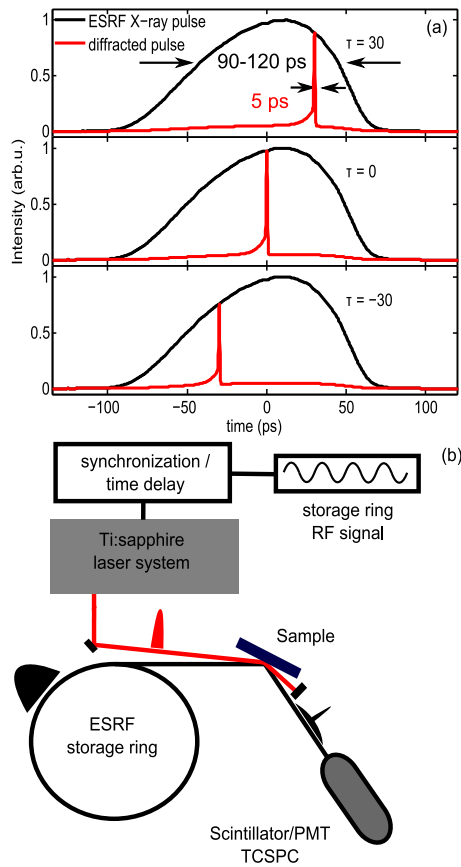


FIG. 1. (a) Cross-correlation of an ultrafast sample response against a 100 ps x-ray probe pulse. The calculated sample diffraction efficiency is modulated by optical excitation of the sample at different delay times τ . Since the sample dynamics last for roughly 5 ps, it is much shorter than the x-ray pulse. (b) Experimental setup at ID09B at the ESRF storage ring (for details see Ref. 13): A Ti:sapphire laser is synchronized to the RF signal from the storage ring. The synchronization allows to delay the laser pulse against the x-ray probe pulse with ps resolution. Diffracted x-ray photons from the sample are captured in a combined scintillator/photomultiplier (PMT) detector and counted in a time-correlated single-photon-counting (TCSPC) module.

sample the synchrotron x-ray pulse. For the cross-correlation measurement, we used a $d = 15.4$ nm thin layer of metallic SrRuO₃ (SRO) grown epitaxially on an SrTiO₃ (STO) substrate. The relevant parameters of these materials are well known.^{16–19} While the SRO layer is opaque for the optical pump light, the STO substrate is transparent. Therefore, energy from the pump pulse is only deposited in the thin layer. Figure 2(a) shows a measurement of the ultrafast sample dynamics upon excitation with a 800 nm optical pump pulse of a duration of 50 fs. The measurement was performed at the plasma X-ray source (PXS) at University of Potsdam which delivers x-ray pulses of ≈ 150 fs duration at the characteristic copper K _{α} energy of 8.047 keV.^{20,21} The pump fluence was set to 30 mJ/cm². The θ -axis in Figure 2(a) has been converted to match the measurements from ESRF. Upon optical excitation, the layer peak shifts to

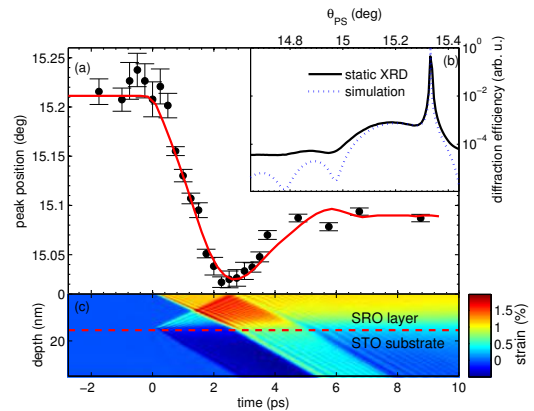


FIG. 2. (a) Measurement (black dots) and simulation (red solid line) of the center of mass shift of the SRO layer peak upon excitation with an ultrashort optical pump pulse. The measurement is performed at the PXS at University of Potsdam. (b) Measurement (black solid line) and simulation (blue dotted line) of the static x-ray diffraction curve of a 15.4 nm thin SRO layer grown epitaxially on an STO substrate. (c) Simulation using a masses and springs model of the coherent phonon dynamics upon impulsive optical excitation of the SRO layer.

smaller angles and reaches a minimum angle of $\theta = 15.02^\circ$ after 2.5 ps. At later times, the peak shifts back to a quasi-stationary position around an angle of 15.1° . This position is reached at a delay of 5 ps. The timescale of the peakshift results from the ratio of the sample thickness and the velocity of sound in the sample. The sample thickness of 15.4 nm represents a good trade-off between the duration of coherent phonon propagation and diffraction efficiency from the SRO layer. Figure 2(b) shows a static XRD measurement of the structure. The STO substrate peak appears at an angle of 15.33° . Due to the small layer thickness, the layer peak has a width of 0.12° . The dynamics in the sample, which leads to the observed peak shift, is illustrated in Figure 2(c). This graph shows a simulation using a masses and springs model,²² which accounts for coherent phonon propagation and for heat diffusion from the excited layer to the substrate. Optical excitation triggers coherent expansion waves which are launched at the layer-substrate and layer-air interface, respectively, and propagate into the SRO layer. The lattice expansion is shown in red colors. At the same time, a compression wave, which is shown in dark blue colors, is launched at the layer-substrate interface. This compression wave directly propagates into the substrate. At a delay of roughly 1.3 ps, the layer peak shifts across the angle of the quasi-stationary peak position. The reason is the interference of the excited strain waves from both interfaces, as shown in Figure 2(c). The maximum shift occurs at 2.5 ps, when both expansion waves have propagated through the layer. While the strain wave that was launched at the sample surface now propagates into the substrate, the other strain wave is reflected at the sample surface and propagates back through the layer. Reflection at the surface also converts the expansion wave into a compression wave. Therefore, the layer peak position is shifted to larger θ -angles for delays larger than 2.5 ps. The quasi-stationary peak position is reached,

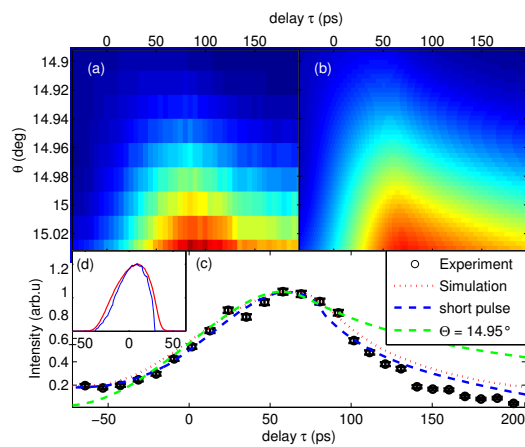


FIG. 3. (a) Two-dimensional measurement of the cross-correlation between the x-ray pulse from ESRF and the optically excited sample. The temporal delay is plotted against the x-axis, the y-axis corresponds to the Bragg angle of the sample. The diffracted intensity is coded in colors. The duration of the measured dynamics increases for larger Bragg angles. (b) Simulated cross-correlation (same axis as (a)). The probe pulse employed for this simulation is shown in the red solid line in (d). (c) Transient diffraction data (black diamonds) measured at a Bragg angle of 14.9° . The dashed and dotted lines are calculated transient signals assuming an ESRF probe pulses shape that was extracted by a deconvolution of the data (blue) and measured by a streak camera (red). The green dashed transient was calculated by setting $\theta = 14.95^\circ$ at the sample. The temporal resolution is reduced as a result of a thermal peak shift of the excited layer. (d) ESRF x-ray pulse shapes used for the calculations. The color code corresponds to (c).

when both strain waves have propagated into the substrate. The layer peak relaxes to its equilibrium position via heat diffusion from the hot layer to the substrate. This process is much slower than the coherent phonon dynamics and occurs on a nanosecond timescale.²³ Hence, after the layer peak has shifted to its quasi-stationary position, the diffraction efficiency is constant on the timescale of the incident x-ray pulse. Due to the constructive interference of both expansion waves, there is an angular range, where the peak shift is governed exclusively by the propagation of coherent phonons in the sample. Therefore, in the appropriate angular range, the sample shows a modulation of its x-ray diffraction efficiency which lasts for only 5 ps. We exploit this feature as an ultrafast probe of the x-ray pulse from the synchrotron.

Measurements of the cross-correlation signal between the ESRF x-ray pulse and the ultrafast sample response are shown in Figure 3(a) for Bragg angles from 14.89° to 15.03° . The excitation fluence was set to 15 mJ/cm^2 . Since the duration of the optical pulse is 600 fs, which is significantly faster than the propagation time of the coherent phonons through the layer, it can be omitted in the analysis of the correlation signal. Figure 3(b) shows a simulation in the same angular range that reproduces the measurement. A cut along the delay time axis is shown in Figure 3(c) for a Bragg angle of 14.9° . The measured transient has a full width at half maximum (FWHM) duration of 100 ps. Together with the experimental data, we plot a calculated pump-probe signal that was obtained by cross-correlating the simulated sample response with an ESRF probe pulse. The simulation shown in the red dotted line was

obtained by using the ESRF pulse profile as measured by a streak camera. It is shown in Figure 1(a) and in the red solid line in Figure 3(d), respectively. This pulse has a FWHM duration of ≈ 100 ps. The blue solid line in Figure 3(d) shows the shape of the ESRF x-ray pulse as extracted from a deconvolution of the simulated sample response out of the measured data. The data have been slightly smoothed for that procedure. This pulse, which has a FWHM duration of 85 ps, was used to calculate the blue dashed transient shown in Figure 3(c). It yields an even better representation of the data compared to the red transient that was calculated using the measured ESRF pulse. This concurs with the observations from previous experiments at the ID09B beamline at ESRF, which indicate a pulse length of the order of 80 ps in 16-bunch mode. Hence, the determination of the x-ray pulse length using our cross-correlation technique seems to characterize the x-ray pulse more accurately than the streak-camera measurement.

The green transient in Figure 3(c) shows a measurement where the Bragg-angle on the sample was set to $\theta = 14.95^\circ$. The slow decay at positive pump-probe delays stems from thermal relaxation from the excited layer to the substrate and the subsequent shift of the layer peak to larger angles. This effect deteriorates the temporal resolution in the cross-correlation measurement. Note that the rising edge coincides with the red and blue curves, since in all cases the rise of the pump-probe signal is determined by coherent phonon dynamics. However, the relative background at negative delays of the green dashed line in Figure 3(c) appears smaller compared to the other transients. This results from the fact that the diffraction background at negative delays is constant for all Bragg-angles, while the peak diffraction increases for increasing θ -angles of the sample.

In conclusion, we performed a time-domain sampling measurement of a 100 ps x-ray probe pulse using the ultrafast response of a laser-excited thin SRO film grown on an STO substrate. Excitation of the film with an ultrashort optical pulse triggers the propagation of coherent phonons, which modulate the diffraction efficiency in the sample. Already 5 ps after optical excitation, the sample reaches a quasi-equilibrium state that is stable for the remaining duration of the incident x-ray pulse. Our experiment is easy to reproduce and may be used for efficient time-zero determination and for measuring the shape of the x-ray probe pulse.

We thank the BMBF for funding the project via 05K10IP1.

¹M. F. DeCamp, D. A. Reis, D. M. Fritz, P. H. Bucksbaum, E. M. Dufresne, and R. Clarke, *J. Synchrotron Radiat.* **12**(2), 177–192 (2005).

²J. Larsson, P. A. Heimann, A. M. Lindenberg, P. J. Schuck, P. H. Bucksbaum, R. W. Lee, H. A. Padmore, J. S. Wark, and R. W. Falcone, *Appl. Phys. A: Mater. Sci. Process.* **66**, 587–591 (1998).

³D. A. Reis, M. F. DeCamp, P. H. Bucksbaum, R. Clarke, E. Dufresne, M. Hertlein, R. Merlin, R. Falcone, H. Kapteyn, M. M. Murnane, J. Larsson, T. Missalla, and J. S. Wark, *Phys. Rev. Lett.* **86**(14), 3072–3075 (2001).

⁴M. Trigo, Y. M. Sheu, D. A. Arms, J. Chen, S. Ghimire, R. S. Goldman, E. Landahl, R. Merlin, E. Peterson, M. Reason, and D. A. Reis, *Phys. Rev. Lett.* **101**(2), 025505 (2008).

⁵M. Herzog, D. Schick, W. Leitenberger, R. Shayduk, R. M. van der Veen, C. J. Milne, S. L. Johnson, I. Vrejoiu, and M. Bargheer, *New J. Phys.* **14**(1), 013004 (2012).

⁶M. Herzog, W. Leitenberger, R. Shayduk, R. van der Veen, C. J. Milne, S. L. Johnson, I. Vrejoiu, M. Alexe, D. Hesse, and M. Bargheer, *Appl. Phys. Lett.* **96**(16), 161906 (2010).

- ⁷P. H. Bucksbaum and R. Merlin, *Solid State Commun.* **111**, 535 (1999).
- ⁸J. M. H. Sheppard, P. Sondhaus, R. Merlin, P. H. Bucksbaum, R. W. Lee, and J. S. Wark, *Solid State Commun.* **136**, 181 (2005).
- ⁹M. Herzog, A. Bojahr, J. Goldshteyn, W. Leitenberger, I. Vrejoiu, D. Khakhulin, M. Wulff, R. Shayduk, P. Gaal, and M. Bargheer, *Appl. Phys. Lett.* **100**(9), 094101 (2012).
- ¹⁰S. Mukamel, "Principles of Nonlinear Optical Spectroscopy" (Oxford University Press, New York, 1995).
- ¹¹H. Enquist, H. Navirian, R. Nueske, C. von Korff Schmising, A. Jurgilaitis, M. Herzog, M. Bargheer, P. Sondhaus, and J. Larsson, *Opt. Lett.* **35**(19), 3219–3221 (2010).
- ¹²Z. Chang, A. Rundquist, J. Zhou, M. M. Murnane, H. C. Kapteyn, X. Liu, B. Shan, J. Liu, L. Niu, M. Gong, and X. Zhang, *Appl. Phys. Lett.* **69**, 133 (1996).
- ¹³H. A. Navirian, M. Herzog, J. Goldshteyn, W. Leitenberger, I. Vrejoiu, D. Khakhulin, M. Wulff, R. Shayduk, P. Gaal, and M. Bargheer, *J. Appl. Phys.* **109**(12), 126104 (2011).
- ¹⁴S. Anfinrud, P. A. Srajer, V. Moffat, K. Schotte, F. Techert, and M. Wulff, "Third-Generation Hard X-ray Synchrotron Radiation Sources. Source Properties, Optics, and Experimental Techniques" (John Wiley & Sons, Inc., 2002).
- ¹⁵M. Cammarata, L. Eybert, F. Ewald, W. Reichenbach, M. Wulff, P. Anfinrud, F. Schotte, A. Plech, Q. Kong, M. Lorenc, B. Lindenau, J. Rübiger, and S. Polachowski, *Rev. Sci. Instrum.* **80**(1), 015101 (2009).
- ¹⁶R. O. Bell and G. Rupprecht, *Phys. Rev.* **129**, 90–94 (1963).
- ¹⁷Y. H. Ren, M. Trigo, R. Merlin, V. Adyam, and Q. Li, *Appl. Phys. Lett.* **90**, 251918 (2007).
- ¹⁸S. Yamanaka, T. Maekawa, H. Muta, T. Matsuda, S. Kobayashi, and K. Kurosaki, *J. Solid State Chem.* **177**(10), 3484–3489 (2004).
- ¹⁹G. J. Fischer, Z. Wang, and S.-I. Karato, *Phys. Chem. Miner.* **20**, 97–103 (1993).
- ²⁰D. Schick, A. Bojahr, M. Herzog, C. von Korff Schmising, R. Shayduk, W. Leitenberger, P. Gaal, and M. Bargheer, *Rev. Sci. Instrum.* **83**(2), 025104 (2012).
- ²¹F. Zamponi, Z. Ansari, C. von Korff Schmising, P. Rothhardt, N. Zhavoronkov, M. Woerner, T. Elsaesser, M. Bargheer, T. Trobitzsch-Ryll, and M. Haschke, *Appl. Phys. A* **96**(1), 51–58 (2009).
- ²²M. Herzog, D. Schick, P. Gaal, R. Shayduk, C. von Korff Schmising, and M. Bargheer, *Appl. Phys. A* **106**(3), 489–499 (2012).
- ²³R. Shayduk, H. A. Navirian, W. Leitenberger, J. Goldshteyn, I. Vrejoiu, M. Weinelt, P. Gaal, M. Herzog, C. von Korff Schmising, and M. Bargheer, *New J. Phys.* **13**(9), 093032 (2011).

Paper XIII

Ultrafast Switching of hard x-rays

P. Gaal, **D. Schick**, M. Herzog, A. Bojahr, R. Shayduk, J. Goldshteyn, H. A. Navirian, W. Leitenberger, I. Vrejoiu, D. Khakhulin, M. Wulff, and M. Bargheer

J. Synchrotron Rad. accepted, (2013)

Ultrafast Switching of hard X-rays

Peter Gaal,^{a,*} Daniel Schick,^b Marc Herzog,^b
 Andre Bojahr,^b Roman Shayduk,^a
 Jevgeni Goldshteyn,^b Wolfram Leitenberger,^b
 Ionela Vrejoiu,^c Dmitri Khakhulin,^d Michael Wulff^d
 and Matias Bargheer^{a,b}

^aHelmholtz-Zentrum Berlin für Materialien und Energie GmbH, Wilhelm-Conrad-Röntgen Campus, BESSY II, Albert-Einstein-Str. 15, 12489 Berlin Germany, ^bInstitut für Physik und Astronomie, Universität Potsdam, Karl-Liebknecht-Str. 24-25, 14476 Potsdam Germany, ^cMax-Planck-Institut für Mikrostrukturphysik, Weinberg 2, 06120 Halle Germany, and ^dEuropean Synchrotron Radiation Facility (ESRF), 6 rue Jules Horowitz 38000 Grenoble France

We present a new concept for shortening hard x-ray pulses emitted from a third generation synchrotron source down to few picoseconds (ps). Our device, which we call the PicoSwitch, exploits the dynamics of coherent acoustic phonons in a photo-excited thin film. A characterization of the structure demonstrates switching times of ≤ 5 ps and a peak reflectivity of $\approx 10^{-3}$. The device is tested in a real synchrotron-based pump-probe experiment and reveals features of coherent phonon propagation in a second thin film sample, thus demonstrating the potential to significantly improve the temporal resolution at existing synchrotron facilities.

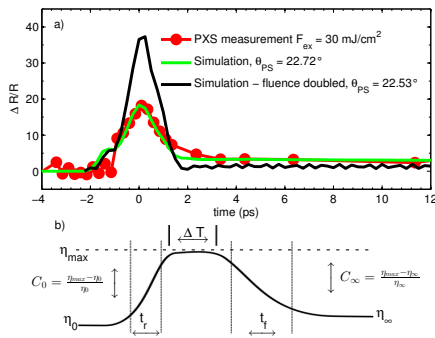
1. Introduction

Ultrafast structural dynamics can be monitored by time-resolved x-ray techniques, provided that the probing x-ray pulse is sufficiently short.(Bargheer *et al.*, 2006; Rousse *et al.*, 2001) Unfortunately, large-scale facilities like synchrotrons, which offer the best experimental conditions in terms of stability, tunability and brilliance, typically do not deliver pulses shorter than 100 ps. An exception is the so-called low- α mode (Abo-Bakr *et al.*, 2002), where the synchrotron is able to generate pulses as short as 5 ps. However, the low- α mode is only available a few weeks per year, since it reduces the x-ray intensity at all beamlines connected to the storage ring. To date, various schemes exist, that can manipulate or resolve the time structure of a synchrotron x-ray pulse. All of them are indirect in the sense that they do not act on the x-ray pulse itself. Either the electron bunch in the storage ring is manipulated (e.g., femtoslicing (Schoenlein *et al.*, 2000; Beaud *et al.*, 2007) or orbit deflection using RF cavities (Zholents *et al.*, 1999)), or electrons generated in photocathodes are used to spatially map the temporal structure of the synchrotron pulse on a screen.(Enquist *et al.*, 2010; Chang *et al.*, 1996) The highest temporal resolution at synchrotron sources is obtained by using electron slicing schemes, which leads to 150 femtosecond

(fs) pulses.(Schoenlein *et al.*, 2000; Beaud *et al.*, 2007) However, these schemes result in a rather low photon flux. Highly improved experimental conditions are found at new facilities like free-electron-laser (FEL) sources.(Emma *et al.*, 2010; Pile, 2011; Geloni *et al.*, 2010) However, the large demand for ultra-short, brilliant and stable x-ray pulses from the ultrafast community is not yet satisfied.

Several early attempts were made to manipulate the time structure of the synchrotron x-ray pulse directly. Early experiments reported switching of hard x-rays resulting in pulses of 100 ps duration and more.(Wark *et al.*, 1989; Zolotoyabko & Quintana, 2004; Allam, 1970; Grigoriev *et al.*, 2006; Navirian *et al.*, 2011) A promising concept is based on optical phonons (Bucksbaum & Merlin, 1999), however, it could not yet be realized experimentally.(Sheppard *et al.*, 2005) A modified approach exploiting acoustic phonons (Herzog *et al.*, 2010) demonstrated a modulation of the switching-contrast ratio of $\Delta R/R = 24.1$ during 1 ps. However, the first modulation maximum is followed by several post pulses, which significantly protracts the switching time.

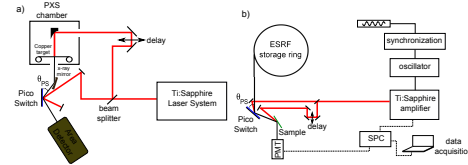
Here we present a new concept, that builds on the experience of previous approaches. We excite coherent strain waves in a thin metallic oxide film in order to modify the diffraction efficiency of the structure at a fixed Bragg angle on a picosecond time scale. An exemplary gate is shown in Figure 1 b). A good switch provides short rise- and fall times t_r and t_f and a short on-time ΔT . Also the diffraction efficiency before (η_0) and after (η_∞) the switching should be low, whereas it should be high in the on-state (η_{max}). This automatically increases the switching contrast C_0 and C_∞ . The contrast is defined as $C_i = (\eta_{max} - \eta_i)/\eta_i$. Figure 1 a) shows the measured and simulated time-dependent diffraction efficiency of the particular PicoSwitch structure discussed below in this article. After introducing the experimental method of ultrafast x-ray diffraction (UXRD) in the next section, we present a full characterization of the PicoSwitch both experimentally and theoretically in Section 3. In Section 4 we apply our approach in a real synchrotron based ultrafast pump-probe experiment. Results of this experiment are discussed in Section 5.


Figure 1

a) Measurement (red bullets) and simulations (green and black solid lines) of the PicoSwitch. The measurement was performed at the Plasma X-ray Source (PXS) at the University of Potsdam. The simulation (green line) shows excellent agreement with the measured data. A larger contrast and switching efficiency is predicted for higher pump fluences (black line). The angle θ_{PS} is the x-ray diffraction angle as defined in Figure 2 a). b) Gate parameters defining the performance of an x-ray switch: turn-on time ΔT , rise- and fall-time t_r and t_f , respectively, diffraction efficiency before (η_0), during (η_{max}) and after (η_{∞}) switching and contrast before (C_0) and after (C_{∞}) switching.

2. Experimental Setups

We performed ultrafast x-ray diffraction (UXRD) experiments at the Plasma X-ray Source (PXS) (Schick *et al.*, 2012) at the University of Potsdam and at the ID09B beamline at the European Synchrotron radiation Facility (ESRF) in Grenoble, France. A schematic of the setups is shown in Figure 2 a) and b), respectively. A high-power laser yielding ultrashort laser pulses is employed to excite the sample and the PicoSwitch, respectively. At the University of Potsdam we use a commercial Coherent Legend Duo system which provides optical pulses ($\lambda = 800$ nm) with a duration of 40 fs at a repetition rate of 1 kHz. For x-ray generation, the laser pulses are focused on a copper target in a vacuum chamber. The target is wrapped on a system of spools together with debris protection tapes. Interaction of the the highly intense laser pulses with the copper target leads to the emission of characteristic Cu K_{α} x-ray ($E = 8.047$ keV) bursts of 150 fs duration.(Schick *et al.*, 2012; Zamponi *et al.*, 2009) The temporal delay between optical pump and x-ray probe pulses is realized by a mechanical delay stage. Since the x-ray probe pulse is generated by the same laser as the pump beam, both are perfectly synchronized. X-ray photons, which are emitted in a solid angle of 4π , are collected with a Montel x-ray focusing mirror having an image ratio of 1:7. The mirror is mounted 875 mm from the sample. The 4π emission angle and the focal distance reduce the angular resolution to approximately 0.1° in a diffraction experiment, as indicated by the gray shaded area in Figure 4 d) and e). Reflected x-ray photons from the sample are detected with a CMOS hybrid-pixel area detector (Dectris Pilatus 100K).


Figure 2

a) Typical UXRD setup: The PXS at the University of Potsdam delivers 150 fs x-ray pulses at an energy of 8.047 keV. A detailed description of the PXS is given in reference (Schick *et al.*, 2012; Zamponi *et al.*, 2009). Laser parameters are: pulse energy 8 mJ, pulse duration 40 fs and repetition rate 1 kHz. The pump fluence was set to 30 mJ/cm^2 . b) Synchrotron-based pump-probe experiment: A Ti:sapphire laser system (Coherent Legend) is synchronized to the repetition rate of the ESRF storage ring with an accuracy of ≤ 5 ps between the x-ray and laser pulses. Laser parameters are: pulse energy 1.5 mJ, pulse duration 600 fs and repetition rate 1 kHz. The pump-probe scheme is shown in Figure 4 a) in detail. X-ray photons diffracted from the sample are captured in a photo-multiplier (PMT) and counted in a single photon counting (SPC) unit.

For the experiments at the ID09B beamline at the ESRF the storage ring was running in 16-bunch mode, delivering monochromatized x-ray pulses at an energy of 12 keV and a duration of 90-120 ps.(Cammarata *et al.*, 2009) The beamline is equipped with a commercial laser system (Coherent Legend) which yields 800 nm optical pulses with an energy of 1.5 mJ and a duration of 600 fs at a repetition rate of 1 kHz. The laser oscillator was electronically phase-locked to the synchrotron repetition rate, which allows for timing the delay t between the amplified optical and x-ray pulses with an accuracy better then 5 ps. This is significantly shorter than the x-ray pulse duration. The gated probe pulse reflected by the PicoSwitch is inherently synchronized to the pump laser after switching. For the second optical path, a mechanical delay stage has been introduced to realize the pump-probe delay τ . X-ray photons have been detected with a plastic scintillator (BC400-series) attached to a Hamamatsu photomultiplier tube (H7422). The detector signal was fed to a single-photon counting unit controlled by a computer.

It is important to note, that the different x-ray energies used during the PXS and the ESRF experiments, lead to two different angular ranges in the diffraction data presented in this contribution. We preserved the original angular scales to clearly distinguish the different experiments. The x-ray response of the sample is essentially the same for both x-ray energies used in the experiments. All diffraction data shown were recorded on the (002) reflection of SrTiO_3 (STO) (substrate peak) and SrRuO_3 (SRO) (layer peak). At an x-ray energy of 12 keV, the maximum of the (002) reflection of SRO appears at 15.2° (Figure 3 a). These data are recorded at the ESRF. At an x-ray energy of 8.047 keV, the SRO layer peak appears at 23.03° (Figure 3 b). These data are recorded at the PXS at the University of Potsdam.

3. PicoSwitch Characterization

The PicoSwitch consists of a thin SRO layer with a thickness of $d_{SRO} = 15.4$ nm which was epitaxially grown on an STO

substrate.(Vrejoiu *et al.*, 2006) A static rocking curve recorded at the ID09B beamline at the ESRF is shown by the green line in Figure 3 a). Note in particular, that the peak reflectivity of the (002) SRO reflection at x-ray energies from 8 keV to 12 keV is $\approx 10^{-3}$. This corresponds to the highest achievable diffraction efficiency in the on-state, as defined in Figure 1 b). The black line is a simulation of the diffraction profile from the structure using dynamic diffraction theory.(Als-Nielsen, 2011)

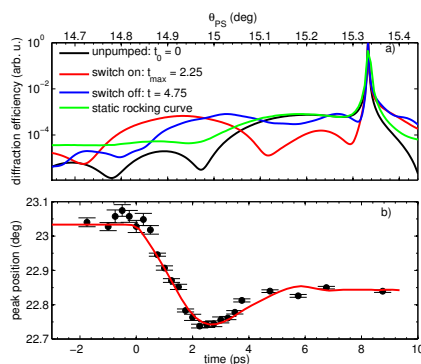


Figure 3

Characterization of the PicoSwitch: a) green: measured diffraction curve of the PicoSwitch. The data were recorded at the ID09B beamline at ESRF at an x-ray energy of 12 keV. Black: simulation of the unexcited structure; red: simulation for maximum layer expansion 2.25 ps after optical excitation; blue: simulation at $\tau = 4.75$ ps after optical excitation. At this delay all coherent sound waves have propagated into the substrate. b) Ultrafast shift of the layer peak measured at the PXS at University of Potsdam with an x-ray energy of 8.047 keV.

To record the ultrafast response of the PicoSwitch to the optical excitation, we resort to the ultrafast x-ray diffraction (UXRD) setup at the PXS at the University of Potsdam.(Schick *et al.*, 2012) Figure 3 b) shows the shift of the SRO layer peak as a function of the delay after excitation of the PicoSwitch with an ultrashort 800 nm pump pulse. The interpretation of coherent phonon dynamics of an excited layer is straightforward (Sokolowski-Tinten *et al.*, 2011) and the red solid line shows a simulation using a linear-chain model.(Herzog *et al.*, 2012b) Excitation of the PicoSwitch with an ultrashort optical pulse launches coherent expansion waves starting at the air/SRO and SRO/STO interfaces through the SRO-layer, shifting the layer Bragg peak to lower angles. The expansion waves propagate at the sound velocity in SRO of $v_{SRO} = 6.3$ nm/ps.(Herzog *et al.*, 2012a) Reflection of the strain wave at the surface converts the expansion that was launched at the SRO/STO interface into a compression wave, which propagates back through the layer and into the substrate, thus shifting the Bragg peak back to about 2/3 compared to the maximum expansion. Due to the perfect matching of the acoustic impedances of SRO and STO (Herzog *et al.*, 2012a), there is no reflection at the interface. The coherent dynamics in the SRO film last for $\tau_{switch} = 2 \cdot d_{SRO} / v_{SRO} \leq 5$ ps, i.e., the time it takes for the strain waves to propagate back and forth through the layer. For

later times, the peak position is given by the remaining heat expansion, and heat conduction cools the layer on a nanosecond timescale.(Shayduk *et al.*, 2011) Hence, there is an angular range, which extends from 22.85° to 22.75° in Figure 3 b), where the ultrafast coherent phonon propagation is responsible for the rise and fall of the diffraction efficiency. This range can be exploited for ultrafast x-ray switching. For the experiments conducted at the ESRF at an x-ray photon energy of 12 keV, this angular range extends from 14.9° to 14.75° (Figure 3 a)). In order to quantitatively compare the experimental signal with theory we feed the spatio-temporal strain map calculated in a linear-chain model into a simulation of the dynamical x-ray diffraction, yielding the x-ray response of the PicoSwitch $R(t, \theta)$.(Herzog *et al.*, 2012b) The result shows excellent agreement with the measured dynamics of the peak shift demonstrated in Figure 1 a) when keeping the angle of the PicoSwitch fixed. Figure 3 a) shows the simulations in a broader angular range for an x-ray energy of 12 keV. The red curve represents a simulated rocking curve at a time delay of 2.25 ps after excitation. At this moment the thin SRO layer is maximally expanded. The blue curve, which is simulated for a delay of 4.74 ps depicts the situation where the coherent compression wave has propagated into the substrate and thus terminates the coherent dynamics in the PicoSwitch.

4. Synchrotron-based pump-probe experiment

Now we apply the PicoSwitch, which was characterized in the previous section by simulations and measurements at the University of Potsdam, in a real synchrotron-based pump-probe experiment to study the impulsive expansion of a photoexcited metallic layer. These experiments were performed at ID09B beamline at ESRF. The output of a Ti:sapphire laser amplifier is split into two beams in order to pump the PicoSwitch and the sample separately with delays t and τ , respectively. The pump fluence was set to 15 mJ/cm² on both the PicoSwitch and the sample. A detailed schematic of the experimental setup is shown in Figure 4 a) and 2 b). The electronic delay t is set so that the diffraction efficiency of the switch is turned on and off approximately when the maximum of the 100 ps x-ray pulse from the synchrotron impinges on the PicoSwitch. It is held constant during the experiment. The pump-probe delay τ shifts the optical pump pulse for the sample against the shortened x-ray pulse. The sample under investigation was a 70 nm metallic SRO layer grown on an STO substrate.(Vrejoiu *et al.*, 2006) The dynamics in the sample can be understood in the framework of coherent phonon propagation as described before. We employ this structure as a reference to test the achievable time resolution with the gated x-ray probe pulse. The diffraction angle of the sample θ_s is set to the maximum of the SRO layer peak. Figure 4 b) shows the measured relative change of the diffracted x-ray intensity (black bullets) as a function of the pump-probe delay τ . The green dash-dotted, black solid, red dotted and blue dashed lines represent simulations of the x-ray response assuming the simulated shortened probe pulses depicted in Figure 4 c) with the same color code. The shape of the switched pulse is

determined by the Bragg angle θ_{PS} chosen on the PicoSwitch and by the pump fluence. The simulated signals plotted as lines in Figure 4 b) depict the normalized correlation of the samples x-ray response $R(t)$ at the fixed angle θ_S with the shortened probe pulse $P(t, \theta_{PS})$ for various diffraction angles θ_{PS} of the PicoSwitch:

$$X_c(\tau, \theta_{PS}) = \frac{\int_{-\infty}^{\infty} P(t, \theta_{PS}) \cdot R(\tau + t) dt}{\int_{-\infty}^{\infty} P(t, \theta_{PS}) \cdot R(-\infty) dt} \quad (1)$$

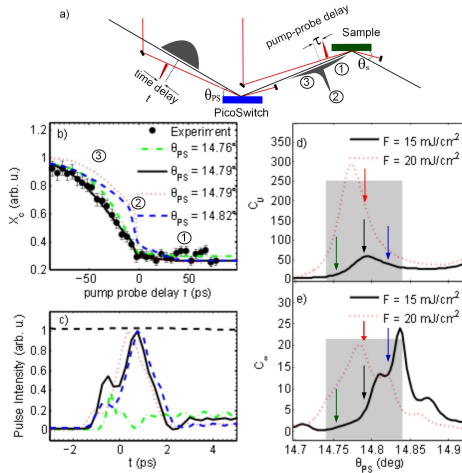


Figure 4

Synchrotron-based time-resolved experiment: a) sketch of the experimental setup showing the fixed timing t of laser and x-ray pulses and the pump probe delay τ . If the optical excitation pulse arrives earlier at the sample than the gated section of the x-ray probe pulse, the pump-probe delay τ is positive. The probe pulse is divided into three sections: leading edge (1), ultrafast gate (2) and trailing edge (3). b) Measured (black dots) and simulated (green dash-dotted, black solid, blue dashed and red dotted lines) pump-probe correlation signal X_c . The errorbars indicate a confidence interval of $\pm 32\%$. The simulations were obtained with Equation 1. The angle θ_{PS} is color coded. All simulations are for the fluence $F=15 \text{ mJ/cm}^2$ used in the experiment. Only the red dotted curve is simulated for an optimized fluence of 20 mJ/cm^2 . c) Shortened x-ray probe pulses for different incident angles on the PicoSwitch color coded as in b). The black dashed line is the original x-ray probe pulse. d) Simulated initial (C_0) and e) final (C_∞) contrast as defined in Figure 1 for different Bragg angles on the PicoSwitch. The black solid lines show a simulation for a pump fluence of 15 mJ/cm^2 . The red dotted lines show a contrast for stronger excitation with a fluence of 20 mJ/cm^2 . The colored vertical arrows mark the angles where the probe pulses in b) and c) where calculated. The gray shaded area marks the angular resolution of the PXS measurement.

5. Discussion

In the following we explain the impact of different probe pulse shapes on the measured signal. For a better understanding, we divide the gated probe pulse shown in Figure 4 a) in three sections: (1) and (3) are determined by the initial and final contrast C_0 and C_∞ , respectively, while (2) represents the ultrafast gate from the PicoSwitch. Figure 4 b)-e) present the main results of the synchrotron-based optical pump - x-ray probe experiment

with the shortened x-ray probe pulse. Experimental data are presented in Figure 4 b) (black bullets).

Figure 4 d) and e) show the angle dependence of the initial and final contrast ratio C_0 and C_∞ , respectively. The angles θ_{PS} , used in the simulations shown in Figure 4 b) and c) are marked by color coded arrows. The black solid line is calculated for a pump fluence of 15 mJ/cm^2 , the red dotted line shows the contrast for a fluence of 20 mJ/cm^2 . Note that features appearing in X_c at positive pump-probe delays stem from badly suppressed background photons in the leading edge of the probe pulse marked (1) in Figure 4 a). Features at negative τ originate from the trailing edge of the probe pulse, which is marked (3) and is determined by the thermal relaxation of the PicoSwitch after optical pumping. (Shayduk *et al.*, 2011) The sharp drop in X_c , which is observed in the red, blue and black simulation in Figure 4 b) is caused by the short and intense section of the probe pulse and is marked (2).

Our experimental data are best reproduced by the simulation shown by the black solid line in Figure 4 b). It shows a rather slow initial decay (3) and it is flat after the gated probe pulse (1), i.e., for positive τ . This indicates a large initial contrast C_0 , which is marked by the black arrow in Figure 4 d). The sharp drop from $X_c = 0.4$ to $X_c = 0.25$ at $\tau = 0 \text{ ps}$ indicates the response to the ultrafast switching (2).

The simulation for larger θ_{PS} (blue dashed line) shows a lower initial and higher final contrast, leading to deviations from the observed correlation (black bullets). The dash-dotted green line shows a case where both the initial and final contrast C_0 and C_∞ are lower. The dash-dotted green probe pulse in Figure 4 c) shows almost no ultrafast switching characteristics. Instead, the contrast ratio changes abruptly from C_0 to C_∞ . Hence, the ultrafast feature at $\tau = 0 \text{ ps}$ disappears and in addition there are deviations from the measured signal at negative τ . The best simulated performance could be obtained by increasing the pump fluence, as shown by the red dotted line in Figure 4 b) and c). Due to limited beamtime, a corresponding measurement could not be realized. In essence, Figure 4 shows that we have performed an ultrafast x-ray diffraction experiment with a synchrotron probe pulse which was shortened to approximately 2 ps as indicated in Figure 4 c) by the black line.

For an optimized performance in future applications the PicoSwitch must be pumped with about 33% higher optical pump fluence. The simulation shown by the red dotted line in Figure 4 b) and c) demonstrates an increased initial and final contrast at the θ_{PS} chosen in the experiment. This parameter setting on the PicoSwitch would result in a correlation signal X_c shown in the red dotted line in Figure 4 b). The corresponding probe pulse is shown in Figure 4 c). The essential difference to the pulse used in the experiment is the higher contrast. The switching time is identical. Thus, the PicoSwitch is suitable for generating probe pulses that are capable of resolving ultrafast dynamics on a picosecond timescale. We would like to point out that the PicoSwitch can sustain even higher fluences up to 40 mJ/cm^2 without degradation. The generated x-ray pulses are limited in duration to few picoseconds and are therefore longer than the pulses obtained through slicing of

the electron bunch. The achievable photon flux is comparable. However, the PicoSwitch experiment is significantly easier to implement. The temporal stability and angular resolution of the gated x-rays are determined by the synchrotron source. This is a significant advantage compared to laser plasma sources, such as the PXS at the University of Potsdam. We think that the PicoSwitch could be employed to improve the performance of synchrotron sources for time-resolved experiments in the future.

6. Conclusion

In conclusion, we have characterized and applied an ultrafast x-ray switch for gating synchrotron x-ray pulses on picosecond timescales. The shape of the shortened pulse can be adjusted by selecting the Bragg angle on the switch and by tuning the pump fluence. The switching relies on coherent phonon dynamics which modulate the diffraction efficiency. The rise and fall times t_r and t_f are determined by the layer thickness and the speed of sound in the material. We demonstrated a high switching contrast with a maximum diffraction efficiency of $\eta_{max} \approx 10^{-3}$. The structure allows for repetitive switching and no long-term degradation effects have yet been observed. Hence, the device is suited for permanent installation in time-resolved beamline setups. The applicability of the PicoSwitch was demonstrated in a synchrotron-based pump-probe experiment where we measured coherent lattice dynamics in a nanostructured sample with picosecond resolution.

We thank the BMBF for funding the project via 05K10IP1.

References

- Abo-Bakr, M., Feikes, J., Holldack, K., Wüstefeld, G. & Hübers, H.-W. (2002). *Phys. Rev. Lett.* **88**, 254801.
- Allam, D. (1970). *J. Phys. E*, **3**, 1022.
- Als-Nielsen, J. (2011). *Elements of Modern X-ray Physics*. John Wiley & Sons, Ltd, 2nd ed.
- Bargheer, M., Zhavoronkov, N., Woerner, M. & Elsaesser, T. (2006). *ChemPhysChem*, **7**(4), 783–792.
- Beaud, P., Johnson, S. L., Streun, A., Abela, R., Abramsohn, D., Grolimund, D., Krasniqi, F. S., Schmidt, T., Schlott, V. & Ingold, G. (2007). *Phys. Rev. Lett.* **99**, 174801.
- Bucksbaum, P. H. & Merlin, R. (1999). *Solid State Commun.* **111**, 535.
- Cammarata, M., Eybert, L., Ewald, F., Reichenbach, W., Wulff, M., Anfinrud, P., Schotte, F., Plech, A., Kong, Q., Lorenc, M., Lindemann, B., Rübiger, J. & Polachowski, S. (2009). *Review of Scientific Instruments*, **80**(1), 015101.
- Chang, Z., Rundquist, A., Zhou, J., Murnane, M. M., Kapteyn, H. C., Liu, X., Shan, B., Liu, J., Niu, L., Gong, M. & Zhang, X. (1996). *Appl. Phys. Lett.* **69**, 133.
- Emma, P., Akre, R., Arthur, J., Bionta, R., Bostedt, C., Bozek, J., Brachmann, A., Bucksbaum, P. H., Coffee, R., Decker, F.-J., Ding, Y., Dowell, D., Edstrom, S., Fisher, A., Frisch, J., Gilevich, S., Hastings, J., Hays, G., Hering, P., Huang, Z., Iverson, R., Loos, H., Messerschmidt, M., Miahnahri, A., Moeller, S., Nuhn, H.-D., Pile, G., Ratner, D., Rzepiela, J., Schultz, D., Smith, T., Stefan, P., Tompkins, H., Turner, J., Welch, J., White, W., Wu, J., Yocky, G. & Galayda, J. (2010). *Nat. Photonics*, **4**(9), 641–647. 10.1038/nphoton.2010.176.
- Enquist, H., Navirian, H., Nueske, R., von Korff Schmising, C., Jurgilaitis, A., Herzog, M., Bargheer, M., Sondhaus, P. & Larsson, J. (2010). *Opt. Lett.* **35**(19), 3219–3221.
- Geloni, G., Saldin, E., Samoylova, L., Schneidmiller, E., Sinn, H., Tschentscher, T. & Yurkov, M. (2010). *New Journal of Physics*, **12**(3), 035021.
- Grigoriev, A., Do, D.-H., Kim, D. M., Eom, C.-B., Evans, P. G., Adams, B. & Dufresne, E. M. (2006). *Applied Physics Letters*, **89**(2), 021109.
- Herzog, M., Bojahr, A., Goldshteyn, J., Leitenberger, W., Vrejoiu, I., Khakulin, D., Wulff, M., Shayduk, R., Gaal, P. & Bargheer, M. (2012a). *Appl. Phys. Lett.* **100**(9), 094101.
- Herzog, M., Leitenberger, W., Shayduk, R., van der Veen, R., Milne, C. J., Johnson, S. L., Vrejoiu, I., Alexe, M., Hesse, D. & Bargheer, M. (2010). *Appl. Phys. Lett.* **96**(16), 161906.
- Herzog, M., Schick, D., Gaal, P., Shayduk, R., von Korff Schmising, C. & Bargheer, M. (2012b). *Appl. Phys. A*, **106**(3), 489–499.
- Navirian, H. A., Herzog, M., Goldshteyn, J., Leitenberger, W., Vrejoiu, I., Khakulin, D., Wulff, M., Shayduk, R., Gaal, P. & Bargheer, M. (2011). *J. Appl. Phys.* **109**(12), 126104.
- Pile, D. (2011). *Nat. Photonics*, **5**, 456–457.
- Rousse, A., Rischel, C. & Gauthier, J.-C. (2001). *Rev. Mod. Phys.* **73**(1), 17–31.
- Schick, D., Bojahr, A., Herzog, M., von Korff Schmising, C., Shayduk, R., Leitenberger, W., Gaal, P. & Bargheer, M. (2012). *Rev. Sci. Instrum.* **83**(2), 025104.
- Schoenlein, R. W., Chattopadhyay, S., Chong, H. H. W., Glover, T. E., Heimann, P. A., Shank, C. V., Zholents, A. A. & Zolotov, M. S. (2000). *Science*, **287**, 2237.
- Shayduk, R., Navirian, H. A., Leitenberger, W., Goldshteyn, J., Vrejoiu, I., Weinelt, M., Gaal, P., Herzog, M., von Korff Schmising, C. & Bargheer, M. (2011). *New Journal of Physics*, **13**(9), 093032.
- Sheppard, J. M. H., Sondhaus, P., Merlin, R., Bucksbaum, P. H., Lee, R. W. & Wark, J. S. (2005). *Solid State Commun.* **136**, 181.
- Sokolowski-Tinten, K., Horn von Hoegen, K. M., von der Linde, D., Cavalleri, A., Siders, C. W., Brown, F. L. H., Leitner, D. M., Toth, C., Barty, C. P. G., Squier, J. A., R., W. K. & Kammler, M. (2011). *J. de Physique IV*, **11**, Pr2–473–Pr2–477.
- Vrejoiu, I., Le Rhun, G., Pintilie, L., Hesse, D., Alexe, M. & Gösele, U. (2006). *Adv. Mater.* **18**, 1657.
- Wark, J. S., Whitlock, R. R., Hauer, A. A., Swain, J. E. & Solone, P. J. (1989). *Phys. Rev. B*, **40**, 5705–5714.
- Zamponi, F., Ansari, Z., von Korff Schmising, C., Rothhardt, P., Zhavoronkov, N., Woerner, M., Elsaesser, T., Bargheer, M., Trobitzsch-Ryll, T. & Haschke, M. (2009). *Appl. Phys. A*, **96**(1), 51–58.
- Zholents, A., Heimann, P., Zolotov, M. & Byrd, J. (1999). *Nuclear Instruments and Methods in Physics Research Section A: Accelerators, Spectrometers, Detectors and Associated Equipment*, **425**(1â2), 385–389.
- Zolotoyabko, E. & Quintana, J. P. (2004). *Rev. Sci. Instr.* **75**, 699.

Paper XIV

Direct time-domain sampling of subterahertz coherent acoustic phonon spectra in SrTiO₃ using ultrafast x-ray diffraction

R. Shayduk, M. Herzog, A. Bojahr, **D. Schick**, P. Gaal, W. Leitenberger, H. A. Navirian, M. Sander, J. Goldshteyn, I. Vrejoiu, and M. Bargheer

Phys. Rev. B 87, 18 (2013)

Direct time-domain sampling of subterahertz coherent acoustic phonon spectra in SrTiO₃ using ultrafast x-ray diffraction

Roman Shayduk,^{1,*} Marc Herzog,² Andre Bojahr,² Daniel Schick,² Peter Gaal,¹ Wolfram Leitenberger,² Hengameh Navirian,² Mathias Sander,² Jevgenij Goldshteyn,¹ Ionela Vrejoiu,³ and Matias Bargheer^{1,2}

¹*Helmholtz-Zentrum Berlin für Materialien und Energie GmbH, Wilhelm-Conrad-Röntgen Campus, BESSY II, Albert-Einstein-Str. 15, 12489 Berlin, Germany*

²*Institut für Physik und Astronomie, Universität Potsdam, Karl-Liebknecht-Str. 24-25, 14476 Potsdam, Germany*

³*Max-Planck-Institut für Mikrostrukturphysik, Weinberg 2, D-06120 Halle, Germany*

(Received 18 December 2012; revised manuscript received 22 March 2013; published 7 May 2013)

We synthesize sub-THz longitudinal quasimonochromatic acoustic phonons in a SrTiO₃ single crystal using a SrRuO₃/SrTiO₃ superlattice as an optical-acoustic transducer. The generated acoustic phonon spectrum is determined using ultrafast x-ray diffraction. The analysis of the generated phonon spectrum in the time domain reveals a k -vector dependent phonon lifetime. It is observed that even at sub-THz frequencies the phonon lifetime agrees with the $1/\omega^2$ power law known from Akhiezer's model for hyper sound attenuation. The observed shift of the synthesized spectrum to the higher q is discussed in the framework of nonlinear effects appearing due to the high amplitude of the synthesized phonons.

DOI: 10.1103/PhysRevB.87.184301

PACS number(s): 63.20.-e, 61.05.cp

I. INTRODUCTION

The increasing importance of coherent phonon spectroscopy in material science is related to the growing problem of heat dissipation in modern nanoscale devices. This problem is impossible to solve without detailed understanding of underlying phonon-phonon and phonon-electron interactions on the nanoscale. One of the methods to study these processes is coherent phonon spectroscopy, in which a particular phonon spectrum is excited coherently in the sample and detected optically. Research efforts in this direction resulted in significant progress in generation and detection of coherent phonons in various materials. The available phonon frequency has reached the THz acoustic limit¹ and basically the whole phonon frequency range nowadays could be excited coherently. However, convenient optical detection methods based on Raman^{2,3} or Brillouin⁴ scattering allow for the observation of phonons excited only in the vicinity of the Brillouin zone center. Therefore, sub-THz acoustic phonons could be accessed optically only in multilayer structures, in which the acoustic dispersion branch backfolds many times inside a mini-Brillouin zone of a multilayer.⁵ Modern progress in pulsed laser techniques as well as in multilayer fabrication has led to a set of successful experiments in which the coherent zone-folded superlattice phonons have been optically excited and detected.⁵⁻⁷ However, these optical methods are insensitive to the THz frequency phonons which have propagated into the bulk of the crystal due to the unfolding of the phonon dispersion curve. Convenient optical methods based on Brillouin scattering in this case have a detection limit in the 100 GHz range given by the wave vector magnitude of the optical light.^{8,9} Recently, ultrafast x-ray diffraction (UXRD) has become available to extend the accessible phonon frequency range to above 100 GHz. It has been used successfully to study both the time-domain structure of optically excited zone-folded coherent acoustic phonons in epitaxial multilayers,¹⁰ as well as to observe the propagation of unfolded phonons into the bulk.¹¹

In this paper we report our new UXRD experiments from coherent quasimonochromatic longitudinal acoustic phonons

in SrTiO₃ synthesized by fs-laser excitation of SrRuO₃/SrTiO₃ (SRO/STO) epitaxial multilayers. Using UXRD we determine the laser excited phonon spectrum in SrTiO₃ and monitor the modification of the spectrum in the time domain. The epitaxial multilayers were prepared using pulsed laser deposition.¹² The experiments are carried out at the BESSY EDR beamline using a unique setup for a 1 MHz repetition rate UXRD experiments.

The experiments are done in a traditional scheme which uses an optical delay line to change the time interval between the optical pump and the x-ray probe pulses. We use infrared optical pulses with the wavelength of 1.03 μm for pumping and 8 keV x-rays for probing the lattice dynamics. The important feature of this setup is the simultaneous acquisition of the x-ray photons scattered from the sample before and after the pumping optical pulse. This makes the x-ray intensity difference signal sensitive only to those changes in the crystal lattice which were exclusively initiated by the optical pulses. For further details we refer to a recent publication describing the setup.¹³

II. THEORY

A. Synthesis of quasimonochromatic coherent acoustic phonons

Recent studies showed that the optical excitation of a metal transducer by a sequence of ultrashort laser pulses is an efficient method to generate sub-THz quasimonochromatic longitudinal acoustic (LA) phonons.¹⁴⁻¹⁶ In essence, the repetitive generation of bipolar strain pulses by the laser-excited transducer¹⁷ forms a phonon wave packet of narrow spectral bandwidth propagating throughout the substrate. In this report we consider a different approach which uses a spatial repetition instead of a temporal one, i.e., the excitation of a periodic metal-dielectric multilayer (superlattice) with a single ultrashort laser pulse [see Fig. 1(a)]. This way the so-called superlattice phonon mode is excited,^{10,18-21} which subsequently unfolds into the substrate thereby forming LA phonon wave packets with similarly narrow spectral

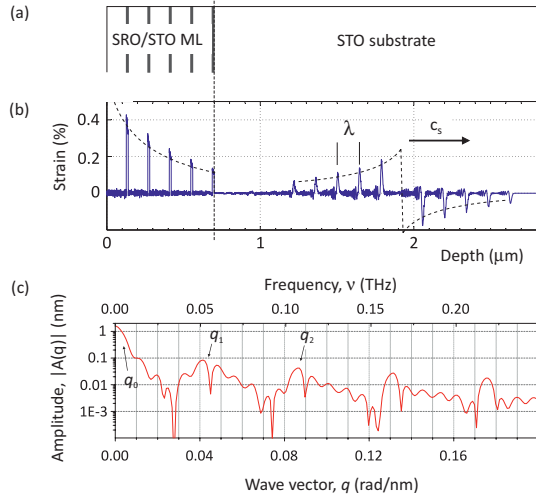


FIG. 1. (Color online) (a) Sketch of the five-period epitaxial SrRuO₃/SrTiO₃ multilayer on top of the SrTiO₃ substrate. (b) Calculated strain profile in the sample along the surface normal, taken at 250 ps after the multilayer excitation. (c) Calculated spectrum of the strain pulse in the wave vector and frequency domains induced by the optical excitation. The vertical scale stands for the excitation fluence of 6 mJ/cm² used in the experiment.

bandwidth.^{11,20} In most cases the laser-induced coherent lattice dynamics may be calculated using either a model of a continuous elastic medium¹⁷ or a linear-chain model (LCM) of masses and springs.²⁰ Here we employ the latter approach which will be more appropriate for short-period superlattices and automatically accounts for the acoustic phonon dispersion. The details of the numerical model can be found in Ref. 20. The excellent agreement of such a linear-chain model with related optical and UXRD experiments has been previously demonstrated for various sample structures.^{16,19–23}

Further we consider linear chain calculations for a five-period SRO/STO multilayer with the spatial period $D = 140$ nm which is schematically shown in Fig. 1(a). The structural parameters of the sample which are determined by static high-resolution x-ray diffraction (HRXRD)²⁴ are collected in Table I. In addition, the longitudinal sound velocities of the individual materials are shown.²⁵ The results of the linear-chain calculations using the parameters given in Table I and the experimental pump fluence of 6 mJ/cm² are shown in Figs. 1(b) and 1(c).

The graph in Fig. 1(b) shows the calculated one-dimensional strain profile in the sample 250 ps after the

TABLE I. Structural and mechanical properties employed in the calculations.

Material	Lattice constant	Thickness	Sound speed
Substrate STO	3.905 Å	10 μm	7.9 nm/ps
STO in ML	3.92 Å	127 nm	7.8 nm/ps
SRO in ML	3.95 Å	13 nm	6.3 nm/ps

excitation. Figure 1(c) plots the spectral amplitude of the linear-chain eigenvectors (normal modes) as a function of the eigenfrequency. This amplitude spectrum is solely determined by the initial conditions.²⁰ For the bulk STO substrate the eigenvectors are plane elastic waves with wave vector q satisfying the well-known dispersion relation of acoustic phonons.²⁶ As Fig. 1(b) illustrates, the optical excitation of the metal layers of the multilayer system results in the generation of a coherent strain wave packet propagating into the STO substrate at the longitudinal sound velocity.²⁰ The resulting wave packet inside the STO substrate attains the particular shape shown in Fig. 1(b), namely, five leading compression pulses and five trailing expansion pulses which are separated by $\lambda \approx 140$ nm, respectively. In other words, the metal/dielectric multilayer acts as the photoacoustic transducer synthesizing the coherent LA phonon wave packet in the STO substrate. The sharp static profile of the thermal strain inside the multilayer [see Fig. 1(b)] remains unchanged with time because the linear chain model neglects the effect of heat diffusion. The heat diffusion in multilayers is a complicated separate topic which lays out of the scope of this paper. In this paper we focus on the coherent lattice dynamics in the STO substrate which occur at a later timescale when the effect of heat diffusion within the multilayer does not play a role. For the detailed description of the wave packet strain profile and its generation we refer to our earlier works.²⁰

The calculated amplitude spectrum in Fig. 1(c) contains several equidistant peaks. The most pronounced peak at $q_0 = 0$ rad/nm is responsible for the overall bipolar shape of the wave packet.^{17,20} The width of the peak is determined by the total thickness of the multilayer ($\Delta q \approx \pi/5\lambda$). The peak around $q_1 = 2\pi/\lambda \approx 0.046$ rad/nm corresponds to the characteristic spatial period λ of the wave packet. The nonsinusoidal shape of the wave packet gives rise to the higher harmonics at integer multiples of q_1 .

Altogether, we find that using a periodic metal-dielectric multilayer as photoacoustic transducer we can generate LA phonon wave packets similar to the quasimonochromatic wave packets produced by multiple-pulse excitation of a thin metal film.^{14–16} In both cases the wave packets exhibit narrow spectral bandwidth and higher harmonics of lower amplitude.

B. Ultrafast x-ray diffraction from sub-THz elastic waves

The x-ray diffraction from crystals which are subject to a strong acoustic field is a well-established topic.^{27–29} However most of the previous studies deal with strain fields generated by surface acoustic wave (SAW) transducers. Such devices normally generate acoustic waves with wavelengths longer than either the x-ray extinction length or the x-ray coherence length. The x-ray diffraction from a crystal lattice perturbed by such waves results in modifications of the Bragg peak shape within the Darwin width or in the appearance of diffuse scattering contributions in the vicinity of the peak.^{30,31} The description of the x-ray scattering from such waves usually requires dynamical x-ray diffraction theory.

Here we consider quasimonochromatic coherent LA phonons which in fact are elastic waves at hypersonic frequencies. The corresponding wave vectors q are large enough to allow for coherent Bragg-like scattering of x rays

from the associated “moving gratings.” Due to the sufficiently high q vectors of the quasimonochromatic phonons the x-ray scattering contributes in the off-Bragg region in which the x-ray scattering efficiency from the bulk of the crystal is small. This allows us to probe the x rays exclusively scattered from the wave packet with only minor perturbation by the bulk-scattered x-ray wave field.

In this section we introduce the necessary theoretical basis which allows a thorough interpretation of the UXRD experiments. Since we intend to apply the following theory to study the laser-induced structural dynamics in one dimension we restrict ourselves to a one-dimensional formulation.

A plain elastic wave with wave vector q contributes to the scattered x-ray intensity if the x-ray scattering vector Q is given by

$$Q = G \pm q, \quad (1)$$

where G is a reciprocal lattice vector and $Q = |\mathbf{k} - \mathbf{k}_i|$ is the x-ray scattering vector.^{16,32–34}

From simulations of the scattered x-ray intensity using dynamical theory of x-ray diffraction one finds that the x-ray intensity scattered from the crystal perturbed by a bunch of elastic waves can be well described by the equation

$$\langle I_p(Q) \rangle_t = I_{up}(Q) + \alpha A(q)^2, \quad (2)$$

where $I_p(Q)$ and $I_{up}(Q)$ is the scattered x-ray intensity from the perturbed and unperturbed crystal, respectively. The angle brackets stand for time averaging. The function $A(q)$ is the spectral amplitude of the elastic wave with wave vector magnitude $q = |Q - G|$ and α is some constant. It is worth showing here that formula (2) is equivalent to the expression describing thermal diffuse scattering (TDS) from acoustic phonons.³⁵ To show this we need to relate the energy of a classical plane elastic wave in the crystal with the phonon population. The energy of plane elastic waves in the classical linear theory of elasticity is proportional to the squared product of the wave amplitude A and frequency ω

$$E(\omega) \propto A^2 \omega^2. \quad (3)$$

In a crystal lattice this corresponds to the energy of the corresponding vibrational normal mode which is associated with a single harmonic oscillator. According to quantum mechanics the energy of a harmonic oscillator with angular frequency ω is

$$E(\omega) = \hbar \omega \left(n + \frac{1}{2} \right), \quad (4)$$

where n is the excitation level. That is, the energy of the vibrational normal modes is quantized and n refers to the number of phonons in the crystal having the angular frequency ω . Therefore, the following relationship between the excited classical amplitude spectrum of elastic waves and the phonon population holds

$$A(q_i)^2 \propto \left(n(\omega_i) + \frac{1}{2} \right) / \omega_i \approx \frac{n(\omega_i)}{\omega_i}, \quad (5)$$

in which index i identifies the normal mode. The combination of Eqs. (2) and (5) yields

$$\langle I_p(Q) \rangle_t - I_{up}(Q) \propto \frac{n(Q - G)}{\omega(Q - G)}, \quad (6)$$

which is a one-dimensional equivalent of the relation for TDS derived by Warren.³⁵

We thus conclude that UXRD from a quasimonochromatic strain pulse directly measures the squared spectral amplitudes of the plane elastic waves constituting the strain pulse. As an example we consider the reciprocal lattice vector G_{002} of STO and rewrite Eqs. (2) and (6) into

$$A(q) \propto \sqrt{\langle I_p(G_{002} + q) \rangle_t - I_{up}(G_{002} + q)} \quad (7)$$

$$n(q) \propto \omega(q) (\langle I_p(G_{002} + q) \rangle_t - I_{up}(G_{002} + q)). \quad (8)$$

In the standard θ - 2θ geometry applied in our UXRD experiments, the magnitude of the phonon wave vector q is

$$q = \frac{4\pi}{\lambda_X} |\sin \theta - \sin \theta_0|, \quad (9)$$

where λ_X is the x-ray wavelength, θ is the x-ray incidence angle with respect to the sample surface [(001) crystallographic plane], and θ_0 is the Bragg angle.

To demonstrate that Eq. (7) is applicable to our case we compare the calculated amplitude spectrum of the laser-excited strain waves to the dynamical UXRD simulations from the same acoustically perturbed sample.¹⁹ The calculated spectrum for the laser fluence of 6 mJ/cm² is plotted in Fig. 2 as a red solid line. The dynamical UXRD calculations are performed for 200 time steps within the interval from 100 ps to 300 ps after the excitation and then time averaged. The blue symbols in Fig. 2 show the scaled time averaged square root of the intensity differences [cf. (7)] obtained from the dynamical UXRD calculations.

We see that the curves almost coincide although the fine structure of the UXRD-related curve (blue symbols) slightly

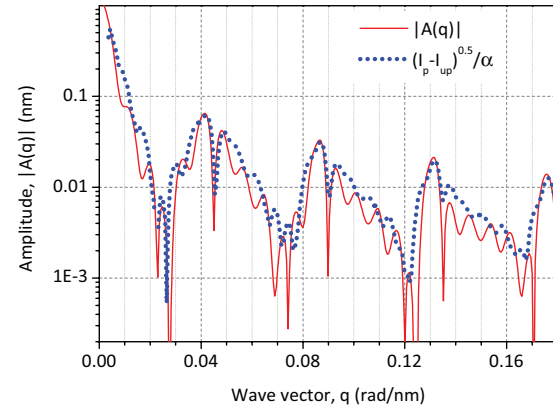


FIG. 2. (Color online) Comparison of the calculations of the spectral strain amplitudes of phonons with the corresponding x-ray intensity difference signal of perturbed-unperturbed structures. The red solid line indicates the calculated phonon spectrum in the sample in the q domain. The values in the vertical axis correspond to the phonon spectral amplitudes calculated for the excitation fluence of 6 mJ/cm². The blue bullets show the square root of the x-ray intensity difference signal calculated for the perturbed and unperturbed structures. The vertical scale factor for the UXRD signal is arbitrary.

deviates from the actual spectrum (red solid line). This is due to the fact that the scattered x-ray intensity from a propagating strain wave packet actually oscillates in the time domain at each fixed q vector with the frequency of the corresponding phonon mode. These oscillations were successfully observed in pioneering experiments with the advent of UXRD.^{32–34} The classical explanation for the oscillations is the interference of x rays scattered from a moving grating (elastic wave) and the x rays scattered from the static component of the crystal lattice. This is an x-ray analog of Brillouin oscillations in all-optical experiments.³⁶ In our case, as we can see, this interference is not very strong. Therefore, the shape of the blue curve slightly depends on the averaging time window. To eliminate these artifacts, the averaging time window should be either much longer than any phonon vibration period or we need to fit an integer number of vibrations for each q . The averaging over many vibrational periods is not possible in our case, because the actual phonon lifetime is only several vibration periods as we will see later.

To finish this section we briefly review the conditions at which the approximation (7) should be valid:

(i) The interatomic displacement in the strain wave is much less than the interatomic distance

$$|r_m - r_n| \ll_{m \neq n} |a(m - n)|, \quad (10)$$

in which a is the interatomic distance, and m and n are the index number of atoms. This is required by the perturbation theory of x rays scattered from a dynamical lattice.³⁵

(ii) The wave vector of a phonon is much smaller than any reciprocal lattice vector:

$$q \ll G. \quad (11)$$

This is necessary to avoid the signal overlap from the adjacent Bragg reflections of the crystal.

(iii) The wavelength of a phonon mode is much smaller than both the x-ray coherence and the x-ray extinction lengths:

$$q \gg \frac{1}{l}, \quad (12)$$

in which l is either x-ray coherence or x-ray extinction lengths, depending on which one is larger.

(iv) The x-ray intensity is time averaged over many vibrational periods.

III. EXPERIMENTAL RESULTS

We performed UXRD experiments on the laser-excited five-period SRO/STO multilayer with the structure parameters presented in Table I. In this section we present the experimental results which evidence the presence of a propagating quasimonochromatic LA phonon wave packet. We discuss the dynamics of the first- and second-order transient diffraction peaks and the corresponding dynamics of the strain pulse.

In the experiment we acquire the x-ray photons scattered from the sample 50 ns before each optical pulse and at a given probe delay after each optical pulse. The corresponding scattered x-ray intensities from the perturbed and unperturbed sample are thus defined as I_p and I_{up} , respectively. The time resolution of the experiments was 100 ps due to the limited

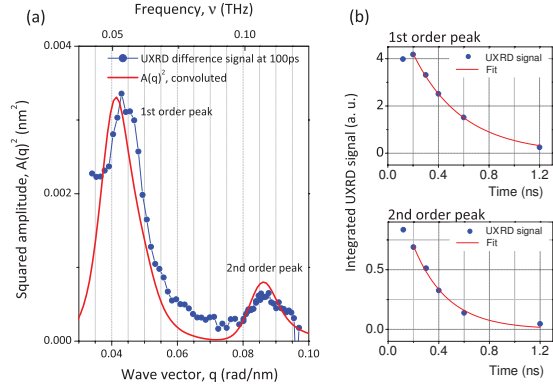


FIG. 3. (Color online) (a) The solid dots show the UXRD difference signal with an arbitrary vertical scale factor. Red is the calculated spectrum of the synthesized wave packet. (b) The integrated UXRD difference signal of the first two order phonon peaks as a function of time. The solid lines indicate the exponential fit.

x-ray pulse length, therefore the measured x-ray intensity is time averaged over multiple phonon vibrations.

Figure 3(a) shows the measured x-ray intensity difference signal $I_p - I_{up}$ (blue symbols) in the vicinity of the STO (002) Bragg peak (not visible) at 100 ps after the laser-pulse excitation. The experimental incidence angle θ has been converted into the phonon wave vector using Eq. (9). The vertical scale for the measured data is arbitrary. The UXRD data exhibit the first- and second-order spectral components of the synthesized quasimonochromatic phonon wave packet inside the STO substrate at wave vectors $q_1 \approx 0.045$ rad/nm and $q_2 \approx 0.09$ rad/nm, respectively. Given the longitudinal sound velocity in STO (cf. Table I), the linear phonon dispersion relation of acoustic phonons implies the corresponding hypersonic frequencies $\nu_1 \approx 55$ GHz and $\nu_2 \approx 110$ GHz. The nonvanishing contributions between the phonon peaks are due to the diffraction from the laser-heated multilayer. However, since the lattice constants throughout the multilayer are larger than that of the substrate (cf. Table I), the x-ray scattering from the multilayer is rather weak in this angular range. The red solid line in Fig. 3(a) shows the squared amplitude spectrum of the propagating sound wave as obtained from the linear-chain model. The shown spectrum includes the convolution with a Gaussian resolution function having a full width at half maximum (FWHM) of $15 \times 10^{-3} \text{ nm}^{-1}$ to fit the angular resolution of the UXRD experiment. The main contribution to the XRD peak broadening is due to the sample bending according to the stationary laser heat load.¹³ The UXRD signal shows very good agreement with the convoluted spectrum in terms of position, relative intensity and width of the first and second-order phonon peaks. This verifies the relation between the measured x-ray intensity and the amplitude spectrum of the coherent strain wave derived in Eq. (7).

In the following we discuss the intensity changes of the measured phonon peaks with time. During the first 100 ps after laser excitation the intensity of the phonon peaks builds up¹⁶ due to the unfolding of the initially excited superlattice phonon

TABLE II. Comparison of the experimentally observed UXRD intensity decay time τ_{exp} , the apparent decay time due to x-ray absorption τ_{abs} , and the derived phonon lifetime τ_{ph} for the first- and second-order phonon peaks. The corresponding standard deviations $\sigma_{\text{exp/abs}}$ are also shown.

q , rad/nm	τ_{abs} , ps	τ_{exp} , ps	τ_{ph} , ns
0.045	450	373 ± 12	2.2 ± 0.5
0.09	450	235 ± 30	0.49 ± 0.13

mode into the substrate.^{11,20} Subsequently, the integrated intensity of the phonon peaks decays exponentially as is evidenced by the blue symbols in Fig. 3(b). The red solid lines show fits according to the function

$$f(t) = \Delta I_0 e^{-\frac{t}{\tau_{\text{exp}}}}, \quad (13)$$

where the two fitting parameters ΔI_0 and τ_{exp} are the amplitude and decay time of the measured signal. The data points before 200 ps after the excitation were excluded from the fit since the wave packet may not yet be fully propagated from the multilayer to the substrate. The extracted decay times τ_{exp} and standard deviations σ_{exp} are shown in Table II.

There are two major reasons for the observed decrease of the UXRD peak intensities. First, the absorption of the x rays by the crystal reduces the sensitivity of the x rays to the wave packet as it propagates deeper into the substrate. Second, the dissipation of energy from the elastic wave due to the finite phonon lifetimes leads to a decay of the strain amplitude.

Considering the first reason, the decay time of the UXRD signal exclusively due to x-ray absorption is related to the x-ray absorption coefficient $\mu = 0.056 \mu\text{m}^{-1}$ by

$$\frac{1}{\tau_{\text{abs}}} = \frac{2\mu c_s}{\sin \theta} = \frac{8\pi\mu c_s}{Q\lambda_x}, \quad (14)$$

where $c_s = 7.9 \text{ nm/ps}$ is the longitudinal sound speed in the substrate.²⁵ The relative variation of the x-ray scattering vector Q during the presented UXRD experiments is 10^{-3} , which implies that τ_{abs} is virtually independent of the observed phonon wave vectors q . In the measured off-Bragg region the x-ray extinction due to dynamical x-ray diffraction is negligible, therefore only the angular independent x-ray absorption is relevant. Under the chosen experimental conditions we estimate a signal decay time of $\tau_{\text{abs}} \approx 466 \text{ ps}$ due to the x-ray absorption. Nevertheless, since this value is critical for the correct interpretation of the experimental data, we have performed dynamical XRD calculations based on results of the linear-chain lattice dynamics in harmonic approximation which excludes the effect of phonon damping.^{16,20} The simulations yield the q -independent value of $450 \pm 5 \text{ ps}$ for the decay constant due to x-ray absorption which we will use in the following.

Regarding the second reason for the decay of the UXRD phonon signals, we assume an exponential law for the decrease of the phonon population $n(q,t)$ and define the associated decay time τ_{ph} . According to Eq. (7) the corresponding intensity of the scattered x rays possesses the same decay constant. Therefore, the UXRD signal decay mechanisms

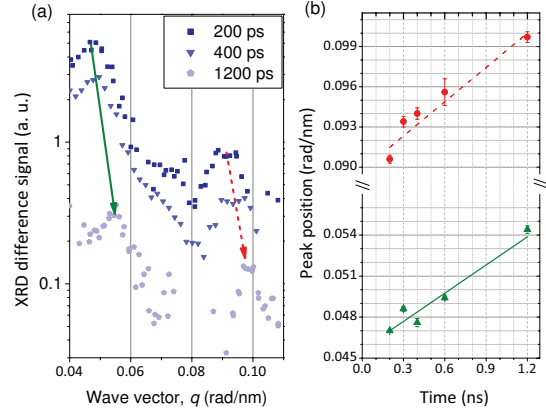


FIG. 4. (Color online) (a) Transient first- and second-order phonon diffraction peaks at various probe delays. The intensity decay due to sound attenuation is accompanied by a continuous shift to larger wave vectors as is indicated by the arrows. (b) First- and second-order peak position determined by Gaussian fits as a function of time delay. The solid lines show the linear fits to the experimental points.

introduce the relationship between the phonon lifetimes τ_{ph} , x-ray absorption time constant τ_{abs} , and the experimentally measured time constant τ_{exp} :

$$\frac{1}{\tau_{\text{exp}}} = \frac{1}{\tau_{\text{abs}}} + \frac{1}{\tau_{\text{ph}}}. \quad (15)$$

The phonon lifetimes τ_{ph} extracted from the UXRD experiments according to Eq. (15) are given in Table II for the wave vector magnitudes corresponding to the first- and second-order phonon peaks. The standard deviations σ_{ph} for the phonon lifetimes are calculated from the standard deviations σ_{exp} of the experimental time constants according to the error propagation relation.

The important observation is the fact that the determined lifetimes differ by a factor of ~ 4 whereas the related phonon wave vector differ by a factor of 2. In addition to the signal decay we see a gradual drift of the phonon peak position to higher values of q as the wave packet propagates. This is seen from Fig. 4(a), in which the phonon spectrum is shown for different time delays. In the following section we discuss the physical interpretation of the described observations.

IV. DISCUSSION

The central observation from the transient phonon-induced diffraction peaks presented in the previous section is the apparent quadratic decrease of the phonon lifetime with phonon wave vector q . This observation is in agreement with the $1/\omega^2$ law predicted by the Akhiezer's sound attenuation mechanism.³⁷

There are basically two theories which explain the attenuation of hypersonic waves in dielectric crystals due to incoherent anharmonic phonon-phonon scattering. These are

the Landau-Rumer theory³⁸ and the Akhiezer theory³⁷ which have different application limits:

$$\omega \ll \frac{1}{\tau_{\text{th}}} \quad \text{Akhiezer} \quad (16)$$

$$\omega \gg \frac{1}{\tau_{\text{th}}} \quad \text{Landau-Rumer}, \quad (17)$$

where ω is the angular frequency of the hypersonic wave and τ_{th} is the mean thermal phonon relaxation time. That is, in both cases the elastic energy of hypersound waves decreases with time due to the interaction with incoherent thermal phonons. The mean thermal phonon relaxation time τ_{th} can be estimated from the thermal conductivity k , heat capacity C_V , average sound speed v_s , and mass density ρ by the relation²⁶

$$k = \frac{1}{3}\rho C_V v_s^2 \tau_{\text{th}}. \quad (18)$$

For STO at room temperature Eq. (18) yields $\tau_{\text{th}} \approx 0.26$ ps. The experiments are performed at room temperature. More precisely, the sample persisted at around 400 K during the actual measurements due to the thermal load from the laser.¹³ Condition (16) is fulfilled for this temperature range. That is, for the presented experiments Akhiezer's theory of relaxation damping could be applied, hereby explaining the observed ratio of the phonon lifetimes for the first- and second-order phonon diffraction peaks. However the UXR data exhibit additional features which cannot be explained within Akhiezer's sound attenuation model. We extracted the transient peak positions by Gaussian fits to the data shown in Fig. 4(a), and the results are plotted as symbols in Fig. 4(b). The solid lines indicate linear fits to the phonon peak positions as a function of time. Clearly, a gradual shift of the first- and second-order spectral components to higher q values can be observed as the phonon wave packet propagates deeper into the STO substrate.

A recent study revealed the nonlinear propagation of large-amplitude sound wave packets in STO at room temperature.²² In addition to the Akhiezer-like attenuation of the coherent LA phonons the authors observed transient changes of the acoustic spectrum due to coherent anharmonic phonon-phonon scattering within the wave packet. The lattice anharmonicity gave rise to a strain-dependent longitudinal sound velocity. In particular, the sound velocity of compressive (tensile) parts of the wave packet was found to increase (decrease) with the strain amplitude. This effect led to an anomalous dispersion of the wave packet and the corresponding modification of the phonon spectrum.

Accordingly, we expect the first compressive half of the wave packet shown in Fig. 1(b) to propagate faster than the second tensile half. Moreover, the individual pulses inside the respective parts also exhibit different velocities due to the exponential amplitude distribution determined by the optical penetration of the pump light in SRO. For both the compressive and tensile parts of the strain pulse the spatial separation λ of the individual pulses of the wave packet is reduced as it propagates, i.e., the wavelength of both subpackets is decreased. This explains the observed shift of the phonon peaks to larger q values.

The presented UXR data thus evidence the influence of two different effects on the propagation of LA phonon wave

packets generated by periodic multilayers. First, the inevitable attenuation of the wave packets by Akhiezer's relaxation damping and, second, the change of spatial and spectral shape of the wave packet by nonlinear sound propagation. Both effects influence the observed phonon lifetime, however, for a quantitative determination of the respective contributions additional measurements have to be performed. The results of our earlier all-optical experiments having much stronger excitation were successfully explained solely in the framework of nonlinear acoustics.²² We believe that at the presented experimental conditions the influences of both damping mechanisms, the nonlinear acoustic propagation and the Akhiezer's relaxation, are comparable.

UXRD has the advantage of measuring the lattice dynamics directly and quantitatively, i.e., the absolute amplitude of the lattice motion is determined. The wave vector range over which acoustic phonons in bulk material are accessible is very large. In particular resolving the second order phonon peak as presented in this paper or higher orders is possible. The extension of the UXR detection of acoustic phonons in amorphous materials is challenging the available x-ray fluence, since the Bragg spots are dispersed in diffraction rings.

On the other hand all-optical picosecond acoustics,^{3,4,7,8,17} in principle, do not require crystalline materials and for transparent media, the propagation of strain pulses can be monitored over longer distances. With current technology femtosecond time resolution is standard in all-optical experiments, while it is still a challenge in x-ray technology, which was essentially resolved by free-electron lasers. High time-resolution permits the determination of the wave-vector-dependent sound velocity in addition to the damping time. We believe that the UXR-based methods and the all-optical methods do not compete with each other but complete each other, together providing a more complete picture of the complex coherent phonon dynamics for a broader range of frequencies and wave vectors and for a broader class of materials and experimental conditions.

V. CONCLUSIONS

This report presents ultrafast x-ray diffraction (UXRD) studies on laser-excited periodic SrRuO₃/SrTiO₃ multilayers which are epitaxially grown on a SrTiO₃ substrate. The ultrafast heating of the metallic SrRuO₃ layers by ultrashort laser pulses generates coherent longitudinal acoustic phonons which eventually propagate into the substrate as a quasimonochromatic coherent LA phonon wave packet at hypersonic frequencies. We discussed the properties of such wave packets in detail and derived equations which show that UXR is a powerful tool to measure the spectral phonon population and its dynamics. The presented UXR data evidence the formation of a quasimonochromatic coherent phonon wave packet. We extracted the phonon lifetimes of the first- and second-order peaks of the phonon spectrum. The observed quadratic decrease of the phonon lifetime with increasing phonon wave vector q is in accordance with Akhiezer's mechanism of relaxation damping. Shifts of the peaks corresponding to the excited phonons to larger q values are interpreted as a

modification of the spatial shape profile due to the nonlinear wave propagation leading to a strain dependent sound velocity. This considerably modifies the observed phonon lifetimes. In essence, UXRd provides a detailed and direct view on the complex nonlinear evolution of phonon-wave packets, including incoherent damping of the phonon amplitude by coupling to

other modes and specific coherent changes of the wave vector spectrum.

ACKNOWLEDGMENT

We thank the BMBF for funding via 05K 2012-OXIDE.

*roman.shayduk@helmholtz-berlin.de

- ¹A. Q. Wu and X. Xu, *Appl. Phys. Lett.* **90**, 251111 (2007).
- ²C. V. Raman and K. S. Krishnan, *Nature* **121**, 501 (1928).
- ³G. C. Cho, W. Kütt, and H. Kurz, *Phys. Rev. Lett.* **65**, 764 (1990).
- ⁴R. Y. Chiao, C. H. Townes, and B. P. Stoicheff, *Phys. Rev. Lett.* **12**, 592 (1964).
- ⁵C. Colvard, R. Merlin, M. V. Klein, and A. C. Gossard, *Phys. Rev. Lett.* **45**, 298 (1980).
- ⁶C. Colvard, T. A. Gant, M. V. Klein, R. Merlin, R. Fischer, H. Morkoc, and A. C. Gossard, *Phys. Rev. B* **31**, 2080 (1985).
- ⁷A. Bartels, T. Dekorsy, H. Kurz, and K. Köhler, *Phys. Rev. Lett.* **82**, 1044 (1999).
- ⁸S. Brivio, D. Polli, A. Crespi, R. Osellame, G. Cerullo, and R. Bertacco, *Appl. Phys. Lett.* **98**, 211907 (2011).
- ⁹W. Kaiser and R. Zurek, *Phys. Lett.* **23**, 668 (1966).
- ¹⁰M. Bargheer, N. Zhavoronkov, Y. Gritsai, J. C. Woo, D. S. Kim, M. Woerner, and T. Elsaesser, *Science* **306**, 1771 (2004).
- ¹¹M. Trigo, Y. M. Sheu, D. A. Arms, J. Chen, S. Ghimire, R. S. Goldman, E. Landahl, R. Merlin, E. Peterson, M. Reason, and D. A. Reis, *Phys. Rev. Lett.* **101**, 025505 (2008).
- ¹²I. Vrejoiu, M. Alexe, D. Hesse, and U. Gösele, *Adv. Funct. Mater.* **18**, 3892 (2008).
- ¹³H. Navirian, R. Shayduk, W. Leitenberger, J. Goldshteyn, P. Gaal, and M. Bargheer, *Rev. Sci. Instrum.* **83**, 063303 (2012).
- ¹⁴J. D. Choi, T. Feurer, M. Yamaguchi, B. Paxton, and K. A. Nelson, *Appl. Phys. Lett.* **87**, 081907 (2005).
- ¹⁵C. Klieber, E. Peronne, K. Katayama, J. Choi, M. Yamaguchi, T. Pezeril, and K. A. Nelson, *Appl. Phys. Lett.* **98**, 211908 (2011).
- ¹⁶M. Herzog, A. Bojahr, J. Goldshteyn, W. Leitenberger, I. Vrejoiu, D. Khakhulin, M. Wulff, R. Shayduk, P. Gaal, and M. Bargheer, *Appl. Phys. Lett.* **100**, 094101 (2012).
- ¹⁷C. Thomsen, H. T. Grahn, H. J. Maris, and J. Tauc, *Phys. Rev. B* **34**, 4129 (1986).
- ¹⁸M. Herzog, W. Leitenberger, R. Shayduk, R. van der Veen, C. J. Milne, S. L. Johnson, I. Vrejoiu, M. Alexe, D. Hesse, and M. Bargheer, *Appl. Phys. Lett.* **96**, 161906 (2010).
- ¹⁹M. Herzog, D. Schick, W. Leitenberger, R. Shayduk, R. M. van der Veen, C. J. Milne, S. L. Johnson, I. Vrejoiu, and M. Bargheer, *New J. Phys.* **14**, 013004 (2012).
- ²⁰M. Herzog, D. Schick, P. Gaal, R. Shayduk, C. von Korff Schmising, and M. Bargheer, *Appl. Phys. A* **106**, 489 (2012).
- ²¹A. Bojahr, D. Schick, L. Maerten, M. Herzog, I. Vrejoiu, C. von Korff Schmising, C. J. Milne, S. L. Johnson, and M. Bargheer, *Phys. Rev. B* **85**, 224302 (2012).
- ²²A. Bojahr, M. Herzog, D. Schick, I. Vrejoiu, and M. Bargheer, *Phys. Rev. B* **86**, 144306 (2012).
- ²³P. Gaal, D. Schick, M. Herzog, A. Bojahr, R. Shayduk, J. Goldshteyn, H. A. Navirian, W. Leitenberger, I. Vrejoiu, D. Khakhulin, M. Wulff, and M. Bargheer, *Appl. Phys. Lett.* **101**, 243106 (2012).
- ²⁴R. Shayduk, H. A. Navirian, W. Leitenberger, J. Goldshteyn, I. Vrejoiu, M. Weinelt, P. Gaal, M. Herzog, C. von Korff Schmising, and M. Bargheer, *New J. Phys.* **13**, 093032 (2011).
- ²⁵R. O. Bell and G. Rupprecht, *Phys. Rev.* **129**, 90 (1963).
- ²⁶N. D. Ashcroft and N. W. Mermin, *Solid state physics*, 1st ed. (Saunders College, Fort Worth, 1976).
- ²⁷I. R. Entin, *Phys. Status Solidi A* **106**, 25 (1988).
- ²⁸W. Sauer, T. H. Metzger, J. Peisl, Y. Avrahami, and E. Zolotoyabko, *Physica B* **248**, 358 (1998).
- ²⁹E. Zolotoyabko and J. P. Quintana, *J. Synchrotron Radiat.* **9**, 60 (2002).
- ³⁰B. Sander, E. Zolotoyabko, and Y. Komem, *J. Phys. D: Appl. Phys.* **28**, A287 (1995).
- ³¹E. Zolotoyabko and I. Polikarpov, *J. Appl. Crystallogr.* **31**, 60 (1998).
- ³²A. M. Lindenberg, I. Kang, S. L. Johnson, T. Missalla, P. A. Heimann, Z. Chang, J. Larsson, P. H. Bucksbaum, H. C. Kapteyn, H. A. Padmore, R. W. Lee, J. S. Wark, and R. W. Falcone, *Phys. Rev. Lett.* **84**, 111 (2000).
- ³³D. A. Reis, M. F. DeCamp, P. H. Bucksbaum, R. Clarke, E. Dufresne, M. Hertlein, R. Merlin, R. Falcone, H. Kapteyn, M. M. Murnane, J. Larsson, T. Missalla, and J. S. Wark, *Phys. Rev. Lett.* **86**, 3072 (2001).
- ³⁴J. Larsson, A. Allen, P. H. Bucksbaum, R. W. Falcone, A. Lindenberg, G. Naylor, T. Missalla, D. A. Reis, K. Scheidt, A. Sjögren, P. Sondhaus, M. Wulff, and J. S. Wark, *Appl. Phys. A* **75**, 467 (2002).
- ³⁵B. E. Warren, *X-ray diffraction*, 2nd ed. (Dover Publications, INC., New York, 1990).
- ³⁶A. Bojahr, M. Herzog, L. Maerten, D. Schick, J. Goldshteyn, W. Leitenberger, R. Shayduk, P. Gaal, I. Vrejoiu, and M. Bargheer (unpublished).
- ³⁷A. I. Akhieser, *Zhur. Eksp.: Teoret. Fiz.* **8**, 1330 (1938).
- ³⁸L. D. Landau and G. Rumer, *Phys. Z. Sovjetunion* **11**, 8 (1937).

Paper XV

Brillouin scattering of visible and hard X-ray photons from optically synthesized phonon wavepackets

A. Bojahr, M. Herzog, S. Mitzscherling, L. Maerten, **D. Schick**, J. Goldshteyn, W. Leitenberger, R. Shayduk, P. Gaal, and M. Bargheer

Opt. Express 21, 18 (2013)

Brillouin scattering of visible and hard X-ray photons from optically synthesized phonon wavepackets

A. Bojahr,¹ M. Herzog,¹ S. Mitzscherling,¹ L. Maerten,¹ D. Schick,¹ J. Goldshteyn,² W. Leitenberger,¹ R. Shayduk,² P. Gaal,² and M. Bargheer^{1,2,*}

¹*Institut für Physik & Astronomie, Universität Potsdam, Karl-Liebknecht-Str. 24-25, 14476 Potsdam, Germany*

²*Helmholtz Zentrum Berlin, Albert-Einstein-Str. 15, 12489 Berlin, Germany*

*bargheer@uni-potsdam.de

<http://www.udkm.physik.uni-potsdam.de>

Abstract: We monitor how destructive interference of undesired phonon frequency components shapes a quasi-monochromatic hypersound wavepacket spectrum during its local real-time preparation by a nanometric transducer and follow the subsequent decay by nonlinear coupling. We prove each frequency component of an optical supercontinuum probe to be sensitive to one particular phonon wavevector in bulk material and cross-check this by ultrafast x-ray diffraction experiments with direct access to the lattice dynamics. Establishing reliable experimental techniques with direct access to the transient spectrum of the excitation is crucial for the interpretation in strongly nonlinear regimes, such as soliton formation.

© 2013 Optical Society of America

OCIS codes: (290.5900) Scattering, stimulated Brillouin; (320.5390) Picosecond phenomena

References and links

1. H. J. Eichler, P. Günter, and D. W. Pohl, *Laser induced dynamic gratings*, vol. 50 of *Springer series in optical sciences* (Springer, Berlin [u.a.], 1986).
2. R. Vacher and L. Boyer, "Brillouin scattering: A tool for the measurement of elastic and photoelastic constants," *Phys. Rev. B* **6**, 639–673 (1972).
3. J. A. Rogers, A. A. Maznev, M. J. Banet, and K. A. Nelson, "Optical generation and characterization of acoustic waves in thin films: Fundamentals and applications," *Annual Review of Materials Science* **30**, 117–157 (2000).
4. V. Wang and C. R. Giuliano, "Correction of phase aberrations via stimulated Brillouin scattering," *Opt. Lett.* **2**, 4–6 (1978).
5. R. Y. Chiao, C. H. Townes, and B. P. Stoicheff, "Stimulated Brillouin scattering and coherent generation of intense hypersonic waves," *Phys. Rev. Lett.* 592–595 (1964).
6. K. A. Nelson, R. Casalegno, R. J. D. Miller, and M. D. Fayer, "Laser-induced excited state and ultrasonic wave gratings: Amplitude and phase grating contributions to diffraction," *J. Chem. Phys.* **77**, 1144–1152 (1982).
7. C. Thomsen, H. T. Grahn, H. J. Maris, and J. Tauc, "Surface generation and detection of phonons by picosecond light pulses," *Phys. Rev. B* **34**, 4129–4138 (1986).
8. H. N. Lin, R. J. Stoner, H. J. Maris, and J. Tauc, "Phonon attenuation and velocity measurements in transparent materials by picosecond acoustic interferometry," *J. Appl. Phys.* **69**, 3816–3822 (1991).
9. P. J. S. van Capel and J. I. Dijkhuis, "Optical generation and detection of shock waves in sapphire at room temperature," *Appl. Phys. Lett.* **88**, 151910 (2006).
10. P. J. S. van Capel, H. P. Porte, G. van der Star, and J. I. Dijkhuis, "Interferometric detection of acoustic shock waves," *J. Phys.: Conf. Ser.* **92**, 012092 (2007).

11. O. L. Muskens and J. I. Dijkhuis, "High amplitude, ultrashort, longitudinal strain solitons in sapphire," *Phys. Rev. Lett.* **89**, 285504 (2002).
12. P. J. S. van Capel and J. I. Dijkhuis, "Time-resolved interferometric detection of ultrashort strain solitons in sapphire," *Phys. Rev. B* **81**, 144106 (2010).
13. A. Bojahr, M. Herzog, D. Schick, I. Vrejoiu, and M. Bargheer, "Calibrated real-time detection of nonlinearly propagating strain waves," *Phys. Rev. B* **86**, 144306 (2012).
14. T. Pezeril, C. Klieber, S. Andrieu, and K. A. Nelson, "Optical generation of gigahertz-frequency shear acoustic waves in liquid glycerol," *Phys. Rev. Lett.* **102**, 107402 (2009).
15. M. Herzog, A. Bojahr, J. Goldshteyn, W. Leitenberger, I. Vrejoiu, D. Khakhulin, M. Wulff, R. Shayduk, P. Gaal, and M. Bargheer, "Detecting optically synthesized quasi-monochromatic sub-terahertz phonon wavepackets by ultrafast x-ray diffraction," *Appl. Phys. Lett.* **100**, 094101 (2012).
16. S. Brivio, D. Polli, A. Crespi, R. Osellame, G. Cerullo, and R. Bertacco, "Observation of anomalous acoustic phonon dispersion in SrTiO₃ by broadband stimulated Brillouin scattering," *Appl. Phys. Lett.* **98**, 211907 (2011).
17. E. Pontecorvo, M. Ortolani, D. Polli, M. Ferretti, G. Ruocco, G. Cerullo, and T. Scopigno, "Visualizing coherent phonon propagation in the 100 GHz range: A broadband picosecond acoustics approach," *Appl. Phys. Lett.* **98**, 011901 (2011).
18. W. E. Bron, "Spectroscopy of high-frequency phonons," *Reports on Progress in Physics* **43**, 301 (1980).
19. Z. Chen, B. C. Minch, and M. F. DeCamp, "High wavevector optical phonons in microstructured bismuth films," *Opt. Express* **18**, 4365–4370 (2010).
20. G.-W. Chern, K.-H. Lin, Y.-K. Huang, and C.-K. Sun, "Spectral analysis of high-harmonic coherent acoustic phonons in piezoelectric semiconductor multiple quantum wells," *Phys. Rev. B* **67**, 121303 (2003).
21. N. M. Stanton, R. N. Kini, A. J. Kent, M. Henini, and D. Lehmann, "Terahertz phonon optics in GaAs/AlAs superlattice structures," *Phys. Rev. B* **68**, 113302 (2003).
22. M. F. Pascual-Winter, A. Fainstein, B. Jusserand, B. Perrin, and A. Lemaître, "Spectral responses of phonon optical generation and detection in superlattices," *Phys. Rev. B* **85**, 235443 (2012).
23. T. C. Zhu, H. J. Maris, and J. Tauc, "Attenuation of longitudinal-acoustic phonons in amorphous SiO₂ at frequencies up to 440 GHz," *Phys. Rev. B* **44**, 4281–4289 (1991).
24. C. Klieber, E. Peronne, K. Katayama, J. Choi, M. Yamaguchi, T. Pezeril, and K. A. Nelson, "Narrow-band acoustic attenuation measurements in vitreous silica at frequencies between 20 and 400 GHz," *Appl. Phys. Lett.* **98**, 211908 (2011).
25. S. Ayrihac, M. Foret, A. Devos, B. Rufflé, E. Courtens, and R. Vacher, "Subterahertz hypersound attenuation in silica glass studied via picosecond acoustics," *Phys. Rev. B* **83**, 014204 (2011).
26. E. Burkel, "Phonon spectroscopy by inelastic x-ray scattering," *Rep. Prog. Phys.* **63**, 171 (2000).
27. P. Eisenberger, N. G. Alexandropoulos, and P. M. Platzman, "X-ray Brillouin scattering," *Phys. Rev. Lett.* **28**, 1519–1522 (1972).
28. A. M. Lindenberg, I. Kang, S. L. Johnson, T. Missalla, P. A. Heimann, Z. Chang, J. Larsson, P. H. Bucksbaum, H. C. Kapteyn, H. A. Padmore, R. W. Lee, J. S. Wark, and R. W. Falcone, "Time-resolved x-ray diffraction from coherent phonons during a laser-induced phase transition," *Phys. Rev. Lett.* **84**, 111–114 (2000).
29. D. A. Reis, M. F. DeCamp, P. H. Bucksbaum, R. Clarke, E. Dufresne, M. Hertlein, R. Merlin, R. Falcone, H. Kapteyn, M. M. Mumane, J. Larsson, T. Missalla, and J. S. Wark, "Probing impulsive strain propagation with x-ray pulses," *Phys. Rev. Lett.* **86**, 3072–3075 (2001).
30. K. Sokolowski-Tinten, C. Blome, C. Dietrich, A. Tarasevitch, M. Horn von Hoegen, D. von der Linde, A. Cavaliere, J. Squier, and M. Kammler, "Femtosecond x-ray measurement of ultrafast melting and large acoustic transients," *Phys. Rev. Lett.* **87**, 225701 (2001).
31. M. Bargheer, N. Zhavoronkov, Y. Gritsai, J. C. Woo, D. S. Kim, M. Woerner, and T. Elsaesser, "Coherent atomic motions in a nanostructure studied by femtosecond x-ray diffraction," *Science* **306**, 1771–1773 (2004).
32. M. Trigo, Y. M. Sheu, D. A. Arms, J. Chen, S. Ghimire, R. S. Goldman, E. Landahl, R. Merlin, E. Peterson, M. Reason, and D. A. Reis, "Probing unfolded acoustic phonons with x rays," *Phys. Rev. Lett.* **101**, 025505 (2008).
33. M. Herzog, D. Schick, P. Gaal, R. Shayduk, C. von Korff Schmising, and M. Bargheer, "Analysis of ultrafast x-ray diffraction data in a linear-chain model of the lattice dynamics," *Appl. Phys. A* **106**, 489–499 (2012).
34. A. Bojahr, D. Schick, L. Maerten, M. Herzog, I. Vrejoiu, C. von Korff Schmising, C. J. Milne, S. L. Johnson, and M. Bargheer, "Comparing the oscillation phase in optical pump-probe spectra to ultrafast x-ray diffraction in the metal-dielectric SrRuO₃/SrTiO₃ superlattice," *Phys. Rev. B* **85**, 224302 (2012).
35. H. J. Maris, "6 - interaction of sound waves with thermal phonons in dielectric crystals," in "Principles and Methods," vol. 8 of *Physical Acoustics*, W. P. Mason and R. N. Thurston, eds. (Academic Press, 1971), pp. 279–345.
36. A. Akhiezer, "On the absorption of sound in solids," *J. Phys. (USSR)* **1**, 277 (1939).
37. C. Herring, "Role of low-energy phonons in thermal conduction," *Phys. Rev.* **95**, 954–965 (1954).
38. A. Koreeda, T. Nagano, S. Ohno, and S. Saikan, "Quasielastic light scattering in Rutile, ZnSe, Silicon, and SrTiO₃," *Phys. Rev. B* **73**, 024303 (2006).
39. B. C. Daly, K. Kang, Y. Wang, and D. G. Cahill, "Picosecond ultrasonic measurements of attenuation of longitu-

- dinal acoustic phonons in Silicon,” Phys. Rev. B **80**, 174112 (2009).
40. M. Cardona, “Optical properties and band structure of SrTiO₃ and BaTiO₃,” Phys. Rev. **140**, A651–A655 (1965).
41. V. Mahajan and J. Gaskill, “Doppler interpretation of the frequency shifts of light diffracted by sound waves,” J. Appl. Phys. **45**, 2799 (1976).
42. O. L. Muskens and J. I. Dijkhuis, “Inelastic light scattering by trains of ultrashort acoustic solitons in sapphire,” Phys. Rev. B **70**, 104301 (2004).

1. Introduction

Brillouin scattering describes the inelastic interaction of photons with acoustic phonons, which can be excited or detected by this process. [1] It has important applications in the determination of elastic and photoelastic properties [2, 3] and is used for optical amplifiers or phase conjugation [4]. Stimulated Brillouin scattering can create intense hypersound waves [5], where the wavevector \vec{Q} can be selected by tuning the transient grating induced by two intersecting laser-pulses. The diffraction of a probe pulse then senses the presence of phonons with the imprinted phonon wavevector \vec{Q} [6]. Ultrashort laser pulse excitation of strongly absorbing materials or transducers on transparent substrates generates even larger phonon amplitudes up to 1% strain and can be detected by picosecond acoustics, the time-domain analog of Brillouin scattering [7, 8]. This proved advantageous for investigating anharmonic propagation and damping of phonons and has generated excitement about ultrashort acoustic solitons [9–13]. Similar to transient gratings, optical multipulse excitation enhances a certain wavelength in the hypersound wave [14, 15]. Recently optical broadband probe pulses were used to access many phonon wavevectors simultaneously in picosecond acoustics experiments. [13, 16, 17]

Visible light only interacts with bulk phonons near the Brillouin-zone center, unless impurities are used to enhance the spectroscopy [18]. Optical phonons with high wavevectors in Bismuth have been accessed by microstructuring the film under investigation [19]. The back-folding of the phonon dispersion relation in superlattices can convert acoustic phonons with large wavevector into quasi-optical phonons with detectably small wavevector [20–22]. Alternatively, the acoustic reflection from the backside of the sample or from an interface propagating back to the transducer yields reflectivity modulations of the transducer which can be detected by a probe pulse [23]. The pulse-echo technique was refined by introducing additional thin detector films and combined with acoustic pulse shaping [24] and was extended to the detection of shear waves in glycerol [14]. The Fourier-transform of real-time signals due to pulse-echoes at the transducer or from Brillouin scattering in the bulk yields the spectrum of acoustic phonons. The analysis of the reflection coefficient of such acoustic perturbations was recently discussed in detail [25].

In order to observe high phonon wavevectors in a bulk material directly, shorter probe wavelengths are needed. The phonon dispersion for larger wavevectors is measured by inelastic X-ray scattering, which is essentially Brillouin scattering of X-rays [26, 27]. The new millennium came along with the rapidly developing scientific field of ultrafast X-ray diffraction (UXRD), which allows direct measurement of the lattice oscillation amplitude associated with propagating strain pulses. [28–32] Very recently optically synthesized quasi-monochromatic phonon wavepackets in the 100 GHz range were clearly detected by UXRD as sidebands to bulk Bragg reflections [15].

In this paper we present a unifying view on UXRD and optical picosecond acoustics as two types of Brillouin scattering. The presence of monochromatic phonons in bulk SrTiO₃ is directly evidenced by the scattering of photons. The conceptually simple analysis provides a real-time perspective on the spectral shaping of high-frequency phonon wavepackets by tailored multipulse excitation. In particular, we demonstrate how the optical supercontinuum probe accomplishes a versatile simultaneous broadband sensing of *bulk* phonon wavevectors constituting a large amplitude phonon wavepacket that decays by anharmonic interactions. We

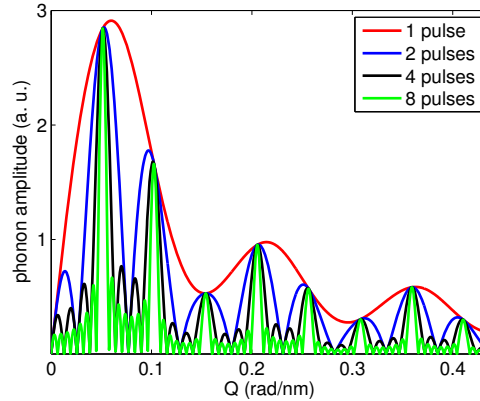


Fig. 1. **Calculated phonon spectra.** Spectral phonon amplitude present in the STO substrate after excitation of a 35 nm LSMO transducer by 1, 2, 4 and 8 pulses with a pulse spacing of $\Delta T = 15.4$ ps. All pulse sequences have the same integrated pulse energy.

believe that this combination of ultrafast X-ray- and optical broadband-detection of phonons will significantly enhance the confidence regarding interpretations of future optical picosecond ultrasound experiments. The supercontinuum detection scheme is also applicable to other quasiparticles such as magnons or polaritons which are generally identified by their dispersion relation $\omega(k)$. The wave-particle duality requires such wave-packet description, in which only a coherent excitation of a broad wavevector-spectrum allows for localization of quasiparticles. Real-time preparation and detection of such wavepackets will aid the understanding and controlling such excitations.

2. Synthesizing quasi-monochromatic phonons

We first discuss how to synthesize coherent quasi-monochromatic phonon wavepackets in the GHz - THz range, using a thin metal transducer of SrRuO₃ (SRO) or La_{0.7}Sr_{0.3}MnO₃ (LSMO) on the material of interest SrTiO₃ (STO). The absorption of an ultrashort light pulse leads to rapid expansion of the metal film. The good acoustic impedance matching of the SRO/LSMO transducer and the STO substrate suppresses reflections at the interface. [13, 33] Consequently, clean bipolar strain pulses without unintended replica are sent into the substrate. [7] The spatio-temporal dynamics can be simulated by a linear-chain model which includes the anharmonicity in the interatomic potentials [13, 33]. In the present simulations we neglected the anharmonic terms according to the moderate excitation fluence. Due to the very fast electron phonon coupling of SRO and LSMO the optically excited electrons are rapidly localized and consequently the spatial profile of the exciting stress corresponds to the absorption of light according to Lambert-Beer's law [34]. A single ultrashort laser pulse generates a broad phonon spectrum in the substrate. The red line in Fig. 1 shows the Fourier-transformed spatial strain pattern of the substrate only. If the heated transducer layer with thickness d is added to the analysis, a strong Fourier-component at $k = 0$ emerges because of the thermally expanded absorbing region. If the pump penetration depth $d_{abs} \gg d$ the calculated excited strain pattern of the substrate yields a bipolar strain pulse with a frequency spectrum centered around $Q = 0.74 \cdot \pi v_t / v_s d$ whereas for $d_{abs} \ll d$ the exponential shaped profile of the induced strain pulse have a spectral maximum at

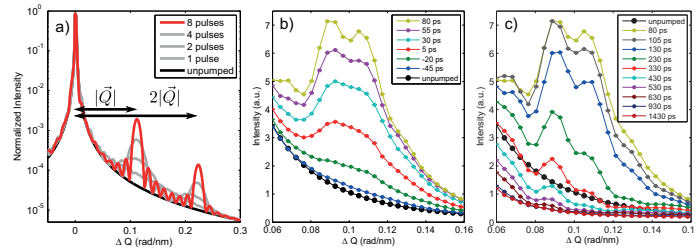


Fig. 2. Birth and decay of phonon-wavepackets observed by UXR. (a) Calculated X-ray diffraction pattern for an STO substrate with a coherent phonon spectrum excited by 1 to 8 pulses. (b) UXR data demonstrating the successive sharpening of the diffraction pattern with 8 excitation pulses separated by 7.2 ps. (c) Same UXR data for larger delay time t showing the decay of the coherent phonons.

$Q = v_t/v_s d_{abs}$. Here d , v_t and v_s are the thickness of the transducer film and the sound velocities of transducer and substrate in [001] direction, respectively. Our conditions are well described by the first limit value because $d_{abs} > d$. For longer excitation pulses, the phonon spectrum is suppressed for wavevectors Q corresponding to phonon frequencies $\omega > 2\pi/\tau_{pulse}$ where τ_{pulse} is the temporal duration of the pump pulse.

Successive excitation of the metal transducer with a sequence of light pulses equally spaced by ΔT in time generates a strain wave traveling into the substrate with a fundamental frequency $\nu = 1/\Delta T$ and contributions of its higher harmonics due to the sharp edges of the strain pulses. As an example we simulate the phonon spectra for a transducer thickness $d = 35$ nm and a pulse spacing of $\Delta T = 15.4$ ps. Figure 1 shows how additional pulses in the pump sequence sharpen the spectrum around $Q = 2\pi/\Delta T v_s$ and its higher harmonics by canceling the amplitude of other wavevectors. Note, that in Fig. 1 the integral pump energy is kept fixed in the simulation. As a consequence, the different pulse trains induce a constant phonon amplitude for the constructive interference, whereas the suppressed modes interfere destructively. Hence, for multipulse excitation, less energy is deposited in coherent phonons, compared to single pulse excitation with the same integral fluence. [33]

3. Inelastic light scattering from directed phonons

The energy quantum $\hbar\omega_s$ of such a strain wave is the longitudinal acoustic phonon with a magnitude of the wavevector $|\vec{Q}| = \omega_s/v_s$. Photons with wavevector \vec{k} are scattered by phonons with wavevector \vec{Q} only in accordance with the energy and momentum conservation. In a crystal with reciprocal lattice vectors \vec{G} , the equation for momentum conservation with \vec{k}' as the wavevector of the scattered photon reads

$$\Delta\vec{k} = \vec{k}' - \vec{k} = \vec{G} + \Delta\vec{Q}. \quad (1)$$

Here we discuss the situation where $\Delta\vec{Q} = \pm\vec{Q}$ is the momentum added to the scattering photon by the creation or annihilation of the particular phonon with wavevector \vec{Q} which was synthesized into the crystal. It is important to see that generating phonons with an optical transducer thin film breaks the symmetry, and only phonons with wavevector \vec{Q} directed into the crystal are generated. Figure 3(a) schematically shows how the creation of an additional phonon with wavevector \vec{Q} leads to a scattering with momentum transfer $\vec{G} + \vec{Q}$. In the geometry depicted in Fig. 3(a), i.e. for a phonon propagating into the crystal, the energy conservation imposes a constraint on the angular frequencies ω' of the scattered and ω of the incident photons:

$$\omega' - \omega = \begin{cases} \omega_s, & \text{if } \Delta\vec{Q} = +\vec{Q} \text{ ;phonon annihilation} \\ -\omega_s, & \text{if } \Delta\vec{Q} = -\vec{Q} \text{ ;phonon creation} \end{cases}, \quad (2)$$

because the stimulated emission of a phonon with wavevector \vec{Q} directed into the substrate acquires its energy from the scattering photon, whereas the annihilation of a phonon with the same \vec{Q} adds energy to the scattering photon and corresponds to a positive wavevector transfer $\Delta\vec{Q} = +\vec{Q}$.

These equations describe an inelastic scattering process which generally leads to an asymmetric scattering geometry, where the incoming and outgoing photon do not have the same angle with respect to the surface. However, the vast difference of the light and sound velocities implies a very small length change of the scattered photon wavevector with respect to the incident one. This quasi-elastic condition leads to a nearly symmetric scattering geometry with $\Delta\vec{k} = \vec{G} \pm \vec{Q}$.

4. Brillouin scattering of X-rays

We first discuss Brillouin scattering in the hard X-ray range [27]. The simulation of the UXRD signal is shown in Fig. 2(a) for the excitation with an increasing number of pump-pulses. All strain pulses have fully entered the substrate and in contrast to Fig. 1 the deposited fluence rises with each absorbed pulse. Figure 2(a) directly shows how the diffraction feature at $\vec{G} + \vec{Q}$ sharpens as more and more bipolar strain pulses are sculptured into the crystal. We performed the corresponding UXRD experiment at the ID09B beamline at the synchrotron source ESRF which provides ~ 100 ps hard X-ray pulses. The SRO transducer film was excited with eight pulses spaced by $\Delta T = 7.2$ ps, consistent with the calculation of Fig. 2(a). Details of the setup were discussed previously [15]. Here, we show an angular resolved analysis of the data recorded with 100 ps time resolution. The spectral narrowing of the feature around $\vec{G} + \vec{Q}$, is qualitatively confirmed in the experiment. When the synthesis of the quasi-monochromatic phonon wavepacket (Fig. 2(b)) was stopped after eight pulses, we observed that this sideband decayed (c.f. Fig. 2(c)) within 130 ps. This is not much longer than it took to create the wavepacket. The corresponding phonon decay is due to anharmonic phonon-phonon scattering processes within the STO substrate [35–39]. Up to now we have shown that the interference of sound waves (phonons) in the crystal created by multiple pulses in fact leads to the predicted quasi-monochromatic phonon wavepacket. UXRD directly measures the shaping of the quasi-monochromatic phonon spectrum in real time. Moreover, we showed that this wavepacket decays on a 100 ps timescale.

5. Brillouin scattering and picosecond acoustics

Now we turn to Brillouin scattering of optical photons from similar phonon wavepackets. In a classical interpretation of Brillouin scattering, the incident electromagnetic wave with wavelength $\lambda_m = \lambda/n(\lambda)$ in the material is diffracted from the Bragg grating given by the strain-induced refractive index modulation according to the photoelastic effect. Here λ and $n(\lambda)$ are the wavelength of the incident electromagnetic wave in vacuum and the wavelength dependent refractive index of the material, respectively. For visible light STO has a refractive index of $n \approx 2.4$. [40] The scattering angle is given by Bragg's law [1]

$$\lambda_m = 2\lambda_s \cdot \sin \theta, \quad (3)$$

implying that for a given scattering angle θ an optical photon with wavelength $\lambda_m = 2\pi n/|\vec{k}|$ is diffracted from a refractive index grating induced by phonons with wavelength $\lambda_s = 2\pi/|\vec{Q}|$ as schematically shown in Fig. 3(b). For a phonon propagating perpendicular to the sample

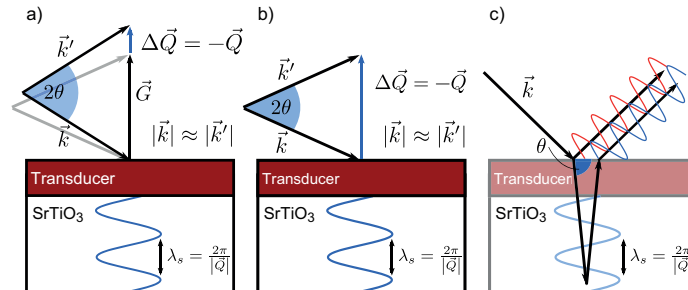


Fig. 3. **Schematics of Brillouin scattering and picosecond acoustics.** (a) Schematic of the inelastic X-ray scattering with creation of a phonon with wavevector $+\vec{Q}$. (b) Schematic of the Brillouin scattering with creation of a phonon with wavevector $+\vec{Q}$. (c) Schematic showing the interference of waves which is used for a time-domain explanation of the observed oscillations (see text).

surface the scattering angle θ is equal to the angle between the incident photon wavevector in the sample and the sample surface. This angle can be easily calculated by Snell's law. Given a strain wave propagating into the crystal, the scattered light undergoes a tiny Doppler-red-shift corresponding to the frequency of the moving sound wave, which can be detected by high-resolution Brillouin scattering experiments. [41, 42]

Eq. (3) is a direct result of the *optical* Laue-condition $\vec{k}' - \vec{k} = \pm\vec{Q}$, (Fig. 3(b)) under quasi-elastic scattering conditions ($|\vec{k}'| \approx |\vec{k}|$), and is in fact Eq. (1) describing Brillouin scattering with $\vec{G} = 0$. For a fixed angle θ Eq. (3) implies that an optical photon with wavelength λ specifically scatters from phonons with the wavevector magnitude

$$Q(\lambda) = \frac{4\pi}{\lambda} n(\lambda) \cdot \sin \theta. \quad (4)$$

For $n(\lambda) = 1$ Eq. (4) defines the well known scattering vector in elastic X-ray scattering theory.

Up to now we have adopted a perspective which is suitable for conventional Brillouin scattering experiments detecting the frequency shift of a narrow-band-laser. In optical picosecond acoustics experiments a laser pulse excites a short bipolar strain pulse with a broad spectrum (Fig. 1, red line). The detection by a time-delayed laser pulse is explained as follows: A part of the supercontinuum probe pulse is diffracted by the refractive index modulation associated with the propagating sound pulse fulfilling Eq. (4) and interferes with the reflection of the probe pulse at the sample surface (Fig. 3(c)). The moving sound pulse leads to a phase change of the diffracted wave which depends on the pump-probe delay t . The resulting intensity of the interfering electric fields is proportional to $\cos(\omega_s t) = \cos(2\pi t/T_s)$ with the period

$$T_s = \frac{\lambda}{2v_s n(\lambda) \sin \theta}. \quad (5)$$

For normal incidence T_s corresponds to the time a soundwave with wavevector \vec{Q} perpendicular to the surface needs to propagate one half of the optical wavelength λ_m . Combining Eqs. (4) and (5) leads to $v_s \cdot Q = 2\pi/T_s = \omega_s$. Hence ω_s is the angular frequency of the phonon with the wavevector \vec{Q} . Such oscillations are in fact observed in all-optical reflectivity experiments [13, 16] using a single optical pump pulse and an ultrashort broadband probe pulse. Figure 4(a) shows the recorded reflectivity change for the LSMO transducer on STO after subtraction of

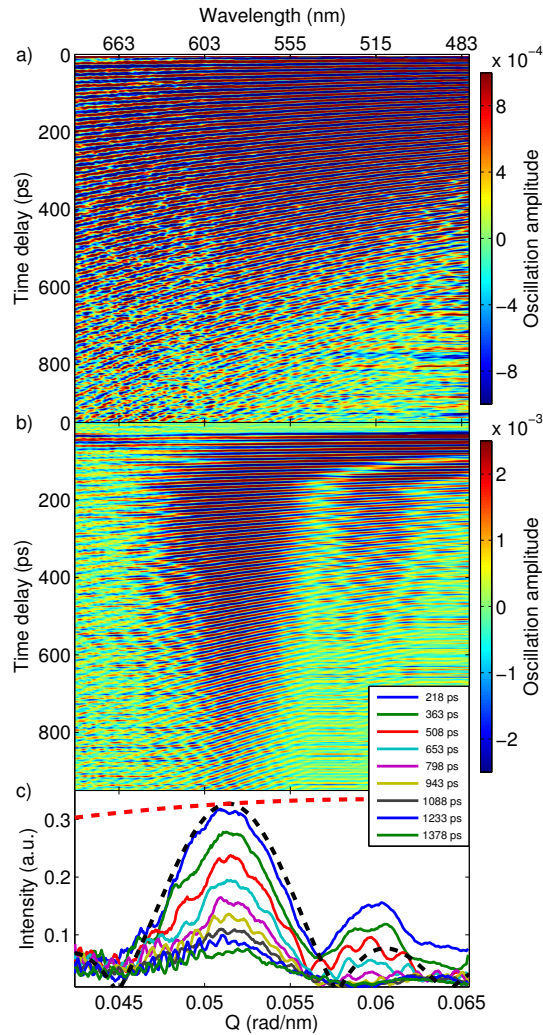


Fig. 4. **Experimental proof for the wavevector selectivity of supercontinuum probe pulses.** (a) Measured transient relative reflectivity change for single-pulse excitation as a function of the phonon wavevector given by Eq. (4). Slowly varying background is subtracted. (b) Same for an excitation with 8 pulses. (c) The dashed lines show the calculated spectral amplitude of the excited phonons for 1 (red dashed) and 8 (black dashed) excitations pulses (reproduced from Fig. 1). The solid lines show short-time Fourier transform data of Fig. 4(b). Each of the extracted datasets was multiplied with the probe wavelength to obtain a quantity proportional to the spectral amplitude of the coherent phonons.

a slowly varying electronic and thermal contribution to the signal. The observed oscillation period depends on the probe wavelength as predicted by Eq. (5) and extends across the entire visible spectrum according to the broad spectrum of the excited coherent phonons calculated to obtain the red line in Fig. 1. Here, Eq. (4) is applied to translate the optical probe wavelength λ into the phonon wavevector \vec{Q} .

6. Selectivity of the supercontinuum probe

Finally, we show that Brillouin scattering with broadband optical probe pulses not only has a mathematical one-to-one correspondence between the optical probe wavelength and a specific phonon with wavevector \vec{Q} (Eq. (4)) but that in fact individual wavevector components can be experimentally discriminated. Similar to the X-ray experiments shown in Fig. 2, we synthesized a monochromatic phonon via excitation of an LSMO transducer by a train of eight optical pump pulses ($\lambda = 800$ nm) with the pulse duration $\tau_{pulse} \sim 100$ fs and separation $\Delta T = 15.4$ ps. Figure 4(b) shows the relative reflectivity change of the sample. After $t \approx 150$ ps oscillations are mainly visible in the vicinity of $|\vec{Q}| = 0.05$ rad/nm. The black dashed line in Fig. 4(c), reproduced from Fig. 1, shows the idealized simulation of the coherent phonon spectrum in the substrate after 150 ps when all bipolar strain pulses have entered the substrate. The excellent agreement of the measured suppression of the reflectivity oscillations in certain wavelength regions of Fig. 4(b) with the simulated destructive interference in the phonon spectrum confirms both the wavevector-selective probing process and the shaping of quasi-monochromatic phonon wavepackets by tailored destructive interference. To support this argument we have extracted the spectral amplitude of oscillations observed in Fig. 4(b) by short-time Fourier-transform and multiplied the spectra by the wavelength of the probe light to get a quantity which is in first approximation proportional to the spectral amplitude of the occupied phonons. [7] The results plotted in Fig. 4(c) show good quantitative agreement of the measured spectra with the predicted spectrum (black dashed line). In particular, the measured spectral width of the main spectral component of the wavepacket exactly matches the prediction, demonstrating the simultaneous spatial and temporal resolution of the supercontinuum pump-probe setup. The higher amplitude of the secondary maximum is due to slight imperfections in the experimental optical pump pulse train, which leads to an imperfect destructive interference of phonon modes. Furthermore, Figure 4(c) directly measures the damping of the phonon amplitude in time. This is analogous to the measured phonon attenuation using UXR (Fig. 2(c)). In particular, both experiments show that high-frequency components of the wavepackets undergo stronger damping.

Scattering experiments using synthesized monochromatic phonon wavepackets thus show directly that both UXR and picosecond ultrasonics are wavevector-selective probes of ultrafast phonon dynamics, which are both described by Eq. (1). The difference of the two methods is that in the X-ray range we have selected the detected phonon wavevector \vec{Q} by tuning the Bragg angle, keeping the light wavelength fixed, whereas for the optical experiment we kept the angle of incidence fixed and measured a broad frequency range using a spectrometer. In principle, the experiments could also be carried out vice versa. More importantly, the absorption of the probe pulses is different. STO has essentially no optical absorption, while the penetration depth for hard X-rays is not larger than $10\mu\text{m}$. Generally, for very short sound wavelengths hard X-rays are definitely the only suitable choice, since the required VUV and XUV photons undergo very strong absorption.

7. Conclusions

In conclusion, we have given a unifying interpretation of ultrafast versions of Brillouin scattering in the ranges of optical and X-ray photon energies. We have synthesized large-amplitude quasi-monochromatic phonon wavepackets and proved that their spectrum and their anhar-

monic decay can be directly observed in both types of experiments. In particular, we showed that the optical supercontinuum is a direct, simultaneous and nonetheless selective real-time probe of the spectra composing a phonon wavepacket in bulk material. We confirmed this interpretation by comparison to UXR D experiments for which the direct access to the spectrum of the lattice strain is obvious. We think that this experimental confirmation will be essential for the interpretation of future experiments where wavevector-selective excitation and probing will be used to measure anharmonic and nonlinear phonon interactions in condensed matter. In particular, we envision experiments on nonlinear phononics as an analog of nonlinear optics, in which we observe sum and difference frequency mixing of synthesized phonons.

Acknowledgments

We thank M. Wulff and D. Kakhulin for their valuable contributions to the synchrotron experiments at the ESRF and I. Vrejoiu for sample growth. A.B. thanks the Leibniz graduate school “Dynamics in new Light” for financial support. This research was made possible through the funding by BMBF via 05K10IP1.

Paper XVI

Thermoelastic study of nanolayered structures using time-resolved x-ray diffraction at high repetition rate

H. A. Navirian, **D. Schick**, P. Gaal, W. Leitenberger, R. Shayduk, and M. Bargheer
Appl. Phys. Lett. under review, (2013)

Thermoelastic study of nanolayered structures using time-resolved x-ray diffraction at high repetition rate

H. Navirian,¹ D. Schick,^{1,*} P. Gaal,² W. Leitenberger,¹ R. Shayduk,² and M. Bargheer¹

¹*Institut für Physik und Astronomie, Universität Potsdam,*

Karl-Liebknecht-Str. 24-25, 14476 Potsdam, Germany

²*Helmholtz-Zentrum Berlin für Materialien und Energie GmbH,*

Wilhelm-Conrad-Röntgen Campus, BESSY II, Albert-Einstein-Str. 15, 12489 Berlin Germany

(Dated: June 17, 2013)

We investigate the thermoelastic response of a nanolayered sample composed of a metallic SrRuO₃ (SRO) electrode sandwiched between a ferroelectric Pb(Zr_{0.2}Ti_{0.8})O₃ (PZT) film with negative thermal expansion and a SrTiO₃ substrate. SRO is rapidly heated by fs-laser pulses with 208 kHz repetition rate. Diffraction of x-ray pulses derived from a synchrotron measures the transient out-of-plane lattice constant c of all three materials simultaneously from 120 ps to 5 μ s with a relative accuracy up to $\Delta c/c = 10^{-6}$. The in-plane propagation of sound is essential for understanding the delayed out of plane expansion.

PACS numbers:

Introduction

Ultrafast heat generation and transport in nanostructures are challenging the classical models of thermoelasticity. For nanosized structures, becoming as small as the heat carrying phonon mean free path, Fourier theory of thermal transport can differ dramatically from bulk samples.[1–4] The material properties on the nanoscale may also differ from equilibrium values for bulk material due to size effects or growth dependent interface resistance. Quasi-instantaneous heating, e.g. by ultrashort laser pulses may lead to non-equilibrium phonon distributions and is much faster than thermal expansion, which is limited by the speed of sound in the material. The resulting dynamic thermal expansion[5–7] due to impulsive thermal stresses has been studied extensively in the context of coherent phonon excitation.[8–11]

Besides the general physical interest, the knowledge of the structural response to instantaneous thermal stresses becomes important for the performance and reliability of novel applications in nanostructures such as optoelectronic devices, MEMS, SASER, and X-ray optics for free electron lasers, in which heat is generated on ultrafast timescales.[1, 2, 12, 13]

Numerical models for the calculation of the complete thermoelastic dynamics on the atomic level exist.[14] They require extensive computational power and a large number of material specific thermal and mechanical constants for an anisotropic sample geometry. Time-resolved experiments, which can access the material-specific structural information on the relevant length and time scales are an essential experimental cross-check for the complete understanding of the complex thermoelastic dynamics in flash-heated nanostructures.

In this study we applied ultrafast X-ray diffraction (UXRD) to measure the transient strains in three lay-

ers of a thin film heterostructure of functional oxide materials simultaneously by exploiting the material specific Bragg reflections. The large penetration depth of hard X-rays yields information also on the buried layers. The combination of ultrashort X-ray pulses with ultrafast Time-Correlated-Single-Photon-Counting (TCSPC) enables covering a pump-probe delay range of nearly five decades and ultra-sensitive detection of lattice constant changes down to $\Delta c/c = 10^{-6}$. Such precise and continuous experimental information provide an excellent experimental test ground for simulations which attempt the description of the physics involving the coupling of heat and strain in complex materials on several time- and lengths scales.

We focus on the experimental strategy and confirm the interpretation by comparing experimental data to a simplified numerical model[15], which treats heat transport and thermal expansion sequentially and briefly discuss the deviations which show the complex three dimensional nature of the problem. Although the thin film structure suggests that a reduced 1D model should be appropriate for short timescales, the comparison of experiment and simulation reveals more complex thermoelastic dynamics from the picosecond to microsecond time scales.

Experimental setup

The experiments were performed on a typical ferroelectric thin film structure. A ferroelectric Pb(Zr_{0.2}Ti_{0.8})O₃ (PZT) layer and a metallic SrRuO₃ (SRO) transducer layer were grown onto a SrTiO₃ (STO) substrate by pulsed laser deposition (PLD).[16] From the detailed characterization by transmission electron microscopy (TEM) and static X-ray diffraction (XRD) in Fig. 1, we derived the layer thicknesses of $d_{\text{PZT}} = 207$ nm and $d_{\text{SRO}} = 147$ nm, as well as the average lattice constants normal to the sample surface of $c_{\text{PZT}} = 4.130$ Å, $c_{\text{SRO}} = 3.948$ Å, and $c_{\text{STO}} = 3.905$ Å.[17]

The UXRD experiments were carried out at the EDR bending magnet beamline at BESSY II at Helmholtz Zentrum in Berlin. The details of the setup were described

*Electronic address: daniel.schick@uni-potsdam.de

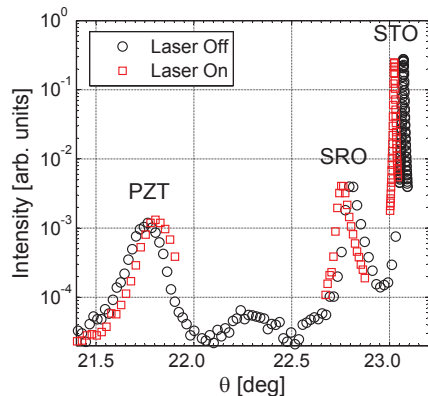


FIG. 1: (Color online) Static rocking curve of PZT, SRO, and STO (002) Bragg reflections (black circles) with no laser on the sample. The red squares show the peak shift of the individual Bragg peaks due to an average temperature increase of approx. 191 K for the laser-on state.

recently.[18] In order to probe a homogeneously excited sample area with 8.9 keV X-rays with a bandwidth of $\delta E/E = 2 \times 10^{-4}$ the beam is focused in the dimension perpendicular to the plane of diffraction and collimated in the diffraction plane down to a spot size of $50 \times 50 \mu\text{m}^2$. The symmetrically diffracted photons were collected by a point-detector with a plastic scintillator (< 0.5 ns rise time). For pumping the sample an Ytterbium-doped fiber oscillator and a three-stage-amplifier laser system were electronically synchronized to the master clock of the storage ring. The laser repetition rate was set to 208 kHz thus determining the pump-probe delay range to 4.8 μs . [18]. The pump pulses with maximum pulse energy $E_P = 10 \mu\text{J}$ at a wavelength $\lambda = 1030$ nm and pulse duration of $\tau = 250$ fs, were sent to the sample via a mechanical delay line.

Results & Discussion

The transient thermoelastic response of the sample is measured by scanning the material-specific (002) Bragg reflections for various pump-probe delays. The static rocking curve is shown in Fig. 1 as black circles. Although the sample is excited with femtosecond laser pulses, the static heat load due to the average pump power leads to a stationary heating and corresponding thermal strains according to the individual expansion coefficients observable by the shifted Bragg peaks (red squares) in Fig. 1. We use the literature value of the linear thermal expansion coefficients for STO and SRO (see Tab. I) to deduce the corresponding temperature rise of the whole sample by approx. $\Delta T = 190\text{K}$, starting from room temperature. For the transient experiments we used nearly two times smaller average laser power causing a smaller temperature rise of approx. $\Delta T = 84\text{K}$ (data not shown). Based on the derived ΔT and the PZT peak shift (Fig. 1), the average linear thermal expansion coefficient nor-

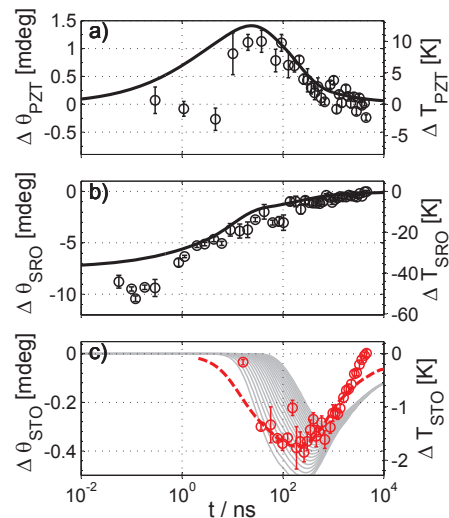


FIG. 2: (Color online) Extracted Bragg peak shifts for (a) PZT, (b) SRO, and (c) STO from the measurements (symbols, left vertical axis) and simulations of the average temperatures (solid lines, right vertical axis) for varying time delays. The right vertical axis assumes thermal expansion coefficients valid in thermodynamic equilibrium. In c) the grey lines indicate the temperature for sample depths from $z = 10$ to 1000 nm and the dashed red line is a simulation of the Bragg peak shift $\Delta\theta(t)$ using dynamical x-ray diffraction theory.

mal to the sample surface of PZT was determined to be approx. $\alpha_{\text{PZT}} = -1.1 \times 10^{-5} \text{K}^{-1}$ for $\Delta T = 190\text{K}$ and $\alpha_{\text{PZT}} = -0.66 \times 10^{-5} \text{K}^{-1}$ for $\Delta T = 84\text{K}$. This temperature dependent negative linear thermal expansion of PZT in z -direction is consistent with literature values for thin films. It is connected to its ferroelectricity which leads to a structural phase transition of the material from cubic to tetragonal below its Curie temperature of approx. 500°C . [19] Heating of PZT leads to a nearly negligible volumetric expansion of the material since the c -axis contraction is compensating the expansion in the a - b -plane while approaching the cubic phase. [19]

For the analysis of the transient rocking curves the Bragg peak shifts $\Delta\theta$ of the three layers after the laser pulse excitation were extracted by fitting the individual Bragg peaks by Gaussian functions. The resulting transients $\Delta\theta(t)$ for each material are plotted in Fig. 2. In total, we cover nearly five decades of time scales [18] without changing the experimental setup, i.e. comparing the diffraction curves for all time scales does not require any intensity scaling and all critical parameters such as the excitation fluence are constant.

The measured peak shift directly yields the strain in each layer via $\epsilon = -\Delta\theta \cot\theta$. [15] For some applications this is already the relevant parameter, as the strain is definitely responsible for the fatigue of high-frequency nan-

odevices. Assuming the literature values for the thermal expansion coefficients of the materials SRO and STO and using the measured value for α_{PZT} , we can moreover deduce the temperature rise $\Delta T = -\epsilon/\alpha$ and qualitatively discuss the observed thermal diffusion and the expected coupled thermoelastic dynamics, keeping in mind that the regular thermal expansion might have to be modified for short timescales if in fact the local population of phonons has strong non-equilibrium character and the thermal stresses are not relaxed yet. For direct reading of temperature changes we nonetheless add a vertical axis to the experimental data in Fig. 2.

The optical femtosecond pump-pulses are exclusively absorbed in the metallic SRO layer, thus rapidly heating this material. The initial expansion dynamics in SRO is beyond the time-resolution of 100 ps, and the associated strain waves were discussed previously.[17, 24] In this paper we focus on the nanosecond time scale. The SRO peak shift $\Delta\theta_{SRO} = 7\text{mdeg}$ at 1 ns observed in Fig. 2 a) implies a transient temperature rise of $\Delta T_{SRO} = 27\text{K}$ averaged over the SRO layer. Fig. 2 b) and c) confirm that at 1 ns the temperature of the adjacent STO and PZT still corresponds to $T = 293\text{K} + 84\text{K} = 377\text{K}$, elevated from room temperature according to the average thermal heating of the entire structure by the 208 kHz excitation seen in static experiments. Heat diffusion from the hot SRO to the adjacent materials leads to the cooling of SRO and a temperature increase in the PZT layer and STO substrate. In fact we can quantify their average heating after 100 ns to be $\Delta T_{PZT} = 6.6\text{K}$ and $\Delta T_{STO} = 1.5\text{K}$. Surprisingly, the heat essentially flows into the PZT layer, although its thermal conductivity is three times lower than that of the substrate (Table I). Moreover at this time the temperature of the PZT layer is higher than the initially excited metal layer: $\Delta T_{PZT}(100\text{ns}) > \Delta T_{SRO}(100\text{ns}) = 5.7\text{K}$. This is a consequence of cooling the sample via the substrate with essentially zero heat dissipation at the sample surface. This behavior is emphasized by the exponentially decaying temperature profile in the 147 nm thick SRO layer which essentially heats the material near the PZT interface. After about 2 μs the data show that the temperatures in the PZT and SRO layers have equilibrated with the substrate temperature ($\Delta T = 0.1\text{K}$) in the first micrometer, which is sensed by the x-rays. Finally, the transient heat load diffuses deeper into the STO substrate, where the extinction depth of the X-rays makes the thermal strains invisible to the current experiment.

While for delay times larger than 50 ns the measured out-of-plane strain can be consistently interpreted as thermal expansion, the situation is more complex for the earlier dynamics. Although the PZT lattice must undoubtedly be heated between 1 - 10 ns since the temperature of SRO is decreasing by about 30%, Fig. 2a) clearly shows no contraction of PZT during this time. In thermodynamic equilibrium the out-of-plane contraction of PZT goes along with an in plane expansion. For our experimental conditions a rough estimation of the

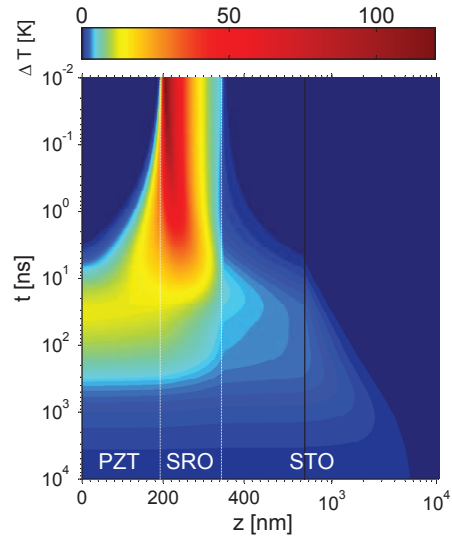


FIG. 3: (Color online) The 2D plot shows the results of the 1D heat equation over delay t and depth z . The color code is not linear. Parts of the x -scale are logarithmic for the STO substrate.

lower limit of the time it takes for the complete evolution of in-plane strains can be calculated from the probe diameter $d_{\text{probe}} = 50\text{ }\mu\text{m}$ and the sound velocity in SRO. The resulting travel time is approx. $t_{\parallel} = 8\text{ ns}$ and gives a lower limit of the lateral strains to evolve within the complete region of observation. This suggests that the epitaxially hindered in-plane expansion prevents the out-of-plane contraction to occur.

Simulation & Discussion

In order to confirm this interpretation, we compare the data with a simplified 1D heat diffusion simulation.[15] We calculate the laser-induced temperature jump in the metallic SRO layer from the material's optical penetration depth of 47 nm, its heat capacity and the laser fluence. The thermal diffusion is modeled by the 1D heat equation.[15] The result is shown in Fig. 3 as a color coded temperature on logarithmic time scale, as well as a logarithmic length scale for parts of the STO substrate. These simulations confirm the interpretations of the experimental data given above, in particular the inversion of the temperature rise in PZT and SRO. The exponentially decaying temperature profile in SRO leads to a very large temperature gradient towards PZT and to a weak gradient with respect to STO. This drives the predominant heat flow into PZT at times $t < 10\text{ ns}$. Around $t = 50\text{ ns}$ the temperature in PZT and SRO is nearly equilibrated and the only direction for heat dissipation is into the substrate.

For verification and analysis of our interpretation it is sufficient to extract the average heating of SRO and PZT from the heat diffusion simulation in Fig. 3 and plot it

	PZT	SRO	STO
<i>lin. therm. exp. coefficient</i> [1/K]:	-0.55×10^{-5} (fit/exp.)	0.88×10^{-5} (Ref. 20)	1×10^{-5} (Ref. 21)
<i>heat capacity</i> [J/mol K]:	120 (Ref. 22)	114 (Ref. 20)	128 (Ref. 21)
<i>thermal conductivity</i> [W/m K]:	3 (fit)	1 (exp.)	10 (Ref. 23)

TABLE I: Parameters for the simulation of the thermoelastic dynamics with according reference.

together with the measured heat expansion in Fig. 2, using the equilibrium expansion coefficients without additional scaling. The excellent agreement for $t > 10$ ns show the self-consistency of our analysis. On the interesting timescale 1 – 10 ns the simulation confirms that PZT is substantially heated after 5 ns, although the out-of plane strain is unchanged.

The analysis of the substrate peak is more complex. To highlight the problem, we compare the temperatures (grey lines in Fig. 2c) obtained in the simulation for different depths of the substrate to the measured peak shift using the bulk expansion coefficient of STO. Alternatively, we use the simulated strain profile to calculate the Bragg peak in the framework of dynamical diffraction and fit the peak position with the same procedure as the experimental data. The result is the red line in Fig. 2 c) which shows excellent agreement up to $t = 1 \mu\text{s}$. Such analysis, especially of the wings of the substrate peak, was discussed for the case of Si crystals.[25] At longer time-scales the heat has diffused into the crystal on the order of the pump-spot size the problem becomes 3D, explaining the deviation.

The structural parameters for the simulations were all determined by experiments[17], and the thermoelastic parameters were taken from literature, see Tab. I. Since all literature values for the simulations were measured statically and for bulk samples, the fit procedure[28] of the simulation started with the STO substrate Bragg peak shift for late times ($t > 10$ ns), see Fig. 2 c).

For a direct comparison of the heat diffusion model to the data on the shortest timescales we could calculate

the transient thermal stresses from the spatio-temporal temperature map and feed them into a 1D linear chain model (LCM) of masses and springs in order to account for the initial ultrafast phonon-dynamics.[26, 27] For the 1-10 ns timescale the restriction to one dimension would, however, still not allow for dissipation of in-plane stresses and we would require a dynamical 2D model.

Conclusion

We applied synchrotron-based UXRD experiments to simultaneously follow the out-of-plane thermal strains of three different materials in a thin film sample over nearly five decades of time scales. Material constants are either taken from literature or their measurement is inherent to the present experiment. The data show that the epitaxial connection to the substrate delays the out-of plane contraction of PZT by about 10 ns, because its in-plane expansion can only take place on the timescale of sound propagation through the excited area. Moreover the data evidences a transient inversion of the temperature gradient between the excited SRO and the initially cold PZT. Simple 1D simulations of the temperature profile confirm this feature and show excellent agreement with the data on intermediate times 10 ns - 1 μs in which the 1D approximation is valid. We believe that similar experiments have to be utilized as a reference for according thermoelastic models on the ultrafast time and nanometer length scales, because of the complexity of the included dynamics.

We thank Ionela Vrejoiu for providing the sample, and the BMBF for the funding via 05K2012 - OXIDE.

-
- [1] K. E. Goodson and Y. S. Ju, Annual Review of Materials Science **29**, 261 (1999).
 - [2] D. G. Cahill, W. K. Ford, K. E. Goodson, G. D. Mahan, A. Majumdar, H. J. Maris, R. Merlin, and S. R. Phillpot, Journal of Applied Physics **93**, 793 (2003).
 - [3] M. E. Siemens, Q. Li, R. Yang, K. A. Nelson, E. H. Anderson, M. M. Murnane, and H. C. Kapteyn, Nature materials **9**, 26 (2010).
 - [4] M. N. Luckyanova, J. Garg, K. Esfarjani, A. Jandl, M. T. Bulsara, A. J. Schmidt, A. J. Minnich, S. Chen, M. S. Dresselhaus, Z. Ren, et al., Science **338**, 936 (2012).
 - [5] D. W. Tang, B. L. Zhou, H. Cao, and G. H. He, Applied Physics Letters **59**, 3113 (1991).
 - [6] Y. C. Lee, Journal of physics. Condensed matter : an Institute of Physics journal **21**, 325702 (2009).
 - [7] S. Stoupin, A. March, H. Wen, D. Walko, Y. Li, E. Dufresne, S. Stepanov, K.-J. Kim, Y. Shvyd'ko, V. Blank, et al., Physical Review B **86**, 054301 (2012).
 - [8] C. Thomsen, H. Grahn, H. Maris, and J. Tauc, Physical Review B **34**, 4129 (1986).
 - [9] O. B. Wright, Journal of Applied Physics **71**, 1617 (1992).
 - [10] C. Rose-Petrucci, R. Jimenez, T. Guo, A. Cavalleri, C. W. Siders, F. Rksi, J. A. Squier, B. C. Walker, K. R. Wilson, and C. P. J. Barty, Nature **398**, 310 (1999).
 - [11] J. Tang, The Journal of chemical physics **128**, 164702 (2008).
 - [12] A. Fainstein, N. Lanzillotti-Kimura, B. Jusserand, and B. Perrin, Physical Review Letters **110**, 037403 (2013).
 - [13] Y. V. Shvyd'ko, S. Stoupin, A. Cunsolo, A. H. Said, and X. Huang, Nature Physics **6**, 196 (2010).
 - [14] I. A. Veres, T. Berer, and P. Burgholzer, Ultrasonics **53**, 141 (2013).
 - [15] R. Shayduk, H. Navirian, W. Leitenberger, J. Gold-

- shteyn, I. Vrejoiu, M. Weinelt, P. Gaal, M. Herzog, C. von Korff Schmising, and M. Bargheer, *New Journal of Physics* **13**, 093032 (2011).
- [16] I. Vrejoiu, G. Le Rhun, N. D. Zakharov, D. Hesse, L. Pintilie, and M. Alexe, *Philosophical Magazine* **86**, 4477 (2006).
- [17] D. Schick, A. Bojahr, M. Herzog, P. Gaal, I. Vrejoiu, and M. Bargheer (2013), arXiv:1301.3336 [cond-mat.mtrl-sci].
- [18] H. Navirian, R. Shayduk, W. Leitenberger, J. Goldshteyn, P. Gaal, and M. Bargheer, *Rev. Sci. Instrum.* **83**, 063303 (2012).
- [19] P.-E. Janolin, B. Fraisse, F. Le Marrec, and B. Dkhil, *Applied Physics Letters* **90**, 212904 (2007).
- [20] S. Yamanaka, T. Maekawa, H. Muta, T. Matsuda, S. Kobayashi, and K. Kurosaki, *J. Solid State Chem.* **177**, 3484 (2004).
- [21] de Ligny D and P. Richet, *Physical review. B, Condensed matter* **53**, 3013 (1996).
- [22] G. a. Rossetti and N. Maffei, *Journal of Physics: Condensed Matter* **17**, 3953 (2005).
- [23] Y. Wang, K. Fujinami, R. Zhang, C. Wan, N. Wang, Y. Ba, and K. Koumoto, *Appl. Phys. Express* **3**, 031101 (2010).
- [24] D. Schick, P. Gaal, A. Bojahr, W. Leitenberger, R. Shayduk, A. Hertwig, I. Vrejoiu, M. Herzog, and M. Bargheer (2013), arXiv:1301.3324 [cond-mat.mes-hall].
- [25] B. C. Larson, T. White, T. Noggle, and J. Barhorst, *Applied Physics Letters* **42**, 282 (1983), ISSN 00036951, URL <http://link.aip.org/link/?APL/42/282/1\&Agg=doi>.
- [26] M. Herzog, D. Schick, P. Gaal, R. Shayduk, C. von Korff Schmising, and M. Bargheer, *Applied Physics A* **106**, 489 (2011).
- [27] M. Herzog, D. Schick, W. Leitenberger, R. Shayduk, R. M. van der Veen, C. J. Milne, S. L. Johnson, I. Vrejoiu, and M. Bargheer, *New Journal of Physics* **14**, 13004 (2012).
- [28] The main fit parameters were the absorbed fluence ($F = 1.8 \text{ mJ/cm}^2$) of the pump pulses as well as the thermal conductivity of PZT. The resulting $\kappa_{PZT} = 3 \text{ W/mK}$ agrees well with the range given in the literature. Although we have determined the linear thermal expansion coefficient of PZT as $-0.66 \times 10^{-5} \text{ K}^{-1}$ in the static measurements, we obtain slightly better agreement for a smaller value of $-0.55 \times 10^{-5} \text{ K}^{-1}$ to get the best fit for the transient experimental data. Experiments of our group on the heat diffusion of single SRO thin films on a STO substrate reveal a smaller thermal conductivity of SRO $\kappa_{SRO} = 1 \text{ W/m K}$ in contrast to the literature value of 5.9 W/m K for bulk SRO.[20]

A.2. X-ray spectra from different tape materials

In order to extend the applicability of the PXS a variation of the emitted X-ray energy and its spectral bandwidth is desirable. I have tested four different metal tapes for the applicability in the PXS in respect to their mechanical stability and X-ray yield. The new tape materials are aluminum (Al), nickel (Ni), brass (CuZn37), and bronze (CuSn6). The current tape material copper (Cu) serves as a reference and is also included in the two alloys brass and bronze. Accordingly, only the zinc (Zn) and tin (Sn) X-ray emission is evaluated for brass and bronze, respectively.

All of the tested tapes are suitable for the use in the PXS in respect to their flexibility and tear resistance. I have characterized the X-ray emission of the various metal tapes with two energy-dispersive X-ray diode detectors made of Si (XR-100CR, AMPTEK INC.) for the low energy range of 1 keV to 10 keV with a resolution of 145 eV and CdTe (XR-100T-CdTe, AMPTEK INC.) for the high energy range of 1 keV to 100 keV with a resolution of 1.2 keV. The according spectra are depicted in Fig. A.1 and Fig. A.2. The main criteria for the applicability of the tape materials, the energy and the maximum X-ray yield of the most intense specific K_α line-emission, are given in Tab. A.1.

Element	Al	Ni	Cu	Zn (brass)	Sn (bronze)
K_α energy [eV]	1486	7478	8047	8638	25271
K_α flux [ph/s 4π sr]	7.1×10^9 *	2.5×10^{11}	5.0×10^{10}	3.1×10^9	9.1×10^7

Table A.1.: Energy of the element-specific K_α X-ray line-emission and the maximum achievable X-ray flux of these lines for the various metal tapes.

*Since the Al K_α line was not detectable with the setup, we integrate the flux of the Al bremsstrahlung over the equivalent energy interval of the Cu K_α line instead.

In conclusion, all of the tested metal tapes are suitable for the application in the PXS. The nickel and brass tapes provide strong characteristic line-emission (Ni K_α and Zn K_α) close to the Cu K_α line. In contrast, when using bronze X-ray energies of up to 25.2 keV from the Sn K_α line can be reached, whereas the X-ray flux could be further improved by choosing different bronze alloys. Aluminum has a very low-energetic K_α line at 1.4 keV which is hard to utilize due to the strong absorption in air and plastics. However, the intense and homogeneous bremsstrahlung background renders aluminum as an alternative tape material for spectroscopic applications.

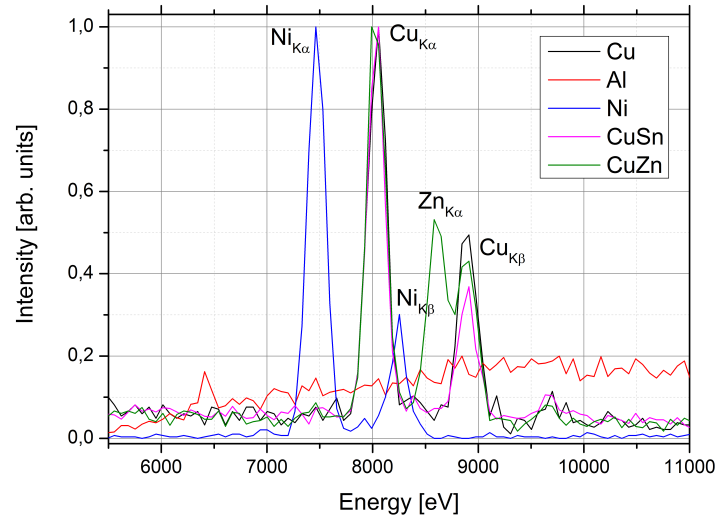


Figure A.1.: X-ray emission spectra of the various metal tapes in the range of 5500 eV to 11 000 eV recorded with the XR-100CR detector.

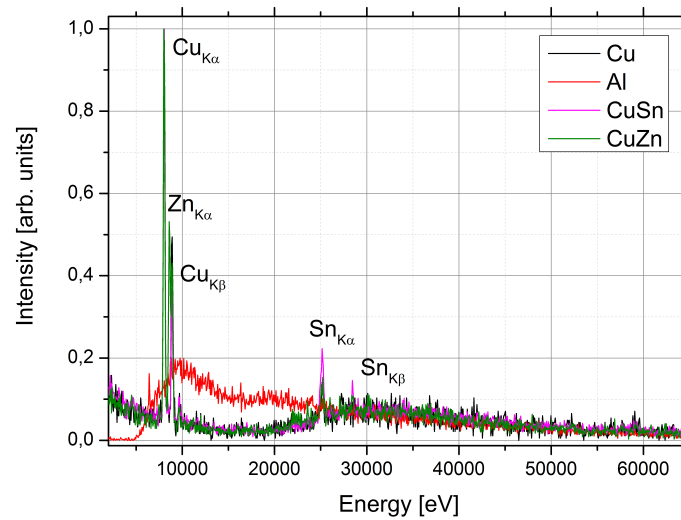


Figure A.2.: X-ray emission spectra of the various metal tapes in the range of 2000 eV to 65 000 eV recorded with the XR-100T-CdTe detector.

A.3. Low-temperature ultrafast X-ray diffraction data

In order to study low-temperature phases of solids with UXRd techniques, I have implemented a cryogen-free cryostat at the PXS. As a first reference experiment I measured the intensity oscillations of SL Bragg peaks due to the photoexcitation of a zone-folded longitudinal acoustical phonon (ZFLAP) mode [34] in a multilayer structure at different temperatures. This SL is made of 15 double layers of which each consists of 7.3 nm metallic $(\text{La}_{0.7}\text{Sr}_{0.3})\text{MnO}_3$ (LSMO) and 13.7 nm ferroelectric $(\text{Ba}_{0.7}\text{Sr}_{0.3})\text{TiO}_3$ (BST) epitaxially grown onto a SrTiO_3 (STO) substrate. The static rocking curve of the sample as measured at the PXS is shown in Fig. A.3. The individual SL Bragg peaks are labeled according to Ref. 99. The blue curve represents a simulation of the X-ray diffraction (XRD) response of the static structure and agrees well with the experimental data. When the sample is excited with a 800 nm pump pulse only the metallic LSMO layers are heated and expand. Eventually, an anti-phase oscillation of the individual layer thicknesses in each double layer builds up, which corresponds to the ZFLAP mode as described in Section 3.2. As a result the transient reflectivity of the individual Bragg peaks of the SL can change significantly on a femtosecond time scale [Paper IX, 62] as it is indicated by the red curve in Fig. A.3 for a tensile strain of 1 % in LSMO.

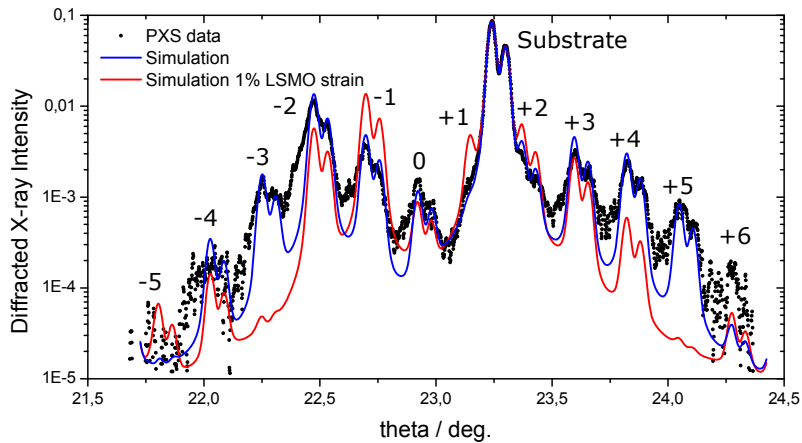


Figure A.3.: Experimental rocking curve of the LSMO/BST SL sample measured at the PXS (black dots). The SL Bragg peaks are enumerated according to Ref. 99. The blue line corresponds to a dynamical X-ray simulation assuming a perfect sample structure. The red line is a simulation additionally assuming a tensile strain of 1 % in the LSMO layers.

First, I have measured the integrated intensity of three different SL Bragg peaks as a function of pump-probe delay at room temperature. The period of these intensity oscillations of approx. 3.9 ps is equal to the period of the ZFLAP mode, c.f. Fig. A.4. However, the amplitude, sign, and waveform of these oscillations depend strongly on the

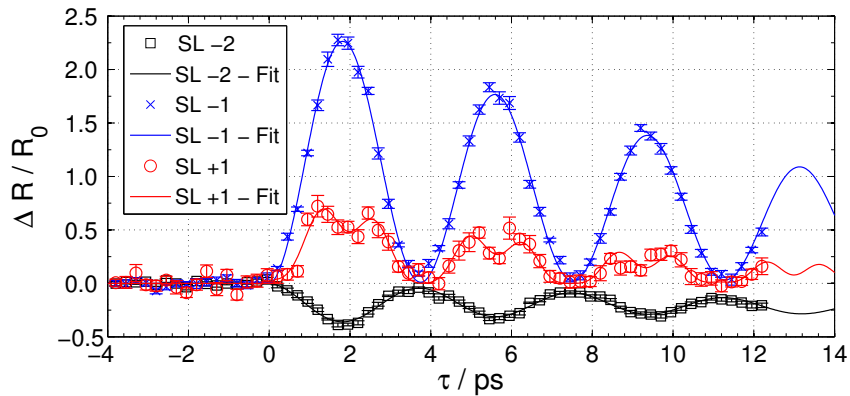


Figure A.4.: Intensity oscillations of three different SL Bragg peaks measured at the PXS at room temperature (symbols) and according fits of the data (solid lines).

location of the according SL Bragg peaks in reciprocal space and are not discussed in detail here.

I applied the cryostat setup to measure the SL-1 Bragg peak intensity oscillation within a temperature range of the sample from 35 K to 325 K. The experimental data was further fitted to extract the oscillation period and amplitude, whereas the latter corresponds to the maximal change of the relative reflectivity $\Delta R/R_0$. The comparison of the amplitude-normalized oscillation at 35 K and 300 K, shown in Fig. A.5, reveals a significant difference of the oscillation period for these two temperatures.

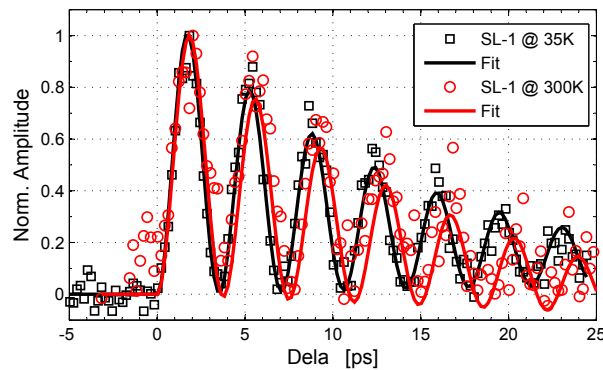


Figure A.5.: The intensity oscillations of the SL-1 Bragg peak at 35 K and 300 K show a significantly different oscillation period. The experimental data (symbols) is fitted (solid lines) and scaled in intensity for better comparison.

The evaluation of the oscillation amplitude and period for more selected temperatures is depicted in Fig. A.6. The decrease of the oscillation period is accompanied by a maximum

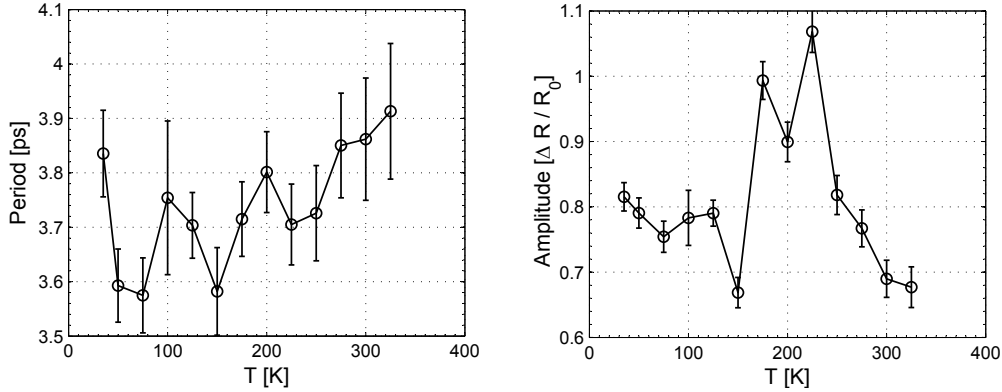


Figure A.6.: The period and amplitude of the SL-1 Bragg peak oscillation is determined by fits of the data for sample temperatures ranging from 35 K to 325 K. The oscillation period decreases from 3.9 ps to 3.6 ps with decreasing temperature. The oscillation amplitude encounters a maximum between 180 K and 250 K. The solid lines are guides to the eye.

of the oscillation amplitude between 180 K and 250 K. The amplitude and period of these Bragg peak intensity oscillations are directly linked to the photoexcited coherent phonons. On the one hand, LSMO is in its ferromagnetic phase below room temperature [100] and hence the excitation of coherent phonons should not change abruptly. On the other hand, BST undergoes a cubic-to-tetragonal phase transition at approx. 280 K, a tetragonal-to-orthorhombic phase transition at approx. 250 K, and an orthorhombic-to-trigonal phase transition at approx. 200 K [101].

In a simple model, the elastic constants in the BST layers change, i.e. they become softer, in the low-temperature phases between 180 K and 250 K which leads to a larger expansion of the neighboring LSMO layers after photoexcitation. As a result the oscillation amplitude increases. The change of the oscillation period mainly depends on the longitudinal sound velocities.

In conclusion, the low-temperature cryostat setup at the PXS was applied successfully to determine the temperature-dependent period and amplitude of an SL Bragg peak intensity oscillation. The observed temperature-dependence of these oscillation parameters can be linked to the structural phase transitions of the BST layers in the SL below room temperature. However, the influence of the ferromagnetism of the LSMO and the ferroelectricity of the BST layers have to be evaluated in more detail. Additionally, the substrate can change the strain states of the SL structure at low-temperatures due to the epitaxial constraints. In accordance to Paper V we are also able to verify the temperature-dependence of the SL oscillations by means of all-optical spectroscopy at low temperatures.